Cranfield University

Christian KNIPPRATH

Mechanical Performance of Binder Yarn Composites

School of Applied Sciences

PhD

Cranfield University
School of Applied Sciences
Department of Materials - Composite Centre

PhD Thesis

Academic Year 2009/2010

Christian KNIPPRATH

Mechanical Performance of Binder Yarn Composites

Supervisor
Dr Alexandros A. SKORDOS

May 2010

This thesis is submitted in partial fulfillment of the requirements for the Degree of Doctor of Philosophy

Abstract

This investigation concerns the mechanical response of binder coated carbon tow preforms and laminates. The main focus is on evaluating and modelling the robustness of preforms whilst the methodologies developed are also applied to cured laminates produced using the binder coated preforms. Conventional manufacturing techniques were altered to address the differences in behaviour due to the presence of the binder with the development of infusion schedules. These involve lower temperatures, which eliminate the possibility of binder reactivation during processing. Different development versions of the material in the form of an inhomogeneously or homogeneously bindered tow were characterised in terms of their mechanical response in the preform state. It was observed that the inhomogeneously bindered material had higher modulus and strength in both tension in the fibre direction and shear, while the behaviour of the homogeneous preform is significantly more robust in the transverse to the fibre direction. Laminates produced, using the homogeneously bindered material, were compared to a reference unbindered laminate system, using an aerospace epoxy as a matrix. The out-of-plane properties of the material with binder were superior to the reference laminate, whereas in-plane properties were similar or inferior. The development of models of the mechanical response built around continuum damage mechanics models allowed the simulation of the behaviour of preforms under loading. The implementation of these constitutive models necessitated the development of appropriate parameter estimation techniques capable of solving the inverse problem of identifying the values of 27 material constants that minimise the error between experimental and modelling results. Two novel methodologies were developed and compared to a conventional technique following simplified laminate analysis. The first method performed a gradient-based error minimisation and the second uses the Markov Chain Monte Carlo technique. The gradient-based technique results in a close fit, while this method requires proper definition of the constraints to yield an appropriate solution set. Markov Chain Monte Carlo yields satisfactory results with the additional advantages of overcoming the ill-posedness of the inverse problem without regularisation and providing an output in the form of multivariate probability distributions that can be used directly in stochastic simulations. The material parameters obtained and the corresponding constitutive models were used in finite element models of the mechanical response of preforms and laminates. The models were based on the concept of a combination of shell elements representing sub-laminates and cohesive elements simulating the delamination behaviour of interfaces between them. The performance of the models was evaluated using the case of impact of a spar section for preforms and three point bending for the laminates. The agreement between experimental and simulation results was satisfactory. The validated model was used in the context of a design case study based on a helicopter pitch horn component. The aim was to use the results of a draping analysis in the finite element model to evaluate the effects of the assumption of nominal fibre orientations on design and to combine the results of drape optimisation in respect to fibre shear angle with finite element analysis incorporating damage. The results showed that the use of nominal fibre orientation predicts a good performance of the component, whereas the influence of optimising draping on the mechanical performance was inferior.

Für meine Eltern,Ulrich und Rosemarie,
sowie meinen Bruder Matthias.

Vielen Dank für die Unterstützung,
die ich all die Jahre bekommen habe.

Acknowledgements

I would like to express my gratitude to Dr Alexandros Skordos for his supervision and stimulating discussions. I am very grateful for his support and his endless efforts to improve and guide this work.

I would also like to thank Dr Anthony Pickett for his support on Pam-Crash™ related questions.

Furthermore, I would like to thank Gary Muir and Jim Hurley for all the training sessions on VARTM, manufacturing work and the many last minute jobs just before testing.

I would also like to thank my friends and colleagues that I met during the time that I spend at Cranfield University. Just to name a few. Thank you to: Mehdi Asareh, Usama Attia, David Ayre, Andrea Battisti, Francesca Bortolani, Elisabete Costa, Jerome Cretet, Giuseppe Dell'Anno, Lucia Fusco, Christian Geipel, Cian Harrington, Ben Hopper, James Lander, Jeremy Maginot, Silvia Marson, Andrew Mills, Michał Mleczko, Les Oswald, Ivana Partridge, Maria del Mar Salinas-Ruiz, Nicolas Sergent, Ippokratis Sitaras, Kevin Stevens, Gereon Stefer, János Szabó, Johannes Treiber and Jan Wolters.

I would especially like to thank my family Heather, Alexander, Ulrich, Rosemarie, Matthias, Michael, Jackie, Ashley for their support and patience and our cats Felix and Filou for being cats.

Contents

List of Figures

List of Tables

Nomenclature

Abbreviations

ACF	Autocorrelation function
CBT	Corrected beam theory
CCD	Charge-coupled device
CDM	Continuum damage mechanics
CFRP	Carbon fibre reinforced plastics
COG	Centre of gravity
DCB	Double cantilever beam
DIC	Digital image correlation
ECM	Experimental compliance measurement
ELS	End loaded split
ENF	End notch flexure
EPZ	Embedded process zone
ESEM	Environmental scanning electron microscope
FEM	Finite element method
GA	Genetic algorithm
LCM	Liquid composite moulding
LEFM	Linear elastic fracture mechanics
MCMC	Markov Chain Monte Carlo
NCF	Non-crimped fabric
PTFE	Polyterafluorethylene
ROI	Region of interest
RTM	Resin transfer moulding
SCG	Slow crack growth
SLB	Single leg bending
THP	Time history plot
UD	Unidirectional
VARTM	Vacuum assisted resin transfer moulding

VBA	Visual Basic for Applications
VCCT	Virtual crack closure technique

Operations

$[x]_y$	layup sequence for manufacturing, e.g. $[\pm 45°]_{2s} \rightarrow [+45°, -45°, +45°, -45°, -45°, +45°, -45°, +45°]$
$\langle x \rangle_+$	positive Heavyside function $= \begin{cases} x & \text{if} \quad x \geq 0 \\ 0 & \text{if} \quad x < 0 \end{cases}$
$\langle x \rangle_-$	negative Heavyside function $= \begin{cases} x & \text{if} \quad x < 0 \\ 0 & \text{if} \quad x \geq 0 \end{cases}$
$\dfrac{\partial}{\partial x}$	partial derivative
$\left.\dfrac{\partial}{\partial x}\right\|_y$	partial derivative at constant value y
$\boldsymbol{A} : \boldsymbol{B} = \boldsymbol{A}_{ij}\boldsymbol{B}_{ji}$	double scalar product of two tensors
$\|x\|$	absolute value
$\max(x, y)$	maximum function
$\min(x, y)$	minimum function
$\exp(x)$	exponential function
$\ln(x)$	logarithmic function, base e
$P(A)$	prior or marginal probability of A
$P(A\|B)$	conditional probability of A, given B

Latin characters

A	coupling factor between transverse and shear plastic strains
a	crack length
a_0	initial crack length
B	thermodynamic force conjugate of β stress transformation factor from classical laminate theory between-chain variance
B_a	simplified stress transformation factor from classical laminate theory
B_0	material constant in damage dissipation potential
b	coupling factor between transverse and shear damage width

C	compliance
c	material constant
$\boldsymbol{D}$	damage tensor
D	strain rate parameter
d	damage variable
	cross head displacement
E	elastic modulus
	energy
$\widetilde{E}$	effective elastic modulus
E_D	strain energy
E_f	flexural modulus
F	force
	model response
	energy dissipation function
f	yield criterion
G	shear modulus
G_{IC}	mode I critical energy release rate (or delamination toughness)
G_{IIC}	mode II critical energy release rate (or delamination toughness)
$\boldsymbol{H}$	damage force conjugate
h	specimen half thickness in delamination test
	height
	crack closure parameter
h_{cont}	contact thickness
i	counting index
K	large deflection correction for mode II delamination
k	counting index
L	specimen length for delamination specimens
	support span in three point bending test
l	free arm length for mode II delamination
m	exponent in plasticity power law
	counting index
	slope in mode II calibration plot
N	normal distribution
	load block correction factor for mode II delamination
n	counting index
$\bar{n}$	normal vector

P	probability
p	distribution
$\boldsymbol{q}$	kinematic plastic hardening variable
q	proposal distribution
R	thermodynamic force conjugate of α
r	Metropolis ratio
$\widetilde{R}$	effective thermodynamic force conjugate
$\widehat{R}$	estimated posterior variance
R_0	initial yield stress
$\widetilde{\boldsymbol{S}}$	fourth rank effective elastic stiffness tensor
s	acceptance probability for parameter exchange
s_j^2	within-chain variance of MCMC sequence
$Sens$	normalised parameter sensitivity
SI	sensitivity index
T	temperature parameter
t	time
	force in out-of-plane damage model
	specimen thickness
U	uniform distribution
u	displacement
V_f	fibre volume fraction
v	velocity
W	within-chain variance
$\widetilde{\boldsymbol{X}}$	thermodynamic effective force conjugate
x	coordinate
$\boldsymbol{Y}$	thermodynamic force conjugate
Y	thermodynamic threshold value
	experimental data
y	coordinate
Y_{12}^0	initial shear damage limit
Y_{12}^C	critical shear damage limit
Y_{12}^U	elementary shear damage fracture limit
Y_{22}^0	initial transverse damage limit
Y_{22}^C	critical transverse damage limit
Y_{22}^U	brittle transverse damage limit of the fibre/matrix interface
Z	thermodynamic variable

z	coordinate

Greek characters

α	scalar isotropic hardening variable
	acceptance probability
$\widetilde{\alpha}$	effective scalar isotropic hardening variable
β	scalar damage state variable
	coefficient in plasticity power law
	tempering parameter
γ	correction factor for non-linear fibre compression
Δ	crack opening displacement
	mode I correction factor deduced from the compliance-crack length plot
δ	displacement
$\bar{\delta}$	displacement vector
ε	random noise
$\boldsymbol{\varepsilon}$	strain tensor
$\boldsymbol{\varepsilon}^e$	elastic strain tensor
$\boldsymbol{\varepsilon}^p$	plastic strain tensor
$\dot{\varepsilon}$	strain rate
$\dot{\varepsilon}^e$	elastic part of strain rate
$\bar{\varepsilon}^p$	effective plastic strain
Θ	fibre angle
	parameter set
ν	Poisson's ratio
ρ	density
σ	scalar stress
	standard deviation
$\widetilde{\sigma}$	scalar effective stress
σ_{eq}	equivalent stress, e.g. von Mises stress
$\boldsymbol{\sigma}$	stress tensor
$\widetilde{\boldsymbol{\sigma}}$	effective stress tensor
σ_I	normal stress in out-of-plane damage model
σ_{II}	shear stress in out-of-plane damage model
τ	scalar shear stress
	time

$\boldsymbol{\chi}$	kinematic damage hardening variable
Ψ	Helmholtz free energy
Ψ^d	damage term of Helmholtz free energy
Ψ^e	elastic term of Helmholtz free energy
Ψ^p	plastic term of Helmholtz free energy
ψ_{ij}	element of MCMC sequence
$\bar{\psi}_{.j}$	within-chain mean value of MCMC sequence
$\bar{\psi}_{..}$	between-chain mean value of multiple MCMC sequences

Indices

Subscripts

Numbers used in combination with material properties indicate the material direction, e.g. E_{11} is the elastic modulus in 11-direction.

I	normal direction
II	shear direction
A	achieved value
L	longitudinal direction
max	maximal value
P	predicted value
$prop$	propagation value
s	symmetric ply layup
$start$	start value
T	transverse direction

Superscripts

0	undamaged/initial value
C	critical value
c	compression
d	damage part
e	elastic part
exp	experimental value
f	fibre direction
i	initiation value
	counting index

j	counting index
s	quasi-static value
t	tension
max	maximum value
mod	model response value
p	plastic part
U	ultimate value
u	ultimate value

1 Introduction

1.1 Background

Advanced continuous fibre composite structures find increasing use in the aerospace industry. Composites are the material of choice for many application in the aerospace industry. Their advantage over metals is related to the superior weight/performance ratio. This is reflected in the current aeroplane technology, e.g. Airbus A380 and A400M have 28% and 30% composite by weight whereas the Boeing 787 contains up to 50% by weight. The lighter structures enable the manufacturer to overcome the critical performance issues in aircraft design, such as weight reduction, operation distance and speed. Figure 1.1 illustrates the usage of materials considered in the design of a modern aircraft.

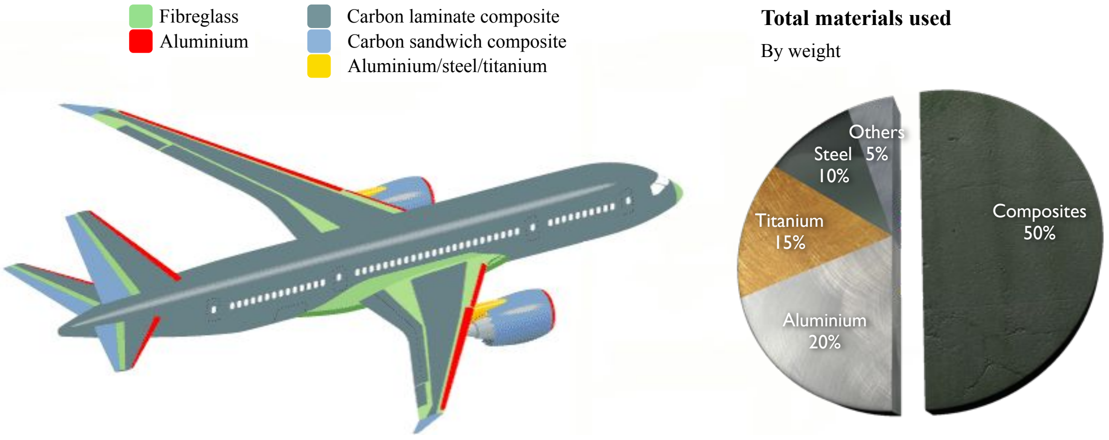

Figure 1.1: Materials used in modern aircraft design: Boeing 787.

Composite manufacturing processing routes used in the aerospace industry can be classified under two main categories:

1. Pre-preg lay up/autoclaving in which layers of pre-impregnated textile are laid up on a rigid tool and then covered by a vacuum bag and sealed. The assembly is placed in an autoclave where the simultaneous action of external pressure and vacuum is combined with heating to achieve consolidation of the

stack of pre-preg layers followed by curing which is initiated by the increased temperature.

2. Liquid composite moulding in which the reinforcement is in dry form usually as a woven or a non crimped fabric and the resin is in liquid form. The dry reinforcement is placed either in a rigid cavity or enclosed between a rigid tool surface and a vacuum bag and the low viscosity resin is infused under the action of vacuum, which in the case of full rigid tooling can be combined with elevated pressure applied to the liquid resin. The assembly is then heated to cure the material.

The lay up/autoclaving route offers a range of advantages, mainly linked to the fact that the resin is incorporated in the reinforcement prior to processing. This results in stabilisation of the fibres in their original positions and a limited degree of misalignment. Furthermore, the use of a high viscosity resin allows the use of toughening modifiers in the polymer formulation. Consequently, the combination of well controlled fibre orientation with tough resins results in the production of high performance composite materials. However, lay up/autoclaving requires a significant degree of manual work which increases processing costs and limits production rates. Liquid composite moulding on the other hand, offers opportunities for automation, minimisation of labour costs and increased production rates. These improvements come at a cost in performance, which is related to the need to handle the reinforcement in a dry form and the resin as a low viscosity liquid. The use of dry fabrics generates more fibre misalignment compared to autoclaving. In addition, the requirement for a low viscosity resin excludes possibilities for resin toughening via modification using high viscosity polymer or particles.

This work presented here is part of the framework 6 European project PreCarBi[1] [1]. The project partners involved in this project were: Toho Tenax Europe GmbH, Huntsman Advanced Materials, Cranfield University, University of Lativa, University of Patras, Swerea SICOMP, ESI Group, Airbus Germany, Airbus Spain, Eurocopter Germany, Fischer Advanced Composite Components AG and Sigmatex.
The main goal of this project is to overcome the performance limitations of composites produced via the liquid moulding route while keeping the process costs low. The potential improvement on process performance is based on the use of polymer binder coated fibre tows, which allow thermal activation and form a robust preform. The main benefit of such an approach is the capability to stabilise the fibre and

---

[1] Materials, Process and CAE Tools Developments for Pre-impregnated Carbon Binder Yarn Preform Composites

minimise fibre misalignment prior to the infusion. Activation of the binder could happen as part of a forming process resulting in the production of a shaped preform, which can be used in subsequent stages of manufacturing. Additional opportunities exist around this concept related to the possibility of incorporating toughening agents in the binder formulation. Such an approach would allow infusion of a low viscosity matrix, which would be modified by the binder upon heating. Processes using bindered preforms preserve all the automation and cost advantages of liquid moulding as the raw materials are still handled in the same way. Moreover, the ability to produce robust shaped preforms might result in process improvement with respect to transportation and storage conditions.

1.2 Aims and objectives

The main aim of this work **is to evaluate and simulate the mechanical behaviour of preforms and laminates manufactured using binder coated fibre tows**. To achieve this, a series of development objectives need to be addressed:

- Development of an experimental protocol for the investigation of the mechanical behaviour of bindered preforms
- Evaluation of the mechanical and damage response of bindered preforms
- Investigation of the effects of the presence of binder on mechanical properties
- Development of material models for damage simulation in preforms
- Development of estimation techniques for the identification of the parameters of composite and preform damage models
- Implementation of finite element simulations of the mechanical and damage response of preforms and laminates
- Validation of material and structural models developed

1.3 Road map

This thesis is organised in 8 chapters as follows:

Chapter 2 is divided into two parts. The first part concentrates on the review of modelling of the mechanical and damage response of composites using continuum models. The development of a thermodynamic framework including inelasticity effects due to plasticity for continuum damage modelling is described. In addition, a review of the testing and modelling of interlaminar mechanics for fibrous composites is presented. The second part provides a review on parameter identification techniques for composites materials. General approaches are presented as well as novel methods with the potential of application to the field, such as the Markov Chain Monte Carlo technique.

Chapter 3 details the materials and procedures used in this study. These include the testing protocols for the characterisation of preforms and laminates and validation of models as well as specimen manufacturing processes.

Chapter 4 reports the results of the experimental test programmes for the preforms and laminates of this study. The focus of this chapter is on the results necessary for parameter estimation in the context of finite element simulation, whilst the experimental results related to validation case studies are also described. Furthermore, a comparison of the response of different types of bindered preforms and of the response of bindered and unbindered laminates is carried out.

Chapter 5 describes the material models developed and the parameter estimation techniques used in this study and reports the results of parameter identification. The material models incorporate the in-plane damage response of the material and the out-of-plane delamination behaviour. Three different parameter estimation techniques are described with their corresponding results. These are the conventional method, a gradient-based error minimisation technique and a method based on Bayesian inference using MCMC.

Chapter 6 describes the finite element strategy used and reports the results of simulations for the validation studies considered as well as a component design case study based on a helicopter pitch horn component.

In chapter 7 an overall discussion of the main results and outcomes of the work is presented, whilst chapter 8 summarises the main conclusions of this work and reviews recommendations for further investigation arising from the results obtained.

Appendix A provides the list of publications related to this study and appendices B and C provide the computer codes used for the automated parameter estimation.

2 Literature review

This chapter reviews the literature in two fields. The framework for continuum damage models is presented first. Here the in-plane and out-of-plane aspects are presented leading to the constitutive damage models which are used. It should be noted that a variety of modelling methods, based on micro-mechanical concepts, are not addressed here as this study focuses on continuum representations. The second part addresses parameter identification techniques for finite element material models. In particular strategies used for composite materials are presented. This part is completed with the illustration of a method for the solution of inverse problems using Markov Chain Monte Carlo. This method is used extensively in particle physics and economics but finds increasing application to a variety of problems in engineering.

2.1 Continuum damage models for composites

This section describes the development of composite damage models addressing the effects for in- and out-of-plane response. For the in-plane direction the motivation and framework are described, which lead to the development of a thermodynamic constitutive damage model. Furthermore, the motivation and development of out-of-plane cohesive interface models is presented.

2.1.1 Thermodynamic framework for constitutive damage models

Two different approaches based on continuum mechanics can be followed for constitutive model development addressing damage coupled with inelasticity effects in a complex material such as composites. The first class of models is based on physical phenomena [2–6] based on Kachanov's [7] concept of effective stresses. The second class evolved within the context of a thermodynamic framework. In this work the focus is centered on the second class of models leading to the development of the Ladevèze model [8–10].

Since both damage (microcracks and microvoids) and inelasticity are present in the material during deformation, a constitutive model should address these two distinct physical modes and should satisfy the basic postulates of mechanics and thermodynamics [11]. This can be effectively achieved through thermodynamic principles [12–14]. In order to establish a constitutive material model which is based on a thermodynamic framework the governing equations are derived from the first and second laws of thermodynamics and the energetic potential expression such as the Helmholtz free energy. Furthermore the irreversibility of damage and inelasticity of the material is regulated by the Clausius–Duhem inequality, the maximum dissipation principle and the energy balance equation [15].

Two aspects need to be addressed when establishing a consistent thermodynamic framework with the aim of describing elastic-plastic material behaviour in combination with damage [16]. The first aspect is how damage effects are applied to the thermodynamic potential (state coupling). The second aspect deals with how the dissipated potentials are coupled (dissipation coupling).

2.1.1.1 Thermodynamic potential state coupling

The state coupling of the thermodynamic potential is possible by following two strategies. In both cases the starting equation is the potential energy which can be given in the form of the Helmholtz free energy as follows [12]:

$$\Psi = \Psi^{e}\left(\boldsymbol{\varepsilon}^{e}, \boldsymbol{D}\right) + \Psi^{p}\left(\boldsymbol{q}, \alpha\right) \tag{2.1}$$

Here $\boldsymbol{\varepsilon}^e$ is the elastic part of the strain tensor and $\boldsymbol{D}$ is the damage tensor which functions as a state variable for the elastic potential Ψ^e. The term Ψ^p corresponds to the plasticity component of the potential, which is associated with the kinematic plastic hardening variable $\boldsymbol{q}$ and the scalar isotropic plastic hardening variable α. In this form the potential considers the inelastic deformation due to plasticity and is also capable to represent the degradation of elastic material constants via the damage tensor. However, the damage tensor addresses the degradation of the elastic material properties due to plasticity [17–19]. Hence an additional term Ψ^d covering the damage effects due to microcracks and microvoids was introduced in [20, 21]. A scalar state variable β is allocated to this term to account for cumulative damage in analogy to the isotropic hardening variable α. In a more general case as presented in [11, 22] where both kinematic and isotropic hardening effects are considered the potential can be expressed as follows.

$$\Psi = \Psi^e \left(\boldsymbol{\varepsilon}^e, \boldsymbol{D}\right) + \Psi^p \left(\boldsymbol{q}, \alpha\right) + \Psi^d \left(\boldsymbol{\chi}, \beta\right) \tag{2.2}$$

The damage term is associated with the state variables β and $\boldsymbol{\chi}$ which is a damage hardening variable analogous to kinematic hardening. The effects of both damage and inelasticity on the elastic constants are represented by the damage tensor as proposed in [7, 23, 24] for an isotropic material. The generalisation for an anisotropic material was developed in [25–27].

In the second approach effective variables are used to couple the thermodynamic state of a damaged material. The classical variables $\boldsymbol{\varepsilon}^e$, $\boldsymbol{q}$ and α in the Helmholtz free energy with kinematic and isotropic hardening are replaced by their effective counterparts $\widetilde{\boldsymbol{\varepsilon}}^e$, $\widetilde{\boldsymbol{q}}$ and $\widetilde{\alpha}$. The damage values are directly applied within the calculation of the effective values. Thus, no additional terms are necessary and the effective values can be directly inserted leading to an expression similar to equation 2.1 [28].

$$\Psi = \Psi^e \left(\widetilde{\boldsymbol{\varepsilon}}^e\right) + \Psi^p \left(\widetilde{\boldsymbol{q}}, \widetilde{\alpha}\right) \tag{2.3}$$

With the use of the effective variables the damage tensor is also eliminated from the potential expression. Although the second approach allows a more compact definition of the potential the additional damage potential term allows more numerical flexibility when addressing dissipation coupling [11].

2.1.1.2 Potential dissipation coupling

Two possibilities exist for dissipation coupling in the form of strong and weak coupling. By using strong dissipation coupling both dissipation mechanisms are linked via a single smooth generalised yield surface and an associated flow rule for the plasticity and damage evolutions. This approach is only applicable for ductile materials, as these models cannot describe all loadings correctly since a hydrostatic stress causes damage before any plastic deformation occurs [28–30].

The weak plasticity/damage coupling approach is advantageous for application to composite materials [20, 22, 25, 31–34]. This approach introduces two independent flow rules in the form of dissipation functions F^p and F^d which address the energy dissipation due to plastic deformation and damage [25, 35]. These functions describe the separate plastic and damage dissipation surfaces, which can be visualised in stress space [36, 37]. For an anisotropic material with mixed hardening (kinematic and isotropic) these functions have the following form [11, 38]:

$$F^p = \sigma_{eq}\left(\widetilde{\boldsymbol{\sigma}} - \widetilde{\boldsymbol{X}}\right) - \left[R_0 + \widetilde{R}\left(\alpha\right)\right] = 0 \tag{2.4}$$

$$F^d = Y_{eq}\left(\boldsymbol{Y} - \boldsymbol{H}\right) + c\boldsymbol{H} : \boldsymbol{H} - \left[B_0 + B\left(\beta\right)\right] = 0 \tag{2.5}$$

Here σ_{eq} is the equivalent stress which is calculated from the effective stress tensors $\widetilde{\boldsymbol{\sigma}}$ and $\widetilde{\boldsymbol{X}}$ which is the effective back stress conjugate to $\boldsymbol{q}$ describing the kinematic hardening of the material. Term F^p describes the isotropic hardening, whereas R_0 is the initial yield stress and $\widetilde{R}$ the effective stress conjugate to α. In a similar fashion, functional F^d is composed of an equivalent stress term Y_{eq} addressing the evolution of the damage surface, which depends on $\boldsymbol{Y}$, the thermodynamic stress conjugate to the damage tensor $\boldsymbol{D}$ and the damage back stress $\boldsymbol{H}$ associated with the damage hardening tensor $\boldsymbol{\chi}$. Furthermore, the second term in equation 2.5 adjusts the units of the equation where c is a scalar material constant. The last term in equation 2.5 describes the evolution of the surface resulting from isotropic hardening due to damage.

The coupling of the two functions is achieved via the damage tensor $\boldsymbol{D}$ which is used in the calculation of the effective values in equation 2.4 and in the stress conjugate $\boldsymbol{Y}$ in equation 2.5. Here the equivalent stress corresponds to a criterion appropriate for the material, e.g. σ_{eq} could have the form of the von Mises yield criterion.

The state and dissipation potentials play a crucial role in the thermodynamic consistent formulation. By following irreversible thermodynamics on the basis of the Helmholtz potential the elastic state equations for a damaged material can be expressed as

$$\boldsymbol{\sigma} = \frac{\partial \Psi^e}{\partial \varepsilon^e} = \widetilde{\boldsymbol{S}}\left(\boldsymbol{D}\right) : \boldsymbol{\varepsilon}^e \tag{2.6}$$

where $\widetilde{\boldsymbol{S}}\left(\boldsymbol{D}\right)$ is the fourth rank effective elastic stiffness tensor [39]. Similarly, the thermodynamic conjugates of the state variables $\boldsymbol{q}$, α, $\boldsymbol{\chi}$, β and $\boldsymbol{D}$ can be obtained from equation 2.2 via partial differentiations as follows [11]:

$$\boldsymbol{X} = \rho\frac{\partial \Psi^p}{\partial \boldsymbol{q}} \quad , \quad R = \rho\frac{\partial \Psi^p}{\partial \alpha} \quad , \quad \boldsymbol{H} = \rho\frac{\partial \Psi^d}{\partial \boldsymbol{\chi}} \quad , \quad B = \rho\frac{\partial \Psi^d}{\partial \beta} \quad , \quad \boldsymbol{Y} = -\rho\frac{\partial \Psi^e}{\partial \boldsymbol{D}} \tag{2.7}$$

The restrictions of the second law of thermodynamics are incorporated in the classical formulation of Clausius-Duhem inequality. The formulation includes the information of the plasticity and damage evolution within the material [12] and is expressed as

$$\boldsymbol{\sigma} : \dot{\boldsymbol{\varepsilon}}^p - R\dot{\alpha} - \boldsymbol{Y} : \dot{\boldsymbol{D}} - B\dot{\beta} \geq 0 \quad . \tag{2.8}$$

This formulation can be extended in such a manner so that the state history is preserved via the introduction of two Lagrange multipliers, $\dot{\lambda}^p$ and $\dot{\lambda}^d$, which are linked to the flow rule expressions as follows [12, 40]

$$\boldsymbol{\sigma} : \dot{\boldsymbol{\varepsilon}}^p - R\dot{\alpha} - \boldsymbol{Y} : \dot{\boldsymbol{D}} - B\dot{\beta} - \dot{\lambda}^p F^p - \dot{\lambda}^d F^d \geq 0 \tag{2.9}$$

This expression can be used to derive the rate parameters by partial differentiation and maximisation. Following this approach the rate parameters can be defined in dependence of the plasticity and damage flow rules [33].

$$\begin{array}{lll} \dot{\boldsymbol{\varepsilon}}^p = \dot{\lambda}^p \dfrac{\partial F^p}{\partial \boldsymbol{\sigma}} & \dot{\boldsymbol{q}} = -\dot{\lambda}^p \dfrac{\partial F^p}{\partial \boldsymbol{X}} & \dot{\alpha} = \dot{\lambda}^p \dfrac{\partial F^p}{\partial R} \\ \dot{\boldsymbol{D}} = -\dot{\lambda}^d \dfrac{\partial F^d}{\partial \boldsymbol{Y}} & \dot{\boldsymbol{\chi}} = -\dot{\lambda}^d \dfrac{\partial F^d}{\partial \boldsymbol{H}} & \dot{\beta} = -\dot{\lambda}^d \dfrac{\partial F^d}{\partial \boldsymbol{B}} \end{array} \tag{2.10}$$

In this way the expressions can be used in combination with the Kuhn-Tucker [12] complementarity condition for both independent dissipation mechanisms as follows:

$$\begin{array}{lllll} \dot{\lambda}^p \geq 0 & , & F^p \leq 0 & , & \dot{\lambda}^p F^p = 0 \\ \dot{\lambda}^d \geq 0 & , & F^d \leq 0 & , & \dot{\lambda}^d F^d = 0 \end{array} \tag{2.11}$$

Equations 2.2 - 2.11 provide a full description of the evolution of the plasticity and damage flow rules.

2.1.2 Damage deactivation

The previous section assumes that the current plasticity/damage state is identical to the state at the end of the previous load step. This assumption remains valid regardless of whether the loading changes from tension to compression. However, if certain materials, including composites, are subjected to compression their undamaged stiffness is recovered due to the closure of microcracks. Thus, these materials recover their initial stiffness completely or partially while the damage state remains frozen [41–43]. Three damage deactivation models able to reproduce this effect are presented in the following.

2.1.2.1 Unilateral damage concept

The stress or strain tensor is split into a positive and negative part via a projection tensor in order to describe microcrack closures properly. Therefore a pair of projection operators are used for tensile and compressive loading [20, 44–46]. When the projection operator is applied only the positive or negative principal components of the strain or stress tensor are extracted. When a simple unilateral damage condition is used, it is assumed that negative principal components of the tensor remain unmodified as long as the loading condition remains.

With the aid of a unilateral damage parameter as introduced by [16, 35, 47] the expressions of the tensile and compressive projection operators can be merged into one operator that is applied to the stress or strain tensor. This simplification allows the transformation from principal stress space into general stress space.

However, this approach may lead to a non-symmetric effective stiffness matrix or to stress-strain discontinuities [48–51]. These discontinuities can occur when the unilateral damage condition influences both diagonal and off-diagonal components of the stiffness matrix and one of the principal strains changes sign whereas the other remain unchanged. To overcome this discrepancy the off-diagonal components of the constitutive matrix must be free from the damage deactivation term [39].

2.1.2.2 Discontinuous damage deactivation

Discontinuous damage deactivation in the case of a uniaxial stress is described in [23, 52]. The effective stress and the corresponding effective elastic modulus are defined as follows:

$$\widetilde{\sigma} = \frac{\sigma}{(1-d)} \quad \text{and} \quad \widetilde{E} = \frac{E}{(1-d)} \tag{2.12}$$

Here σ and E are the stress and the elastic modulus, which are unaffected by the damage variable d. These relations are only valid in cases where microcracks are independent of the loading condition so that a crack remains open under uniaxial compression. However, for some materials microdefects close under compressive loading. A crack closure parameter h is introduced to deal with the difference in tension and compression as follows [53, 54]:

$$h = \begin{cases} 1 & \text{tension} \\ 0 & \text{compression} \end{cases} \tag{2.13}$$

With this parameter it is possible to control the influence of the scalar damage parameter. Expression 2.12 can be rewritten as follows:

$$\widetilde{\sigma}^{\pm} = \frac{\sigma}{(1-dh)} \quad \text{and} \quad \widetilde{E}^{\pm} = \frac{E}{(1-dh)} \tag{2.14}$$

Figure 2.1 illustrates the behaviour of this formulation. The initial elastic modulus is degraded during tensile loading due to the accumulation of damage. During unloading of the material the effective elastic modulus defines the unloading path, however, the damage influence is deactivated when the material enters the compressive region.

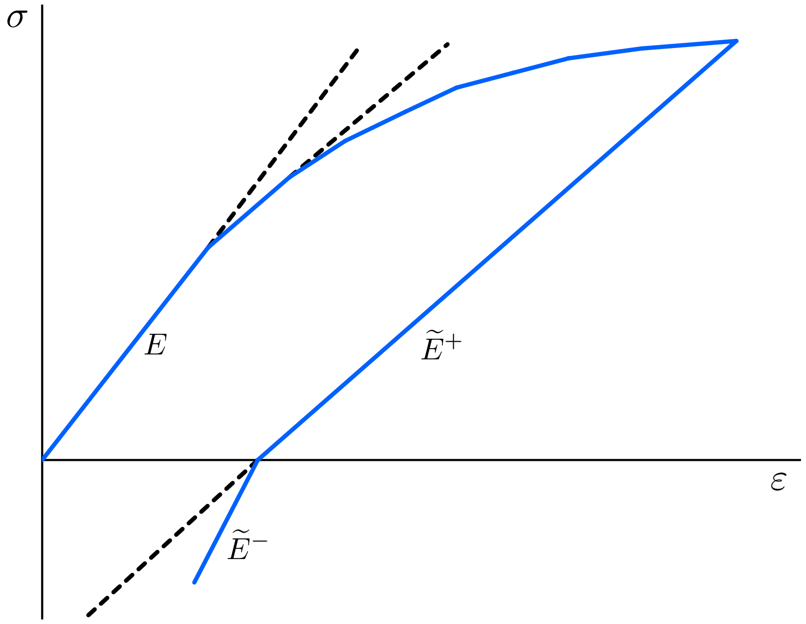

Figure 2.1: Effective elastic modulus with damage deactivation for the compressive region.

2.1.2.3 Continuous damage deactivation

The previous approach is not realistic for microdefects with complicated shapes that may not close completely in compression. A crack closure parameter h_c is defined for the compressive region in order to take such effects into account [55, 56]. Differentiation between tension and compression can be achieved as follows:

$$\widetilde{\sigma}^\pm = \begin{cases} \dfrac{\sigma}{(1-dh)} \\ \dfrac{\sigma}{(1-dh_c)} \end{cases} \quad \text{and} \quad \widetilde{E}^\pm = \begin{cases} \dfrac{E}{(1-dh)} & \text{tension} \\ \dfrac{E}{(1-dh_c)} & \text{compression} \end{cases} \tag{2.15}$$

In practice h_c is often considered a constant to address partial crack closure. For a variety of materials this parameter is set to $h_c = 0.2$ [55]. A bilinear unloading path can be generated following equation 2.15. During unloading the linear relation between stress and strain is given by the positive effective elastic modulus $\widetilde{E}^+$. When the material enters the compressive region the model switches to the compressive effective elastic modulus $\widetilde{E}^-$. However, real materials do not exhibit such bilinear curves, instead crack closure is a process that starts during unloading. The concept of continuous crack closure was proposed in [54] to deal with this effect. This method avoids an instantaneous switch between the two elastic moduli by replacing parameter h with a function $h(\sigma)$ which in its simplest form is linear:

$$h(\sigma) = h_c + (1 - h_c)\frac{\langle\sigma\rangle_+}{\sigma_b} \quad \text{with} \quad \langle x\rangle_+ = \begin{cases} x & \text{if} \quad x \geq 0 \\ 0 & \text{if} \quad x < 0 \end{cases} \tag{2.16}$$

Here σ_b denotes the stress referred to the beginning of unloading. Figure 2.2a illustrates the evolution of the crack closure parameter. Combining equations 2.16 and 2.14 yields a single expression for the modulus of elasticity, which is defined for the tensile and compressive region whist allowing a smooth transition between the two regions.

$$\widetilde{\sigma} = \frac{\sigma}{\left(1 - d\left(h_c + (1 - h_c)\frac{\langle\sigma\rangle_+}{\sigma_b}\right)\right)} \quad \text{and} \quad \widetilde{E} = \frac{E}{\left(1 - d\left(h_c + (1 - h_c)\frac{\langle\sigma\rangle_+}{\sigma_b}\right)\right)} \tag{2.17}$$

Figure 2.2b illustrates the unloading path which is generated when following the above definition for the crack closure behaviour.

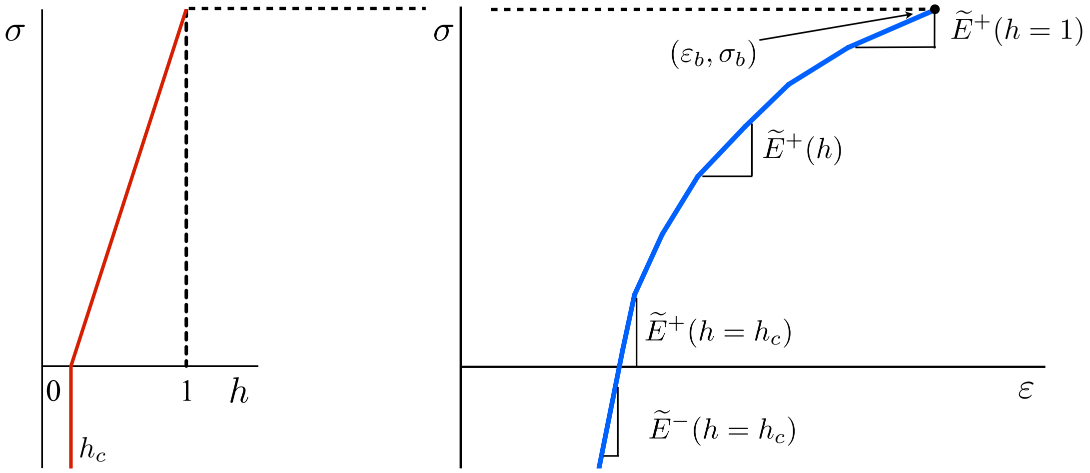

(a) (b)

Figure 2.2: Differentiation between tension and compression with continuous damage deactivation, (a) crack closure parameter for a given stress and (b) deduced effective elastic modulus and stress-strain curve with smooth tension/compression transition.

2.1.3 Ladevèze model

The framework presented in the previous section was adapted by Ladevèze [8, 57] for application to laminated composites. This model is very robust for predicting the response of damaged composites under a variety of conditions. It relies on the method of using state variables and associated thermodynamic forces to express the state of the material. It is based on the assumption of a uniformly distributed damage throughout the thickness of a ply. Damage processes that occur on the micro and mesoscopic scale are smeared within a continuum [8]. The model provides a homogenised representation of a single unidirectional ply where the through the thickness stress component σ_{33} is neglected under the assumption of a plane stress state. Nonetheless a downside of this model is that the fibre direction is uncoupled from the other material directions. Furthermore the Poisson's ratio ν_{12} remains unaffected from damage effects [58, 59].

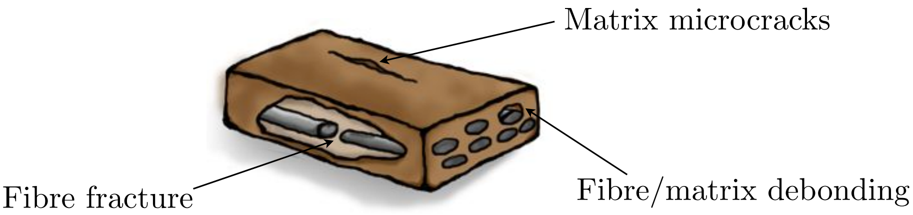

Figure 2.3: Possible types of damage within a ply considered by the Ladevèze in-plane damage model.

The model is capable of describing the following damage mechanisms (see figure 2.3):

Fibre-fracture which is the preferred damage mode from a design perspective as the fibre orientation is adapted for a certain load case and is intended to carry the load.

Matrix-microcracks which occur parallel to the fibre direction. This damage is primarily related to the matrix. However, the cracks can propagate through the component and lower the properties in the fibre direction significantly due to the lack of matrix support under compression.

Fibre/matrix-debonding which is a local separation of the two components and is caused by shear loading.

2.1.3.1 Constitutive law

The material state can be defined through the Helmholtz free energy potential as described in section 2.1.1. However, this energy functional is a theoretical expression and is difficult to validate. Therefore the expression for the strain energy is often used as an adequate representation [9, 31, 32, 60, 61]. The material model uses the following expression for the strain energy E_D of a single ply [8]:

$$E_D = \frac{1}{2}\left[\frac{\langle\sigma_{11}\rangle_+^2}{(1-d_1^{ft})E_{11}^{0t}} + \frac{\langle\sigma_{11}\rangle_-^2}{(1-d^{fc})E_{11}^{\gamma}} - \frac{2\nu_{12}^0}{E_{11}^{0t}}\sigma_{11}\sigma_{22} + \frac{\langle\sigma_{22}\rangle_+^2}{(1-d_2)E_{22}^0} + \frac{\langle\sigma_{22}\rangle_-^2}{E_{22}^0} + \frac{\tau_{12}^2+\tau_{13}^2}{(1-d_{12})\,G_{12}^0} + \frac{\tau_{23}^2}{G_{23}^0}\right] \tag{2.18}$$

Here σ_{ij}, τ_{ij} are the applied stresses, ν_{12}^0 is the undamaged Poisson's ratio in the $1,2$-direction, d_1^{ft}, d_1^{fc}, d_2 and d_{12} are the damage parameters for the respective directions of the material. The term $\left(1-\bar{d}\right)$ is applied to the related undamaged material constants E_{11}^{0t}, E_{11}^{γ}, E_{22}^0, G_{12}^0 and G_{23}^0. Heavyside functions are applied to the longitudinal and transverse direction to distinguish between tensile $\langle\sigma_{ij}\rangle_+$ and compressive $\langle\sigma_{ij}\rangle_-$ loading:

$$\langle\sigma_{ij}\rangle_+ \begin{cases} \sigma_{ij} & \text{if} \quad \sigma_{ij} \geq 0 \\ 0 & \text{if} \quad \sigma_{ij} < 0 \end{cases} \tag{2.19}$$

and

$$\langle\sigma_{ij}\rangle_- \begin{cases} 0 & \text{if} \quad \sigma_{ij} \geq 0 \\ \sigma_{ij} & \text{if} \quad \sigma_{ij} < 0 \end{cases} \tag{2.20}$$

For the transverse direction it is assumed that existing micro-cracks that may have occurred during tensile loading are closed. No further damage takes place during compression and the undamaged elastic modulus E_{22}^0 is not affected by the degradation term under compression. Two damage parameters are introduced in the fibre direction to address different damage states under tension and compression.

The constitutive law is obtained by calculating partial derivatives of the strain energy (see equation 2.18) with respect to each stress component σ_{ij} [62]. Under the assumption of a plane stress state the constitutive law for an orthotropic material can be written in the following form [63]:

$$\begin{Bmatrix} \varepsilon_{11}^e \\ \varepsilon_{22}^e \\ \gamma_{12}^e \\ \gamma_{23}^e \\ \gamma_{13}^e \end{Bmatrix} = \begin{bmatrix} \frac{1}{E_{11}} & -\frac{\nu_{12}^0}{E_{11}} & 0 & 0 & 0 \\ -\frac{\nu_{12}^0}{E_{11}} & \frac{1}{E_{22}} & 0 & 0 & 0 \\ 0 & 0 & \frac{1}{G_{12}^0} & 0 & 0 \\ 0 & 0 & 0 & \frac{1}{G_{23}^0} & 0 \\ 0 & 0 & 0 & 0 & \frac{1}{G_{12}^0} \end{bmatrix} \begin{Bmatrix} \sigma_{11} \\ \sigma_{22} \\ \tau_{12} \\ \tau_{23} \\ \tau_{13} \end{Bmatrix} \tag{2.21}$$

2.1.3.2 Damage evolution

The damage parameters are linked to the energetic dissipation of the material undergoing deformation. Within the Ladevèze model the energy dissipation of the matrix is represented by thermodynamic variables Z_2 and Z_{12} in the transverse and shear direction respectively. These variables are associated with the damage parameters d_2 and d_{12} [60]. Z_2 and Z_{12} are derived using partial derivatives of E_D with respect to the damage parameters:

$$Z_{22} = \left.\frac{\partial E_D}{\partial d_2}\right|_{\tilde{\sigma}, d_{12}} = \frac{1}{2} \frac{\langle \sigma_{22} \rangle_+^2}{E_{22}^0 \left(1 - d_2\right)^2} \tag{2.22}$$

and

$$Z_{12} = \left.\frac{\partial E_D}{\partial d_{12}}\right|_{\tilde{\sigma}, d_2} = \frac{1}{2} \frac{\tau_{12}^2 + \tau_{13}^2}{G_{12}^0 \left(1 - d_{12}\right)^2} \tag{2.23}$$

The thermodynamic variables are coupled to equivalent thermodynamic forces as follows [8]:

$$Y_{22}\left(t\right) = \begin{matrix} \max \\ \tau \leq t \end{matrix} \left(\sqrt{Z_{22}\left(\tau\right)}\right) \tag{2.24}$$

and

$$Y_{12}\left(t\right) = \begin{matrix} \max \\ \tau \leq t \end{matrix} \left(\sqrt{Z_{12}\left(\tau\right) + b Z_{22}\left(\tau\right)}\right) \tag{2.25}$$

In this formulation b is a weighting factor that governs the influence of the transverse component Z_2 on pure shear damage Z_{12} while t and τ denote the time. The equivalent thermodynamic forces Y_2 and Y_{12} define the damage state within a damage region for the two variables d_2 and d_{12} [39]. Hence d_2 is the damage parameter evaluating the transverse damage resulting from micro-cracks in the matrix parallel to the fibre direction and d_{12} is the parameter related to shear damage due to fibre/matrix debonding within the unidirectional ply. The following linear formulae are used to calculate the damage parameters for the current state [8]:

$$d_2 = \begin{cases} \dfrac{\langle Y_{22}\left(t\right) - Y_{22}^0 \rangle_+}{Y_{22}^C} & , \quad d_2 < d_{max} \wedge Y_{22}\left(t\right) < Y_{22}^U \wedge Y_{12}\left(t\right) < Y_{12}^U \\ d_{max} & \end{cases} \tag{2.26}$$

and

$$d_{12} = \begin{cases} \dfrac{\langle Y_{12}\left(t\right) - Y_{12}^0 \rangle_+}{Y_{12}^C} & , \quad d_{12} < d_{max} \wedge Y_{22}\left(t\right) < Y_{22}^U \wedge Y_{12}\left(t\right) < Y_{12}^U \\ d_{max} & \end{cases} \tag{2.27}$$

The set of threshold values Y_2^0, Y_2^C, Y_{12}^0 and Y_{12}^C defines the damage region of the material. Here, superscript 0 corresponds to the damage initiation threshold value, whereas superscript C defines the critical value threshold values. The brittle damage values Y_{12}^U for shear and Y_2^U for the fibre/matrix debonding complete the set of damage region threshold values.

2.1.3.3 Inelastic strains

The material model described in the previous section takes inelastic deformation into account. The total strain ε_i can be decomposed into an elastic and inelastic part to obtain the respective elastic strain ε_i^e and the corresponding plastic part ε_i^p.

$$\varepsilon_i = \varepsilon_i^p + \varepsilon_i^p \tag{2.28}$$

Most materials exhibit a nonlinear response when stressed beyond the elastic threshold stress. After this threshold is exceeded the material response can be described with a conventional strain hardening law where further hardening is governed by a yield criterion [64]. The following anisotropic Hill-type yield criterion is used:

$$f\left(\tilde{\sigma}, R\right) = \sqrt{\left[\frac{\tau_{12}}{(1-d_{12})}\right]^2 + A\left[\frac{\langle\sigma_{22}\rangle_+}{(1-d_2)} + \langle\sigma_{22}\rangle_-\right]^2} - R\left(\bar{\varepsilon}^p\right) \tag{2.29}$$

Parameter A is a coupling factor between shear and transverse plastic strains. Often the square root term is referred to as equivalent stress. This scalar value is compared to the current yield stress $R\left(\bar{\varepsilon}^p\right)$:

$$R\left(\bar{\varepsilon}^p\right) = R_0 + \beta\left(\bar{\varepsilon}^p\right)^m \tag{2.30}$$

Function $R\left(\bar{\varepsilon}^p\right)$ is an isotropic exponential hardening law which depends on the equivalent plastic strain $\bar{\varepsilon}^p$. The initial yield stress R_0 is the initial threshold value which defines the onset of yielding. Parameters β and m are scalar factors that define the gradient of the hardening curve. An example of a strain hardening curve following this law is shown in figure 2.4.

2.1.3.4 Fibre behaviour

For the fibre direction the Ladevèze model does not rely on a description via energetic state variables. Instead a set of threshold criteria with respect to the current strain defines the current damage situation. Furthermore, tension and compression are treated separately with different damage parameters. Under tension the fibres are

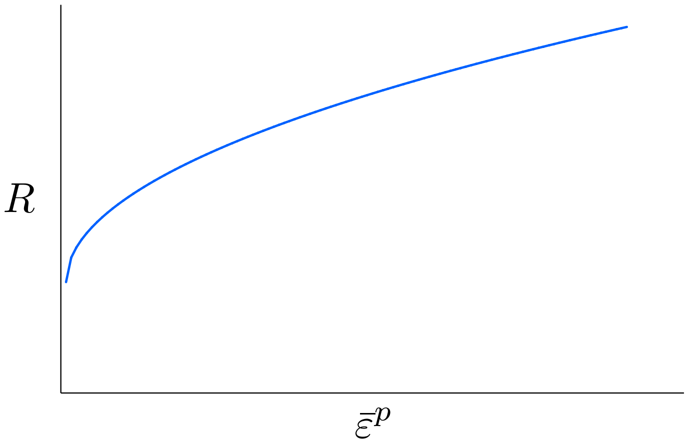

Figure 2.4: Typical strain hardening curve for composites in shear loading.

considered as undamaged until a threshold strain $\left(\varepsilon_i^{ft}\right)$ is exceeded. The strain range between ε_i^{ft} and ε_u^{ft} defines a region of linear damage growth. With increasing strain beyond ε_u^{ft} the damage parameter for tension $\left(d^{ft}\right)$ converges to 1 to enforce total damage. Thus, the material is unable to carry any load. The effective modulus in the fibre direction is calculated as follows, using E_{11}^{0t} as the undamaged tensile modulus:

$$\begin{aligned}
\text{pre-critical:} \quad & E_{11}^{t} = E_{11}^{0t} & & , \quad \varepsilon_{11} < \varepsilon_i^{ft} \\
\text{critical:} \quad & E_{11}^{t} = E_{11}^{0t}\left(1 - d^{ft}\right) \quad , \quad d^{ft} = d_u^{ft}\frac{\varepsilon_{11} - \varepsilon_i^{ft}}{\varepsilon_u^{ft} - \varepsilon_i^{ft}} & & , \quad \varepsilon_i^{ft} \leq \varepsilon_{11} < \varepsilon_u^{ft} \\
\text{post-critical:} \quad & E_{11}^{t} = E_{11}^{0t}\left(1 - d^{ft}\right) \quad , \quad d^{ft} = 1 - \left(1 - d_u^{ft}\right)\frac{\varepsilon_u^{ft}}{\varepsilon_{11}} & & , \quad \varepsilon_u^{ft} \leq \varepsilon_{11} < \infty
\end{aligned} \tag{2.31}$$

The compressive region is defined in a similar manner. Fibres exhibit a non-linear material behaviour under compression due to fibre misalignment and micro-buckling [3]. Parameter γ is used to control the initial compressive modulus in fibre direction E_{11}^{0c} as follows :

$$E_{11}^{\gamma} = \frac{E_{11}^{0c}}{1 + \gamma E_{11}^{0c}\left|\varepsilon_{11}\right|} \tag{2.32}$$

This effective modulus E_{11}^{γ} is then used to determine the compressive modulus E_{11}^{c} as a function of the strain ε_{11} as follows :

$$\begin{aligned}
\text{pre-critical:} \quad & E_{11}^{c} = E_{11}^{0\gamma} & & , \quad \left|\varepsilon_{11}\right| < \varepsilon_i^{ft} \\
\text{critical:} \quad & E_{11}^{c} = E_{11}^{\gamma}\left(1 - d^{fc}\right) \quad , \quad d^{fc} = d_u^{fc}\frac{\left|\varepsilon_{11}\right| - \varepsilon_i^{fc}}{\varepsilon_u^{fc} - \varepsilon_i^{fc}} & & , \quad \varepsilon_i^{fc} \leq \left|\varepsilon_{11}\right| < \varepsilon_u^{fc} \\
\text{post-critical:} \quad & E_{11}^{c} = E_{11}^{0\gamma}\left(1 - d^{fc}\right) \quad , \quad d^{fc} = 1 - \left(1 - d_u^{fc}\right)\frac{\varepsilon_u^{fc}}{\left|\varepsilon_{11}\right|} & & , \quad \varepsilon_u^{fc} \leq \left|\varepsilon_{11}\right| < \infty
\end{aligned} \tag{2.33}$$

The damage parameter is defined in the region $0 \leq d_u^{fc} \leq 1$ where 1 corresponds to total damage. Figure 2.5 shows a representative stress-strain curve for this model under tension and compression.

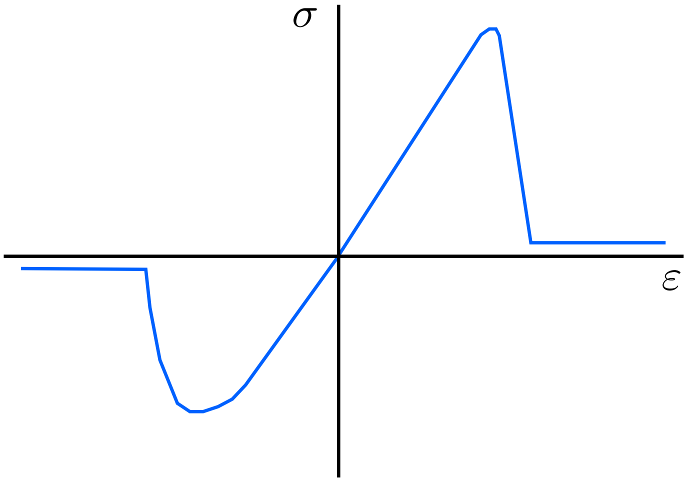

Figure 2.5: Characteristic response in the fibre direction under tensile and compressive loading.

2.1.4 Interlaminar damage mechanics for fibrous composites

2.1.4.1 Damage effects and experimental efforts

Delamination is a dominant form of damage that occurs in laminated composites and layered materials. Such damage can result from impact, blasts or manufacturing defects [65] and leads to a significant reduction of the material performance. Furthermore, it was observed that high stresses within the composite can cause delaminations, which may lead to localised buckling [66, 67]. The resistance of the material to delamination damage and its propagation is governed by the energy release rate for the specific failure mode.

One of the first indications of microscopic damage in laminates is transverse matrix cracking which can initiate other modes of damage such as delamination or fibre breakage. The energy release rate for further cracks and delamination initiation from the tips of existing transverse cracks can be evaluated based on the stress field obtained. However, the damage mode transition from transverse cracking to delamination cannot be expressed by the energy release rates [68, 69].

More complex behaviours are observed in engineering laminates, which have load case specific ply angles. Although a number of experimental studies indicate that the most conservative toughness values are obtained from tests on UD specimens by propagating the interlaminar crack in the fiber direction, there is growing experimental evidence that fracture toughness depends on the interface layup and the direction of the interlaminar crack propagation with respect to the reinforcement directions of the adjacent plies [70]. Brunner and Flüeler [71] explored some of the problems that arise when the standard mode I test method [72] is applied to engineering laminates. When a cross-ply laminate is subjected to biaxial tensile or thermal loading, damage occurs in the form of transverse cracking, splitting and strip-shaped delaminations at the 0°/90° interface. As a result, localised delaminations initiate and grow from the tips of transverse cracks and splits due to high local stresses [73]. The axial moduli of a laminate appear to be almost unaffected by splitting, whereas the value for the Poisson's ratio increases with the accumulation of transverse cracks. Transverse cracks in the 90° ply of cross-ply laminates are generated at lower strain levels under tensile load [74–76]. The transverse cracks cause interlaminar delamination and fibre breakage in the 0° ply at a higher applied strain. Existing models addressing these mechanisms assume homogeneous delamination patterns and are therefore too simplistic to reflect real damage in cross-ply laminates [74]. Moreover the catastrophic fracture of the laminates is caused by fibre breakage in the 0° ply. This event has been addressed in [77, 78].

The interaction between individual delaminations in the same layer was recently addressed in [65]. In these situations damage occurs as an area of parallel delaminations weakening the structure and has the potential to interact with other delaminations and to increase or possibly decrease the likelihood of delamination growth.

A standardised test procedure is only established for mode I delamination [72, 79], whereas in the case of mode II and III only recommendations for the experimental setup exist [80–82]. These test procedures help to classify a resin/fibre system and to determine the values for the critical energy release rate for each mode. The specimens are separated in the laminate mid-plane by a PTFE[1] film in order to create two sub-laminates. The test setups differ in the load introduction depending on the intended failure mode. Although the test recommendations for mode II and III are widely accepted and followed, a full understanding of the mechanical behaviour of the composite has not been developed. Discussions on whether existing methods capture pure mode II and III or whether these methods suffer from interactions with other mechanical phenomenon are ongoing [82, 83]. Delamination depends on effects such as surface morphology, cracking of the adjacent plies, fiber bridging as well as the delamination interface geometry. Traditional fracture toughness characterisation via UD laminates can lead to significant under- or overestimation of material resistance values due to these effects [70]. Blackman et al. [82] compared

---

[1] Polyterafluorethylene

the results for the critical energy release rate in mode II using different test methods. The method proposed for the determination of the values of G_{IIC} is the ELS[2] test. Furthermore, beam theory is used to avoid the need of measuring the crack length during the experiment.

2.1.4.2 Finite element approaches to address delamination effects

Modelling strategies

Fracture mechanics approaches are often used in the context of FE analysis for the simulation of delamination propagation. The employment of only stress-based criteria is not useful due to high stress gradients appearing at the crack fronts. The most prominent fracture mechanic method is the virtual crack closure technique (VCCT) which has been proposed by Rybicki and Kanninen [84] and Raju [85]. This method allows the computation of the energy released at the crack tip with a single calculation, based on the assumption of self-similar propagation. The physical interpretation of VCCT is that the energy released during a virtual crack extension by a length of Δa is equal to the work required to close the crack to its original length, while the external loading remains unchanged [86, 87]. The energies corresponding to mode I and II can be distinguished and computed as the sum of internal reactions at the crack tip and the difference between the displacements of selected nodes in the delaminated area before the tip. The energy released is then compared to the critical value or fracture toughness G_C, and the crack is advanced if this value is exceeded. Crack advancement requires remeshing of the finite element model, which is the greatest limitation of the technique. An extensive review on the method and its implementation to FE is given in [86].

Cohesive interface elements are increasingly used for modelling composites using FE, particularly in the context of delamination [88–91] and failure of adhesive bond-lines [92, 93]. This approach was first introduced by Dugdale [94] and Barenblatt [95]. The idea of this concept is that cohesive tractions act within the plastic deformation zone ahead of a crack tip. The underlying constitutive law relates the interfacial traction components to displacements. Delamination is initiated when the interlaminar traction attains the maximum interfacial strength, and the delamination front is advanced as the local surface fracture energy is consumed. The softening portion of the constitutive law accounts for the complex mechanisms occurring in the volume of material ahead of the crack tip by which large amounts of energy are absorbed in the fracture process [96]. The finite element implementation by Hillerborg et al. [97] was improved by Schellekens and De Borst [98] who were the first to propose a

---

[2] End-loaded Split

separate element for the interface. Further contributions from Wisnom et al. [99], Allix et al. [100], Camanho [101] and others were mainly related to the consideration of mixed-mode propagation.

While the application of the VCCT is limited to the tracking of a single crack path it is computationally effective. However, fracture mechanics does not incorporate the prediction of damage initiation and relies on predefined cracks. For several geometries in structures, these might be difficult to specify [102]. Unlike fracture mechanics, cohesive laws are able to predict both delamination onset and propagation by combining stress-strength-based and energy-based criteria [102]. Interface elements offer the advantage of including both crack initiation and propagation. Hence, computationally expensive crack-path following algorithms are not required. Cracks have the potential to propagate along any path where interface elements are placed, which is more representative of real propagation in composites [103]. However, when using cohesive elements to simulate the interface damage propagation, numerical instability problems arise. These are caused by an elastic snap-back instability. This effect occurs just after the stress reaches the peak strength of the interface. This problem becomes more pronounced for interfaces with high strength and high initial stiffness in combination with a relatively coarse mesh. The issue can be addresses with mesh refinement, however, such a step is costly in computational efficiency [104].

Modelling concepts

A major issue when using interface models is the parameter identification from experimental results [105]. The identification of interface models for composite delamination is complicated by the fact that the experiments cannot be directly done on the interface, hence indirect information must be derived from tests. Non-uniqueness of solutions and localisation problems can falsify the results. Although analytical models help to understand and predict the behaviour of the complete composite, they are often not able to explain the relevant mechanical interactions [106].

A notable amount of work has been performed to validate cohesive interface elements in simple test cases to investigate the use of different constitutive models for the interface elements [102, 107–110]. One common constitutive model is characterised by a linear degradation after the delamination onset [111, 112] whilst another possibility is to an exponential softening response [113].

An approach proposed for the incorporation of delamination in finite element simulations is the combination of shell elements and cohesive interfaces. Bruno et al. [114] generated a two-dimensional model containing multi-layered shell elements connected via interface elements in a similar was as presented in [60, 115]. The method resulted in more accurate energy release rate evaluation compared to results obtained with a local continuum approach. Allix and Blanchard [116] developed finite element models, also based on the cohesive interface concept, which work on the meso-scale level. These models describe the behaviour of a single ply to address the damage mechanisms such as fibre breakage, transverse micro-cracking and debonding of adjacent layers. More complex conditions were addressed in recent modelling studies. In [117] the interactions of multiple delaminations in cross-ply laminates were successfully simulated with cohesive interface elements. Furthermore, cohesive element based models showed good performance under impact conditions [108, 109, 118, 119].

2.2 Parameter identification techniques

2.2.1 Parameter estimation for composite materials

Traditional experimental methods for the determination of material properties aim to create homogeneous stress fields within a specimen. This is achieved by the specimen geometry and the test setup, which are designed and specified in accordance to test standards [83, 120]. The interpretation of these tests is based on simple analytical formulae allowing the determination of material parameters [121]. For example, the Young's moduli in different material directions can be deduced from tensile tests and are found by dividing the constant stress by the measured strain. A variety of methods have been developed to acquire the strain values, such as strain gauges, holography and speckle interferometry [122, 123]. The improvement in computational image processing has resulted in increasing popularity of full-field non-contact measurement techniques such as digital image correlation [124, 125]. A number of repetitions are required in all these methods to obtain statistically relevant results.

Vibration tests offer an alternative non-destructive enhancement to the traditional experimental methods when only the elastic material parameters are required, [126]. When a laminate plate is forced to vibrate, its dynamic response, eigen frequencies and eigen modes depend on the geometry, boundary conditions, density, number of layers, stacking sequence and elastic properties. The natural frequencies can be measured accurately and the vibration test can be repeated on the same specimen while test specific rigs are not required [127]. This method was first employed for unidirectional material [128] before further improvements on the method allowed the analysis of more complex stacking sequences [129–131]. The material parameters can be determined from the vibration tests using an inverse approach. Therefore a model of the plate, e.g. Rayleigh-Ritz or finite element, allows the determination of the unknown material parameters in an iterative manner, in which the material parameters in the model are updated until the experimental and model responses match [132]. In this form the procedure can be treated as an optimisation problem. The simplest objective functions are ordinary least squares or weighted least squares of the estimation error [130, 133] and require no a priori knowledge of the possible parameter values [134]. Another approach to assess the error is the use of a Bayesian error function, which consists of two different weighted parts. The first corresponds to the difference between the model and experimental response and the second part assesses the difference between the current and initial model parameter values. This enables the analyst to place either more confidence in the experimental data or in the model parameter values [135, 136]. However, this method requires that the initial guess of the model parameters is not too far from the target values, which in the case of a laminate can be found using laminate theory and micromechanics [134]. In both cases, the minimum of the objective error function can be computed through an iterative algorithm. Walton [135] combined the Bayesian error function with a Newton-Raphson algorithm. The drawback of this method is the requirement to start the search within a convergence domain, which contains the minimum. However, the primary reason behind the lack of success for a gradient-based solution in solving the inverse problem on more complex laminate layups appears to be related to the high non-linearity and the existence of many local optima [137, 138]. Hence, genetic algorithms (GAs) have attracted attention for solving such optimisation problems [139]. Unlike the gradient-based method, GAs avoid getting trapped in a local minimum as they perform a search within a range in the solution space. Furthermore, the search mechanisms employed by GAs possess an implicit parallelism, which enables rapid sampling within the solution space [132]. Thus, GAs are capable to address non-linear problems without a sensitivity analysis and an initial guess [140, 141]. GAs are sometimes computationally extensive for small-scale problems and suffer from slow convergence rates near the global solution, when compared with conventional local gradient-based techniques [137]. Furthermore the computational effort required for solving a problem can increase exponentially with the size of the parameter vector [142].

2.2.2 Markov Chain Monte Carlo

The Markov Chain Monte Carlo (MCMC) method is a well established tool for the solution of inverse problems and is widely used in physics and econometrics

[143]. The general idea of this method is based on Bayes' conditional probability theorem [144] which utilises continuous prior and posterior probability distributions in combination with a discrete distribution for experimental data. Bayes' theorem associates prior and conditional probabilities of two events in the following form:

$$P(A|B) = \frac{P(B|A)\,P(A)}{P(B)} \tag{2.34}$$

Here equation 2.34 utilises the notation of Bayesian inference where

- $P(A|B)$ corresponds to the conditional probability of an event A in relation to a given event B. This expression is also referred to as the posterior probability as the expression depends on a specific values of B.
- $P(B|A)$ is the conditional probability or likelihood of B given A.
- $P(A)$ represents the prior or marginal probability of A. Here the information of event B is not taken into account.
- $P(B)$ is the prior or marginal probability of B and acts as a normalising constant.

Event B represents a sample from a repeatable experiment while A is a sample from a proposition or hypothesis [145]. Hence, the posterior probability $P(A|B)$ measures the plausibility of a hypothesis under the condition of experimental information. The prior probability $P(A)$ can be construed as a limiting frequency for the degree of belief that the hypothesis A is true. Given these definitions Bayes' theorem can be written in a proportional form as follows, where the posterior probability depends on the likelihood and prior distribution:

$$P(theory|data) \propto P(data|theory)\,P(theory) \tag{2.35}$$

In this sense equation 2.35 can be used to describe the way in which the theory needs to be modified with respect to experimental data.

The MCMC method was first presented in the form of the Metropolis algorithm in 1953 by a group of physicists from the Los Alamos National Laboratory [146, 147]. The method was applied to compute the potential fields of molecules in liquids. The underlying algorithm was later modified to be applicable to more general problems by Hastings [148], a development, which is known as the Metropolis-Hastings algorithm.

The MCMC method was already a well established method in the field of statistical physics [149] before the method was applied to other fields in the 1990s [150]. It is capable of solving inverse problems, while such problems are often subject to ill-posedness. The MCMC method is conceptually able to overcome this problem. It first found great success in econometric and financial modelling [151–154] before other fields in science. These fields vary from machine learning and optimal sampling [155, 156], extreme value problems [157, 158] to heat transfer modelling [159–161].

2.2.2.1 Metropolis-Hastings algorithm

The Metropolis-Hastings algorithm works in an iterative manner and draws a sample from an approximate distribution of a parameter in each cycle. By accepting or rejecting the proposed sample this distribution is ultimately improved and converges to the target distribution $p\left(F\left(\Theta\right)|Y\right)$. Here Θ represents the parameter which is used to calculate the model response $F\left(\Theta\right)$ and Y represents the experimental data. In its simplest form the application of the algorithm comprises two steps. Initially a sequence starts from an initial guess value Θ_0. In the first step a new sample for Θ_i is drawn from a proposal distribution $q\left(\Theta_i|\Theta_{i-1}\right)$ [145, 162]. The shape of this proposal distribution can be chosen arbitrarily, but should represent the parameter range appropriately. It is often convenient to contemplate a normal distribution for $q\left(\Theta_i|\Theta_{i-1}\right)$, which uses the current sample Θ_{i-1} as mean value. With such a proposal distribution, the probability density decreases with distance away from the current sample. [163, 164]. In the second step of the iteration, it is decided whether the sample Θ_i is accepted or rejected. Therefore the Metropolis ratio is calculated using the following expression:

$$r = \frac{p\left(F\left(\Theta_i\right)|Y\right) \cdot q\left(\Theta_i|\Theta_{i-1}\right)}{p\left(F\left(\Theta_{i-1}\right)|Y\right) \cdot q\left(\Theta_{i-1}|\Theta_i\right)} \tag{2.36}$$

The proposed value is accepted if $r \geq 1$. However, if the Metropolis ratio is smaller than 1 the value is accepted with a probability of $U \leq r$, where U is a random variable from a uniform distribution $U\left(0,1\right)$ in the interval 0 to 1. Otherwise the proposed value is rejected and set to $\Theta_i = \Theta_{i-1}$. Regardless of the outcome of this process the step counts within the progression of the sequence. Furthermore, it is more convenient to use the acceptance probability α, which condenses the conditions described for the Metropolis ratio, as follows:

$$\alpha = \min\left\{1, \frac{p\left(F\left(\Theta_i\right)|Y\right) \cdot q\left(\Theta_i|\Theta_{i-1}\right)}{p\left(F\left(\Theta_{i-1}\right)|Y\right) \cdot q\left(\Theta_{i-1}|\Theta_i\right)}\right\} \tag{2.37}$$

The remarkable property of this algorithm is that it generates samples of Θ with a probability density similar to the posterior distribution $p\left(F\left(\Theta\right)|Y\right)$. Hence it

can be interpreted as an iterative mode finding algorithm which accepts steps that increase the posterior distribution while accepting decreases occasionally [143].
The initial method proposed [146] considered only symmetric proposal distributions in the form of $q(\Theta_i|\Theta_{i-1}) = q(\Theta_{i-1}|\Theta_i)$. With the generalisation undertaken in [148] asymmetric proposal distributions could also be considered. Table 2.1 shows a schematic of the Metropolis–Hastings algorithm.

```
intialise $\Theta_0$
for $i = 1$ to $n$ do
    draw sample $\Theta_i \sim q(\Theta_i|\Theta_{i-1})$

    calculate acceptance probability
        $\alpha = \min\left\{1, \frac{p(F(\Theta_i)|Y) \cdot q(\Theta_i|\Theta_{i-1})}{p(F(\Theta_{i-1})|Y) \cdot q(\Theta_{i-1}|\Theta_i)}\right\}$
    if $U \leq \alpha$ then
        accept $\Theta_i$
    else
        set $\Theta_i = \Theta_{i-1}$
    end if
end for
```

Table 2.1: Metropolis-Hastings algorithm.

Random walk Metropolis-Hastings algorithm

The Random walk Metropolis-Hastings algorithm is a modification of the conventional algorithm described in the previous section. The proposal distributions are chosen to be symmetric similar to the initial Metropolis algorithm. This leads to a simplification when drawing new samples. Due to the symmetry of both distributions no proposal distribution is required and the new sample can be computed easily from a noise level ε in the form of a normal distribution, which is applied to the parameter value from the previous step. Table 2.2 outlines the Random walk Metropolis-Hastings algorithm.
As a result of the simplification only the posterior distributions with respect to Θ_i and Θ_{i-1} need to be determined for the acceptance probability α.

2.2.2.2 Convergence assessment

A critical issue when applying the MCMC method is to assess the convergence and consequently to determine the appropriate termination condition. When running a single MCMC chain with only a small number of parameters the posterior distribution is a good indication of convergence. Here convergence means that the samples

```
intialise $\Theta_0$
**for** $i = 1$ to $n$ **do**
    draw sample using $\varepsilon \sim N(0, \sigma_\varepsilon) \rightarrow \Theta_i = \Theta_{i-1} + \varepsilon$

    calculate acceptance probability
        $\alpha = \min\left\{1, \frac{p(F(\Theta_i)|Y)}{p(F(\Theta_{i-1})|Y)}\right\}$
    **if** $U \leq \alpha$ **then**
        accept $\Theta_i$
    **else**
        set $\Theta_i = \Theta_{i-1}$
    **end if**
**end for**
```

Table 2.2: Random walk Metropolis-Hastings algorithm.

represent the target distribution adequately. However, when multiple chains are sampling in parallel or a large set of parameters are modelled, relying solely on the evolution of the posterior distribution is controversial and might not provide enough information to make this decision. A variety of methods were developed and many diagnostic tools are available to analyse the output of a running MCMC [165, 166]. A comprehensive review on the different methods for assessing convergence is given in [165, 167].

Gelman and Rubin [168] developed an approach which monitors the estimated posterior variance $\widehat{R}$ of each parameter while using multiple parallel chains. In order to compute this value for a running MCMC it is necessary to constantly update B and W, the between-chain and within-chain variance respectively, using the following expressions:

$$B = \frac{n}{m-1} \sum_{j=1}^{m} \left(\bar{\psi}_{.j} - \bar{\psi}_{..}\right)^2 \quad \text{with} \quad \bar{\psi}_{.j} = \frac{1}{n} \sum_{i=1}^{n} \psi_{ij} \quad \text{and} \quad \bar{\psi}_{..} = \sum_{j=1}^{m} \bar{\psi}_{.j} \tag{2.38}$$

$$W = \frac{1}{m} \sum_{j=1}^{m} s_j^2 \quad \text{with} \quad s_j^2 = \frac{1}{n-1} \sum_{i=1}^{n} \left(\psi_{ij} - \bar{\psi}_{.j}\right)^2 \tag{2.39}$$

Here the the index n is indicating the length of the chain while m is the number of parallel chains. ψ_{ij} represents the value at a certain iteration i within a chain j. Hence B is calculated and constantly updated after each iteration using the within- and between-chain mean value $\bar{\psi}_{.j}$ and $\bar{\psi}_{..}$ respectively as shown equation 2.38. The within-chain variance s_j^2 corresponds to $\bar{\psi}_{.j}$ and is used in the computation of W.

It is now possible to update the marginal posterior variance $\widehat{var}^{+}(\psi|Y)$ using a weighted average of the given W and B:

$$\widehat{var}^{+}\left(\psi|Y\right) = \frac{n-1}{n}W + \frac{1}{n}B \tag{2.40}$$

The estimated posterior variance $\widehat{R}$ for a running MCMC is computed from the weighted simulated sequences, divided by the average of the variances within each chain with respect to each parameter, using the following expression:

$$\widehat{R} = \sqrt{\frac{\widehat{var}^{+}\left(\psi|Y\right)}{W}} \tag{2.41}$$

During the runtime of the chain, $\widehat{R}$ approaches 1 in case of convergence. Advocates of this method stop the simulation if $\widehat{R}$ reaches a value less than 1.2 for all parameters [166]. Nonetheless it is often useful to plot the traces of a representative parameter subset in addition to the method described [165, 166].

2.2.2.3 Parallel tempering

In the case of a multi-modal target distribution the Metropolis–Hastings algorithm as introduced in 2.2.2.1 can get trapped in a local mode and fail to explore the remaining modes of notable probability. This problem is comparable to the discrepancy encountered with the gradient based solution where the solver fails to exit a minimum in nonlinear model fitting. One solution to the problem is to use simulated annealing where a temperature parameter with the property $1 \leq T < \infty$ is introduced [169, 170]. Here $T = 1$ resembles the desired target distribution and is referred to as cold sample while values for $T \gg 1$ are referred to as hot samples. Such values for T flatten the target distribution and allow the acceptance of a broader range of proposed parameters. Thus, these distributions are less likely to be trapped in local modes.

Parallel tempering is another approach utilising the concept of the temperature parameter and the advantage of parallel chains [171]. Further refinements of this concept followed in [172–175]. With parallel tempering a tempering parameter defined as

$$\beta = \frac{1}{T} \tag{2.42}$$

is introduced. According to the definition of T, β varies between 1 and 0, where the application of $\beta = 1$ results in a cold chain. The tempering parameter is applied as follows:

$$\begin{aligned} \pi\left(F\left(\Theta\right)\left|Y,\beta\right.\right) &= p\left(\Theta\right)\cdot p\left(Y|F\left(\Theta\right)\right)^{\beta} \\ &= p\left(\Theta\right)\cdot \exp\left\{\beta \ln p\left(Y|F\left(\Theta\right)\right)\right\} \quad \text{for} \quad 0<\beta<1 \end{aligned} \tag{2.43}$$

This tempered posterior distribution makes use of equation 2.35 (see also equation 5.56). Discrete values of the tempering parameter are assigned to each chain and therefore result in a ladder with different temperatures.

After each iteration cycle with n_S steps a parameter swap algorithm is initiated which proposes to swap parameters between two chains if $U_1 \sim U\left[0,1\right] \leq {}^{1}/{n_S}$, where U_1 is a random number from a uniform distribution. If the swap is proposed a chain m is randomly selected to swap the parameter set with its adjacent chain $m+1$[3]. A swap is accepted if $U_2 \sim U\left[0,1\right] \leq s$, where U_2 is another random variable from a uniform distribution between 0 and 1 and s is the acceptance probability defined as follows.

$$s = \min\left\{1, \frac{\pi\left(F\left(\Theta_{m+1}\right)\left|Y,\beta_m\right.\right)\cdot\pi\left(\Theta_m|Y,\beta_{m+1}\right)}{\pi\left(F\left(\Theta_{m}\right)\left|Y,\beta_m\right.\right)\cdot\pi\left(\Theta_{m+1}|Y,\beta_{m+1}\right)}\right\} \tag{2.44}$$

This algorithm is outlined in table 2.3. This approach overcomes the problem of a mode trapped chain. Chains with higher temperature can lead to extremely different parameter sets while lower chains within the ladder allow the possibility to refine these sets.

```
if $\Delta n = n_S$ then
    draw random value $U_1 \sim U\left[0,1\right]$
    if $U_1 \leq \frac{1}{n_s}$ then
        pick chain randomly

        calculate swap probability:

            $s = \min\left\{1, \frac{\pi\left(F\left(\Theta_{m+1}\right)\left|Y,\beta_m\right.\right)\cdot\pi\left(\Theta_m|Y,\beta_{m+1}\right)}{\pi\left(F\left(\Theta_{m}\right)\left|Y,\beta_m\right.\right)\cdot\pi\left(\Theta_{m+1}|Y,\beta_{m+1}\right)}\right\}$

        accept swap if $U_2 \sim U\left[0,1\right] \leq s$
    end if
end if
```

Table 2.3: Algorithm for parallel tempering.

Nonetheless a suitable choice of β_m is necessary as adjacent chains require a degree of overlap in order to achieve a satisfactory acceptance probability for the exchange

---

[3] If m equals the last chain in the set, the first chain is selected as the next adjacent chain, e.g. $m=4$, $m+1=1$.

operation. Furthermore, only the results from the cold chain are used in inference, while the results from the remaining chains are usually disregarded [143].

3 Experimental techniques and manufacturing

This chapter specifies the materials, manufacturing processes and experimental techniques used in this work. Described experimental techniques cover both laminates and preforms which are based on unbindered and bindered versions of the same carbon fibre yarn. The characterisation programme carried out aims at producing information which is used in the material laws of subsequent modelling of the mechanical and damage behaviour of laminates and preforms. Furthermore the production processes of components used for model validation in the case of preforms are also described.

3.1 Materials

The following materials were used in this work and are subsequently described in further detail:

- Carbon fibre yarn
- Bindered yarn (homogeneously and inhomogeneously)
- Epoxy resin
- Miscellaneous materials

3.1.1 Reference carbon fibre yarn

A commercially available high tenacity filament yarn designated as HTS40 distributed by Toho Tenax [176] was used as reference material. This material finds application in areas such as aerospace or automotive industry. To produce woven materials single fibre yarns spooled from several threads are woven together forming a fabric. Similarly unidirectional (UD) material is produced by parallel aligned fibre yarns, where a resulting single ply is usually held together by a nylon thread. Both of these arrangements are distributed in a dry state but can also be acquired as pre-pregs. Table 3.1 summarises the properties of the 12 k / 800 tex version of the yarn used.

Property	Unit	HTS40
Number of filaments	–	12000
Nominal linear density	tex	800
Filament diameter	μm	7
Density	$^{g}/_{cm^3}$	1.77
Tensile strength	MPa	4300
Tensile modulus	GPa	240
Elongation at break	–	1.8%

Table 3.1: Characteristics of HTS40.

3.1.2 Bindered yarn

The bindered materials used in this work were based on the HTS40 yarn and were produced by Toho Tenax in the context of the European project PreCarBi [1]. Two versions of the material were utilised. Both types are based on the same binder chemistry but differed in the dispersion of the binder. They are denoted as inhomogeneously and homogeneously bindered yarn and are described in detail in the following subsections. For confidentiality reasons the exact formulation of the binder is not reported in this thesis.

3.1.2.1 Inhomogeneously bindered yarn

In the inhomogeneously bindered yarn 7% by mass of binder is distributed within the yarn and on its surface in the form of particles. However, with this material version the actual particle size varies and is difficult to determine mainly due to the aggregation of several particles. Hence particles in the range of 0.2-100 μm were observed [177]. A tests series carried out in [177] was aimed to determine the initial reaction temperature of the binder. The results show that binder particles activation starts at 85°C. A reactivation of the binder is also possible due to the thermoplastic formulation of the binder. A schematic representation of the yarn is shown in figure 3.1a whilst figure 3.1b (courtesy of M. Asareh [177]) illustrates an ESEM[1] image showing the distribution of the binder.

---

[1] Environmental scanning electron microscope

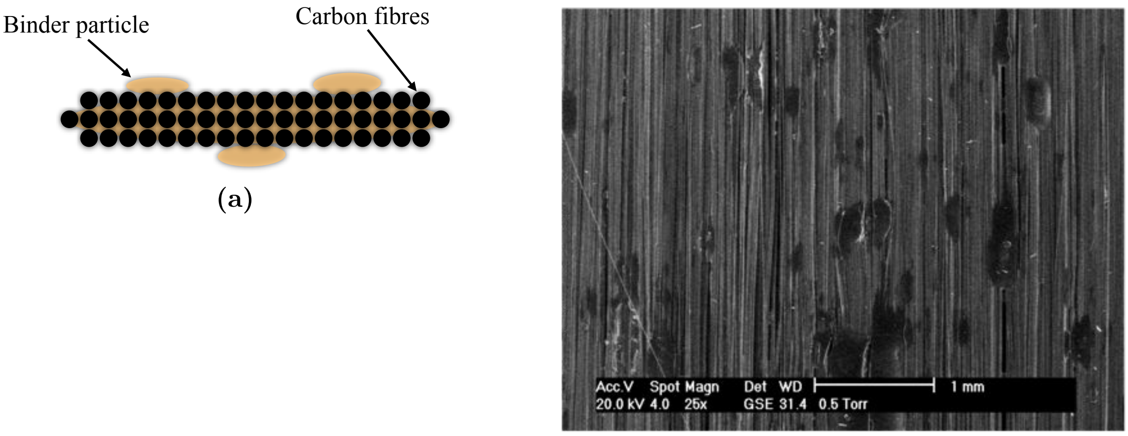

(a)

(b)

Figure 3.1: Fibre yarn with inhomogeneous binder distribution, (a) schematic representation and (b) ESEM picture.

3.1.2.2 Homogeneously bindered yarn

Similarly to the inhomogeneously bindered fibre the homogeneously bindered yarn contains 7% by mass of binder. For this material version the manufacturing process was modified and resulted in a homogeneous binder distribution throughout the yarn. Figure 3.2a illustrates the schematic configuration and figure 3.2b (courtesy of M. Asareh [177]) shows an ESEM image of the tow. In the context of this work homogeneously bindered fibres were used in the manufacturing of both preforms and laminates. The same thermal profile for the binder that applies to the inhomogeneously bindered yarn was also used for this material.

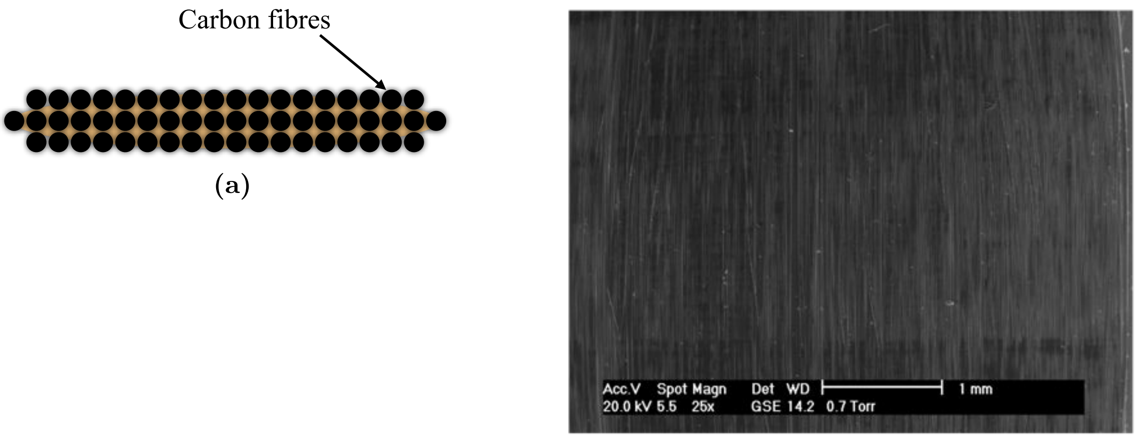

(a)

(b)

Figure 3.2: Fibre yarn with homogeneous binder distribution, (a) schematic representation and (b) ESEM image.

3.1.3 Hexcel HexFlow® RTM6

The epoxy resin HexFlow® RTM6 [178] utilised in this work is a mono-component system appropriate for liquid moulding applications. The process temperature profile for RTM6 is illustrated in figure 3.3. For the infusion the tool is heated up to 120°C. After the infusion is completed the tool is heated up further and held at 160°C for 75 min to cure the resin. This process is followed by a post-cure cycle where the component is removed from the mould and held at 180°C for 120 min .

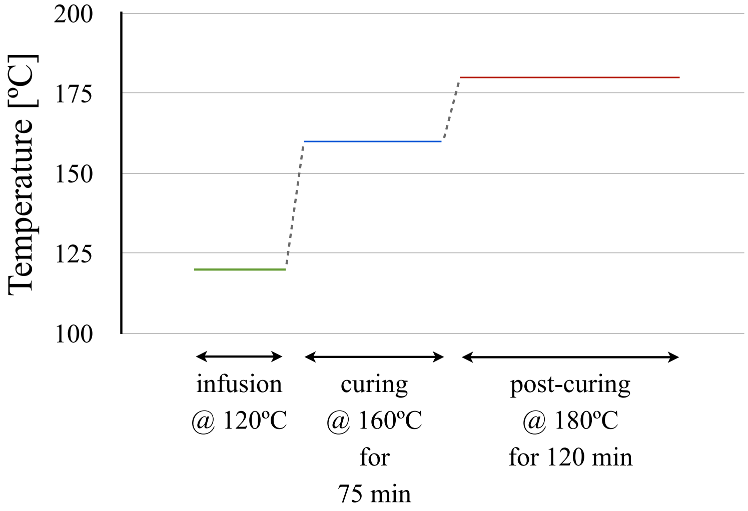

Figure 3.3: Cure cycle for RTM6 as provided by the manufacturer.

Table 3.2 lists the mechanical properties of the cured resin as stated by the manufacturer. Furthermore, the published values for the uncured and cured resin density at 25°C are 1.11 $^{g}/_{cm^3}$ and 1.14 $^{g}/_{cm^3}$ respectively while the fracture toughness in mode I is stated as 168 $^{J}/_{m^2}$.

Property	Unit	Tensile	Flexure
Strength	MPa	75	132
Modulus	GPa	2.89	3.3
Strain to failure	–	3.4%	-

Table 3.2: Characteristic properties of HexFlow® RTM6 as provided by the manufacturer.

3.1.4 Miscellaneous

3.1.4.1 Huntsman Araldite® 420 A/B adhesive system

Aluminium tabs were used to transfer the load effectively in in-plane and out-of-plane tests. These tabs were bonded onto the surfaces of the specimens using

Araldite® 420. This epoxy adhesive is supplied by Huntsman Advanced Materials and is suitable for aerospace applications. The adhesive is mixed from two components, hardener and epoxy, in weight ratio of 4 : 10. Subsequently the adhesive paste is applied onto the specimen surface and the tab. Afterwards the adhesive is cured in the oven for 4 hrs at 50°C. The shear strength of the material at room temperature is 37 MPa as stated by the manufacturer [179]. Shear properties can be improved by post-curing the adhesive for up to 24 hrs at 70°C. If necessary it is possible to remove the tabs from specimens by heating the adhesive to 150°C.

3.1.4.2 N1000 infusion flow media

A flow medium from Richmond Aircraft Products [180] was used for the infusion process. The medium is designated as Infusion Flow N1000 is a nylon mesh which is suitable for resin infusions with a processing temperatures of up to 205°C. A flow media supports the formation of a uniform resin flow front and contributes to a complete saturation during the infusing process.

3.1.4.3 Aerovac A100 peel ply

A peel ply was placed underneath and on top of the laminate to obtain the same surface finish for both sides of the test specimens. A peel ply made up of tightly woven nylon, designated as Aerovac A100, with an areal weight of 75 $^{g}/_{m^2}$ and a thickness of 0.153 mm was used. The maximum recommended temperature for this material is 205°C [180]. After the infusion process the easily removable peel ply will stick to the laminate. In general the use of a peel ply is optional and leads to a rough surface finish, rather than a smooth one which depends on the tool surface. The use of a peel ply needs to be considered when calculating the amount of resin needed for the infusion as a small amount of resin is absorbed by the peel ply.

3.1.4.4 SM Tacky-Tape® sealant tape

The SM 5142 Tacky-Tape® [181] is a sealant tape made from synthetic rubber which is used for vacuum bagging. Air-tight conditions can be maintained during the infusion process due to the strong adhesive properties of this tape. The tape is applied to a clean tool while a release paper remains attached to one side of the tape. After the vacuum bag is positioned the release paper is removed to allow adhesion between the bag and the tape. This tape can be applied to composite or metal tools and allows easy removal for de-bagging. The tape has a service temperature range from room-temperature up to 204°C while the application temperature ranges from

7°C to 120°C.

3.1.4.5 VACtite G48 vacuum bag

The VACtite G48 vacuum bag is a 0.05 mm thick nylon foil with a maximum usage temperature of 205°C [182]. For application the bag is positioned above the laminate and the sealant tape. With the removal of the release paper from the sealant tape the vacuum bag is in direct contact to the adhesive tape. The removal of the release paper starts from one corner following the remaining edges around the tool. Any wrinkles in the bag caused during the sealing process can lead to unwanted leaks.

3.2 Manufacturing process

The first part of this section describes the manufacturing process used to produce test coupons for material characterisation. Three different types of carbon fibre yarns were used within the specimen production. A set of panels was produced from inhomoegeneously and homogeneously binder coated carbon tows. These were used for the production of preform specimens. In addition, laminates were manufactured using unbindered and homogeneously bindered carbon fibre yarns in combination with the commercial epoxy resin (RTM6). In the second part of this section the process modifications necessary for the manufacturing of bindered laminates are described. The application of binder can lead to complications in the infusion operation. Hence the variations for this step which lead to the successful infusion of bindered preforms are presented. The last subsection describes the manufacturing of the components which were used for the validation of finite element simulations related to three point bending and a preform impact scenario.

3.2.1 Process steps

The manufacturing process for preforms comprises of a ply lay-up and a binder activation step. Afterwards the specimens can be cut from the resulting panel and prepared for testing. This procedure was used for the manufacturing of inhomogeneously and homogeneously bindered preform specimens. For the production of the laminates infusion and curing steps are added to the process whilst activation is only necessary for laminates based on homogeneously bindered yarns. Figure 3.4 illustrates the process steps associated with the manufacturing of different material types.

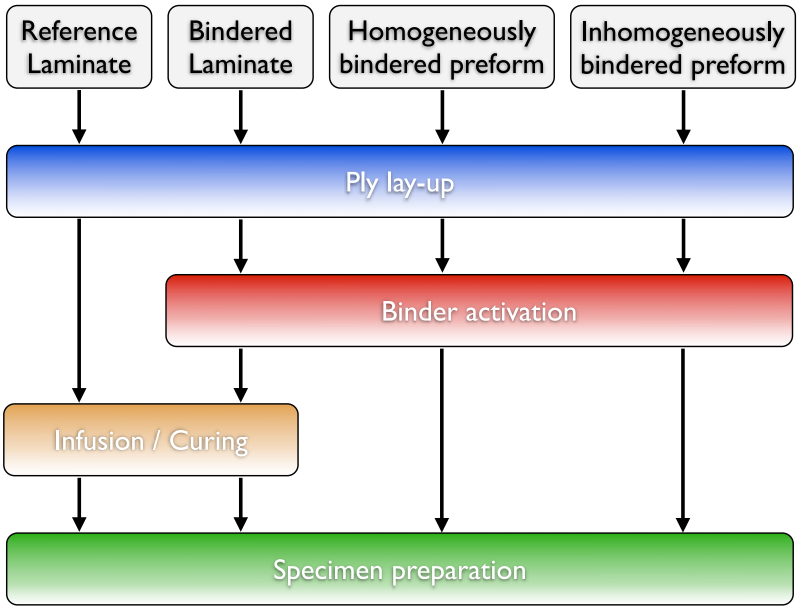

Figure 3.4: Manufacturing steps for different materials.

3.2.1.1 Ply lay-up

In an initial manufacturing process of unidirectional (UD) material each ply was laid up, aligned by hand and afterwards taped onto the tool surface prior to activation, as shown in figure 3.5. This method was found to be inefficient and subject to significant variability.

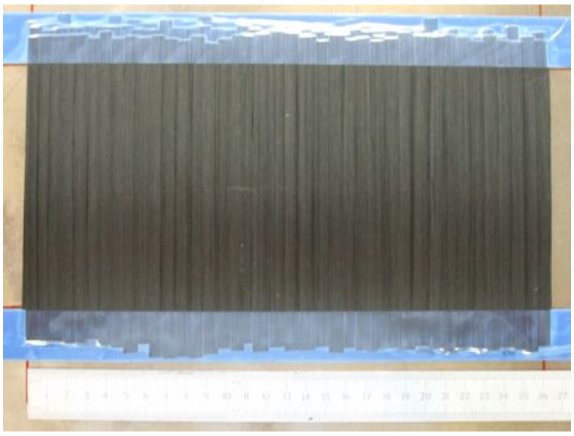

Figure 3.5: Unidirectional arrangement of binder coated fibres produced by hand lay-up prior to activation.

A tow alignment tool was designed to enable the production of UD preforms from carbon fibre yarn in an efficient manner. The tool, shown in figure 3.6, consists of two bridges which are mounted on a frame. In addition, the bars at each end of the frame contain a set of pins, with a 5 mm spacing, to ensure consistent fibre alignment. The pins on each side also lock the tows and maintain fibre tension.

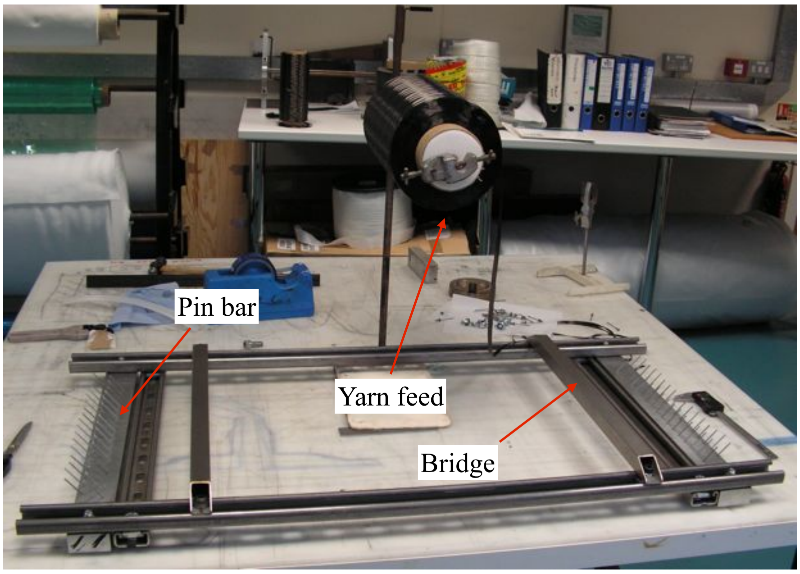

Figure 3.6: Tow alignment tool for panel production.

Figure 3.7 illustrates the manufacturing process of UD panels using the tow alignment tool. The process consists of four repetitive steps:

- UD ply is arranged on the tow alignment tool while the fibre yarn is pulled directly from the bobbin.
- Double sided adhesive tape is used to stack each ply onto the tool. The alignment of the frame is ensured with the aid of clamps.
- Layers are cut off from the tow alignment tool, whilst two metal bars are positioned on each side to prevent movement of the yarns.
- The tool is prepared for the next ply, using another layer of double sided tape.

The downside of this method is the accumulation of more waste material compared to the hand layup as the usable area is defined between the two bridges. However, the wastage can be minimised to some extend by shifting the pin bars closer to the bridges.

When unbindered material is used, a layer of peel ply is situated on the tool under the first layer, for the subsequent infusion process. With this tow alignment tool, ply arrangements such as ±67.5° which are normally difficult to manufacture can be laid up very accurately and rapidly.

In order to achieve a thickness of greater than 3 mm for the out-of-plane specimens 24 plies were laid up on the tool. Furthermore a 0.01 mm thick PTFE[2] film is placed

---

[2] Polyterafluorethylene

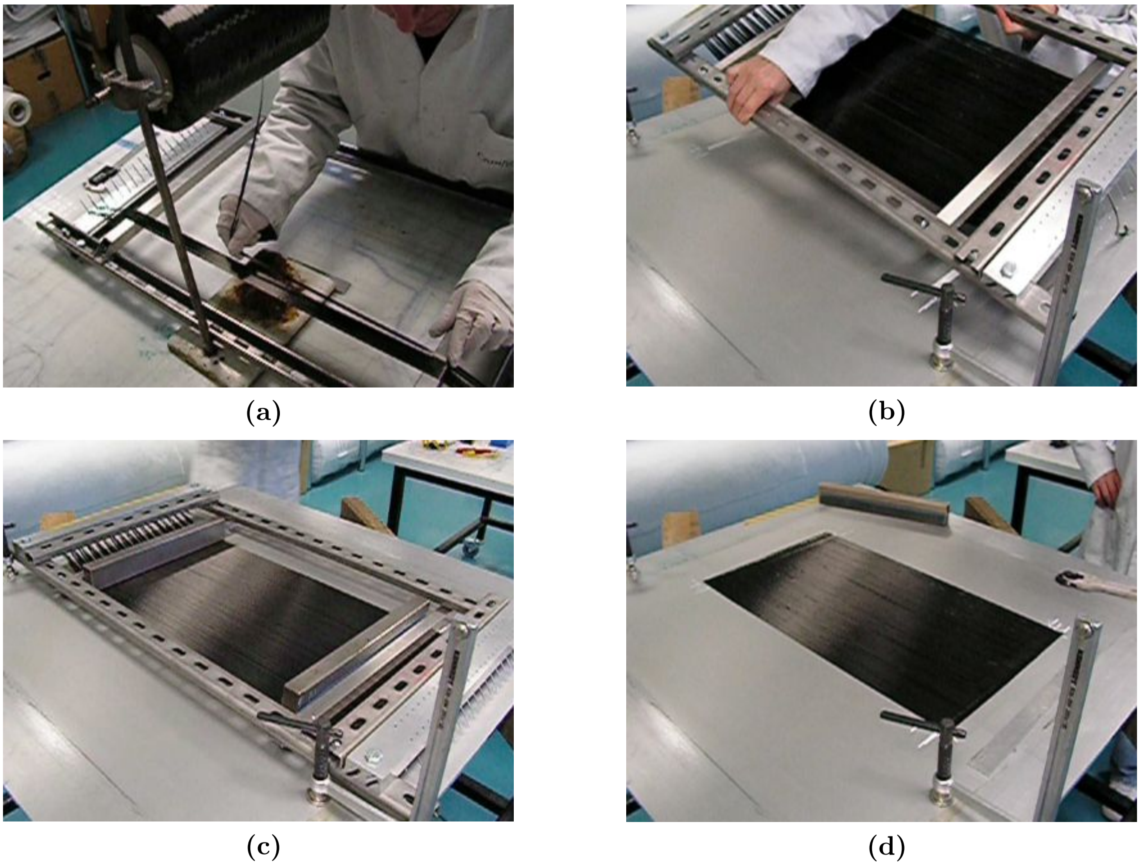

Figure 3.7: Lay-up procedure using the tow alignment tool.

in the mid-plane to ensure an initiated crack for the experiment. Figure 3.8 shows the minimum dimensions of the panels as recommended in [79].

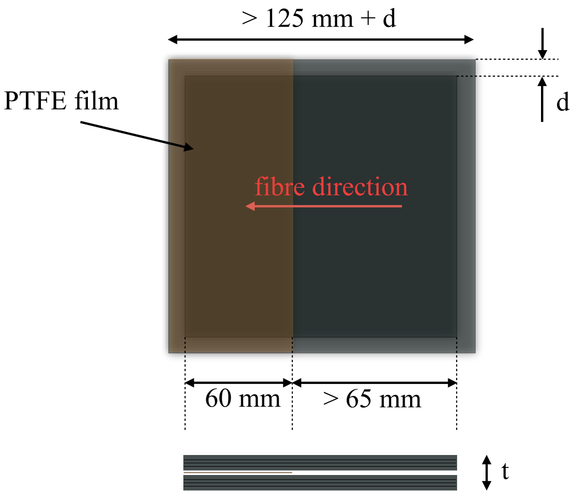

Figure 3.8: DCB and ELS panel dimensions.

3.2.1.2 Binder activation

A combination of heat and pressure is applied to the prepared panel to activate the thermoplastic binder in the material. In an initial step the produced panel is sealed under a vacuum bag and pressure is applied via a vacuum pump in order to guarantee an acceptable adhesion while ensuring fibre alignment. Here the atmospheric pressure is reduced to a value of 20 mbar (98% vacuum). This condition is preserved for a duration of 30 min whilst the tool temperature is kept at 140°C. At this stage the binder transforms from a solid to a viscous state. During the subsequent cool down process the pressure remains applied to guarantee the compaction of the material, while the binder solidifies and establishes bonds between the tows. As a result the panel remains in this shape and is available for further processing such as cutting to the exact dimensions prior to infusion.

The possibility of reactivating the thermoplastic binder was exploited when preparing the DCB and ELS panels where the panel with 24 layers was separated in four batches of 6 layered sub-panels. In a second step these sub-panels were merged with the same activation conditions.

This procedure was used as a standard approach for the preform material. However, for the production of bindered laminates this activation procedure resulted in panels which were very difficult to infuse. A series of experiments were performed to identify an activation procedure which allows a successful infusion (see section 3.2.2).

3.2.1.3 Infusion and curing

Figure 3.9 illustrates the setup for VARTM[3] infusions used in this work. Prior to the resin infusion a peel ply is placed under and on top of the panel. Furthermore a piece of flow media is also located above the peel ply to ensure uniform resin distribution over the width of the panel. Subsequently the assembly is sealed under a vacuum bag.

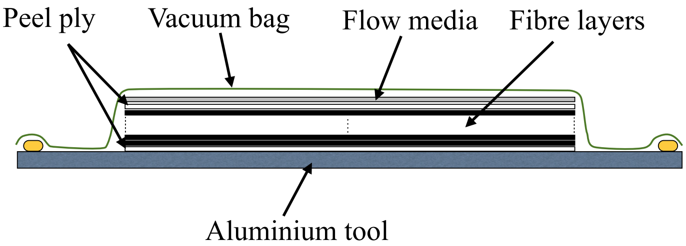

Figure 3.9: Schematic of the infusion setup.

Some modifications to this standard arrangement were undertaken. Thus, sealing

---

[3] Vacuum assisted resin transfer moulding

tape was placed along the edges of the panel in order to guide the liquid resin and avoid unwanted race tracking (see figure 3.10a). Moreover the resin inlet side was also restricted with sealing tape and only a small area was covered with flow media as illustrated in figure 3.10b. The latter arrangement was undertaken with the aim of achieving a slow moving flow front which is necessary for achieving a good infiltration especially for panels with a unidirectional layup.

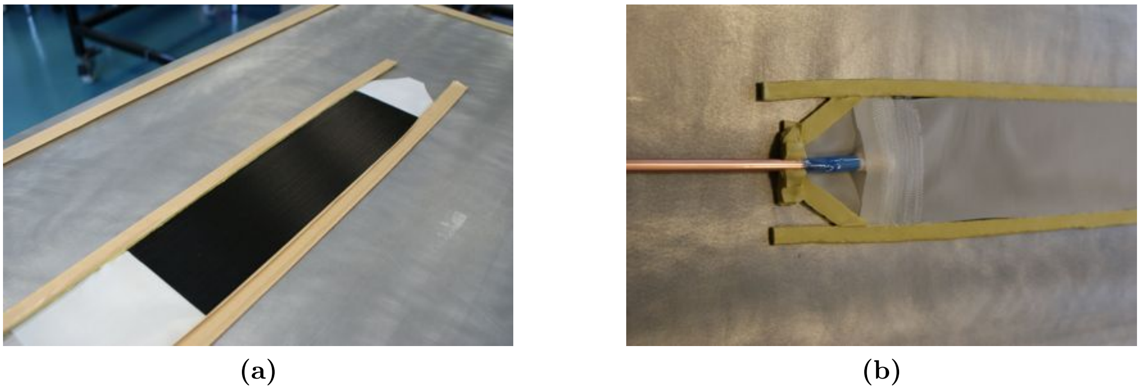
(a) **(b)**

Figure 3.10: Infusion preparation.

A vacuum pump was connected to the outlet valve while the tool was heated up to 120°C. The resin was infused locally through the inlet valve as shown in figure 3.11a. Similarly to the production of the preform material the vacuum pump reduces pressure to 20 mbar, which corresponds to 98% vacuum. Figures 3.11a-3.11d show different stages during the progress of UD panel infusion.

After the infusion was completed the curing process for the resin started (see figure 3.3). Therefore the inlet was closed while maintaining the vacuum from the outlet side and increasing the temperature gradually to 160°C. Hence the pressure gradient from inlet to outlet side is balanced which leads to a uniform panel thickness. The tool remained under these conditions for 75 min when the target temperature of 160°C was reached in order to cure the resin. Subsequently all panels are post-cured together at 180°C for 120 min under free-standing conditions.

3.2.1.4 Specimen preparation

Specimens were cut to the dimensions dictated by the ASTM standards [79, 183–185]. Afterwards the quality was reviewed and end tabs were glued onto the surfaces of the specimens using Huntsman Araldite® 420 A/B to improve the grip and minimise stress concentrations. Table 3.3 lists all the dimensions for the test programme including end tab dimensions. The same dimensions were also used for the preform specimens. However, except for the tensile specimens in fibre direction, the end tabs

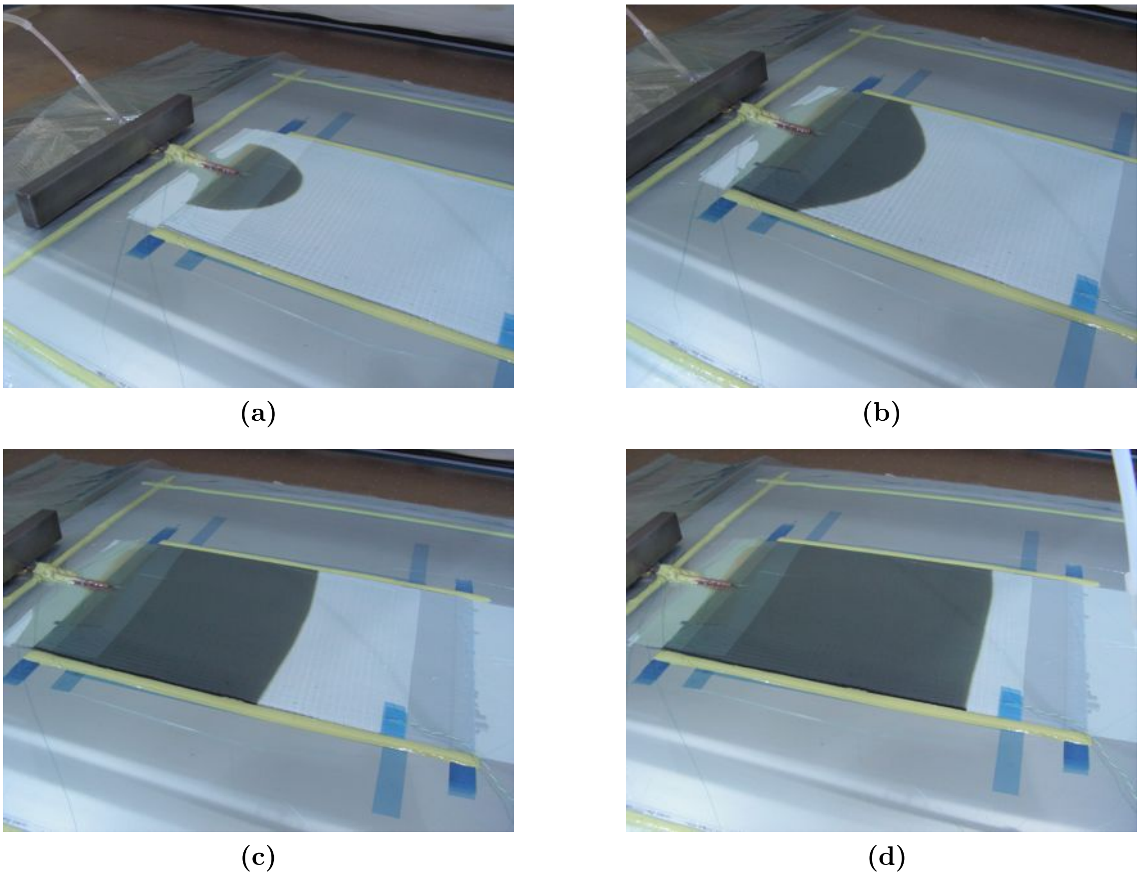

Figure 3.11: VARTM infusion of a UD panel.

were simply replaced by adhesive tape due to the lower material strength.

Throughout this work specimens for mode I and II delamination tests were manufactured from the same panels in order to simplify the production process. Hence the recommended specimen dimensions for mode I [72] were also applied to mode II specimens. The dimensions were chosen to coincide with 200×20 mm and to satisfy the requested minimum length for mode I specimens as listed in table 3.4. However, for the bindered laminate the minimum specimen length of 125 mm was used due to the infusion difficulties caused by the binder.

After cutting the specimens load blocks were bonded onto the surfaces. Figure 3.12 and 3.13 show the schematic geometrical properties for mode I and II delamination test coupons. In the case of the DCB tests the load blocks are bonded onto the top and bottom surface of the two sub-laminates, whereas for ELS coupons only one load block is glued onto the surface of the lower sub-laminate.

Lay-up	Specimen dimension	End tab dimension	ASTM Standard
$[0^\circ]_8^t$	250×15 mm	50×15×1 mm	D3039/3039M
$[0^\circ]_{16}^c$	110×10 mm	50×10×1 mm	D3410/D3410M-03
$[+45^\circ]_{2s}$	250×25 mm	50×25×1 mm	D3518/D3518M-01
$[\pm45^\circ]_{2s}$	250×25 mm	50×25×1 mm	D3518/D3518M-01
$[\pm67.5^\circ]_{2s}$	250×25 mm	50×25×1 mm	D3518/D3518M-01
$[90^\circ]_8$	200×25 mm	50×25×1 mm	D3039/3039M

Table 3.3: Overview of in-plane specimen dimensions.

Property	Symbol	Unit	Carbon fibre	Tolerance
Width	b	[mm]	20.0	± 0.5
Minimum length	L	[mm]	125.0	-
Thickness	$2h$	[mm]	3.0	± 0.1

Table 3.4: Recommended specimen dimensions for out-of-plane specimens.

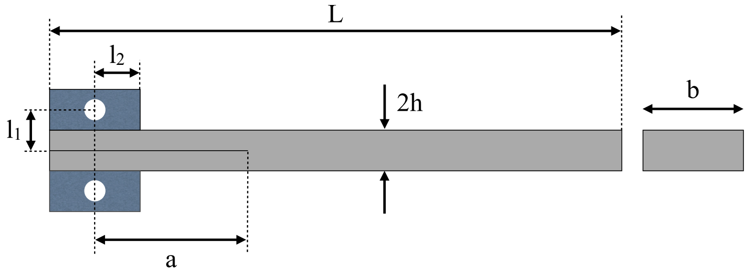

Figure 3.12: Specifications for specimens tested in mode I.

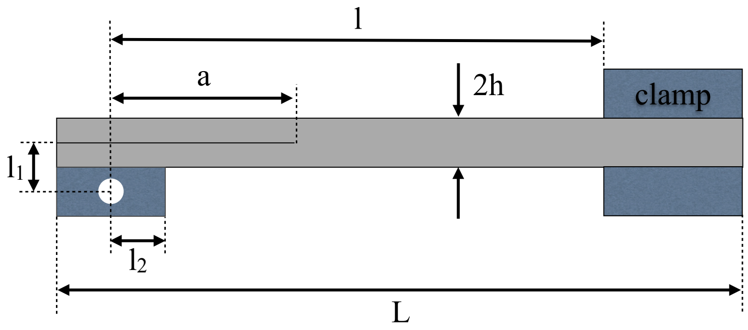

Figure 3.13: Specifications for specimens tested in mode II.

After the load blocks are attached to the specimens the side surface is spray painted with white primer. This spray paint is relatively brittle hence the crack tip is clearly visible while propagating during the test. A scale is then drawn on the painted surface relative to the initial crack length (see figure 3.14). Subsequently the crack is opened to the initial pre-crack length. Thereby the inserted PTFE film ensures that the crack remains in the mid-plane.

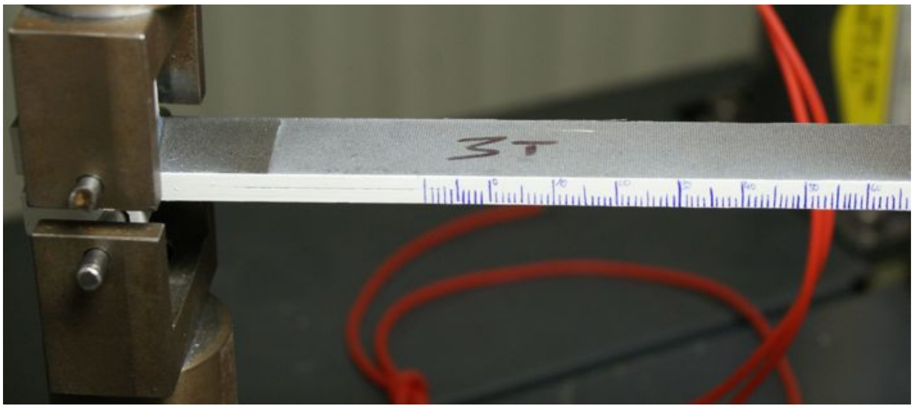

Figure 3.14: Scale to track the crack length on the side of a DCB specimen.

3.2.2 Process variations for bindered laminates

Dry spots were noticed in the inspection of the laminate panels manufactured from bindered yarns after the infusion. As part of identifying a viable manufacturing process for the bindered laminate another infusion method was also investigated. Figure 3.15a shows an RTM[4] tooling. The preform was activated with the standard procedure described in section 3.2.1.2 and positioned within the tooling frame.

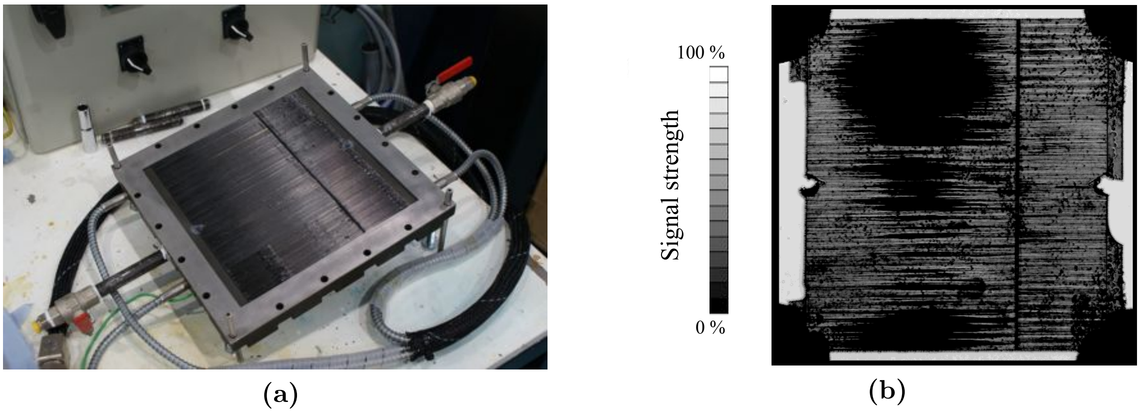

(a)

(b)

Figure 3.15: UD panel production via RTM infusion, (a) tooling and (b) infusion assessment via C-scan.

However, this method did also not lead to the expected result. Figure 3.15b shows the result of a C-scan in which the panel's attenuation of the transmitted pulse is measured. The attenuation of the signal is influenced by voids, delaminations, state of resin cure, fibre volume fraction, condition of the fibre/matrix interface and any unwanted inclusions. Here infused sections of the panel are shown in light grey while uninfused areas, shown in black, absorb the transmitted impulse. As a result it was decided to reduce the pressure during the activation process while using VARTM as

---

[4] Resin transfer moulding

standard infusion method.

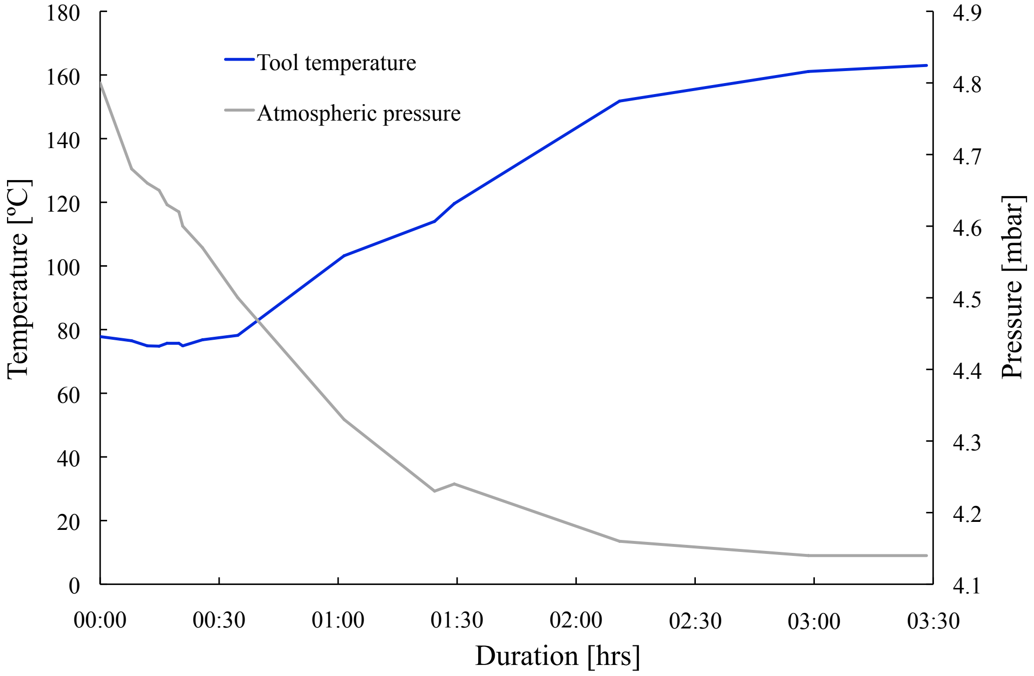

Figure 3.16: Infusion protocol for preform material using VARTM.

Preforms from homogeneously bindered fibre yarns were manufactured by using only 12% of vacuum (887 mbar) while maintaining the standard temperature and duration. Thus a lower compaction of the preform compared to the standard activation method was carried out. The lower compaction leads to the development of channels which improve the resin distribution throughout the preform. Furthermore the binder shows the first signs of thermal activation at 85°C [177]. Hence the infusion was performed with a target tool temperature of 80°C in order to avoid binder reactivation and consolidation of the preform prior to the resin introduction. Figure 3.16 illustrates the tool temperature and pressure conditions during the modified infusion process. Here the temperature was measured with thermocouples which were attached to the tool surface. After the introduction of the resin, the inlet was closed while the vacuum pump remained attached on the outlet side. After 40 min the cure cycle was started by ramping up the temperate to 160°C.

Figure 3.17 shows the result of a C-scan performed on a bindered UD laminate manufactured for transverse specimens. The attenuation field of the transmitted signal is plotted over the panel size to identify imperfections. Here no indication of significant imperfections were found.

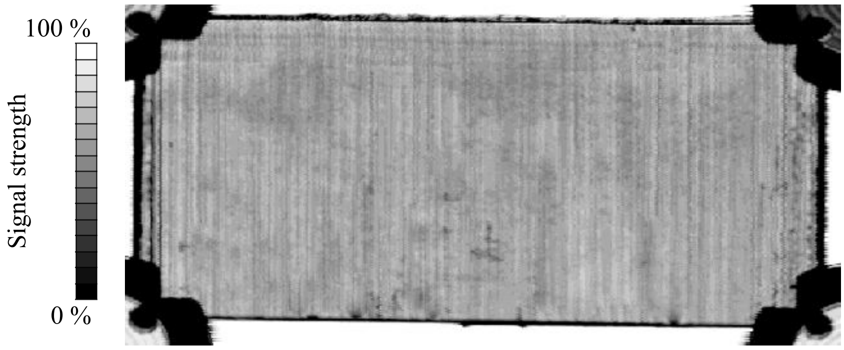

Figure 3.17: C-scan result for a successful infusion on a preform.

3.2.3 Components for finite element validation

Components were manufactured for the validation of finite element simulations. The simulation of a three point bending test was chosen due to the simplicity of the experiment. The outcome of this test leads to the determination of the flexural modulus of elasticity but also provides a load deflection curve which can be compared to data obtained from simulations. The second component manufactured for validation purposes is a preform spar section, which is tested under impact.

3.2.3.1 Three point bending specimens

The specimens for the three point bending experiment were manufactured with the reference carbon fibre yarn. Specimens were cut from the same panel as the compression specimens for the in-plane test programme. For three point bending specimens the same dimensions were used as for the compression specimens (110×10×2.4 mm). After the specimens were cut and polished no further preparation was necessary to undertake the experiment.

3.2.3.2 Preform spar section

The preform spar sections for the validation of finite element simulations were manufactured following the activation profile for preforms. Prior to activation double sided adhesive tape was used to fix strips of homogeneously bindered fibres onto the outer surface of a solid aluminium tooling block as shown in figure 3.18. The aluminium tool has overall dimensions of 185×160×98 mm, the sides evolve under a 84° angle from the base area while a radius of 14 mm creates a fillet along the edges of the top surface. The final fabrication of the component is an eight layer $[0°/90°]_{2s}$ stacking sequence laid up by hand. The assembly was then placed in a vacuum bag and maximum vacuum was applied via a pump. Subsequently the tool was placed

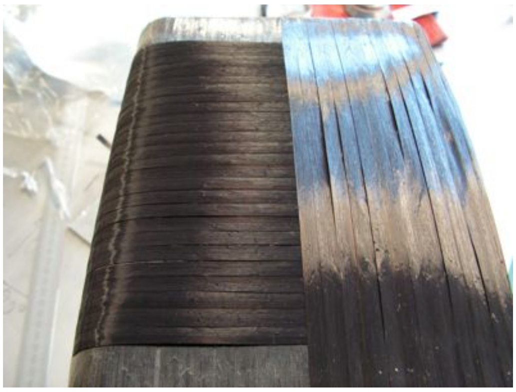

Figure 3.18: Layup of the preform spar section.

onto a hot plate. The surface temperature of the tool was monitored with a thermocouple located on the side surface of the aluminium block. The 30 min countdown for activation started when a tool temperature of 140°C was reached. After the tool cooled down to ambient temperature the vacuum pump was detached and the component was removed from the tool. The final dimensions of the component are governed by the region defined by the double sided adhesive tape (see figure 3.19a). The components were equally trimmed to the same dimensions of 144×158×78 mm. During the inspection of the components wrinkles were found in the fillet segments. These wrinkles could be explained by the difference in thermal expansion in the different material layers where the inter-ply slip is affected by thermal contractions in the through-thickness direction of the component. For laminate components with curved geometries this effect tends to cause distortions at enclosed angles [186–188]. Apart from the occurrence of the the wrinkles in the fillet sections the components were manufactured without defects. The robustness of the component was evaluated

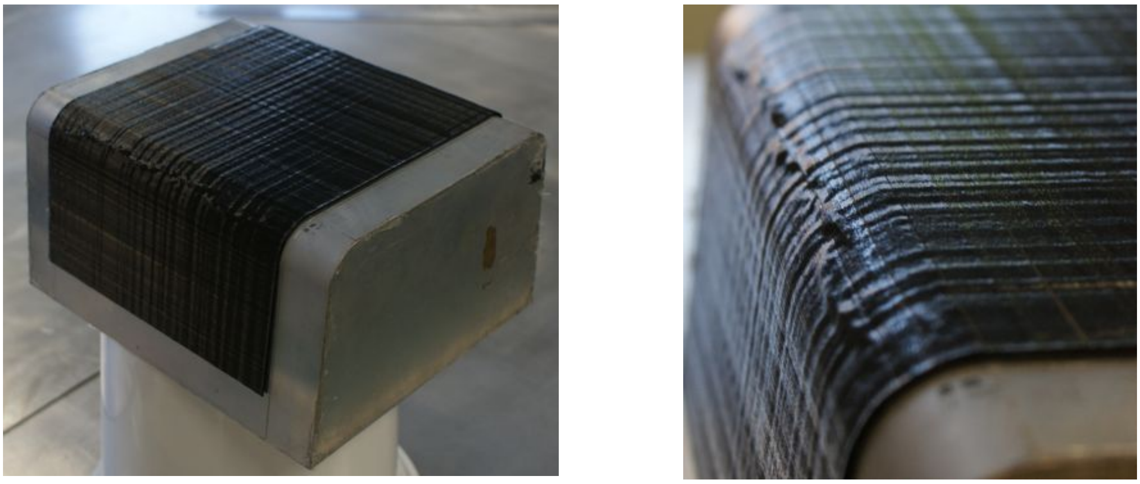

(a)

(b)

Figure 3.19: Preform spar section after activation.

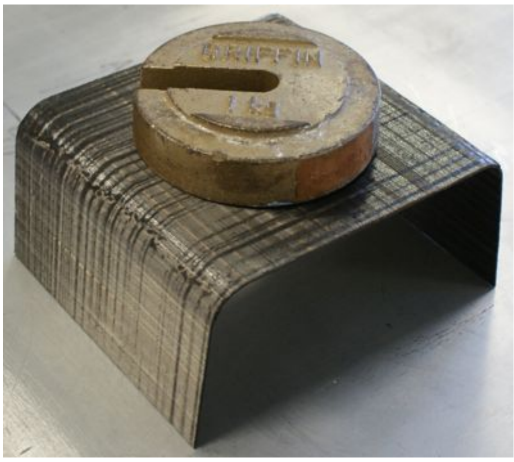

Figure 3.20: Robustness demonstration of the preform spar section.

with an initial test using a 1 kg weight. This weight was placed on the top segment of the spar section as shown in figure 3.20. The component was able to withstand the load and did not show any signs of fibre debonding.

3.3 Test protocols

A set of experiments is necessary to extract the material model parameters for the continuum damage model presented in section 2.1.3. The protocol comprises five different tests specific to this continuum damage model [8, 57]. Tensile and compressive tests were carried out on unidirectional coupons. With the results it is possible to extract the undamaged values for the Poisson's ratio, elastic moduli as well as the critical strain threshold values for tension and compression. Furthermore, the ultimate damage threshold values corresponding to fibre rupture and compressive damage are determined from these data. The compressive factor describing the non-linear fibre compressive behaviour is also deduced from the compressive experiments. The compressive and tensile tests in the fibre direction are preformed under monotonous loading while cyclic loading/unloading tests with increasing load levels under tension were performed on $[\pm 45°]_{2s}$ coupons. The cyclic tests allow the deduction of the undamaged shear modulus and the energetic threshold values for critical, initial and elementary shear damage. In addition, initial yield stress and hardening coefficients can be determined.

Loading/unloading cycles are also performed on $[+45°]_{2s}$ laminates to determine the undamaged transverse elastic modulus and the coupling factor between transverse and plastic shear strains. Furthermore, $[\pm 67.5°]_{2s}$ coupons are used to determine the energetic threshold values for critical, transverse and brittle transverse damage limit

for the matrix interface. In addition experiments on $[+45°]_8$ and $[\pm67.5°]_{2s}$ coupons can be used to contribute to the determination of shear and transverse values using transformation rules from classical laminate theory.
The material model described in section 2.1.3 is also used for the simulation of the bindered preform material. However, due to the missing support of the resin matrix compressive experiments were not performed on the preform material. Hence the test plan was reduced by excluding the compressive experiments on $[0°]_{16}$ specimens. In addition to this standard test protocol, cyclic tests in the fibre direction are also carried out. The results obtained are not used to determine the material parameters for the material model but are useful for the investigation of the material behaviour and will possibly find application in future work. Furthermore, the test protocol is extended by coupons with a $[90°]_8$ layup that were tested with respect to alternative parameter determination techniques as described in chapter 5.
DCB[5] and ELS[6] tests were carried out to determine the values for the interlaminar fracture toughness for mode I and II respectively. The data obtained were also used to determine the parameters for initial normal and shear delamination stress for the cohesive elements of the finite element model.

3.3.1 In-plane tests

The tensile and compressive tests were carried out on an Instron 5500R test machine [189]. This electromechanical test machine is computer controlled and allows testing under quasi-static conditions. Here specimens were tested with a constant cross-head displacement rate of 0.1 $^{\mathrm{mm}}/_{\mathrm{min}}$. A 100 kN load cell was used in the experiments performed on the laminated material. Lower loads were required for the preform material. Thus 5 kN and 100 N load cells were used in this case. Force and cross-head displacement were recorded by a data acquisition system which is directly connected to the test machine.
Material characteristics such as ultimate tensile strength, modulus of elasticity and yield points can be directly deduced from the data obtained with this setup. Nonetheless due to compliance effects within the testing machine it is advantageous to obtain the strains from the specimen surface. In the case of the laminate material, the strains were measured using a digital image correlation (DIC) system [190] which generates the complete displacement field from one surface of the specimen. Therefore the specimen surface is sprayed with a random speckle pattern of black dots on a layer of white primer prior to testing as shown in figure 3.21.

---

[5] Double-Cantilever Beam

[6] End-Loaded Split

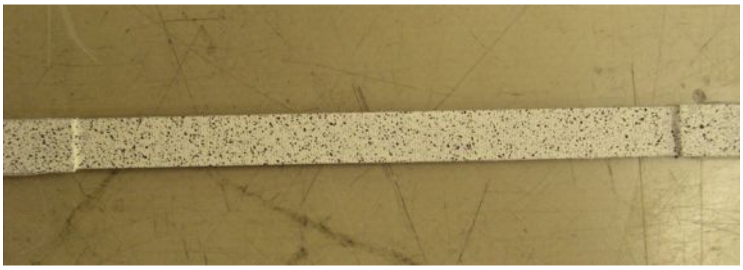

Figure 3.21: Specimen painting for the digital image correlation strain field measurement.

The system is connected to the testing machine and reads the output of the load cell. Hence the output can be synchronised with images acquired throughout the experiment via two 1.4 MPixel cameras mounted on a tripod as shown in figure 3.22. Sufficient lighting is essential for the digital image correlation system to allow successful analysis of painted surfaces. The specimen is clamped at the tabbed top and bottom areas.

Figure 3.22: Stereo camera system mounted on a tripod.

Prior to testing it is necessary to calibrate the dual camera system. A dotted grid is rotated at different angles as shown in figure 3.23 while static images are taken. A cubic volume is generated from these images containing the region of interest (ROI). If testing conditions remain unchanged throughout the whole duration of the test programme it is not necessary to perform the calibration again. However, it is a good idea to verify the calibration prior to testing. Therefore a short series of pictures on the unloaded specimen are taken and an analysis is performed on this data to assess whether recalibration is necessary.

After the experiment the acquired synchronised images are analysed via a correlation algorithm. This algorithm tracks deformation changes of the paint speckle pattern in small distinct areas called subsets. Therefore the algorithm relates the relative displacement from the initial undeformed state and computes a three-dimensional

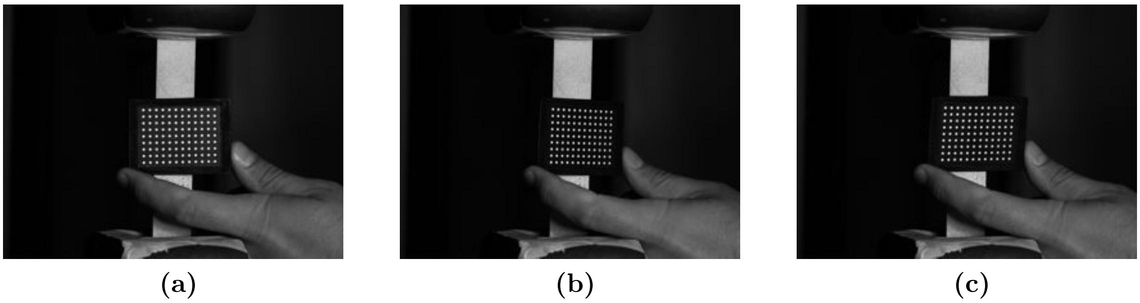

Figure 3.23: Calibration for stereo image system with target plate.

deformation field from the synchronised images. Figure 3.24 illustrates the visualised strain field in the 22-direction as a two-dimensional projection onto the specimen surface and as a three-dimensional representation.

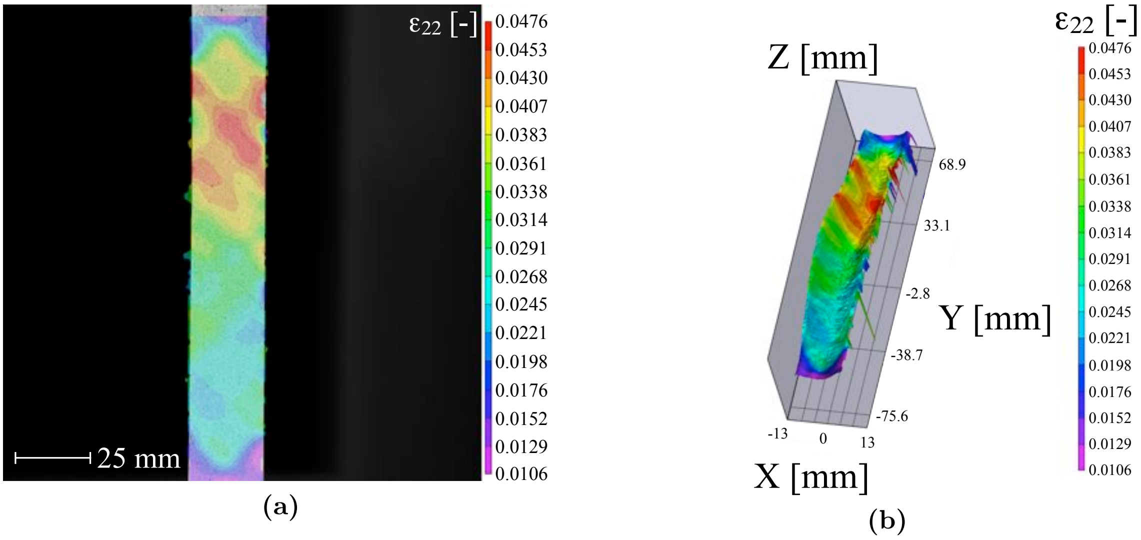

Figure 3.24: Exemplary results obtained with the DIC system, (a) projected strain field onto specimen surface and (b) 3D plot of the strain field.

The strain field from the specimen centre was extracted to take advantage of the uniform strain distribution. The results from the DIC system were exported to a text file for further processing. This file contains the information on the relative image pair, load cell output and computed strains in X, Y and Z-direction of the specimen for each increment. The DIC method has the advantage of being a non-contacting measuring method and therefore the deformation field is obtained without actually influencing the experiment. This system can also be used as a two-dimensional system in cases where out-of-plane movements are negligible. The setup is then simplified with the use of only one camera.

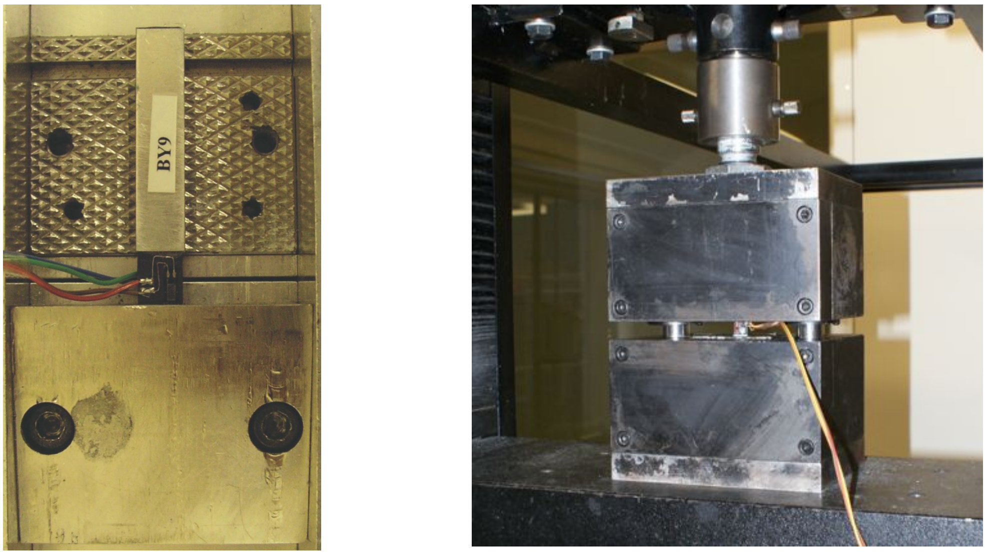

(a) (b)

Figure 3.25: Components for a compressive loading experiment (a) jaws for specimen alignment (b) guiding blocks.

In compression experiments the specimen is gripped on the top and bottom side with jaws as shown in figure 3.25a. Subsequently, the specimen is placed in the compression rig which consists of two solid steel blocks that are guided with two rods on each side to ensure the alignment and prevent buckling of the specimen (see figure 3.25b). An adequate light source could not be installed due to the limited accessible space between the guiding blocks. This limitation results from the geometry of the compression specimens used with a measuring surface of 10×10 mm (see figure 3.25b).

(a) (b)

Figure 3.26: Compression specimen (a) front and (b) rear side.

Two electrical resistance strain gauges (FLA-5-11) [191] were bonded to the front and rear surface of the specimen to measure the strains as shown in figure 3.26. The strains were recorded independently via a data acquisition box in combination with a LabVIEW program [192]. The recorded strains were synchronised with the force output from the test machine. Figure 3.27 illustrates a characteristic result from a valid compression experiment. The stress-strain curves as obtained from the front and rear surface of the specimens are plotted along each other. The occurrence of buckling effects would be directly visible in such a plot. Compressive modulus values from both strain curves are averaged for further analysis following the test standard [184]. According to this standard a relative error between corresponding strain values is calculated. For the validity of the experiment this error is required not to exceed a threshold value of 10%.

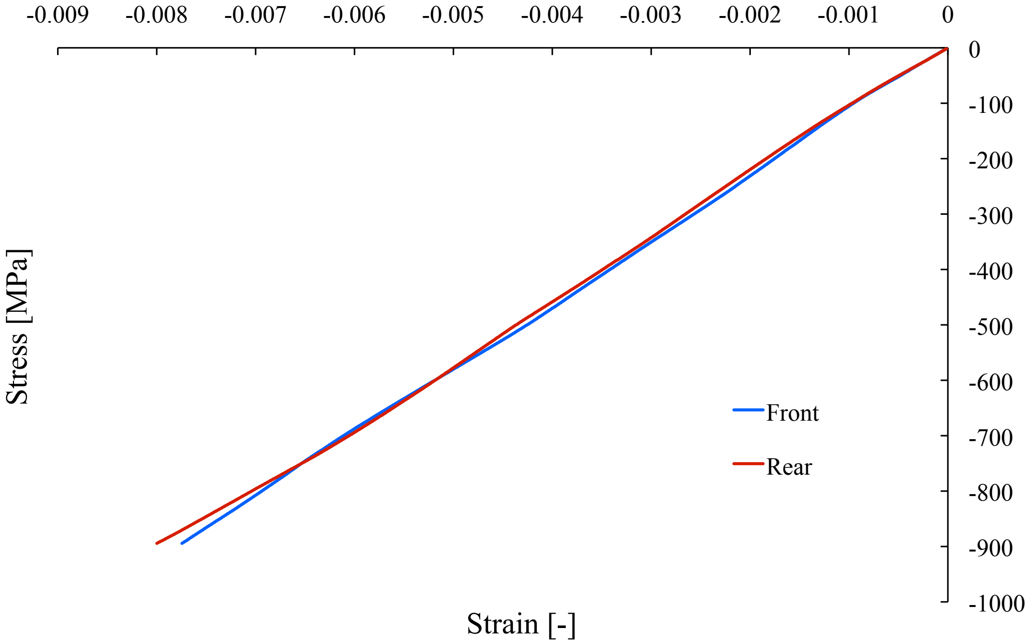

Figure 3.27: Compressive stress-strain curves obtained from frontal and rear strain gauges.

For the initial in-plane characterisation experiments on the inhomogeneously bindered preform material a laser extensometer was used [193] as it was uncertain whether a layer of paint on the font surface could affect the results[7]. Preform specimens also need to be handled very carefully during clamping due to the low strength of the material. As part of the test setup reflective stickers were placed on the top and bottom end of the specimen surface as shown in figure 3.28a. The laser extensometer is positioned in front of the specimen. In operation the extensometer emits a laser beam and receives the reflections from the stickers on the specimen surface with a charge-coupled device (CCD) which converts the signal to a digital value. The laser extensometer and the Instron 5500R test machine are connected to a data acquisition system. The data sets from the load cell and the extensometer are synchronised and acquired using a LabVIEW program.

---

[7] These experiments also showed that the material exhibits relatively high robustness. Hence specimens made with homogeneously bindered yarn were tested using the DIC equipment.

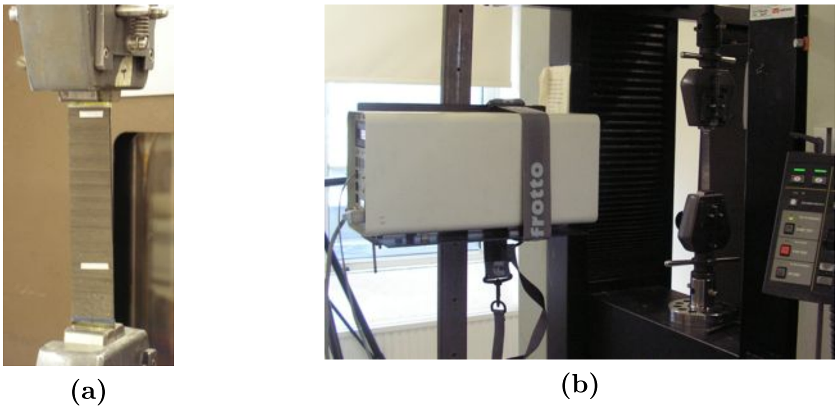

(a) (b)

Figure 3.28: Test setup for transverse loading.

3.3.2 Out-of-plane tests

Experiments to determine the values for the interlaminar fracture toughness for mode I and II were performed on a Zwick Z010 test machine [194] equipped with a 2 kN load cell. The loads are introduced via load blocks which were bonded onto the specimen surface during the preparation. A constant cross head displacement rate of 2 mm/min was used. The test standard for mode I [79] was followed. So far no standardised test method for mode II delamination testing of fibre-reinforced composites has been established. Hence the guidelines from the ESIS TC4 protocol [80] are used for testing ELS specimens in the context of this work.

The load blocks which are attached to the lower and upper sub-laminate are fixed in the test rig to introduce mode I delamination to the specimen. The progressing cross head displacement of the test machine forces the initiated crack to propagate along the specimen as shown in figure 3.29 . Thereby the inserted PTFE film acts as a crack initiation point from which the propagation can evolve.

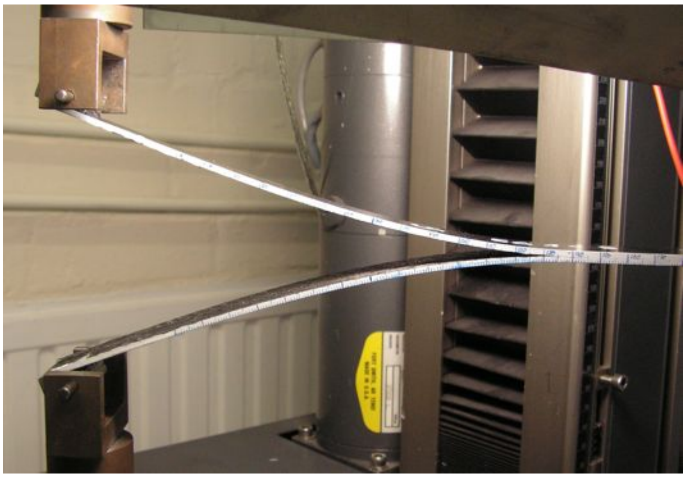

Figure 3.29: Mode I delamination test.

In general the crack follows the path of least resistance. Hence UD specimens are usually not prone to effects such as fibre bridging which can appear on specimens with cross-ply arrangements [71, 195]. Figure 3.30 shows the crack surface of the DCB specimen after a test. The crack initiation via the inserted film is clearly visible by the imprints while the delamination surface demonstrates that the crack remained in the mid-plane of the specimen as intended.

Figure 3.30: Inspection of mode I delamination surface after the experiment.

A calibration is carried out prior to testing in mode II delamination. This calibration is necessary for the analysis of the experiment and compensates for the movement of the sliding clamp. Therefore the specimen is loaded on the unnotched side while the pre-cracked side is clamped as shown in figure 3.31. During this procedure the free arm length is altered between 110-50 mm using a step size of 10 mm. For each free arm length the specimen is loaded to 250 N while the deflection is recorded. A calibration is required for each material type.

After the calibration procedure the specimens can be tested for mode II delamination. Therefore the specimens are positioned in the sliding clamp on their unnotched side with a free arm length of 100 mm. The load block, which is bonded to the lower sub-laminate surface, is connected to the test rig. The applied cross head displacement pulls the lower sub-laminate upwards and forces the crack to propagate by shearing both sub-laminates over each other.

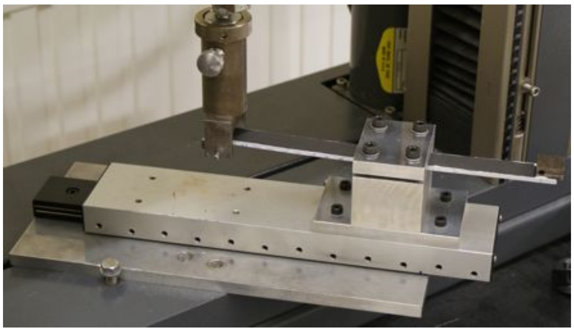

Figure 3.31: ELS specimen setup.

For both delamination experiments the load and cross-head displacement are recorded by the data acquisition system while the propagated crack length is noted and the corresponding force is marked within the acquisition software. Figure 3.32 illustrates a load-displacement curve for mode I crack propagation. Markers indicate the forces corresponding during the crack propagation points in the load-displacement curve.

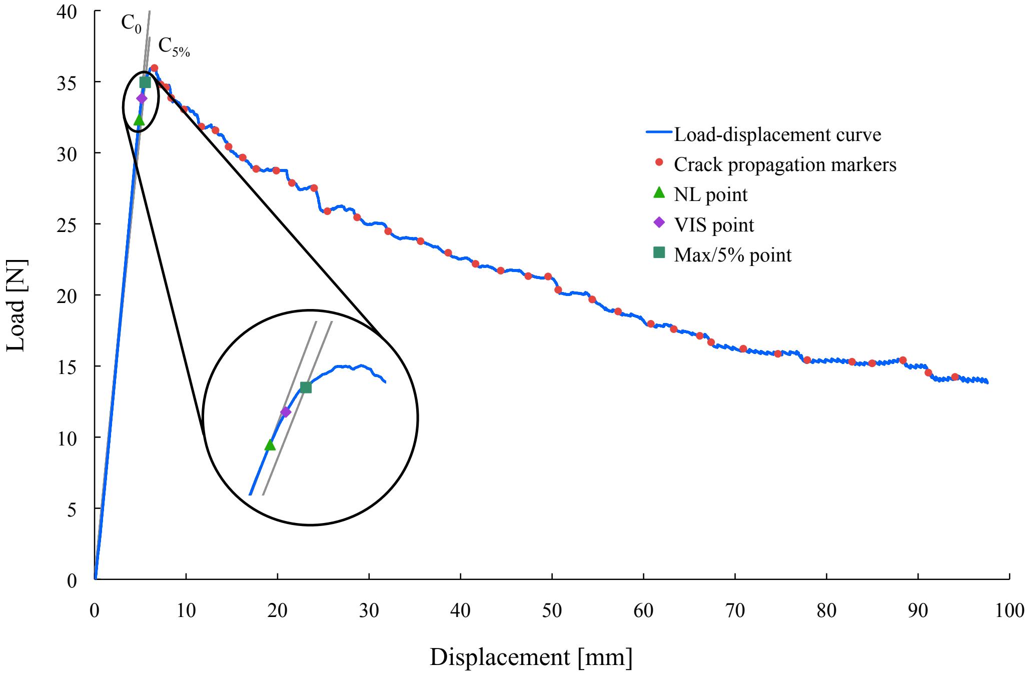

Figure 3.32: Load-displacement curve for a DCB test.

Figure 3.33 illustrates the load displacement curve for mode II delamination. Similarly to mode I crack propagation the material is able to withstand loading up to a maximum values after which the crack propagation starts. The tests were stopped when the crack tip reached the influence zone of the clamp. This effect is visible in the last part of the force-displacement curve where the slope changes towards a positive gradient.

Besides the crack propagation points, as highlighted in figures 3.32 and 3.33 for both delamination modes, additional values are required for the deduction of the critical energy release rates G_{IC} and G_{IIC}.

- The NL point indicates the start of the non-linear portion of the initial load-displacement curve. It can be obtained by plotting a straight line through the linear portion of the load-displacement curve to reveal the point of deviation. The slope of this linear curve leads to the compliance value C_0 of the material.
- The Max/5% point corresponds to the choice of a point in the load-displacement curve depending on which occurs first. To determine the 5% point the initial

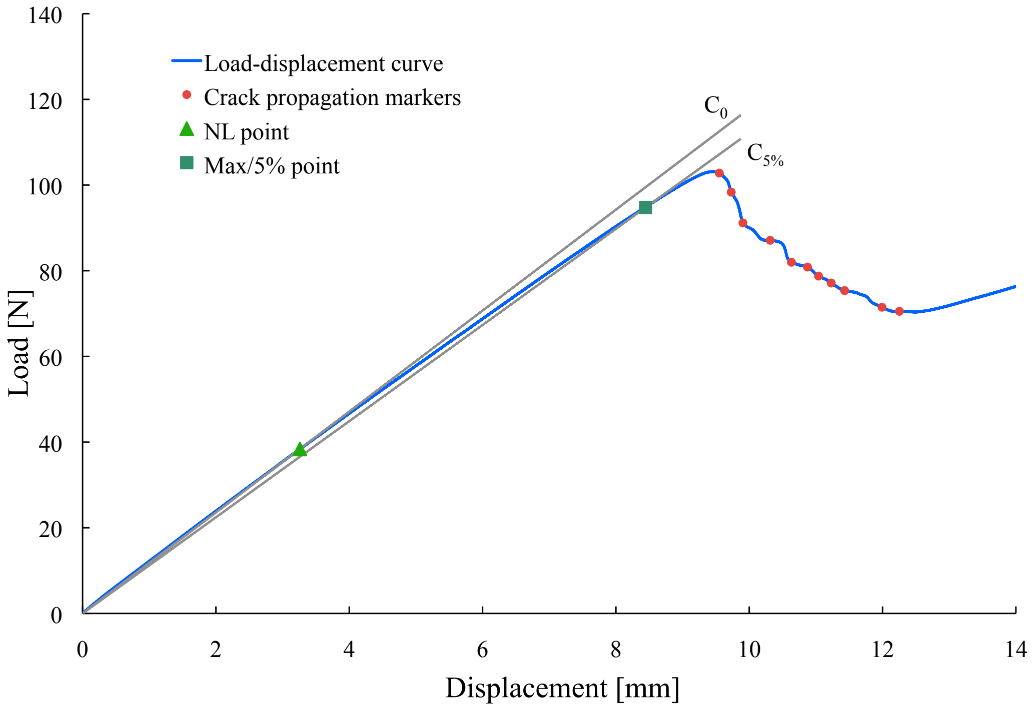

Figure 3.33: Load-displacement curve for an ELS test.

compliance value C_0 is used to calculate a second compliance with $C_{5\%} = 1.05C_0$. By plotting a straight line using this new compliance the 5% point can be identified as the intersection point with the load displacement curve. Unless this intersection point occurs at a larger displacement than the maximum load point the load displacement point of the 5% point is used in the calculation of G_{IC}. Otherwise the point coinciding with the maximum load is used.

- For mode I delamination the VIS point is determined from the first visual observation of the delamination propagation. The corresponding load and displacement data at this point are used for the calculation.

- Propagation points are marked for each crack propagation during the experiment.

The data sets consisting of load, cross head displacement and corresponding crack length at propagation were inserted into an Excel spreadsheet and the resistance curves were generated.

In this work the critical energy release rate G_{IC} was calculated using the corrected beam theory (CBT) method [81, 196]. According to this method the critical energy release rate can be calculated as follows:

$$G_{IC_{CBT}} = \frac{3F\delta}{2b\left(a+|\Delta|\right)}\frac{K}{N} \tag{3.1}$$

where F is the load, δ is the cross-head displacement, b is the width of the specimen, a is the crack length and Δ is the correction factor deduced from the compliance-crack length plot. Parameters K and N are correction factors for large displacements and the load block geometry respectively. The values for K and N are calculated as follows:

$$K = 1 - \frac{3}{10}\left(\frac{\delta}{a}\right)^2 - \frac{2}{3}\left(\frac{\delta l_1}{a^2}\right) \tag{3.2}$$

$$N = 1 - \left(\frac{l_2}{a}\right)^3 - \frac{9}{8}\left[1 - \left(\frac{l_2}{a}\right)^2\right]\frac{\delta l_1}{a^2} - \frac{9}{35}\left(\frac{\delta}{a}\right)^2 \tag{3.3}$$

Here l_1 denotes the distance from the centre of the loading pin to the specimen mid-plane whereas l_2 is the distance from the loading pin centre to the load block edge (see figure 3.12).

For the determination of the critical energy release rate in mode II G_{IIC} was calculated using the experimental compliance method (ECM) as described in [82].

$$G_{IIC_{ECM}} = \frac{3F^3ma^2}{2b} \tag{3.4}$$

Parameter a represents the crack length, F is the load that corresponds to each crack length a_i, m is the slope of the C vs. a^3 plot and b denotes the specimen width. The compliance C is determined from dividing the deflection δ by the load F. Thereafter the final material resistance curves (R-curves), that show the evolution of the apparent delamination toughness versus the crack length, can be plotted.

3.3.3 Components for finite element validation

This section describes the test methods and setups used for experiments utilised to validate finite element models. The standard procedure of testing a three point bending specimens is described and an experiment to evaluate preform material robustness is detailed.

3.3.3.1 Three point bending test

The three point bending test is a standard test used to determine the flexural properties of CFRP composites. This test was chosen for the validation of the material model implementation in the finite element solver Pam-Crash™ [197] due to the simple and efficient execution. The specimens used have the same dimensions as those tested in fibre compression (110×10×2.4 mm) during the in-plane characterisation. Figure 3.34 illustrates a schematic of the setup. The specimen is positioned in the centre of two support cylinders. A third cylinder introduces the load in the mid plane of the specimen. These cylinders have a diameter of 9.98 mm. In accordance with the followed ASTM standard [198] a support span of 48 mm and a cross-head displacement rate of 1.2 mm/min was used for this size of specimen.

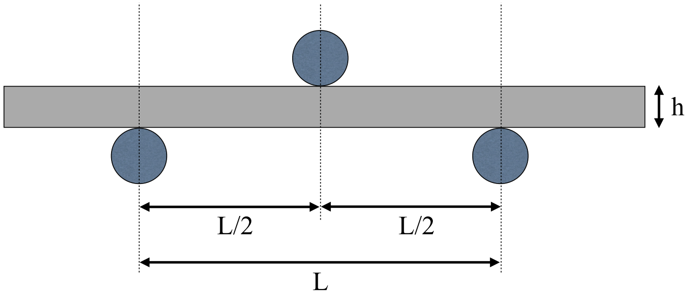

Figure 3.34: Specification for three point bending test.

The tests were performed on an Instron 5500R testing machine equipped with a 5 kN load cell in combination with a laser extensometer. Reflective tape was placed on the side of the specimen as shown in figure 3.35 while the second sticker was attached onto the surface of a metal block. This metal block was positioned under the specimen and between the supports, so that the extensometer receives the laser reflections from the same reference plane.

Figure 3.35: Setup for three point bending test.

The recorded data sets were used to deduce values for the flexural modulus E_f which is later used to validate the material model (see section 6.3.1). It is necessary to record enough data points to determine accurately the slope of the load-deflection curve between 5 and 25% flexural strain. The flexural modulus of elasticity is then calculated using the following formula [198]:

$$E_f = \frac{mL^3}{4bt^3} \tag{3.5}$$

where m is the slope of the initial straight-line portion of the load-deflection curve, L is the support span, b is the specimen width and t is the specimen thickness.

3.3.3.2 Preform spar section impact

Components for the preform spar section were manufactured from the homogeneously bindered material and were tested in the preform material state. A test was developed to characterise the robustness of the material. Results of these tests are reported in section 4.4.2 and are later used for the validation of finite element models (see section 6.3.2).

A Rosand Type 5 Instrumented Falling Weight Impact Tester was used in combination with a high-speed camera system for the impact tests. In general a drop-tower consists of a striker, which is centered by guiding rods on each side. Additional weights can be added to increase the mass of the striker. In this particular setup a load cell is incorporated within two extensions between the striker and a striker head. A variety of striker heads with different shapes and diameters are available for impact testing. Here a striker head with a radius of 20 mm was used. The total mass of the striker system was adjusted to 3.03 kg to obtain a target impact energy of 30 J. This parameter results in a starting height of 1.01 m with a corresponding impact velocity of 4.47 $^{\mathrm{m}}/_{\mathrm{s}}$. The component is located on the impact rig underneath the striker system as shown in figure 3.36. Two clamps hold the preform component in position on the rig whilst the alignment is checked. Therefore the striker is lowered so that the striker head is close enough to the component.

The rig is moved so that the striker head is shifted 7 mm relative to the outer edge of the component for the alignment as shown in figure 3.37. This shift ensures that the preform will not avoid the striker head by sliding over its surface but will be compressed as intended.

Before arming the system a light barrier, which is used for starting the data recording, needs to be adjusted. Therefore the striker is lowered so that the striker head is approximately 5 mm above the component. The target values are entered in the control computer to set up the system for the experiment and the striker is raised up to the calculated height. In addition a second strike prevention can be enabled where high pressure operated dampers are inserted under the striker after the re-

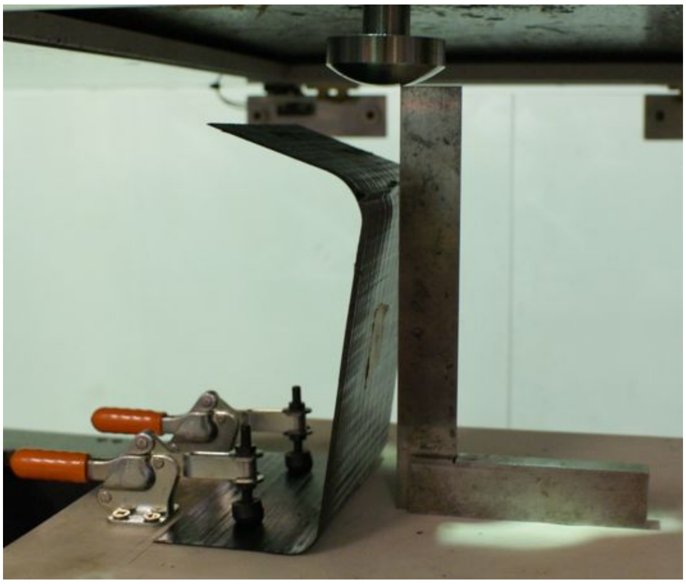

Figure 3.36: Setup for the impact test performed on a preform spar section.

bounce of the impact system. The acquired data provides information of energy, force and velocity evolution throughout the test.

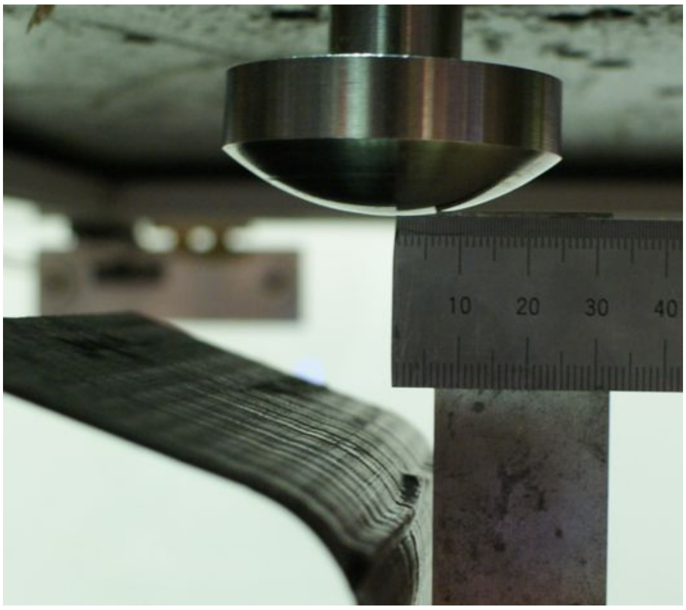

Figure 3.37: Preform spar section alignment for impact test.

In addition to the described setup a Photron FastCam 1024PCI high-speed camera [199] was used. This camera is connected to a PC and allows to record 1000 fps[8] at full 1 MPixel image resolution. Overall the system is able to operate from 60 to 1000 fps at full 1024×1024 Pixels resolution. However, with reduced resolution it is capable to record up to 109500 fps. The electronic shutter is capable of operating

---

[8] frames per second

at 1.5 μs which requires a very strong light source. The camera system was set up to record at full resolution (1024×1024 Pixels) with 1000 fps and a shutter time of 1 fps. The system was triggered by hand in conjunction with the drop tower. A total of 768 frames was sufficient to capture the complete impact.

4 Experimental results

This chapter presents the experimental results of the material characterisation programme and the model validation testing. The characterisation results are reported for each material and the data obtained from the same type of material (preform or laminate) are compared. The characterisation included cyclic loading on the specimens related to transverse and shear properties, whereas uniform quasi-static loading was applied to longitudinal tensile and compression specimens. In addition to these, the results from testing of components used for model validation are presented. These results are compared to the solutions provided by the finite element models in sections 6.3.1 and 6.3.2.

4.1 Test plan overview

The specimens are tested according to the test protocols described in chapter 3.3. The length of preform tensile specimens manufactured from inhomogneously bindered yarns were shortened from 250 mm to 200 mm due to material limitations. Furthermore, the specimen length for out-of-plane specimens for the bindered composite material were shortened from 250 mm to the recommended minimum length of 125 mm due to difficulties in the infusion process. Table 4.1 lists the number of specimens tested for each material and the coupon type.

In order to ensure the feasibility of testing preform material, an initial trial set of experiments was performed using the inhomogeneously bindered yarn. Therefore a minimum test series was carried out. Out-of-plane tests for this material were already undertaken by other consortium members of the PreCarBi project [200].

After the response envelope of the preform material was established on the inhomogeneously bindered yarn an extensive test programme was carried out on the evolved preform material (homogeneously bindered). This test programme included in-plane and out-of-plane experiments. Furthermore, cyclic tensile experiments were performed on a limited amount of specimens to investigate the degradation of the elastic modulus resulting from fibre failure. Due to the limited amount of homogeneously bindered yarn it was decided to manufacture more specimens for the preform characterisation than for the bindered laminate, as more scatter was expected in the preform material response.

A full test programme was also carried out for the reference laminate except the $[+45°]_8$ coupon tests. These tests were omitted as the coupling factors for transverse and shear direction can also be deduced from $[\pm 67.5°]_{2s}$ tests. Similarly to the case of the preform material manufactured using inhomogeneously bindered yarn cyclic tests were also carried out on the reference material under quasi-static conditions. However, it should be noted that these results are not considered in the parameter determination described in chapter 5.

Type	Inhomogeneously bindered yarn	Homogeneously bindered yarn	Reference Laminate	Bindered Laminate
$[0°]_8^t$	2	8	7	3
$[0°]_{16}^c$	-	-	5	4
$[\pm 45°]_{2s}$	3	5	5	3
$[+45°]_{2s}$	-	5	-	3
$[\pm 67.5°]_{2s}$	-	6	3	3
$[90°]_8$	3	4	7	3
DCB	-	5	3	3
ELS	-	5	7	3

Table 4.1: Overview of test specimens.

4.2 Preform materials

The tested preform materials are manufactured using inhomogeneously and an homogeneously bindered yarns (see section 3.1). Specimens for both types of materials were manufactured as described in section 3.2. An initial study for the capabilities of this material was undertaken using the inhomogeneously bindered material.

4.2.1 In-plane properties

A set of five different tests coupons of different fibre orientation and loading conditions are required to characterise a material with respect to the material model described in section 5.1.1. These experiments comprise quasi-static loading in the fibre direction for tension and compression as well as cyclic loading and unloading on $[\pm 45°]_{2s}$, $[+45°]_{2s}$ and $[\pm 67.5°]_{2s}$. Additional tests were carried out on $[90°]_8$ coupons to identify an alternative method for the determination of material parameters.

4.2.1.1 Inhomogeneously bindered material

Tensile specimens of the inhomogeneously bindered material were tested under quasi-static conditions. The resulting elastic moduli of the uniformly loaded specimens are listed in table 4.2, whereas the stress-strain curves obtained are illustrated in figure 4.1. The specimens fail at 1600 MPa and 1800 MPa respectively. Here the curves show good reproducibility. Especially in the lower stress region the curves are matching whereas slight deviation of the stress-strain curves develop in the later part ultimately resulting in differences for the elastic moduli. In comparison the failure strengths in fibre direction of the the laminate system presented in the subsequent sections are in the region of 2400 MPa. For the preform material a 7% binder content is present in the material which means that the test was actually performed on the filaments.

Specimen	Modulus [GPa]	Mean [GPa]	SD [GPa]
$[0°]_8^t$ - 1	133.6	141.0	10.6
$[0°]_8^t$ - 2	148.5		

Table 4.2: Overview of elastic moduli in fibre direction from inhomogeneously bindered preform specimens.

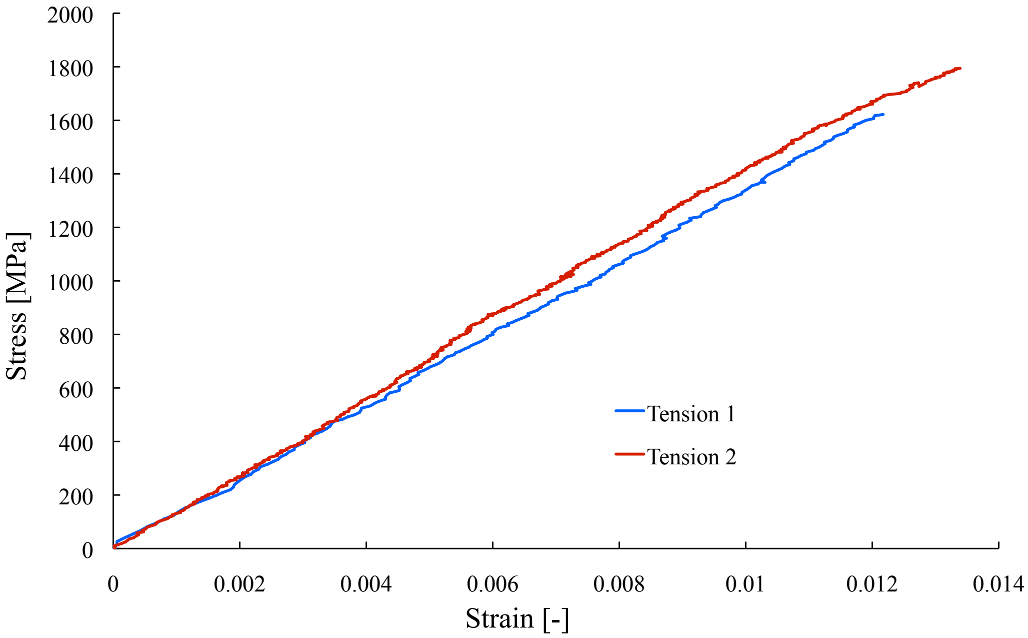

Figure 4.1: Stress-strain curves for tensile tests in the fibre direction performed on inhomogeneously bindered preform.

Figure 4.2 illustrates the cyclic in-plane shear data for the three tested specimens. The first specimen was tested to a higher strain with the aim of observing the high deformation behaviour of the material. Shear specimens in general can be tested to relatively high ultimate strains as there is no appearance of a sudden failure when compared to the failure in fibre or transverse direction. The shear moduli are obtained from the initial slope of the stress-strain curves and are listed in table 4.3. Good agreement for the shear modulus was found and an average value of 2.11±0.1 GPa was obtained from the experiments. Furthermore excellent reproducibility through out the whole experiment was observed.

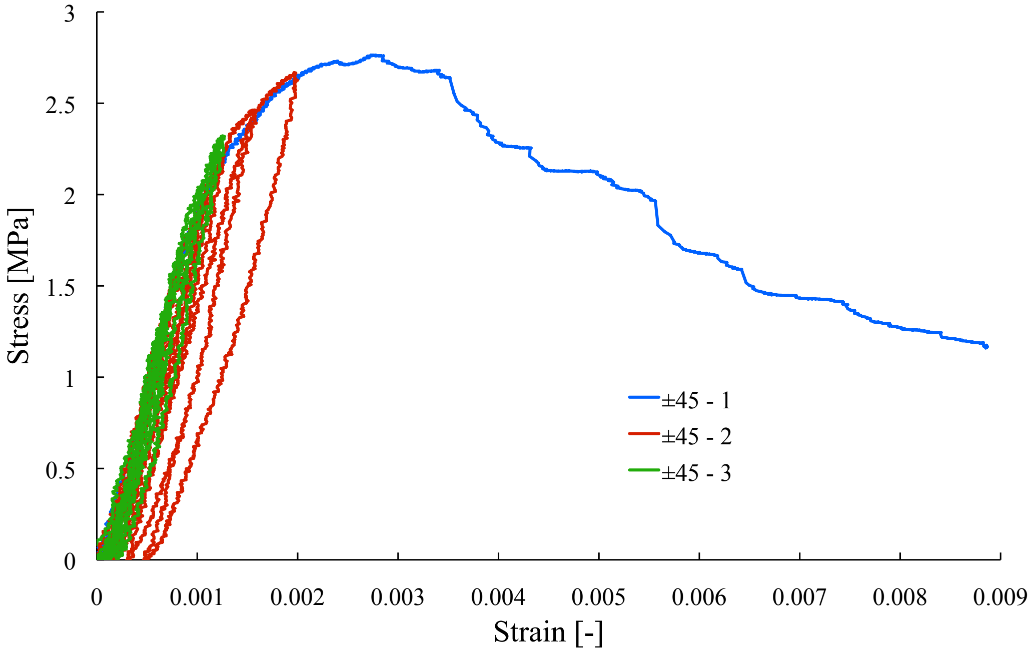

Figure 4.2: Stress-strain curves for shear tests performed on inhomogeneously bindered preform specimens.

Specimen	Modulus [GPa]	Mean [GPa]	SD [GPa]
$[\pm45°]_{2s}$ - 1	2.1	2.1	0.1
$[\pm45°]_{2s}$ - 2	2.0		
$[\pm45°]_{2s}$ - 3	2.2		

Table 4.3: Inhomogeneously preform shear moduli obtained from $[\pm45°]_{2s}$ tests.

The data obtained in [90°] tests are illustrated in figure 4.3. Here the first two experiments undertaken on this material show a similar material response. Test 1 was undertaken only under uniform loading to obtain a general profile for this experiment. Although this experiment can not be used to deduce the full parameter set for the transverse direction it can still be used to deduce the initial elastic modulus. The curve obtained from test 3 differs drastically from the other experiments, which might be caused by the inhomogneously distributed binder or by improper handling of the specimen prior to testing. Hence this experiment is regarded as an outlier and is not considered when identifying the parameters in the later part of this work. The failure strains reported in this section correspond to the maximum stress points of test 1 and 2. Figure 4.4 shows a specimen after testing were single filaments maintain the connection of the lower and upper part of the coupon. The initial transverse moduli can be deduced from the initial slope and lead to the values reported in table 4.4.

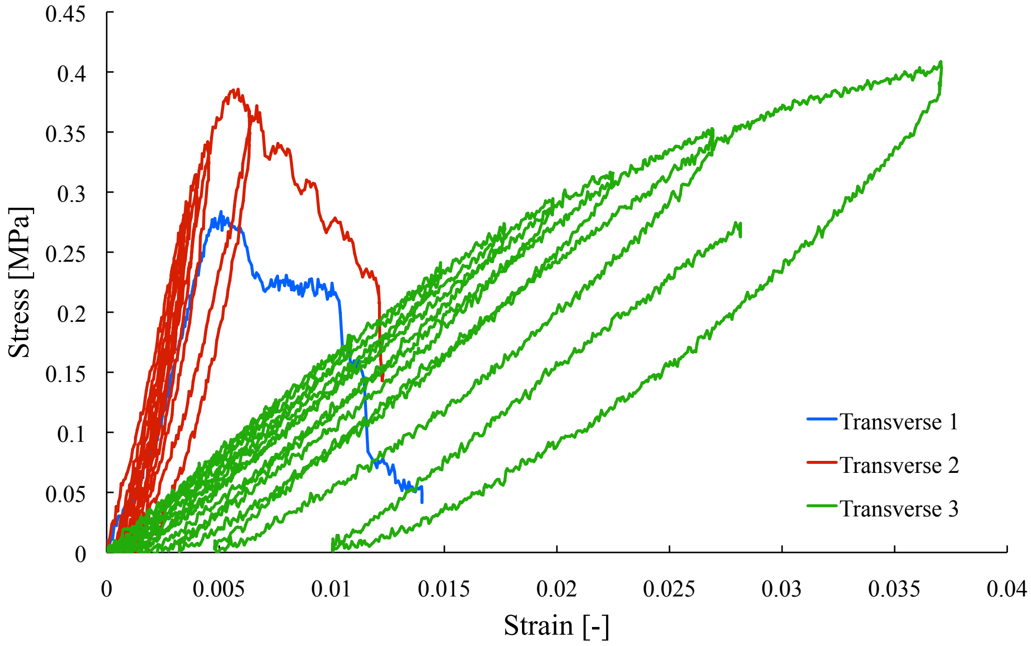

Figure 4.3: Results from transverse experiments with inhomogeneously bindered yarns.

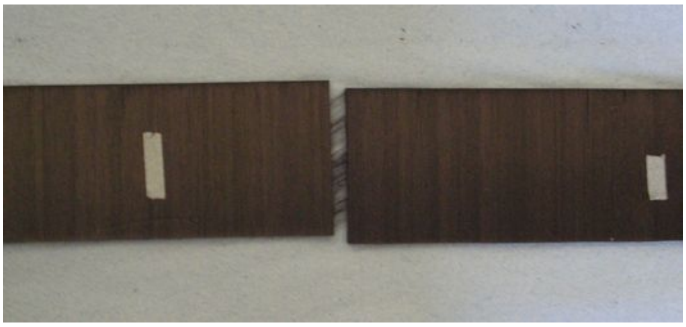

Figure 4.4: Failed transverse specimen as part of the inhomogeneously bindered material test programme.

Specimen	Modulus [GPa]	Mean [GPa]	SD [GPa]
$[90°]_8$ - 1	0.087	0.083 (0.047)	0.006 (0.044)
$[90°]_8$ - 2	0.078		
$[90°]_8$ - 3	0.016		

Table 4.4: Initial transverse moduli for inhomogeneously bindered preform material with corresponding mean value; values in the brackets include the third test.

4.2.1.2 Homogeneously bindered material

A total of eight tensile experiments were carried out on the preform material manufactured from homogeneously bindered yarn. Four specimens were exposed to cyclic loading to investigate the influence of single fibre breaking on the degradation of the elastic modulus. In each cycle the load was increased in comparison to the previous cycle (see figure 4.5). Although the findings of this tests are not used in the context of the modelling work it is possible to deduce the undamaged elastic modulus E_{11}^{0t} from the initial stress-strain curves. The exact procedure is presented in section 5.2.1. Figure 4.6 illustrates the stress-strain curves for all the experiments. For the cyclic experiments (Tensile 4 and 6-8) only the first cycle used for the calculation of E_{11}^{0t} is plotted in this graph. Good agreement for the initial slope of the stress-strain curve was observed with scattered evolution in the later section of the evolution. However, the specimens exposed to cyclic loading fail significantly earlier (700-800 MPa) than the uniformly loaded coupons where loads in the range of 900-1300 MPa are reached. An overview of all moduli is presented in table 4.5 and lead to a value of 136.3±8.3 GPa.The stress-strain curves for the shear experiments are shown in figure 4.7. Here the graphs incorporate a certain amount of scatter especially for the higher stress regions, nonetheless the experiments indicate a good reproducibility. Furthermore, the scatter is reasonable when considering that a supporting matrix is not present in this material. The experiments are stopped after five completed loading/unloading cycles where the maximum stress value of 2.1 MPa is achieved. Results of the initial undamaged shear modulus G_{12}^{0} for each experiment were deduced and vary in the 0.17 - 0.28 GPa range (see table 4.6). The remaining parameter of the set related to damage and accumulation of inelastic deformation in shear direction are determined in the following chapter.

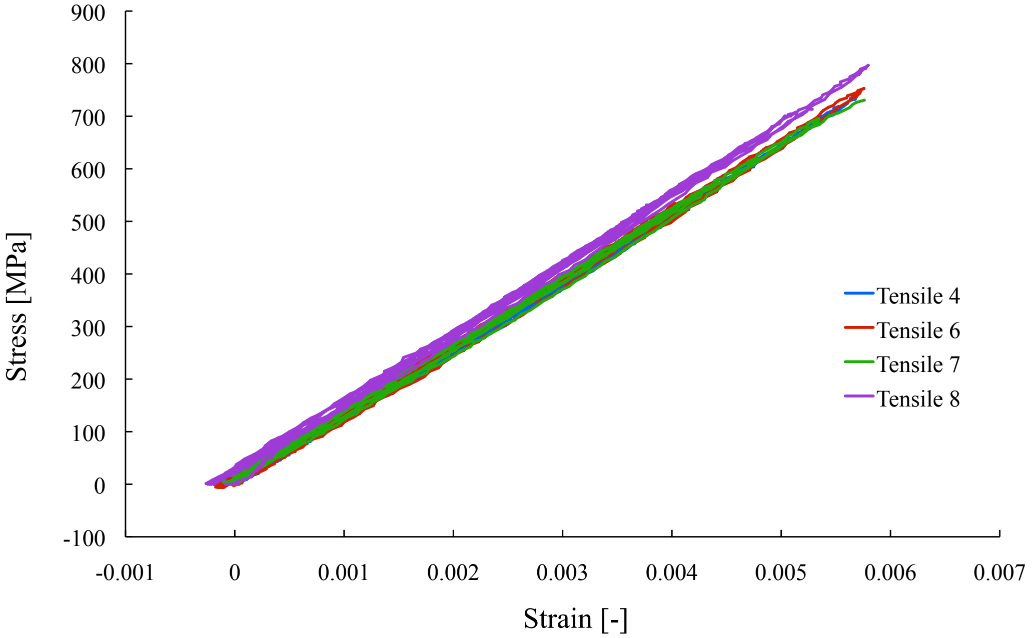

Figure 4.5: Stress-strain curves from cyclic experiments in fibre direction under tensile loading performed on homogeneously bindered fibres.

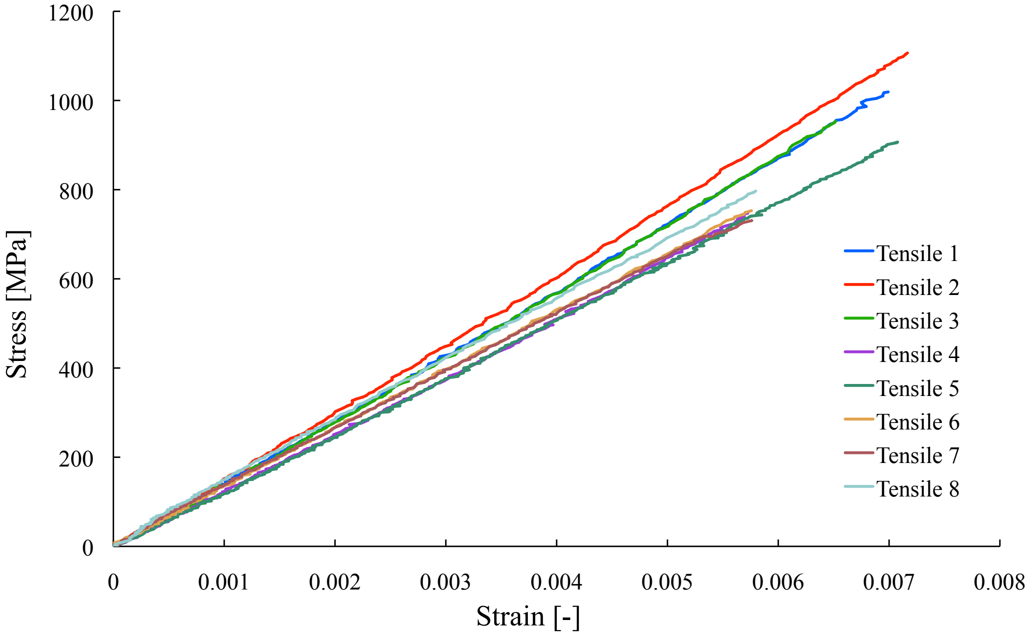

Figure 4.6: Stress-strain curves from tensile experiments with homogeneously bindered fibres.

Specimen	Modulus [GPa]	Mean [GPa]	SD [GPa]
$[0°]_8^t$ - 1	142.2	136.3	8.5
$[0°]_8^t$ - 2	149.7		
$[0°]_8^t$ - 3	145.3		
$[0°]_8^t$ - 4	127.1		
$[0°]_8^t$ - 5	129.1		
$[0°]_8^t$ - 6	130.4		
$[0°]_8^t$ - 7	130.2		
$[0°]_8^t$ - 8	136.4		

Table 4.5: Undamaged tensile elastic moduli in fibre direction for homogeneously bindered preform.

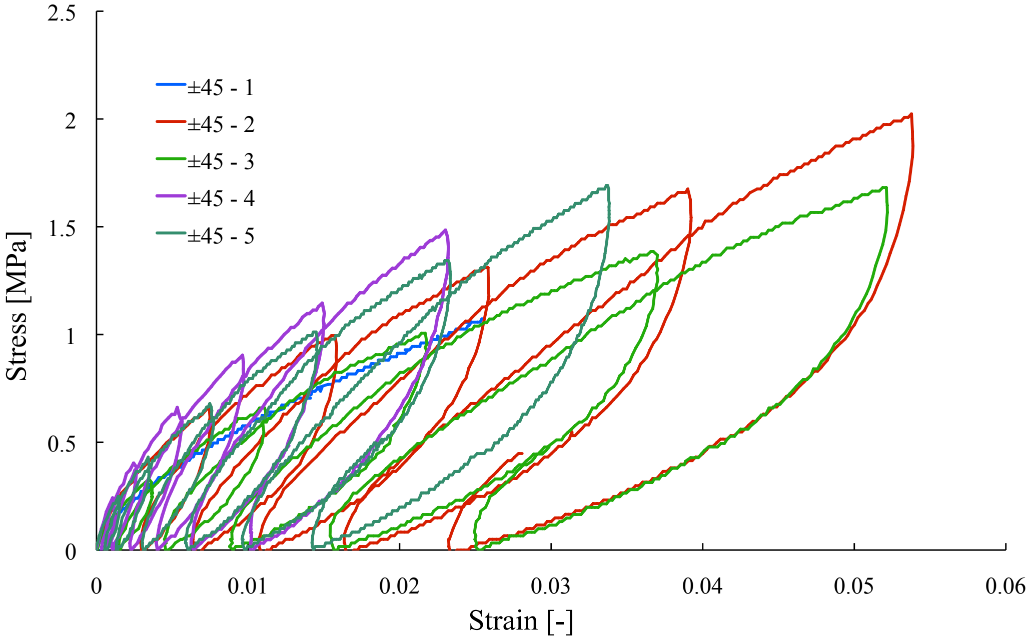

Figure 4.7: Test results for shear specimens manufactured from homogeneously bindered preform panels.

Specimen	Modulus [GPa]	Mean [GPa]	SD [GPa]
$[\pm45°]_{2s}$ - 1	0.28	0.23	0.05
$[\pm45°]_{2s}$ - 2	0.23		
$[\pm45°]_{2s}$ - 3	0.17		
$[\pm45°]_{2s}$ - 4	0.24		
$[\pm45°]_{2s}$ - 5	0.28		

Table 4.6: Undamaged shear moduli obtained from tests on $[\pm45°]_{2s}$ homogeneously bindered preform specimens.

Figures 4.8 and 4.9 show the processed curves for shear and transverse response of the material respectively as obtained in $[+45]_8$ tests. Both material responses were deduced from single coupons using classical laminate theory. In particular the shear responses show good agreement and indicate good reproducibility whereas a notable amount of noise is present in the transverse data. Thus it was not possible to deduce reliable values for the transverse modulus. Nonetheless the moduli deduced from the data (see table 4.6) leads to an average shear modulus of 0.38±0.11 GPa, which is higher than the value obtained from the shear experiment with $[\pm45°]_{2s}$ coupons (0.23±0.05 GPa). In comparison to the shear experiment the achieved failure strengths are much lower within the 0.65 - 0.95 MPa range, which can be explained by the layup of the coupon.

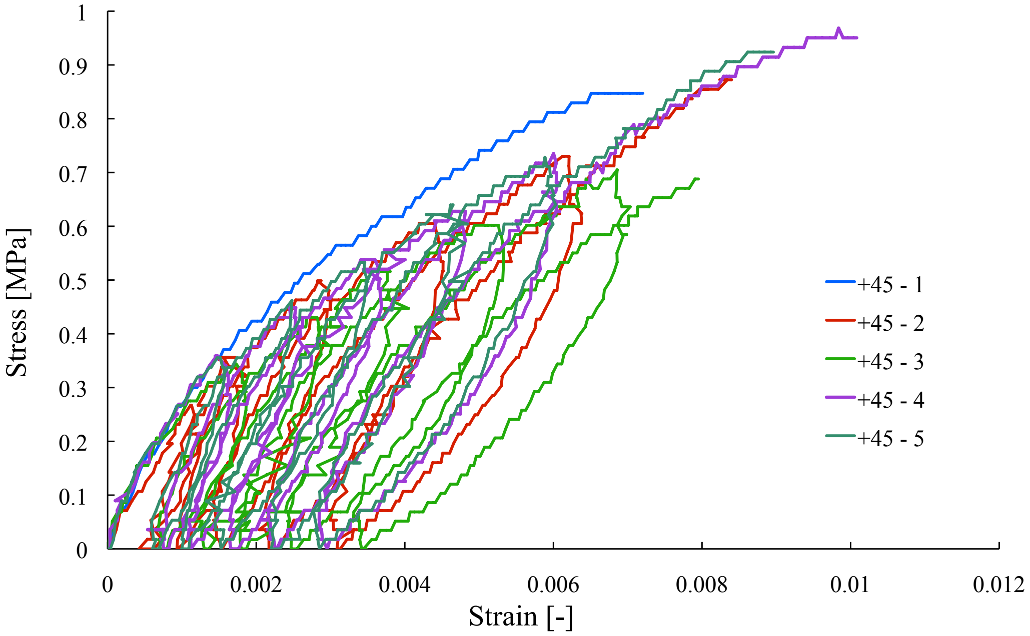

Figure 4.8: Shear responses of $[+45°]_{2s}$ coupons from homogeneously bindered preform panels.

Specimen	Modulus [GPa]	Mean [GPa]	SD [GPa]
$[+45°]_8$ - 1	0.28	0.38	0.11
$[+45°]_8$ - 2	0.26		
$[+45°]_8$ - 3	0.44		
$[+45°]_8$ - 4	0.50		
$[+45°]_8$ - 5	0.43		

Table 4.7: Initial shear moduli deduced from [+45°] homogeneously bindered preform coupons.

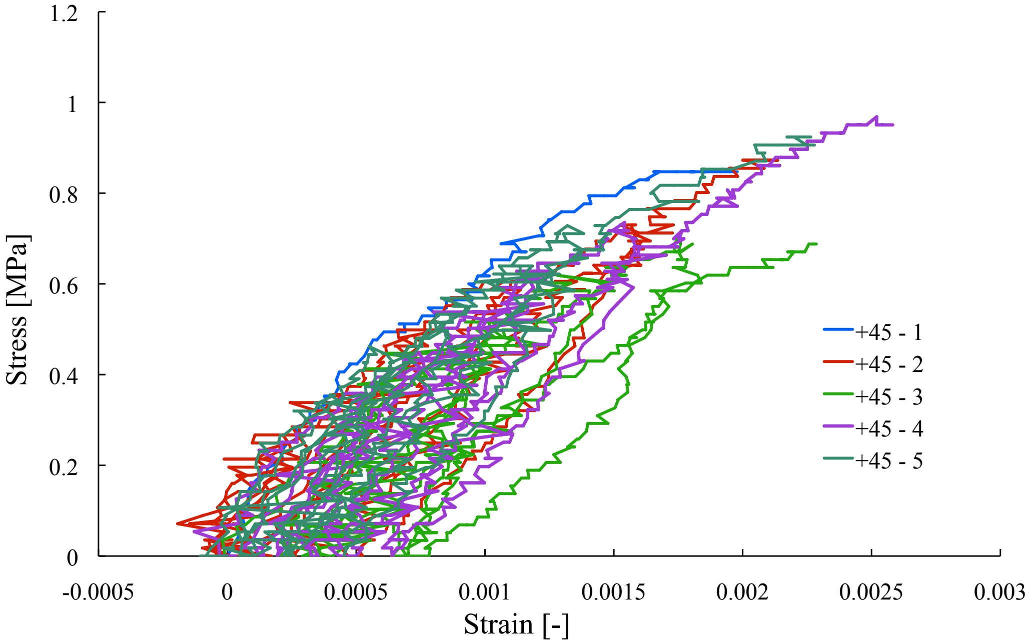

Figure 4.9: Transverse responses of $[+45°]_{2s}$ homogeneously bindered preform coupons.

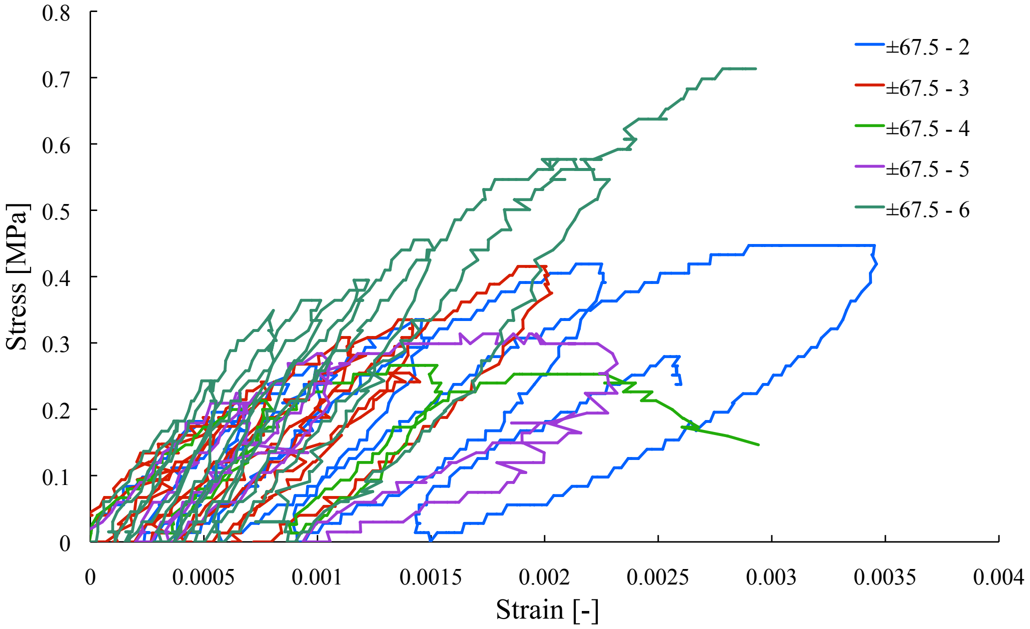

Figure 4.10: Shear responses of $[\pm 67.5°]_{2s}$ coupons manufactured from homogeneously bindered preform panels.

Figures 4.10 and 4.11 illustrate the responses for the shear and transverse direction of the $[\pm 67.5°]_{2s}$ experiments as generated via classical laminate theory. Overall the data for both responses show good reproducibility while only test 4 reaches higher stress values in comparison to the other sets. Furthermore, the noise level is much smaller compared to the $[+45°]_8$ experiments. The moduli for the shear and transverse direction are reported in table 4.8 and 4.9. Similarly to the shear response of the $[+45°]_8$ coupons higher values for the shear modulus are deduced while lower failure strengths and strains were observed. For the deduction of the transverse modulus the test protocol suggests the usage of the transverse responses of the $[+45°]_8$ and $[\pm 67.5°]_{2s}$ experiments. In the case of the $[\pm 67.5°]_{2s}$ experiments the value was averaged leading to a result of 0.7±0.2 GPa.

Specimen	Modulus [GPa]	Mean [GPa]	SD [GPa]
$[\pm 67.5°]_{2s}$ - 2	0.43	0.52	0.11
$[\pm 67.5°]_{2s}$ - 3	0.43		
$[\pm 67.5°]_{2s}$ - 4	0.44		
$[\pm 67.5°]_{2s}$ - 5	0.62		
$[\pm 67.5°]_{2s}$ - 6	0.66		

Table 4.8: Overview of shear moduli deduced from the shear response of $[\pm 67.5°]_{2s}$ specimens manufactured from homogeneously bindered preform panels.

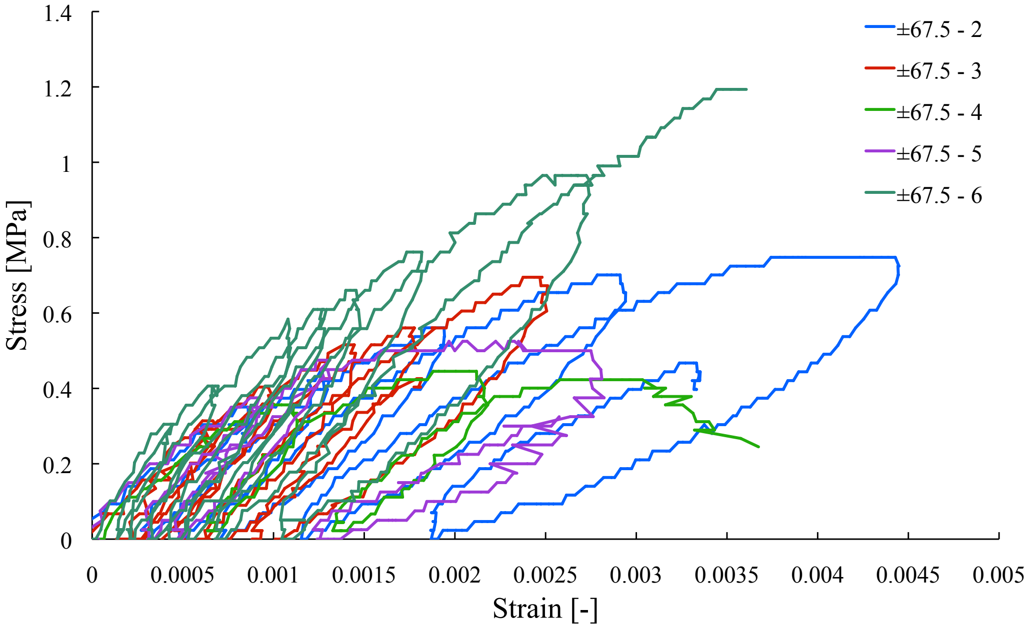

Figure 4.11: Transverse material responses of $[\pm 67.5°]_{2s}$ specimens cut from homogeneously bindered preform panels.

Specimen	Modulus [GPa]	Mean [GPa]	SD [GPa]
$[\pm 67.5°]_{2s}$ - 2	0.55	0.70	0.21
$[\pm 67.5°]_{2s}$ - 3	0.72		
$[\pm 67.5°]_{2s}$ - 4	0.75		
$[\pm 67.5°]_{2s}$ - 5	0.49		
$[\pm 67.5°]_{2s}$ - 6	1.01		

Table 4.9: Moduli determined from transverse responses of $[\pm 67.5°]_{2s}$ preform specimens manufactured with homogeneously bindered material.

The resulting stress-strain curves from transverse experiments are presented in figure 4.12 and show consistent data. Slightly higher failure strengths and strains were obtained when comparing these curves to those of the transverse responses from $[+45°]_8$ and $[\pm 67.5°]_{2s}$. The values for the undamaged transverse moduli as determined from the initial slopes are listed in table 4.10. The outcome of this analysis is particularly interesting as the results obtained lead to an average value of 0.5±0.1 GPa. In comparison a value of 0.7±0.2 GPa was obtained from $[\pm 67.5°]_{2s}$ tests.

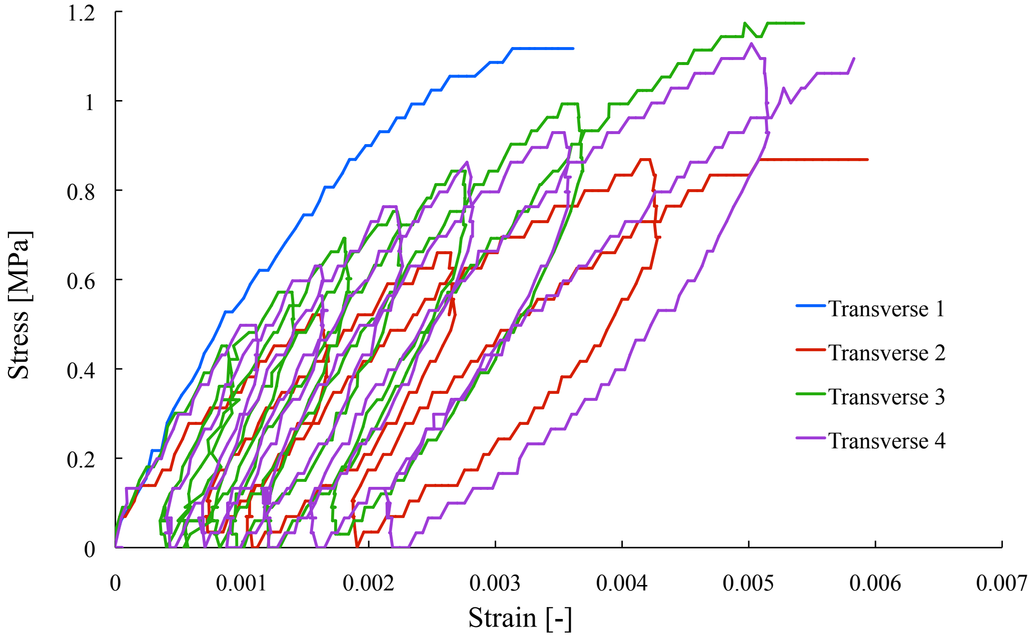

Figure 4.12: Stress-strain results from transverse experiments on homogeneously bindered preform material.

Specimen	Modulus [GPa]	Mean [GPa]	SD [GPa]
$[90°]_8$ - 1	0.50	0.50	0.10
$[90°]_8$ - 2	0.36		
$[90°]_8$ - 3	0.60		
$[90°]_8$ - 4	0.55		

Table 4.10: Transverse moduli obtained from preform specimens with $[90°]_8$ layup for homogeneously bindered panels.

4.2.2 Out-of-plane properties

4.2.2.1 Homogeneously bindered yarn

The curves obtained for mode I fracture toughness versus crack length are presented in figure 4.13. Here the resistance curves show significant differences between the experiments with values for the propagation fracture toughness in the 92 - 243 $^{J}/_{m^2}$ range. The values listed in table 4.11 were computed using the implementation of the corrected beam theory as described by equation 3.1 in an Excel spreadsheet. Table 4.12 lists shows the initiation fracture toughness values for mode I delamination.

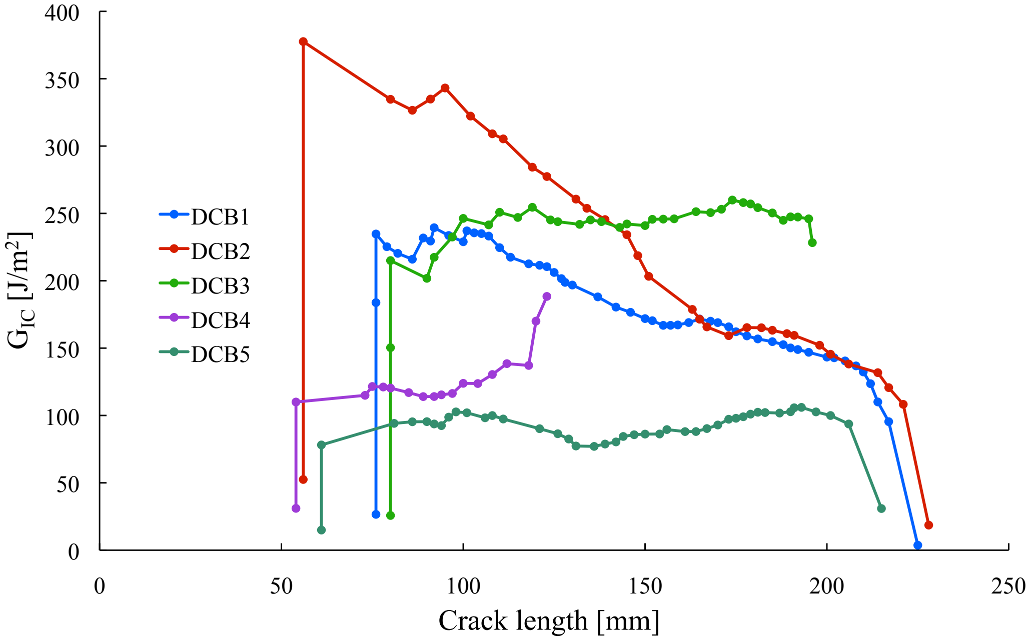

Figure 4.13: Mode I delamination results for preform specimens from homogeneously bindered material.

Specimen	DCB 1	DCB 2	DCB 3	DCB 4	DCB 5
G_{IC} [J/m^2]	180.3	211.5	243.5	129.2	92.1
SD [J/m^2]	44.7	80.8	12.2	20.5	12.5
Mean [J/m^2]	171.3				
SD [J/m^2]	61.1				

Table 4.11: Overview of mode I propagation fracture toughness values of homogeneously bindered preform material.

Specimen	DCB 1	DCB 2	DCB 3	DCB 4	DCB 5
G_{IC}^{ini} [J/m^2]	234.7	377.6	215.0	109.9	78
Mean [J/m^2]	203.0				
SD [J/m^2]	118.2				

Table 4.12: Overview of mode I initiation fracture toughness values of homogeneously bindered preform material.

Figure 4.14 shows the overview of the acquired R-curves for mode II delamination. Similarly to mode I curves reveal significant differences. Test 1 - 4 remain under the 150 $^{\text{J}}/_{\text{m}^2}$ mark, whereas experiment 5 is higher reaching a maximum value of 250 $^{\text{J}}/_{\text{m}^2}$. An Excel spreadsheet with the implementation of the experimental compliance method (see equation 3.4) was used for the calculation of the critical energy release rate values in model II. Table 4.13 lists the propagation results from each experiment while an averaged value of 107 $^{\text{J}}/_{\text{m}^2}$ with a corresponding standard deviation of 62 $^{\text{J}}/_{\text{m}^2}$ was determined. In addition table 4.14 lists the corresponding initiation fracture toughness values with an average value of 67.2±50.3 $^{\text{J}}/_{\text{m}^2}$.

Specimen	ELS 1	ELS 2	ELS 3	ELS 4	ELS 5
G_{IIC} [J/m^2]	58.5	93.1	101.4	69.7	212.6
SD [J/m^2]	29.3	33.3	23.4	19.7	36.6
Mean [J/m^2]	107.1				
SD [J/m^2]	61.5				

Table 4.13: Overview of mode II fracture toughness values for crack propagation on homogeneously bindered preform material.

Specimen	ELS 1	ELS 2	ELS 3	ELS 4	ELS 5
G_{IIC}^{ini} [J/m^2]	16.4	45.9	83.4	43.9	146.4
Mean [J/m^2]	67.2				
SD [J/m^2]	50.3				

Table 4.14: Overview of mode II initiation fracture toughness values of homogeneously bindered preform material.

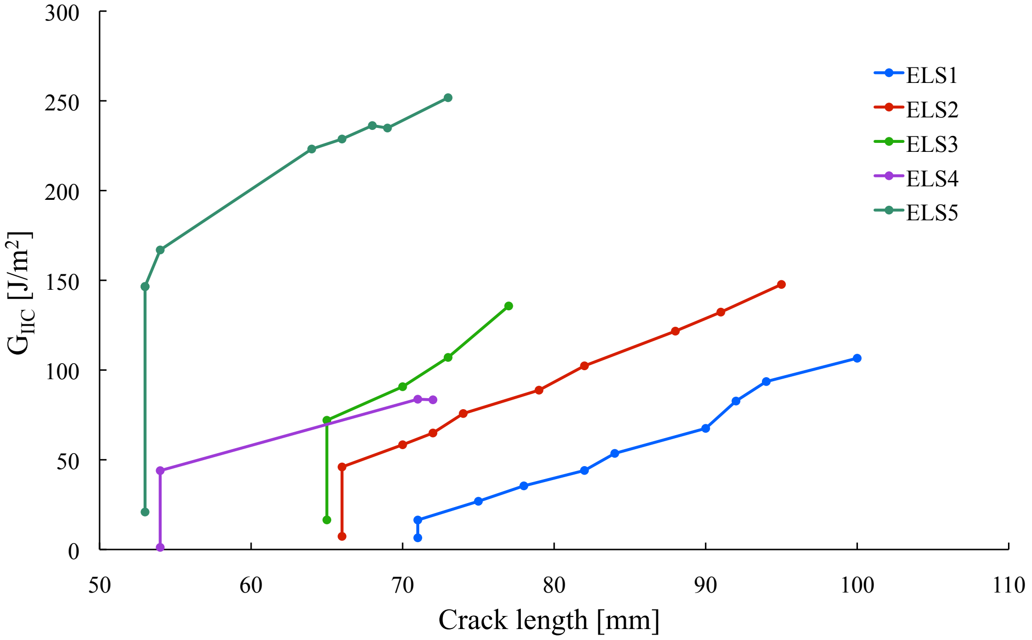

Figure 4.14: Mode II delamination results for ELS preform specimens of homogeneously bindered material.

4.2.3 Material comparison

Tests in the fibre direction on the two preform materials lead to similar results for the undamaged elastic modulus (see figure 4.15). Averaged values of 141±10.58 GPa and 136±8.49 GPa were obtained for the preforms manufactured from inhomogeneously and homogeneously bindered material respectively. This material direction is highly dominated by the properties of the carbon fibres. Both versions of the material are based on the same base material, hence similar moduli are obtained. However, the failure strains and stresses recorded for the inhomogeneously bindered material are approximately double compared to the homogeneously bindered materials. Moreover the resulting values for the inhomogeneously bindered preform material are close to those obtained for the laminated material (see figure 4.35).

In the shear experiments performed on $[\pm 45]_{2s}$ specimens not only the initial slopes for the materials differ significantly but the whole profile of material responses shows a remarkable difference. For the preform material produced from inhomogeneously bindered material a maximum stress of 2.6 MPa is reached at 0.28% strain while the homogeneously bindered material reaches a stress level just below 1.6 MPa with a maximum strain of 5.3%. Large differences were observed for the undamaged shear moduli of the two materials. Results from the inhomogeneously bindered material lead to a modulus of 2.1 GPa which could be influenced by the binder particle sizing. Moduli in such an order of magnitude would be more expected for a laminate material but for a preform. In contrast tests performed on the homogeneously bindered material lead to a value of 0.24 GPa.

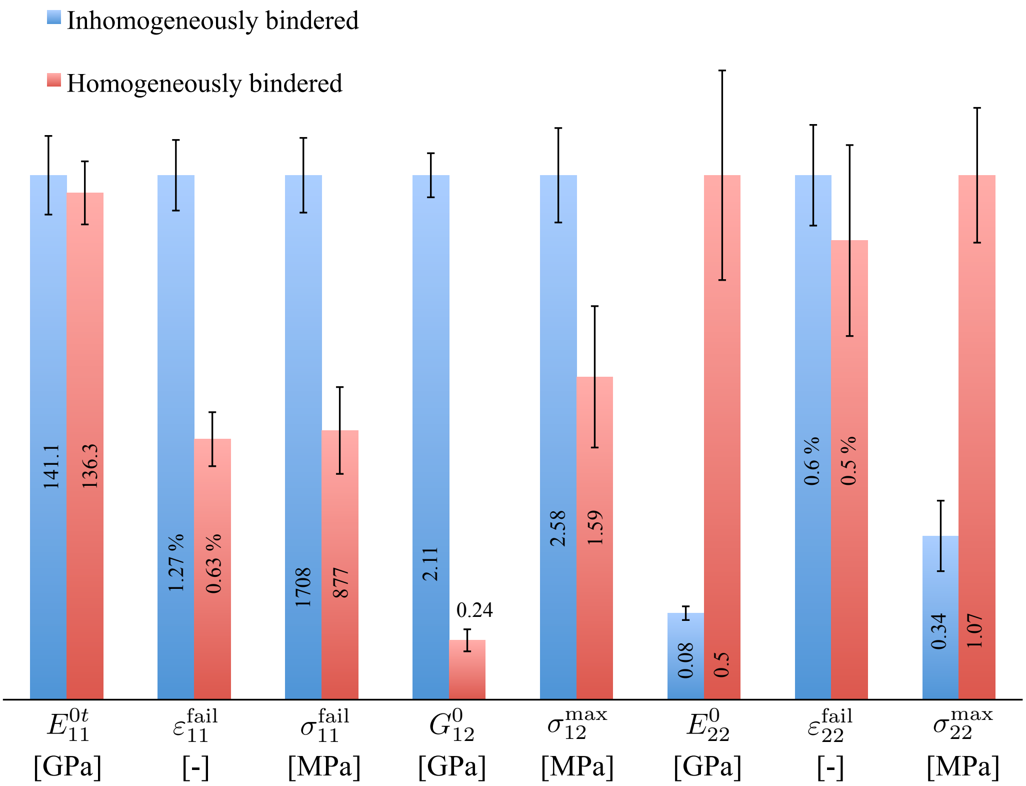

Figure 4.15: Comparison of normalised material properties obtained from preform materials.

In the transverse material direction the homogeneously bindered material shows a much more consistent material response, whereas the inhomogeneously bindered preform response differs within the test series due to the binder distribution. The differences are visible when comparing the initial modulus were values of 0.08 GPa and 0.5 GPa were observed for the inhomogeneously and homogeneously bindered material respectively. Similar values were obtained for the failure strains, whereas higher maximum stresses were observed in the homogeneously bindered material.

4.3 Laminate materials

This section reports the results from mechanical tests performed on the two types of laminates used in this work. Both materials use the mono-compound epoxy resin HexFlow RTM6 as matrix but differ in the choice of tow. The reference laminate is based on the commercially available standard fibre HTS40 distributed by Toho Tenax. The other type of laminate is based on the homogeneously bindered prototype yarn using the same fibre.

4.3.1 In-plane properties

4.3.1.1 Reference laminate

Figure 4.16 shows the stress-strain curves for longitudinal tension extracted from the recorded displacement field. Similarly to the set of experiments performed on the homogeneously bindered preform material, the experimental series for fibre tension was extended with three cyclic tests (see figure 4.17). These experiments are not required from the standard test protocol, however, the data might be used in future work. During the progression of the experiment single fibre rapture occurs and little modulus reduction is observed for the later cycles. The first cycle of these experiments was also used to determine the elastic modulus. All experiments were stopped after a sudden failure. Overall the curves show high reproducibility. Single fibre breaking was observed at strains higher than 1.05%. The fibre splinters were interfering with the painted specimen surface, which is used by the DIC system, which causes a notable amount of noise in the data. Nonetheless the deduced elastic moduli show little scatter resulting in an averages modulus of 157±2.6 GPa (see table 4.15).

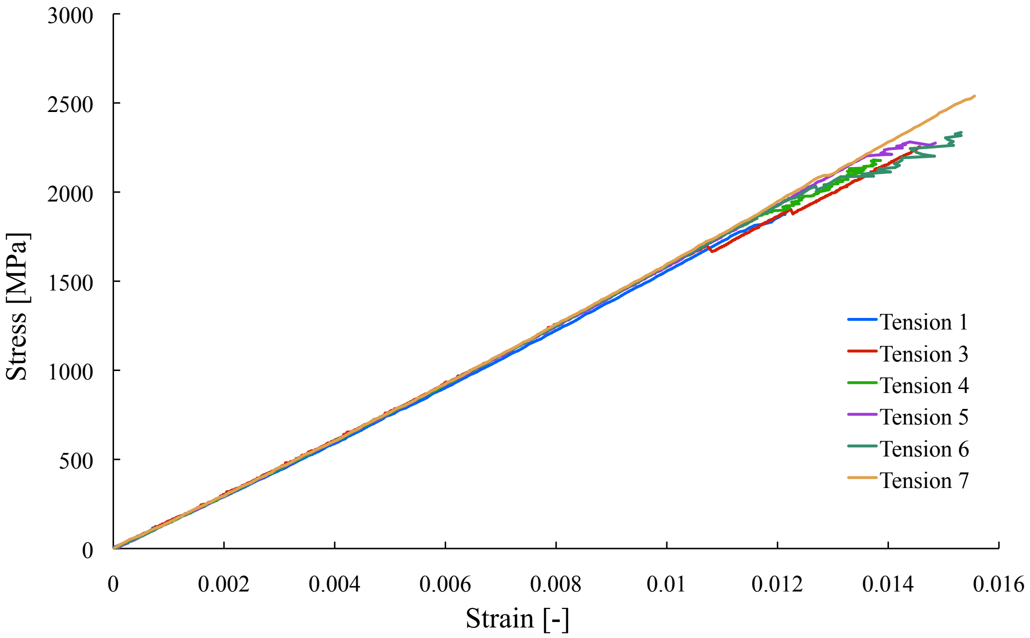

Figure 4.16: Comparison of tensile tests preformed on reference laminate coupons.

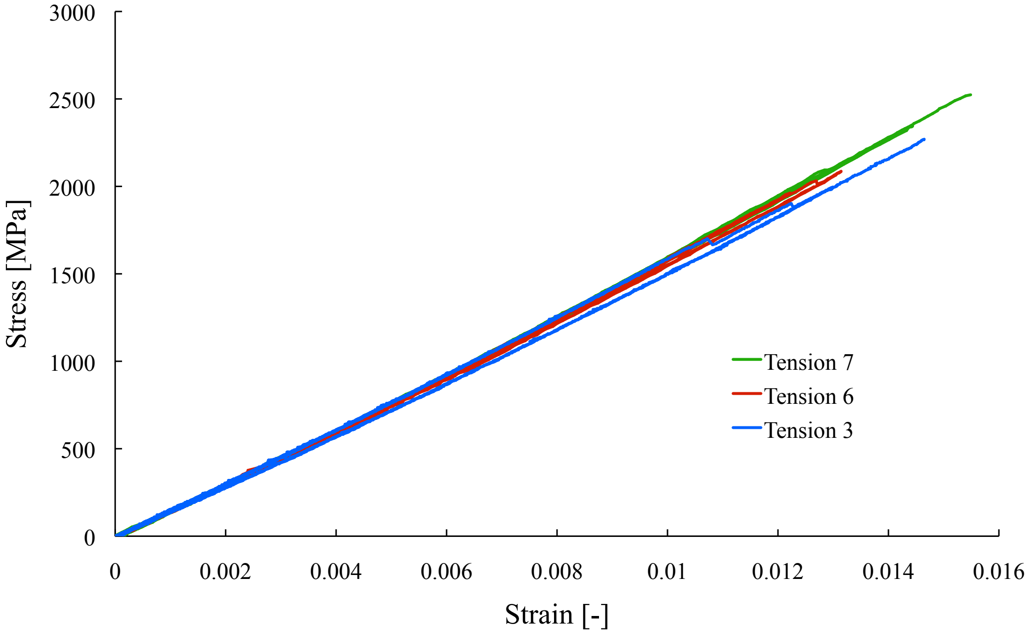

Figure 4.17: Cyclic tension experiments in fibre direction preformed on reference laminate material.

Specimen	Modulus [GPa]	Mean [GPa]	SD [GPa]
$[0°]_8^t$ - 1	152.0	157.0	2.6
$[0°]_8^t$ - 3	156.6		
$[0°]_8^t$ - 4	158.6		
$[0°]_8^t$ - 5	157.6		
$[0°]_8^t$ - 6	158.0		
$[0°]_8^t$ - 7	159.2		

Table 4.15: Initial tensile moduli from reference laminate specimens.

Figure 4.18 shows three fibre compression stress-strain curves. A single stress-strain curve for an experiment is deduced from the separate curves which were recorded via the attached strain gauges on each side of the specimen. The graphs obtained have the same characteristics. The initially linear slope turns into a non-linear section until sudden failure occurs. The compressive moduli are reported in table 4.16. Failure strain and stress vary between the three experiments. However, test 2 and 3 show similar magnitudes for the strains and stresses at failure, whereas test 5 exceeds the results in terms of final stress and strain levels.

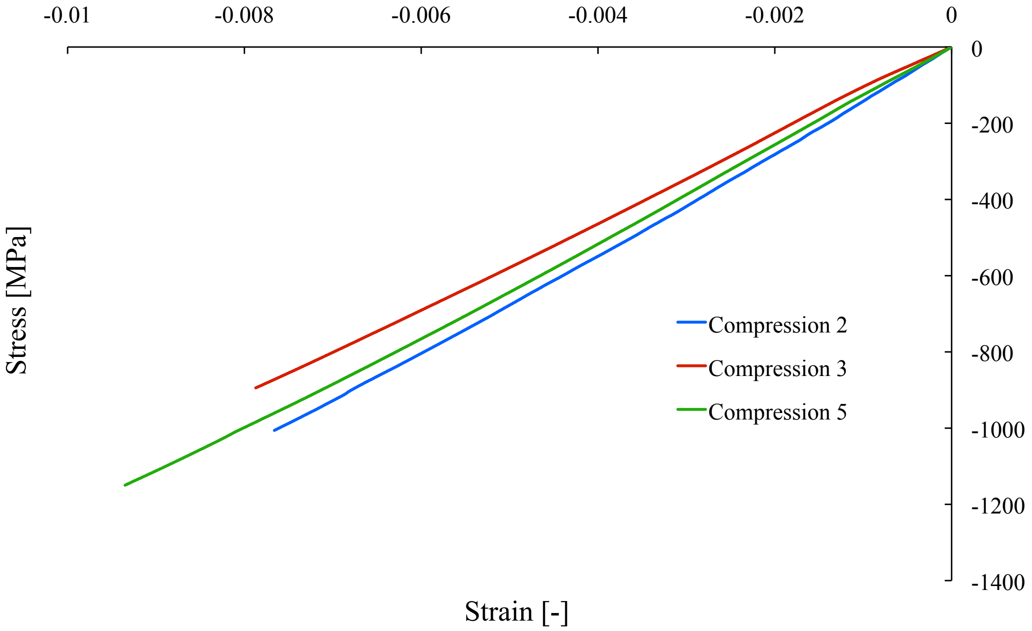

Figure 4.18: Compiled responses of compression experiments performed on reference laminate specimens.

Specimen	Modulus [GPa]	Mean [GPa]	SD [GPa]
$[0°]^c_{16}$ - 2	138.0	128.3	10.2
$[0°]^c_{16}$ - 3	117.7		
$[0°]^c_{16}$ - 5	129.3		

Table 4.16: Compressive moduli from reference laminate tests.

Figure 4.19 illustrates the results of the shear experiments on $[\pm 45°]_{2s}$ specimens. Throughout the test programme five loading/unloading cycles were completed. The curves show excellent reproducibility. In comparison to the preform material a lot less noise is present in the data set while stress and strain levels are much higher. The damage evolution and accumulation of inelastic deformation if clearly visible throughout the evolution of the stress-strain curves. The values for the undamaged shear modulus are listed in table 4.17. Here the values obtained are reproducible and result in a very small standard deviation of 0.16 GPa. The mean value was calculated as 4.77 GPa.

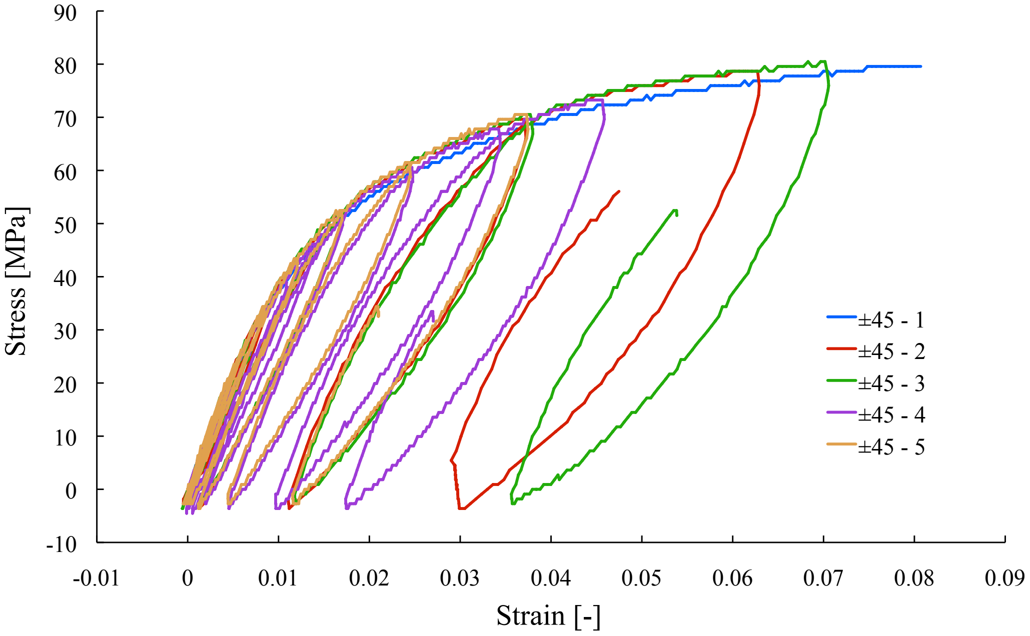

Figure 4.19: Results from shear tests on $[\pm45]_{2s}$ reference laminate specimens.

Specimen	Modulus [GPa]	Mean [GPa]	SD [GPa]
$[\pm45°]_{2s}$ - 1	4.81	4.77	0.16
$[\pm45°]_{2s}$ - 2	4.95		
$[\pm45°]_{2s}$ - 3	4.87		
$[\pm45°]_{2s}$ - 4	4.56		
$[\pm45°]_{2s}$ - 5	4.64		

Table 4.17: Shear moduli deduced from $[\pm45°]_{2s}$ reference laminate coupons.

As shown in figure 4.20 the shear response deduced from the $[\pm67.5°]_{2s}$ laminate exhibits very little inelastic deformation. Furthermore, the data obtained from different experiments match very closely and show very good reproducibility of the results. Overall the stress and strain levels reached in this experiments are very small in comparison to the shear experiments performed with the $[\pm45°]_{2s}$ layup. Again five cycles were completed until failure occurred. When comparing the orders of magnitude with the shear results of $[\pm45°]_{2s}$ laminates it can be observed that these curves only reach maximum failure strengths and strains between 25-28 MPa and 0.52 - 0.56% respectively. The results are not only used to deduce the coupling parameters for the material model but can also be used to contribute to the determination of the shear modulus. However, the moduli obtained from these experiments are slightly higher than those obtained from $[\pm45°]_{2s}$ experiments. Here values in the range of 4.4 - 5.4 GPa were identified with a mean value of 5.02±0.57 (see table 4.18).

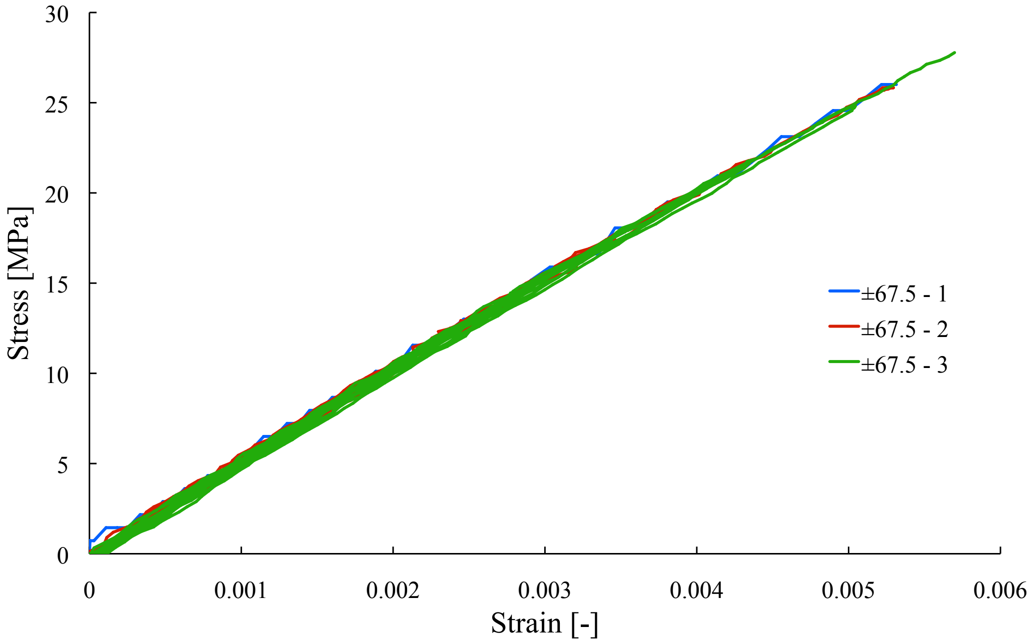

Figure 4.20: Shear responses of $[\pm 67.5°]_{2s}$ reference laminate coupons.

Specimen	Modulus [GPa]	Mean [GPa]	SD [GPa]
$[\pm 67.5°]_{2s}$ - 1	4.36	5.02	0.57
$[\pm 67.5°]_{2s}$ - 2	5.4		
$[\pm 67.5°]_{2s}$ - 3	5.3		

Table 4.18: Initial moduli deduced from the shear response of $[\pm 67.5°]_{2s}$ specimens cut from reference laminate panels.

It is also possible to obtain the transverse response from the $[\pm 67.5°]_{2s}$ laminate using the transformation rules of classical laminate theory (see section 5.2.1) as illustrated in figure 4.21. The resulting graphs provide the necessary results for the transverse behaviour of the laminate as suggested by the standard procedure. The material tests show good agreement for the data curves, hence the transverse moduli vary in the range of 7.3 - 8.9 GPa (see table 4.19). The five cycles completed during the tests also provide the necessary information for the damage evolution in the transverse direction.

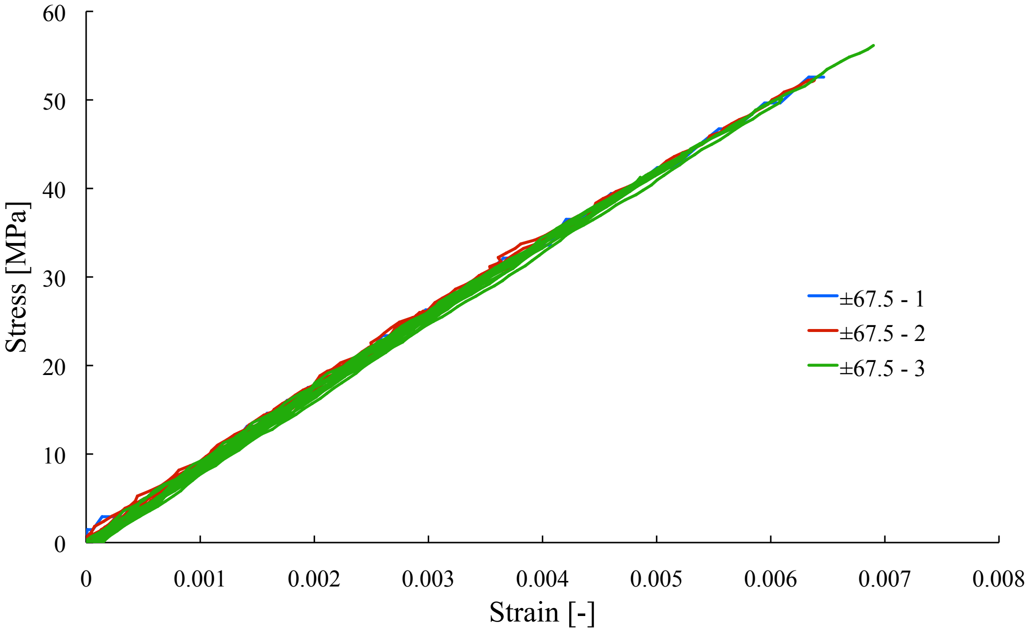

Figure 4.21: Transverse responses from $[\pm 67.5°]_{2s}$ reference laminate specimens.

Specimen	Modulus [GPa]	Mean [GPa]	SD [GPa]
$[\pm 67.5°]_{2s}$ - 1	7.3	8.3	0.9
$[\pm 67.5°]_{2s}$ - 2	8.9		
$[\pm 67.5°]_{2s}$ - 3	8.8		

Table 4.19: Initial moduli deduced from the transverse response of $[\pm 67.5°]_{2s}$ reference laminate coupons.

In addition to the standardised test methods required for the material characterisation for the constitutive damage model an additional set of experiments on transverse specimens with a $[90°]_8$ laminate layup was performed. The results obtained from pure transverse specimens (see figure 4.22) are comparable to the transverse response deduced from $[\pm 67.5°]_{2s}$ coupons. Nonetheless, stress and strain are slightly higher. Furthermore, the transverse moduli obtained with the $[90°]_8$ are higher with a smaller standard deviation compared to the results shown in table 4.19.

Specimen	Modulus [GPa]	Mean [GPa]	SD [GPa]
$[90°]_8$ - 1	9.3	9.6	0.2
$[90°]_8$ - 3	9.8		
$[90°]_8$ - 4	9.4		
$[90°]_8$ - 5	9.7		
$[90°]_8$ - 6	9.8		
$[90°]_8$ - 7	9.8		

Table 4.20: Transverse moduli for reference laminate material obtained from $[90°]_8$ specimens.

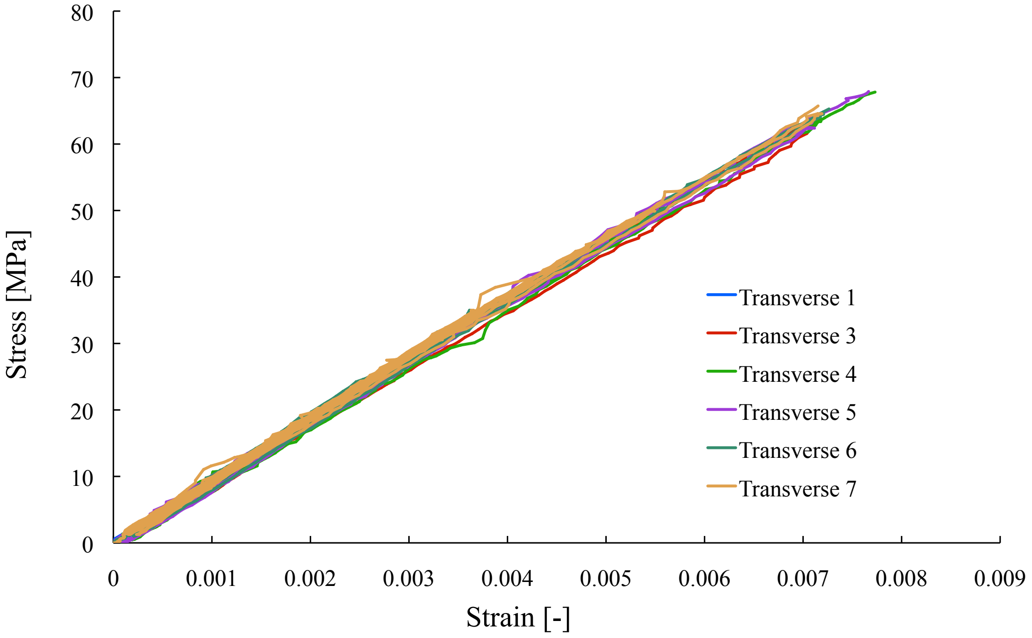

Figure 4.22: Stress-strain curves obtained from transverse experiments on reference laminate specimens.

4.3.1.2 Bindered composite

Three experiments were carried out in the fibre direction on the bindered composite. Figure 4.23 illustrates the resulting stress-strain curves. For all three experiments failure strains close to 1.6% and stresses between 2100 and 2200 MPa were consistently measured. The curves show very good agreement, hence the undamaged elastic modulus is determined with little deviation as listed in table 4.5. Here a value of 125.6±0.8 GPa is obtained.

Specimen	Modulus [GPa]	Mean [GPa]	SD [GPa]
$[0°]_8^t$ - 1	124.7	125.6	0.8
$[0°]_8^t$ - 2	126.0		
$[0°]_8^t$ - 3	126.0		

Table 4.21: Tensile elastic moduli in fibre direction for bindered composite.

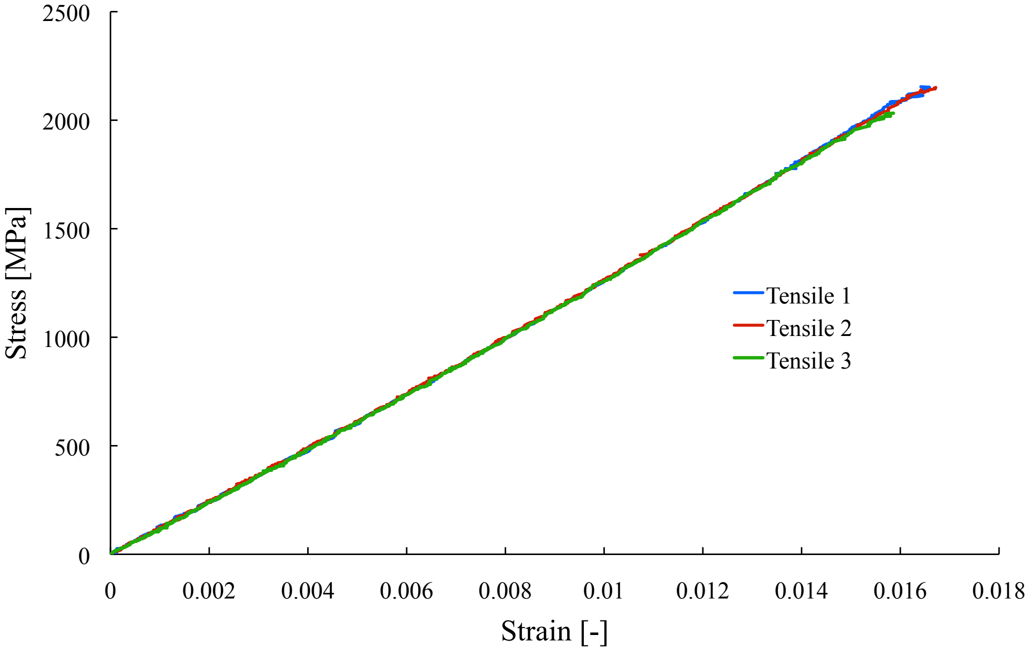

Figure 4.23: Stress-strain responses of tensile tests carried out on specimens of bindered composite.

Four compression tests were also performed in the fibre direction. In these experiments strain gauges are attached on the front and rear side of the specimen. Recorded data from both sides are averaged and stress-strain curves are generated (see also figure 3.27). The averaged curves for each experiment are shown in figure 4.24. These curves differ in their failure strengths while strains of approximately 0.48% were consistently reached for three out of the four experiments. The moduli originating from the initial slopes of the experiments are listed in table 4.22. It is notable that the average elastic modulus is similar to the value obtained in tension. With regard to the reference laminate the compressive modulus is approximately 80% of the tensile modulus while the bindered composite reaches a similar value in both loading directions. However, the bindered composite material also has a lower V_f[1] in comparison to the reference material (51% versus 64%).

Specimen	Modulus [GPa]	Mean [GPa]	SD [GPa]
$[0°]_{16}^{c}$ - 1	144.9	126.5	16.2
$[0°]_{16}^{c}$ - 2	114.3		
$[0°]_{16}^{c}$ - 3	135.1		
$[0°]_{16}^{c}$ - 4	111.5		

Table 4.22: Compressive elastic moduli deduced for bindered composite.

---

[1] Fibre volume fraction

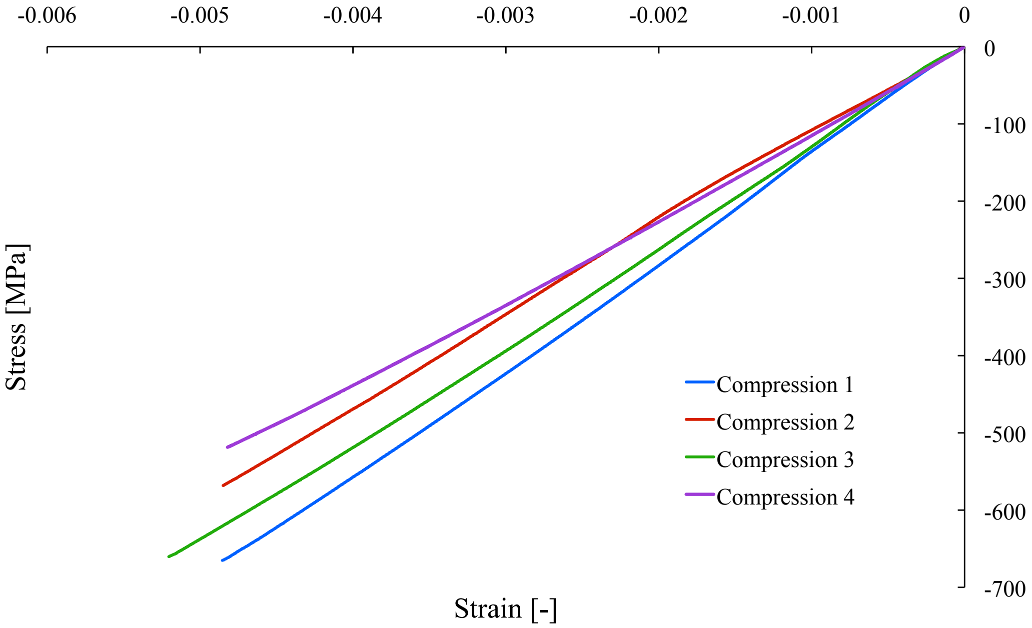

Figure 4.24: Test curve results for compressive experiments obtained from bindered composite material.

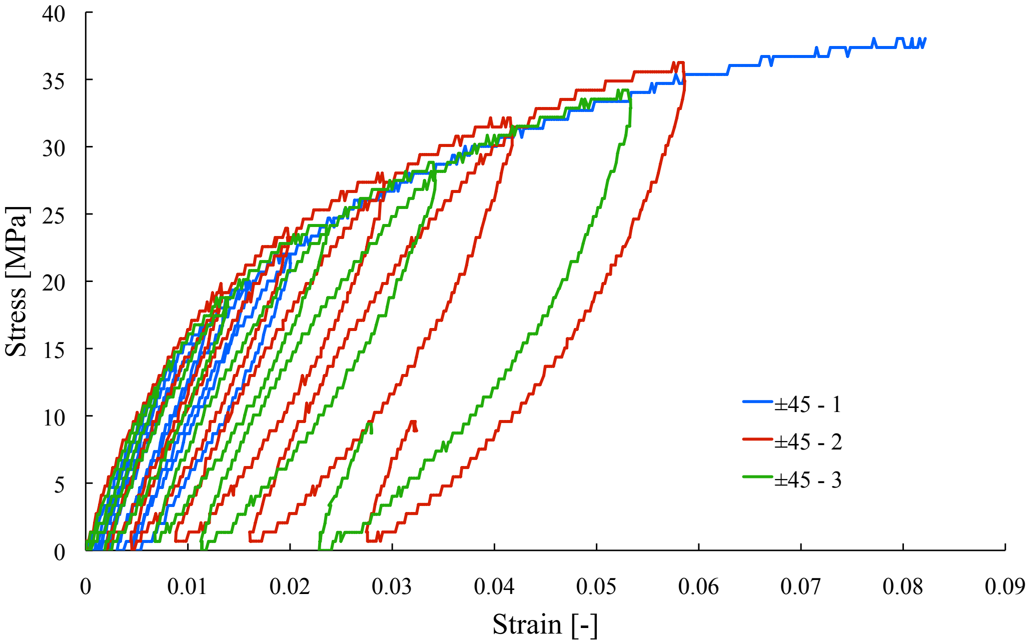

Figure 4.25: Stress-strain curves of shear experiments on $[\pm 45°]_{2s}$ bindered composite specimens.

Figure 4.25 illustrates the stress-strain curves obtained in shear experiments on $[\pm 45°]_{2s}$ coupons. Here, five cycles were completed to produce the necessary information for material properties. The stress-strain curves are reproduced with good agreement between the experiments. Results from the experiments are listed in table 4.24 leading to a value of 2.5±0.5 GPa for the shear modulus.

Specimen	Modulus [GPa]	Mean [GPa]	SD [GPa]
$[\pm 45°]_{2s}$ - 1	1.9	2.5	0.5
$[\pm 45°]_{2s}$ - 2	2.6		
$[\pm 45°]_{2s}$ - 3	2.8		

Table 4.23: Undamaged shear moduli from bindered composite coupons with $[\pm 45°]_{2s}$ layup.

The shear and transverse response were obtained from specimens with a $[+45°]_8$ layup. Figure 4.26 illustrates the shear response of the material. Similarly to shear tests five loading cycles were completed before the coupons were loaded up to failure. The values of the shear modulus are listed in table 4.24 and match the results from pure shear tests on $[\pm 45°]_{2s}$ coupons closely. Both experimental sets yield a mean value of 2.5 GPa. However, the strain and stress levels achieved with the $[+45°]_8$ coupons are significantly smaller. Inelastic deformations are also achieved and allow deduction of coupling and damage parameters.

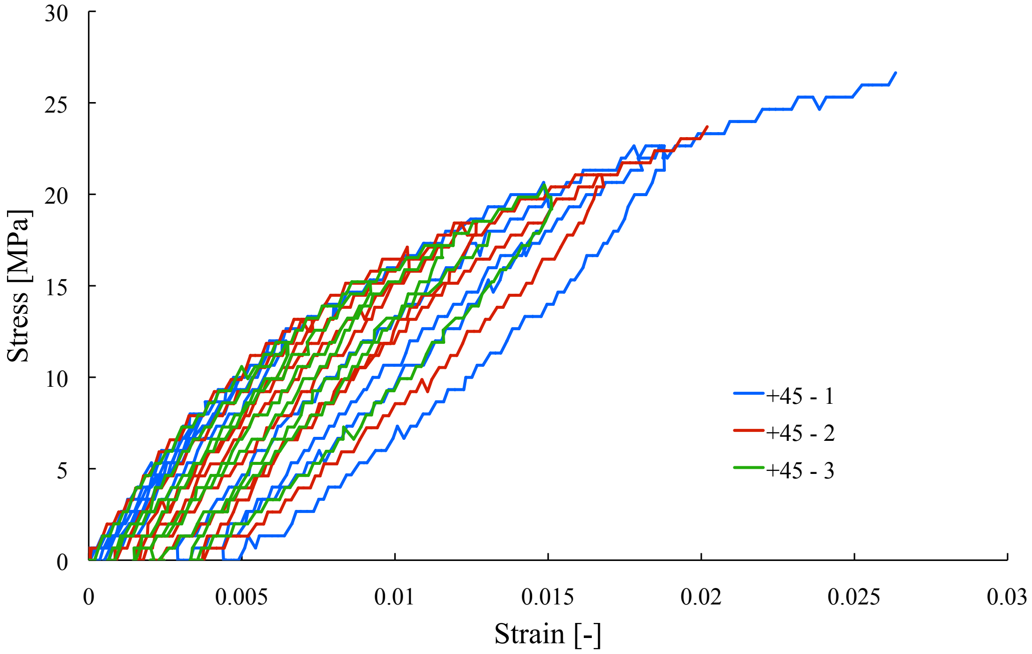

Figure 4.26: Shear response of $[+45°]_8$ bindered composite specimens.

Specimen	Modulus [GPa]	Mean [GPa]	SD [GPa]
$[+45°]_8$ - 1	2.6	2.5	0.1
$[+45°]_8$ - 2	2.5		
$[+45°]_8$ - 3	2.4		

Table 4.24: Shear modulus for bindered composite material deduced from the shear response of $[+45°]_8$ specimens.

The transverse curves obtained from $[+45°]_8$ are shown in figure 4.27. The results are slightly noisier compared to the shear response, however, the plots show matching evolutions and are adequate to obtain representative properties. Table 4.25 summarises the elastic modulus values in the transverse direction. All three experiments lead to similar modulus values of with 5.8, 6.1 and 6.3 GPa. Ultimate strains of 0.38%, 0.47% and 0.55% are reached while the failure strengths vary from 22 - 27 MPa.

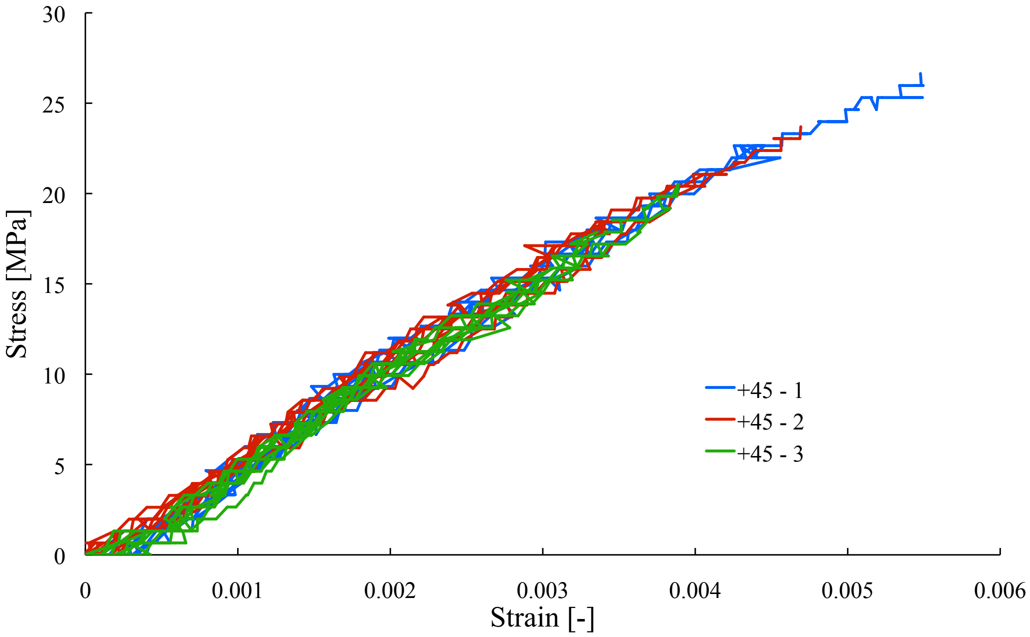

Figure 4.27: Transverse stress-strain response from bindered laminate coupons with $[+45°]_8$ layup.

Specimen	Modulus [GPa]	Mean [GPa]	SD [GPa]
$[+45°]_8$ - 1	6.3	6.1	0.3
$[+45°]_8$ - 2	5.8		
$[+45°]_8$ - 3	6.1		

Table 4.25: Moduli for bindered laminate deduced from the transverse responses of $[+45°]_8$ coupons.

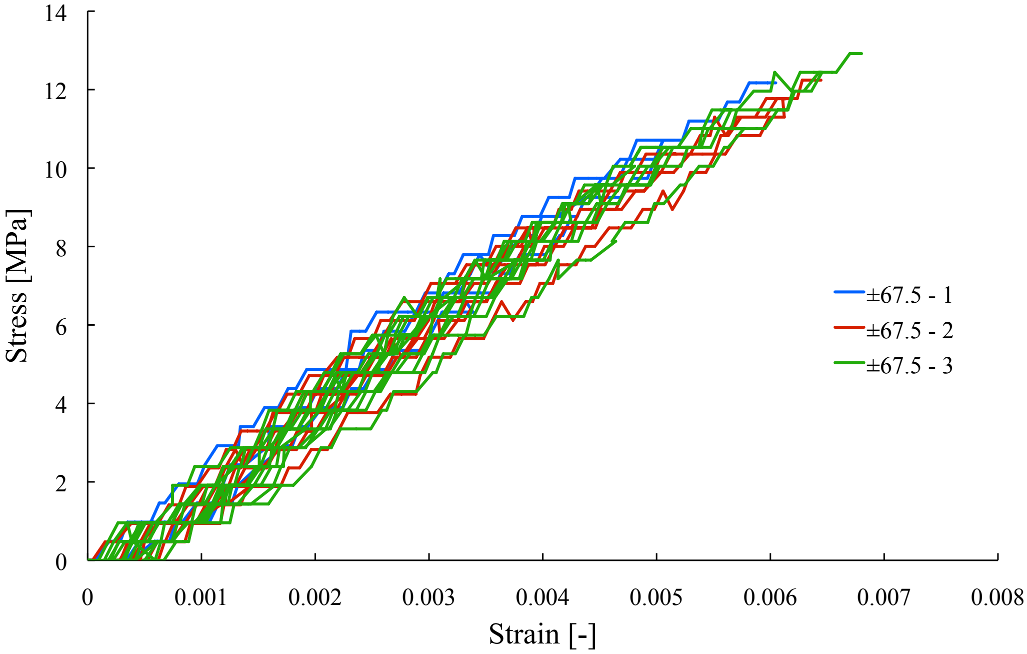

Figure 4.28: Collated shear responses for bindered laminate material obtained from $[\pm 67.5°]_{2s}$ specimens.

Figure 4.28 shows the shear stress-strain curves obtained from three $[\pm 67.5°]_{2s}$ experiments. Here stress levels reached (13 MPa) just exceed the elastic region before specimen failure occurs. Hence the accumulation of the inelastic deformation is not as pronounced as in the pure shear experiments $[\pm 45°]_{2s}$ or even the shear responses from $[+45°]_8$ laminates. In comparison to the average shear modulus from the previous tests the values obtained from this experiment are slightly lower (see table 4.26). Here the shear moduli were 2.3, 2.4 and 2.4 GPa respectively. This results to an average value of 2.33±0.03 GPa.

Specimen	Modulus [GPa]	Mean [GPa]	SD [GPa]
$[\pm 67.5°]_{2s}$ - 1	2.4	2.3	0.03
$[\pm 67.5°]_{2s}$ - 2	2.4		
$[\pm 67.5°]_{2s}$ - 3	2.3		

Table 4.26: Shear moduli of bindered laminate deduced from $[\pm 67.5°]_{2s}$ test.

Figure 4.29 displays the transverse responses of the tested bindered composite material with the $[\pm 67.5°]_{2s}$ layup. The curves coincide and show very good agreement between the experiments hence the values for the transverse modulus yield satisfactory results for the transverse modulus as shown in table 4.27. An average value of 5.5±0.1 GPa is calculated which is lower than the results from the $[+45°]_8$ specimens (6.1±0.3 GPa). Similarly to the shear responses the transverse data for this material reaches strains between 0.6 - 0.7%. Furthermore it is noteworthy that the cyclic loading/unloading curves for both responses are more pronounced compared to the same tests preformed on the reference laminate. The lower fibre content results in a more compliant material response which highlights the influence of the elastic-plastic resin.

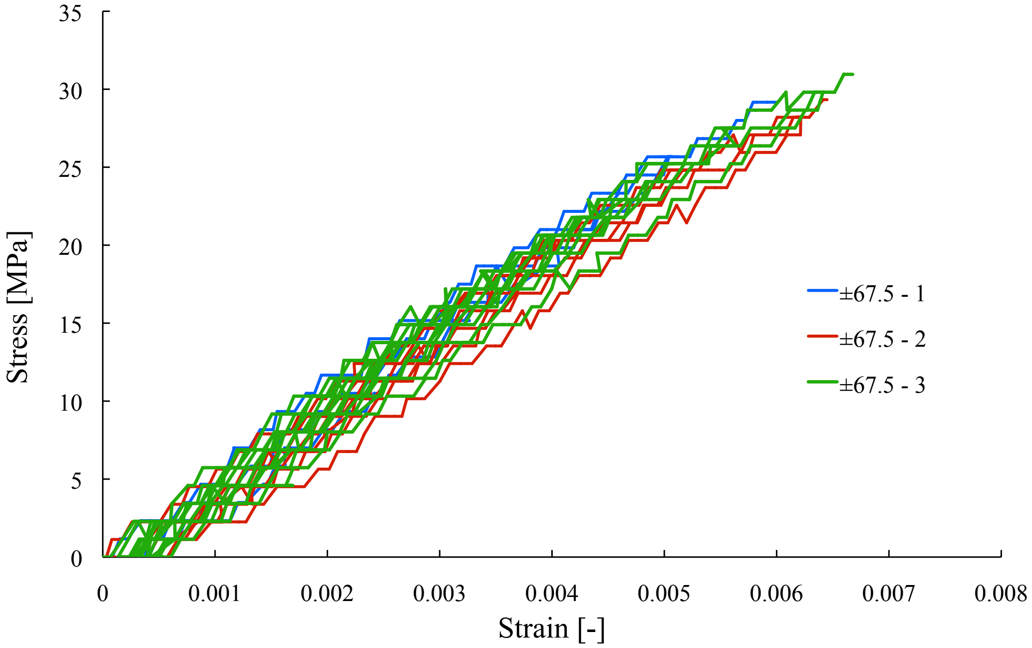

Figure 4.29: Transverse stress-strain responses of bindered laminate deduced from $[\pm 67.5°]_{2s}$ coupons.

Specimen	Modulus [GPa]	Mean [GPa]	SD [GPa]
$[\pm 67.5°]_{2s}$ - 1	5.5	5.5	0.1
$[\pm 67.5°]_{2s}$ - 2	5.4		
$[\pm 67.5°]_{2s}$ - 3	5.6		

Table 4.27: Transverse moduli deduced from $[\pm 67.5°]_{2s}$ experiments on bindered laminate material.

The experiments in the transverse direction can be used to examine the quality of the deduced moduli obtained from the transverse material response of $[+45°]_8$ and $[\pm 67.5°]_{2s}$ coupons respectively. The stress-strain curves of the transverse coupons are illustrated in figure 4.30 while the moduli derived are listed in table 4.28. The elastic modulus is 6±0.2 GPa. This value is higher than the result of the $[\pm 67.5°]_2$ test (5.5 GPa) and just slightly lower than the corresponding $[+45°]_8$ result (6.1 GPa).

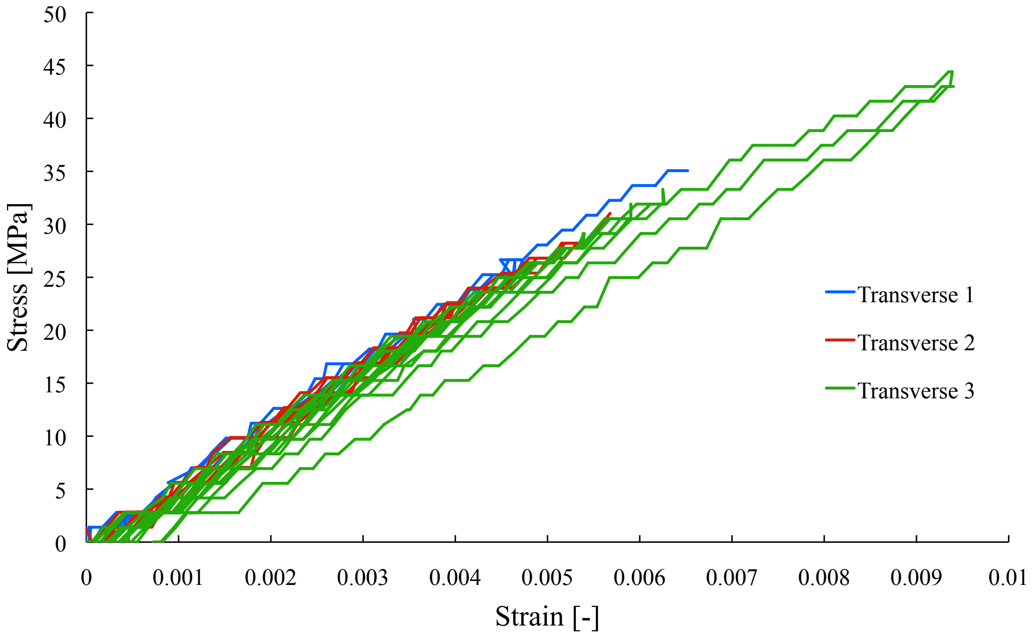

Figure 4.30: Stress-strain curve results from transverse tests on bindered composite coupons.

Specimen	Modulus [GPa]	Mean [GPa]	SD [GPa]
$[90°]_8$ - 1	6.1	6.0	0.2
$[90°]_8$ - 2	6.0		
$[90°]_8$ - 3	5.8		

Table 4.28: Overview of transverse moduli for bindered laminate material determined from $[90°]_8$ specimens.

4.3.2 Out-of-plane properties

Information obtained using the procedure described in section 3.3.2 is employed for the generation of resistance curves for mode I and II respectively. The resulting curves for the reference and the bindered laminate are presented in the following sections.

4.3.2.1 Reference laminate

A compilation of the resistance curves for the mode I delamination is shown in figure 4.31. Here test 1 and 2 show very good agreement and reach a plateau at around 420 $^{J}/_{m^2}$, whereas the curve obtained from experiment 3 shows consistently lower propagation fracture toughness values of around 200 $^{J}/_{m^2}$. The results are listed in table 4.29. Test 3 could be regarded as an outlier. When it is included in the calculation for the fracture toughness a value of 351.5±128.9 $^{J}/_{m^2}$ is obtained, whereas the exclusion of test 3 results in 425.8±9.47 J/m². The three tests provide a result of 210±52 J/m² for the crack initiation fracture toughness (see table 4.30).

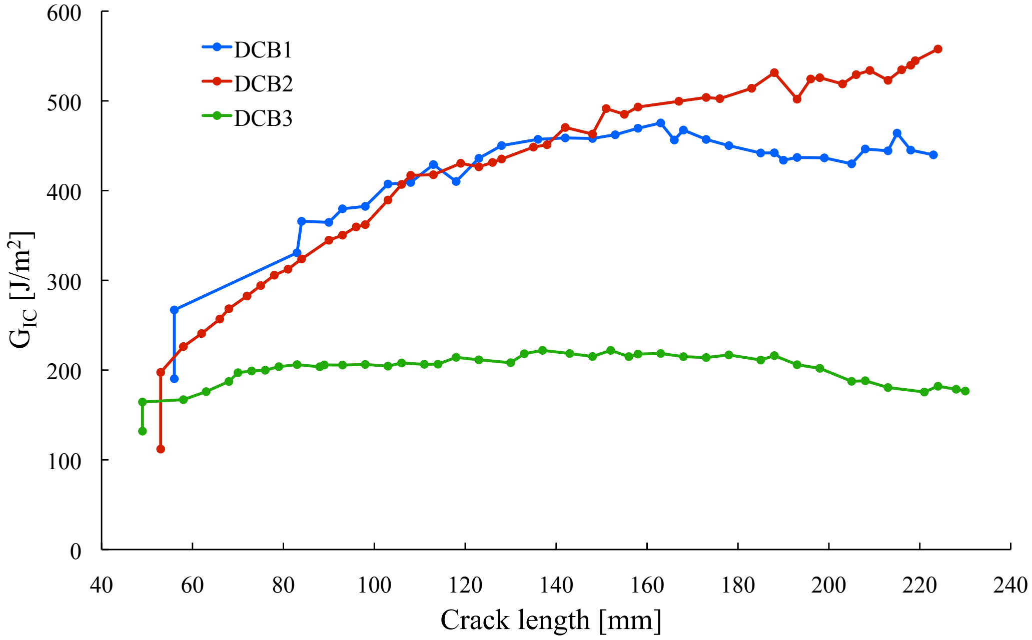

Figure 4.31: DCB results obtained from reference laminate.

Specimen	DCB 1	DCB 2	DCB 3
G_{IC} [J/m^2] SD [J/m^2]	432.5 34.1	419.1 109.3	202.8 14.6
Mean [J/m^2] SD [J/m^2]	351.5 (425.8) 128.9 (9.47)		

Table 4.29: Overview of propagation fracture toughness values for reference laminate material.

Specimen	DCB 1	DCB 2	DCB 3
G_{IC}^{ini} [J/m^2]	164.4	197.5	267.0
Mean [J/m^2] SD [J/m^2]	209.6 52.4		

Table 4.30: Overview of initiation fracture toughness values for reference laminate material.

The mode II results are shown in figure 4.32 and the calculated values for G_{IIC} are listed in table 4.31. The graphs show adequate reproducibility with fracture toughness values between 300 and 500 J/m² which is reflected in the standard deviation of the experiments. Here a critical energy release rate of 431±60 J/m² is calculated from the individual results, where the initiation values for G_{IIC}^{ini} is 382±89 J/m² (see table 4.32).

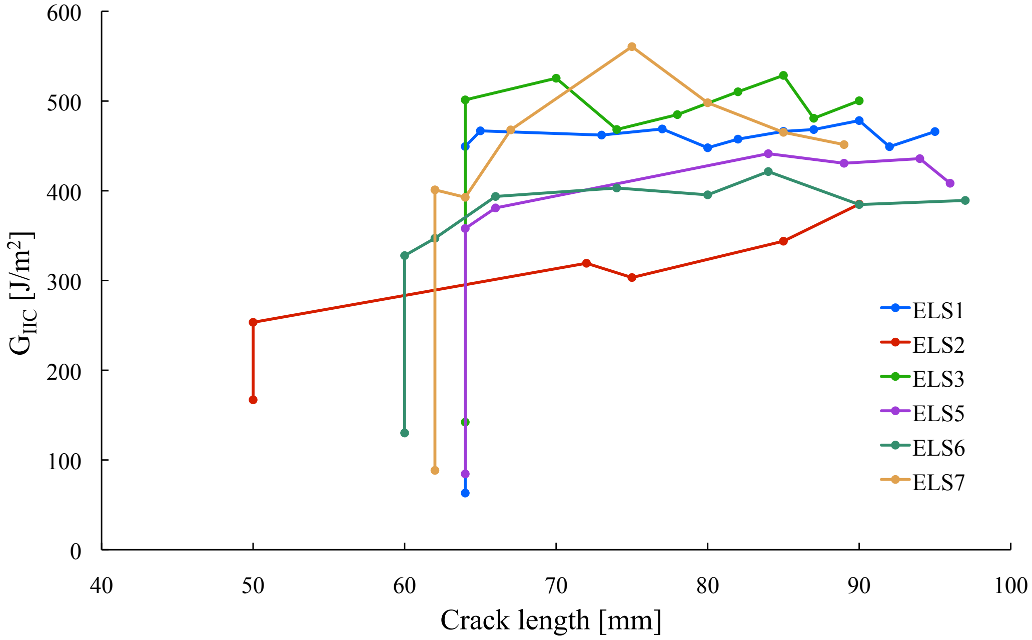

Figure 4.32: Comparison of ELS curves determined from reference laminate specimens.

Specimen	ELS 1	ELS 2	ELS 3	ELS 5	ELS 6	ELS 7
G_{IIC} [J/m^2] SD [J/m^2]	463.1 8.8	337.9 30.9	499.8 21.3	419.4 22.3	390.7 21.0	472.7 50.5
Mean [J/m^2] SD [J/m^2]	430.6 59.9					

Table 4.31: Values for mode II propagation fracture toughness values as tested on reference laminate material.

Specimen	ELS 1	ELS 2	ELS 3	ELS 5	ELS 6	ELS 7
G_{IIC}^{ini} [J/m^2]	449.3	253.4	501.3	357.9	327.8	401.0
Mean [J/m^2] SD [J/m^2]	381.8 88.5					

Table 4.32: Values for mode II initiation fracture toughness values as tested on reference laminate material.

4.3.2.2 Bindered composite

The mode I experiments performed on the bindered composite show high reproducibility (see figure 4.33). The curves evolve identical manner and reach a plateau level of around 650 J/m². Consequently, the determined values for the individual fracture toughness show very little deviation (see table 4.33) with an overall mean value of 636 J/m² and a corresponding standard deviation of 23 J/m². For the initiation fracture toughness in mode I an average value of 514±60 J/m² was obtained (see table 4.34).

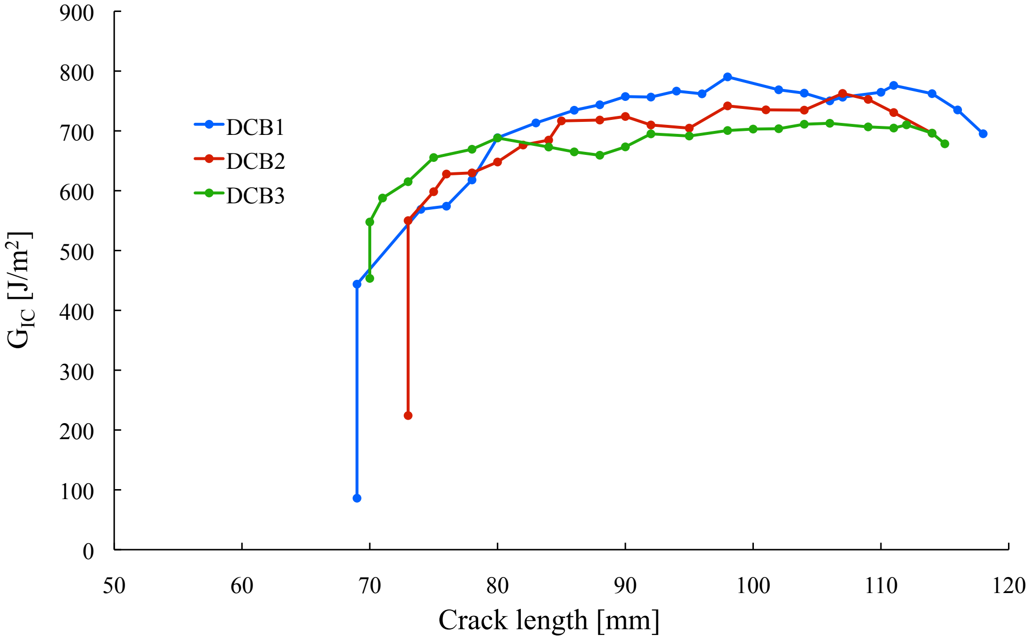

Figure 4.33: Evolution plot critical energy release rate in mode I versus crack length for bindered composite material.

Specimen	DCB 1	DCB 2	DCB 3
G_{IC} [J/m^2]	658.6	611.9	637.9
SD [J/m^2]	198.2	209.7	144.1
Mean [J/m^2]	636.1		
SD [J/m^2]	23.4		

Table 4.33: Propagation fracture toughness values for mode I as obtained from bindered composite specimens.

Specimen	DCB 1	DCB 2	DCB 3
G_{IC}^{ini} [J/m^2]	443.8	550.0	547.7
Mean [J/m^2]	513.8		
SD [J/m^2]	60.7		

Table 4.34: Initiation fracture toughness values for mode I as obtained from bindered composite specimens.

Figure 4.34 illustrates the evolution of the mode II fracture toughness with increasing crack length. The resistance curves show very high reproducibility as listed in table

4.35 leading to a fracture toughness of 820±28 J/m². An initiation fracture toughness of 509±46 J/m² is obtained. The initiation values of the individual tests are listed in table 4.36.

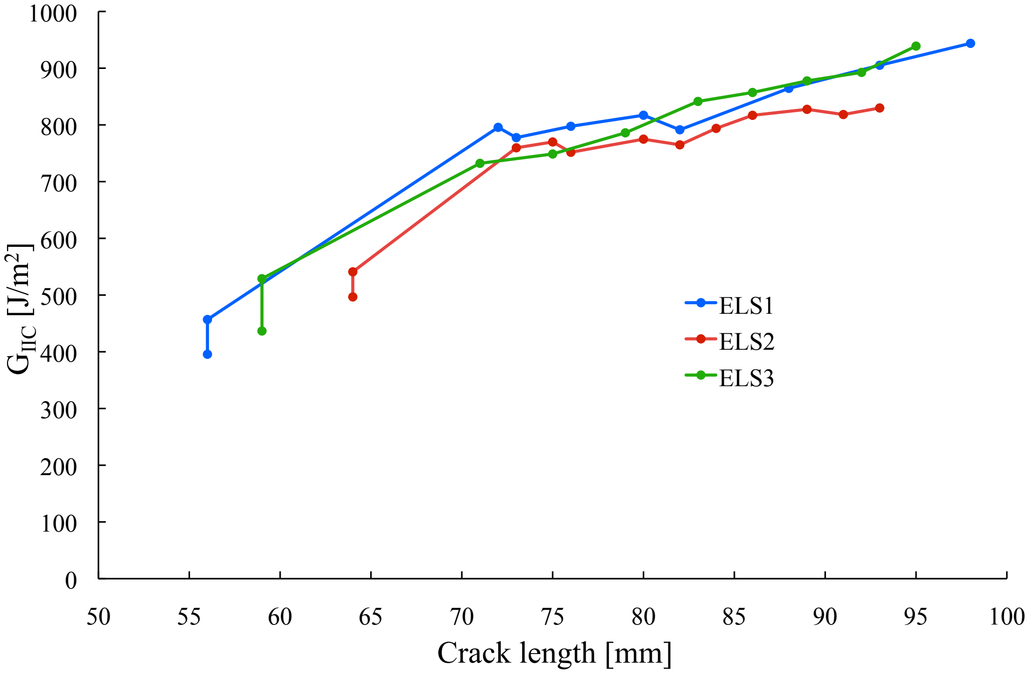

Figure 4.34: Plot of mode II critical energy release rate versus crack length on bindered laminate material.

Specimen	ELS 1	ELS 2	ELS 3
G_{IIC} [J/m^2] SD [J/m^2]	836.6 57.1	790.7 28.6	834.3 67.9
Mean [J/m^2] SD [J/m^2]	820.5 25.9		

Table 4.35: Propagation fracture toughness values for mode II as determined from bindered composite specimens.

Specimen	ELS 1	ELS 2	ELS 3
G_{IIC}^{ini} [J/m^2]	465.8	540.9	528.9
Mean [J/m^2] SD [J/m^2]	508.9 45.5		

Table 4.36: Initiation fracture toughness values for mode II as determined from bindered composite specimens.

4.3.3 Material comparison

Figure 4.35 illustrates an overview of the material data obtained for the laminate materials. It should be noted that due to the manufacturing process the fibre volume fraction for the bindered laminate is lower than that of the reference material. A fibre volume fraction of 64% and 51% was reached for the reference and bindered laminate respectively. The fibre volume fractions for the two laminates were calculated using the densities of fibres and resin provided by the material data sheets in combination with the weight and volume of the panel after infusion.

In the case of the compressive elastic modulus in fibre direction the two materials perform equally with an average value of 128 versus 126 GPa. However, the corresponding compressive failure strengths and strains are 40% higher for the reference material.

In fibre tension an elastic modulus higher by about 20% was obtained in the reference laminate. The tensile failure strain for the bindered composite is higher with a value of 1.75% compared to 1.44% for the reference laminate. Similar failure strengths were obtained for the two materials with 2244 versus 2113 MPa for the reference laminate and bindered laminate respectively.

The shear modulus of the reference material is higher than that of the bindered composite. Similarly, the failure strengths are 50% higher for the reference laminate.

Transverse properties were obtained from pure transverse experiments and tests on $[\pm 67.5°]_{2s}$ specimens. Here the reference material has higher moduli than the bindered composite. The same observation can be made for the failure strength where approximately 41% higher stresses are observed on the reference material compared to the bindered laminate. Similar strain levels are observed for the two materials.

In terms of the out-of-plane properties the bindered composite has higher initiation and propagation values. The average values from the analysis are 352 $\mathrm{J/m^2}$ and 636 $\mathrm{J/m^2}$ for the reference and the bindered laminate material respectively under mode I loading. The reference laminate has an initiation toughness of 210 $\mathrm{J/m^2}$ whereas the bindered composite is capable of withstanding higher loads corresponding to an initiation toughness of 482 $\mathrm{J/m^2}$. Better performance for the bindered laminate is observed in mode II delamination. The value of propagation toughness are 821 $\mathrm{J/m^2}$ and 431 $\mathrm{J/m^2}$, for the bindered and reference material respectively. Similarly the mean initiation values for mode II toughness observed in the bindered composite material are approximately 100 $\mathrm{J/m^2}$ higher than those of the reference laminate.

The superior out-of-plane behaviour of the bindered material is related to the lower fibre volume fraction, which leads to wider resin zones between layers [201].

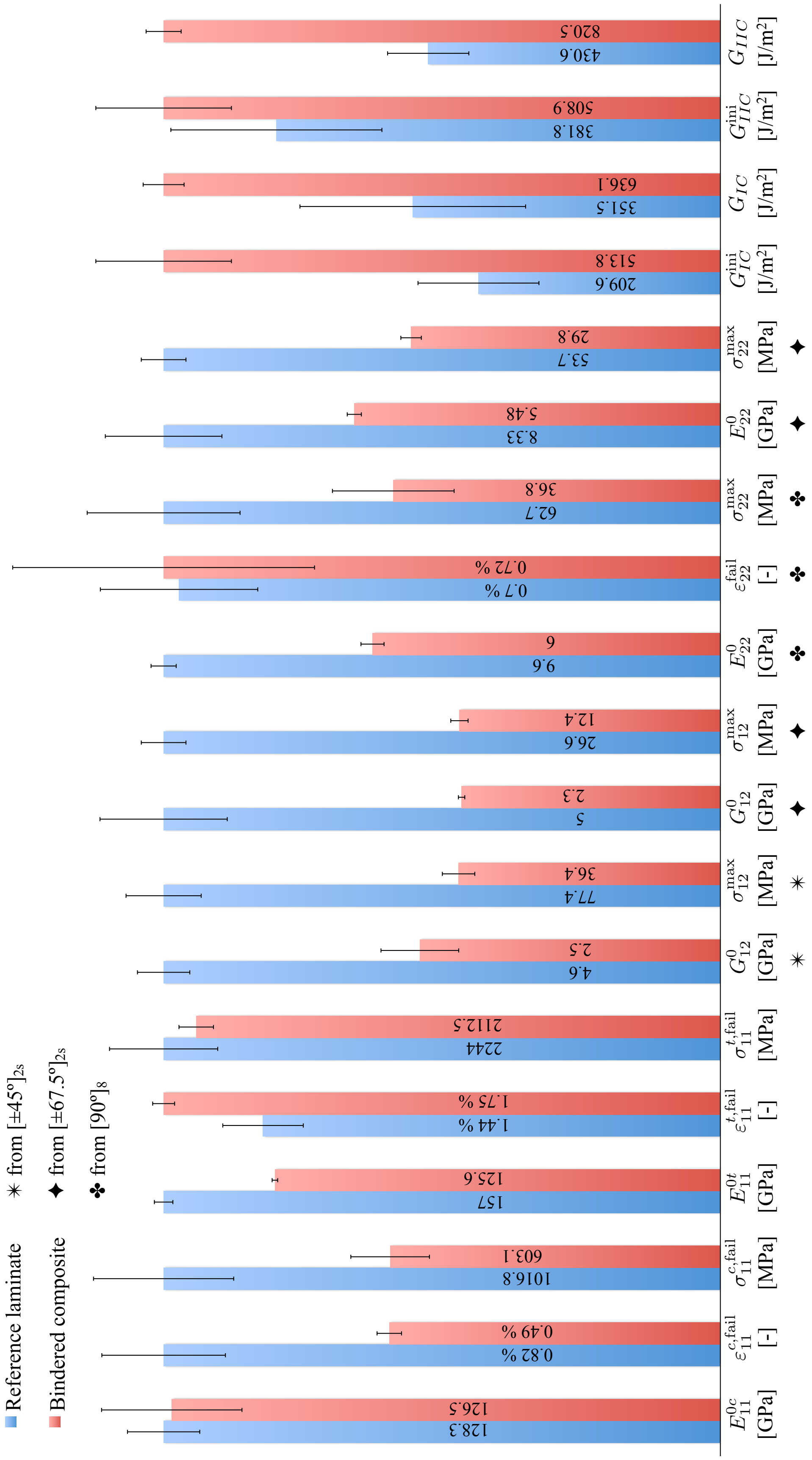

Figure 4.35: Comparison of material properties from reference and bindered laminates.

This effect is similar to observations concerning interleaving [202–204]. In interleaving fracture toughness values of up to ten times greater can be obtained for mode I and mode II [205]. However, these changes are at the expense of in-plane properties and the potential weight saving [206].

4.4 Components for finite element validation

4.4.1 Three point bending

Three point bending tests were undertaken for the purpose of validating the material models which are available through the finite element solver Pam-Crash™. The advantages of this tests are the simple setup, the reproducibility of the results and the straightforward analysis. Figure 4.36 illustrates the load-deflection curves obtained from seven experiments with test coupons manufactured from the reference material. Here test 1 and 4 show a moderately more compliant response than the remaining experiments. However, overall agreement between the experiments can be observed. The data shows the occurrence of failure in the range of 1.6 - 2.1 mm deflection, which corresponds to a load levels of 1000 - 1300 N.

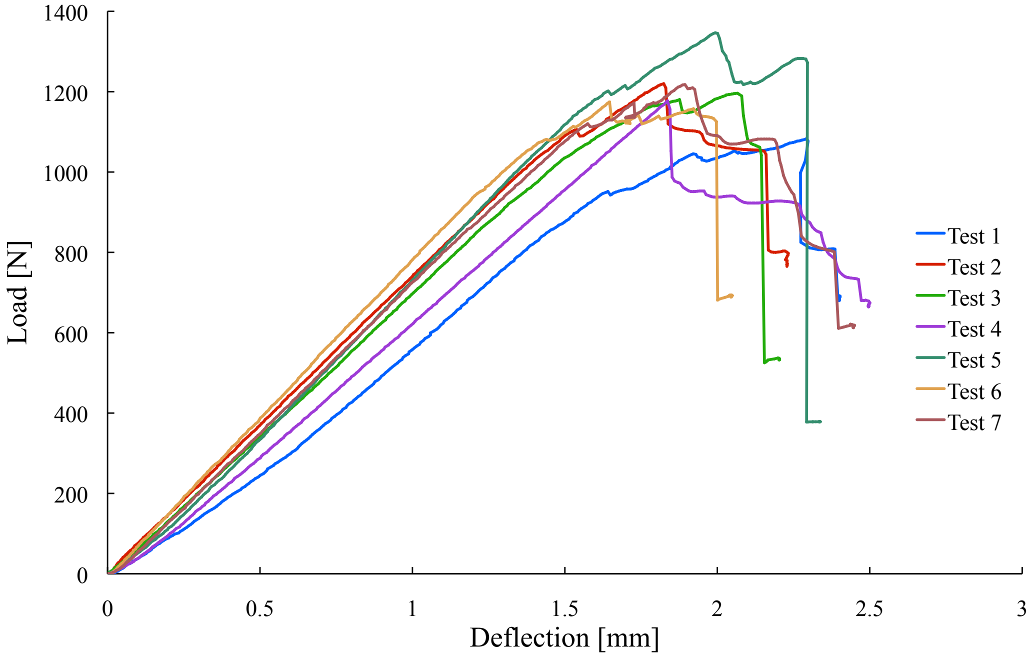

Figure 4.36: Load deflection curves for the three point bending tests.

The initial linear slope of the load-deflection was used for the calculation of the flexural modulus as described in section 3.3.3.1. This is followed by a non-linear section which contains a major peak succeeded by the ultimate failure of the specimen.

Moduli between 133 and 158 GPa (see figure 4.37) were obtained in the performed tests, which results into an average flexural modulus of 146.3±9.8 GPa.

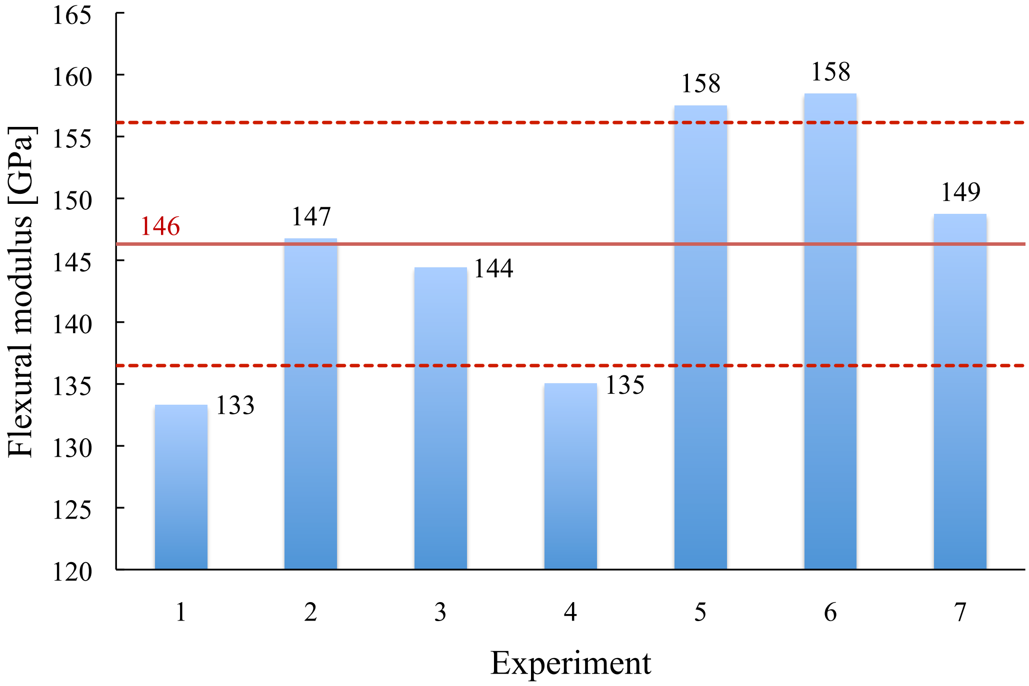

Figure 4.37: Overview of flexural moduli obtained from three point bending experiments.

4.4.2 Preform spar section impact scenario

Table 4.37 lists the predicted and achieved velocities and energies for the three spar section impact experiments.

Identifier	h [m]	v_P [$^{\mathrm{m}}/_{\mathrm{s}}$]	v_A [$^{\mathrm{m}}/_{\mathrm{s}}$]	E_P [J]	E_A [J]
Preform 1	1.006	4.44	4.15	29.88	26.05
Preform 3	1.006	4.44	4.1	29.88	25.42
Preform 4	1.009	4.45	4.15	29.98	26.55

Table 4.37: Predicted and achieved velocities and energies of the preform spar section impact tests.

Here h is the initial height of the impact carriage measured between the component and the impactor head.

With the striker mass of 3.03 kg an initial height of 1 m was calculated, which leads to a predicted impact velocity of 4.4 $^{\mathrm{m}}/_{\mathrm{s}}$. However, the velocities achieved (4.1 $^{\mathrm{m}}/_{\mathrm{s}}$) were lower and resulted into effective energies between 25 and 26 J.

For the two first experiments the velocity profiles, shown in figure 4.38, have similar shapes. The contact between impactor head and specimen is established in the initial part of the curve. In the range of 2 - 35 ms the striker is slowed down further due to the resistance of the preform before the impactor touches the support plane and bounces back at 45 ms. The curves recorded from experiments 1 and 3 show good agreement, whereas the curve recorded in test 4 shows a different behaviour after 20 ms.

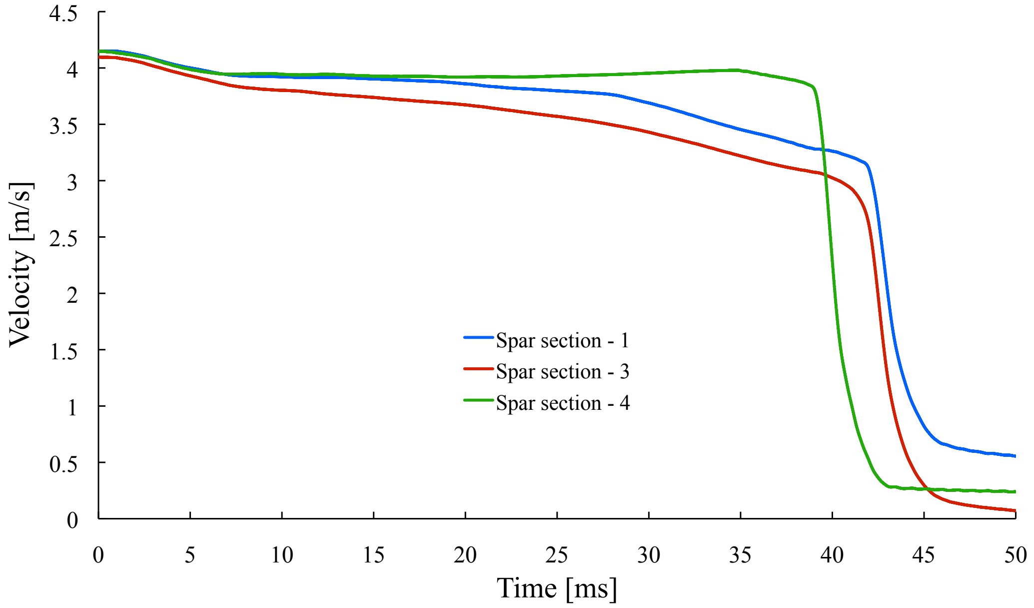

Figure 4.38: Evolution of impactor velocity for the spar section impact experiment.

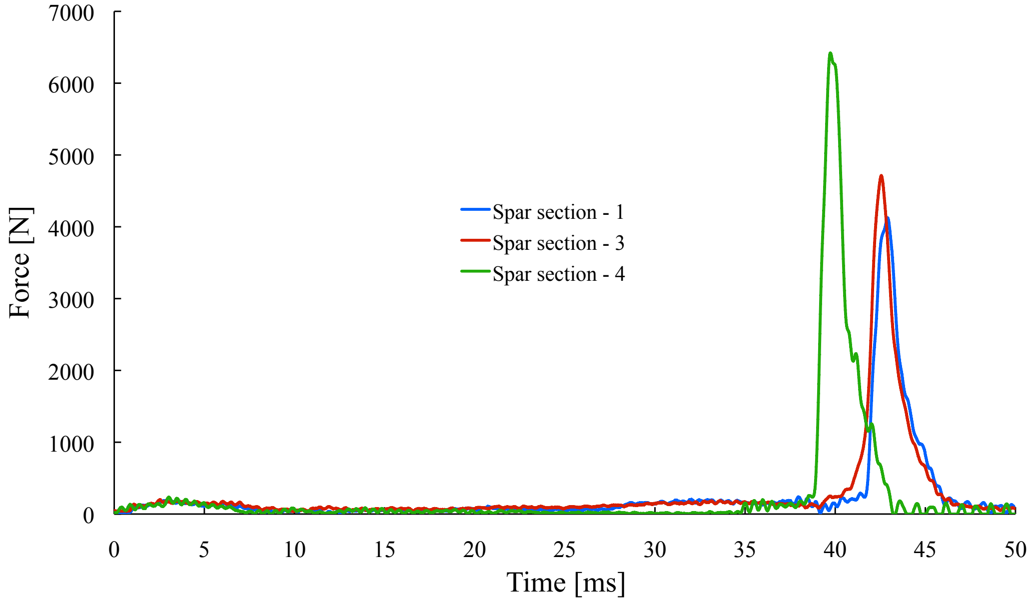

Figure 4.39: Force evolution during impact test on the preform spar section for the complete duration of the test.

Figure 4.39 shows the evolution of force for the during the impact. Good agreement is observed 1 and 3 in terms of peak force. Component 4 shows a higher peak value which appears earlier. All peaks occur after 40 ms and correspond to the impact of the head on the support surface. Figure 4.40 shows the same plot zoomed in the time range up to the 35 ms.

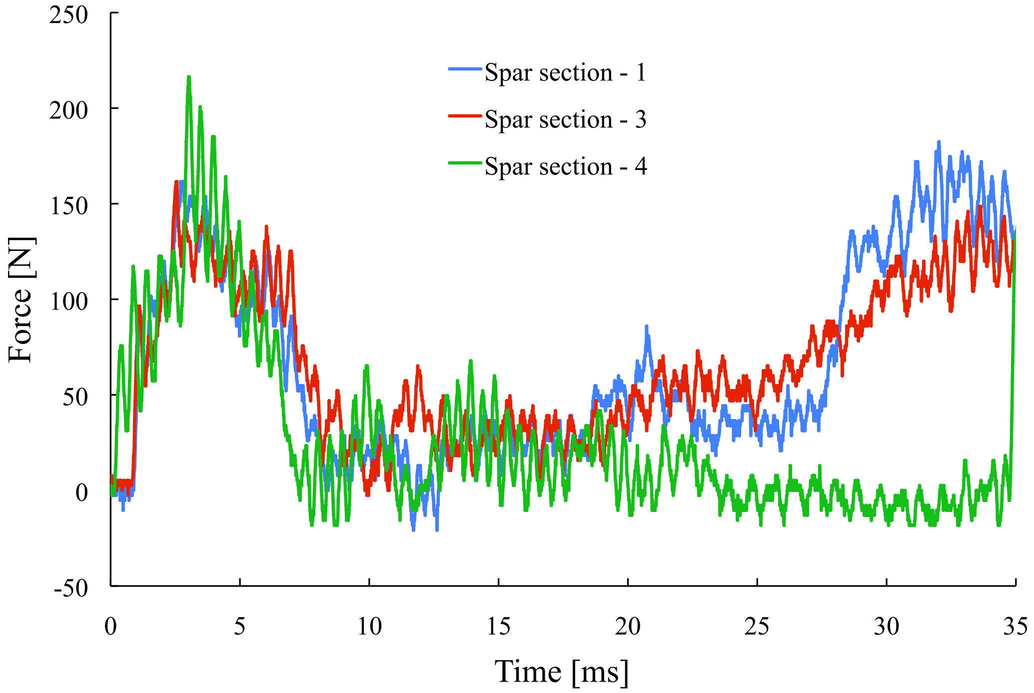

Figure 4.40: Force evolution during impact test on the preform spar section for the initial part of the test.

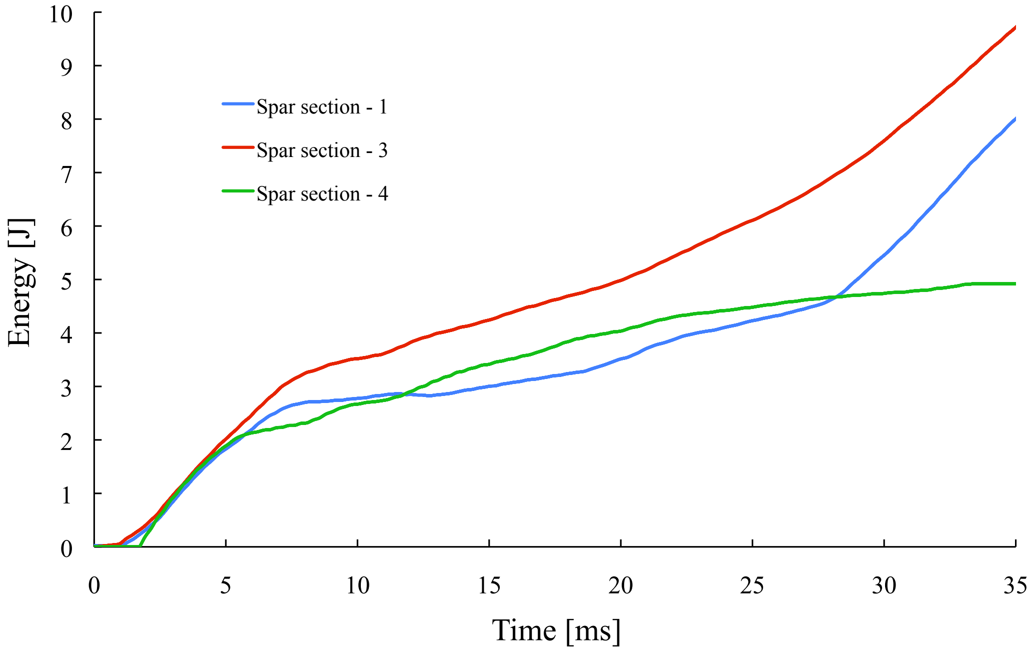

Figure 4.41: Energy evolution for the impact scenarios.

The energy evolution is illustrated in figure 4.41 for the three experiments. After initial contact of impactor head and component is established the energy level increases slightly following the velocity profile. When comparing experiments 1 and 3 with number 4 it is clearly visible that the energy increases with a higher gradient from 30 ms onwards; this effect also corresponds to the observations related to the velocity plot (see figure 4.38). Although an impact energy of 30 J was targeted (see table 4.37) actual energies around 26 J were achieved. The high speed videos for the experiments allow further explanation on the velocity, force and energy plots. Figure 4.42 illustrates the progress of the impact for test 1. Initially the impactor head compresses the spar section and leads to bending of the component at the top segment. The preform continues to deform underneath the striker head and snaps through in the middle of the top surface. Consequently, the upper half is crushed underneath the impactor head. This sequence of events is similar to the high speed video analysis of obtained from experiment 3.

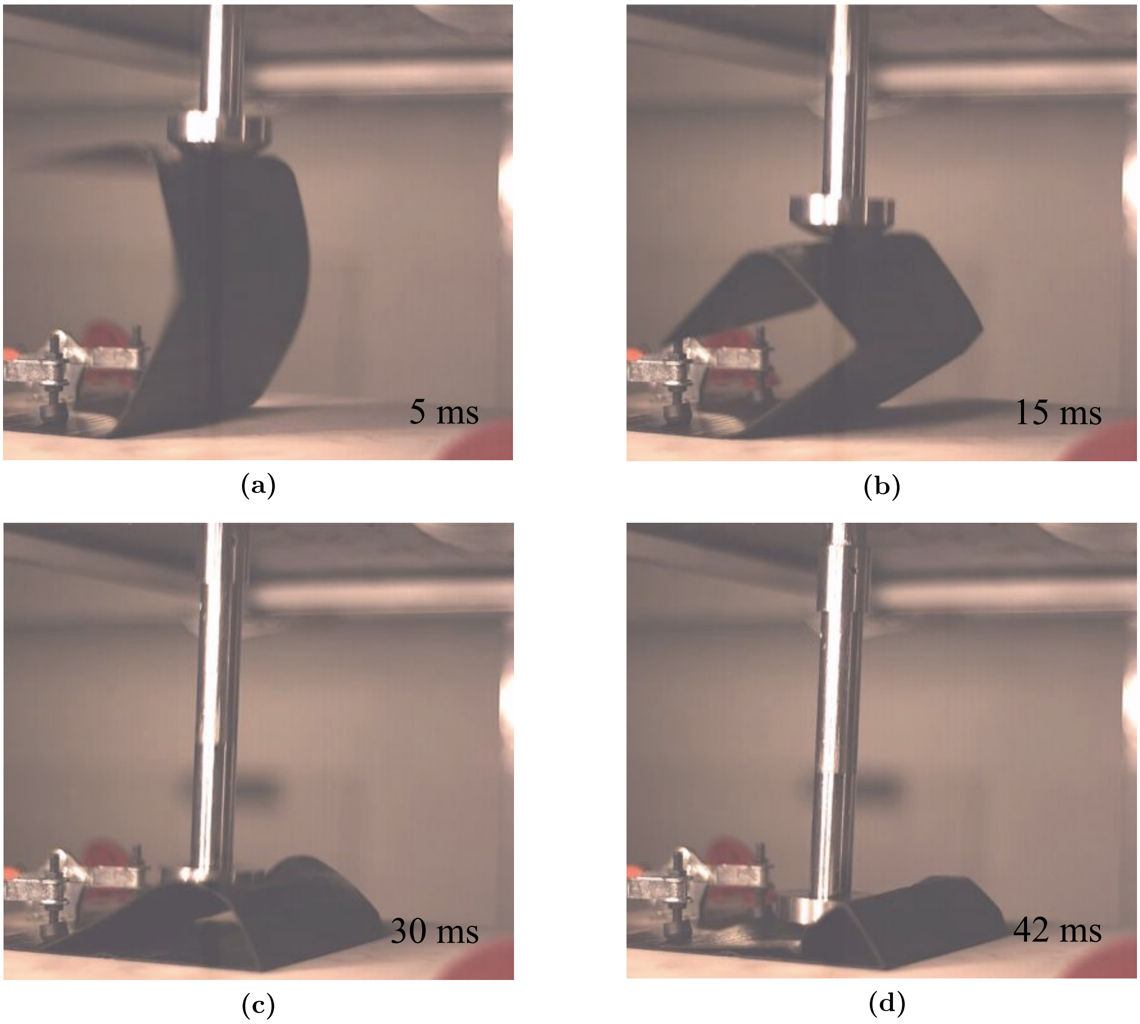

(a) **(b)**

(c) **(d)**

Figure 4.42: Progression of the impact performed on Spar section 1.

The test evolution for experiment 4 is different. As shown in figure 4.43 the beginning of the impact is similar to that of tests 1 and 3, however, during the snap through of the middle section the leg segment slides off underneath the impact head. Hence, the upper part of the component is catapulted outwards. No further interaction is present for the striker head until the support surface is reached.

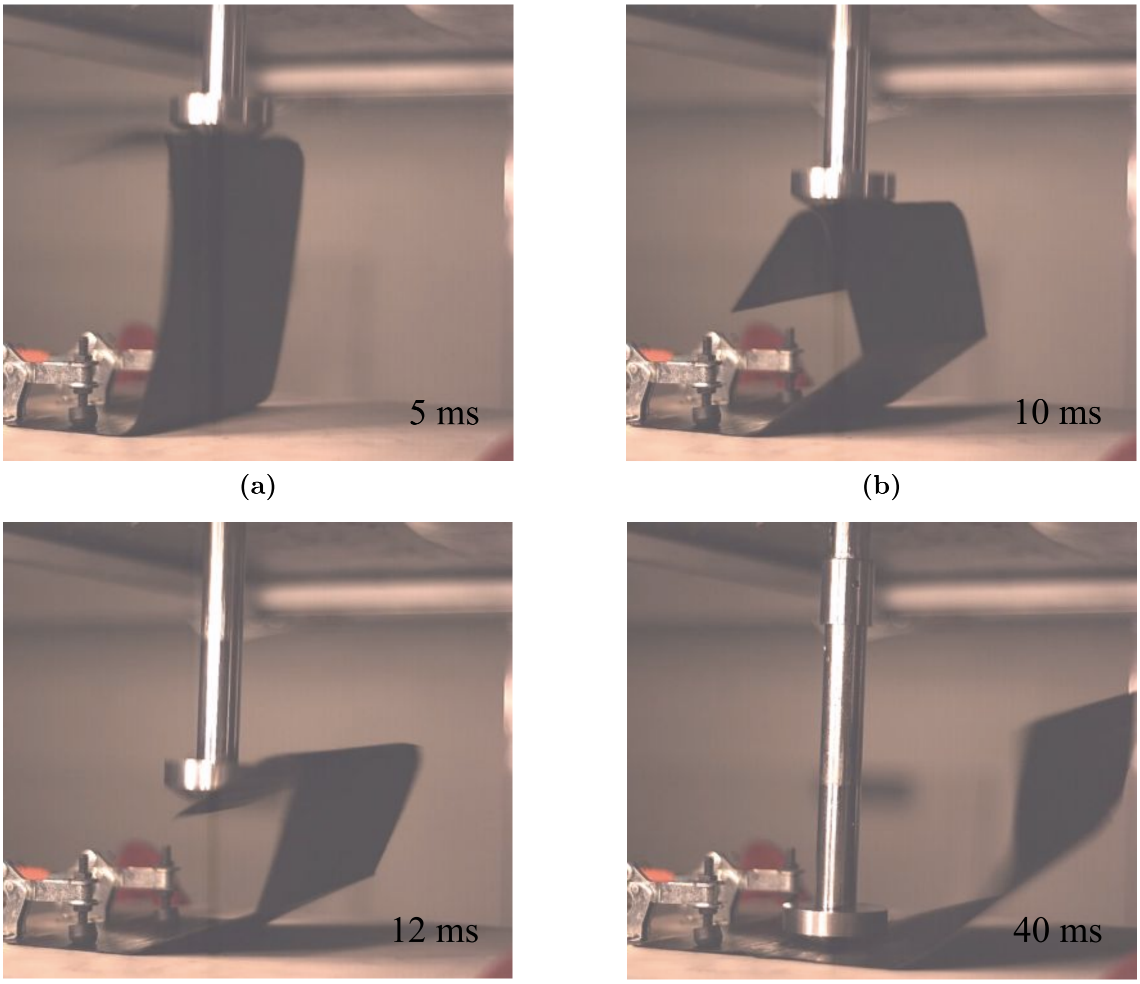

(a) **(b)** **(c)** **(d)**

Figure 4.43: Impact evolution for Spar section 4.

With the aid of the high speed videos it is possible to explain the differences between the tests which are arise in the evolution plots after 20 ms. The significant differences between test 1 and 3 versus 4 are caused by the energy absorption of the upper part of the component which is compressed underneath the impactor head. This effect becomes especially evident when inspecting the force evolution in figure 4.40. Although a certain noise level is present the initial impact is visible in the first 5 ms of the curves. In the time range up to 20 ms the sliding contact between the impactor head and the preform controls the response. From then onwards the curves start to differ more. In the case of test 4 the force level reduces to zero due to the loss of contact before rising up again when the contact with the support takes place. However, for the other two experiments the force level starts rising again after 20 ms as the compressed preform is trapped underneath the impactor head. This effect slows down the impactor head, as shown in the velocity plot in figure 4.38. Ultimately this results into a lower impact velocity, hence lower impact force, and a later contact time with the support as it can be observed in figure 4.39.

5 Material models and parameter identification

This chapter describes the material models for the in- and out-of-plane behaviour of NCF composites and preforms. These are based on two existing concepts for the incorporation of non-linear and damage behaviour in finite element simulations. The in-plane response is described by the model initially proposed by Ladevèze [8], while a cohesive interface model governs the delamination behaviour. Both models are used in an assembly where multi-layered shell are assigned with the Ladevèze model and connected via cohesive interfaces. The conventional technique to extract the parameters from the experimental results is described as part of this chapter. Alternative methods of parameter estimation were investigated in the context of this work. Hence parameter identification was defined as an inverse problem using a parameter vector that is optimised with the aim of minimising the error between model results and experimental data. The development of these material models follows closely current implementations in the finite element code Pam-Crash™[197]. A first attempt was undertaken using a gradient-based solution. Therefore the material model was implemented in Visual Basic for Application while using the gradient-based solver implementation in Microsoft Excel [207] for the error minimisation. In addition, a Markov Chain Monte Carlo approach was used to solve the inverse problem. This approach is based on the concept of Bayesian inference. A comparison of the results obtained using the different techniques is given in the last section of this chapter.

5.1 Material models

5.1.1 In-plane damage model

The constitutive model of a single unidirectional layer incorporates elastic and inelastic components combined with damage variables that affect the elastic part of the material response and govern the post failure behaviour of the material [8]. The elastic part of the constitutive law can be expressed as follows:

$$\begin{Bmatrix} \varepsilon_{11}^{e} \\ \varepsilon_{22}^{e} \\ 2\varepsilon_{12}^{e} \end{Bmatrix} = \begin{bmatrix} \dfrac{1}{E_{11}} & -\dfrac{\nu_{12}}{E_{11}} & 0 \\ -\dfrac{\nu_{12}}{E_{11}} & \dfrac{1}{E_{22}} & 0 \\ 0 & 0 & \dfrac{1}{G_{12}} \end{bmatrix} \begin{Bmatrix} \sigma_{11} \\ \sigma_{22} \\ \sigma_{12} \end{Bmatrix} \tag{5.1}$$

where ε and σ represent the strain and stress components respectively. E_{11}, E_{22} and G_{12} are the moduli and while ν_{12} is the Poisson's ratio. Here index 1 refers to the material direction, which is parallel to the fibres, whereas index 2 is normal to the fibres. The elastic constants depend on damage variables and incorporate non-linearities. The quasi-static modulus in the direction of the fibres can be expressed as

$$E_{11}^{s} = \begin{cases} E_{11}^{0c}\left(1+\gamma\varepsilon_{11}^{e}\right)\left(1-d_{11}^{c}\right) & , \quad \varepsilon_{11}^{e} \leq \varepsilon_{i}^{fc} \\ E_{11}^{0c}\left(1+\gamma\varepsilon_{11}^{e}\right) & , \quad \varepsilon_{i}^{fc} < \varepsilon_{11}^{e} \leq 0 \\ E_{11}^{0t} & , \quad 0 \leq \varepsilon_{11}^{e} < \varepsilon_{i}^{ft} \\ E_{11}^{0t}\left(1-d_{11}^{t}\right) & , \quad \varepsilon_{i}^{ft} \leq \varepsilon_{11}^{e} \end{cases} \tag{5.2}$$

This behaviour allows different initial moduli in tension and compression as well as elastic non-linearity under compression to reproduce micro-buckling. The damage parameters are functions of the strain in the fibre direction and are defined as follows for compression and tension:

$$d_{11}^{c} = \begin{cases} d_{u}^{fc}\dfrac{\varepsilon_{i}^{fc}-\varepsilon_{11}^{e}}{\varepsilon_{i}^{fc}-\varepsilon_{u}^{fc}} & , \quad \varepsilon_{u}^{fc} < \varepsilon_{11}^{e} \leq \varepsilon_{i}^{fc} \\ 1-\left(1-d_{u}^{fc}\right)\dfrac{\varepsilon_{11}^{e}}{\varepsilon_{u}^{fc}} & , \quad \varepsilon_{11}^{e} \leq \varepsilon_{u}^{fc} \end{cases} \tag{5.3}$$

and

$$d_{11}^{t} = \begin{cases} d_{u}^{ft}\dfrac{\varepsilon_{i}^{ft}-\varepsilon_{11}^{e}}{\varepsilon_{i}^{ft}-\varepsilon_{u}^{ft}} & , \quad \varepsilon_{i}^{ft} \leq \varepsilon_{11}^{e} < \varepsilon_{u}^{ft} \\ 1-\left(1-d_{u}^{ft}\right)\dfrac{\varepsilon_{11}^{e}}{\varepsilon_{u}^{ft}} & , \quad \varepsilon_{u}^{ft} \leq \varepsilon_{11}^{e} \end{cases} \tag{5.4}$$

The strain rate dependence is incorporated in the model by appropriate scaling of the stiffness coefficients. While the Poison's ratio is considered to be constant the strain rate dependence of the fibre modulus can be expressed as

$$E_{11} = E_{11}^{s} \left(1 + D_{11} \left|\dot{\varepsilon}_{11}^{e}\right|\right) \tag{5.5}$$

Here D_{11} is a strain rate parameter in the fibre direction. Furthermore, the fibre failure strains also incorporate strain rate dependence expressed as follows:

$$\begin{aligned} \varepsilon_{u}^{ft} &= \varepsilon_{us}^{ft} \left(1 + D_{11}^{R} \left|\dot{\varepsilon}_{11}^{e}\right|\right) \\ \varepsilon_{i}^{ft} &= \varepsilon_{is}^{ft} \left(1 + D_{11}^{R} \left|\dot{\varepsilon}_{11}^{e}\right|\right) \\ \varepsilon_{u}^{fc} &= \varepsilon_{us}^{fc} \left(1 + D_{11}^{R} \left|\dot{\varepsilon}_{11}^{e}\right|\right) \\ \varepsilon_{i}^{fc} &= \varepsilon_{is}^{fc} \left(1 + D_{11}^{R} \left|\dot{\varepsilon}_{11}^{e}\right|\right) \end{aligned} \tag{5.6}$$

Here subscript s corresponds to the quasi-static value of this parameter. Figure 5.1 illustrates the uni-axial material response in the fibre direction for a high and low stain rate. A stiffer material response is followed, with increasing strain rate, however, lower failure strength is obtained. The behaviour in the transverse to the fibre and shear directions involves inelastic strains that result from the evolution of matrix damage. Therefore two damage parameters d_{22} and d_{12} are defined and applied to the quasi-static transverse and shear modulus as follows:

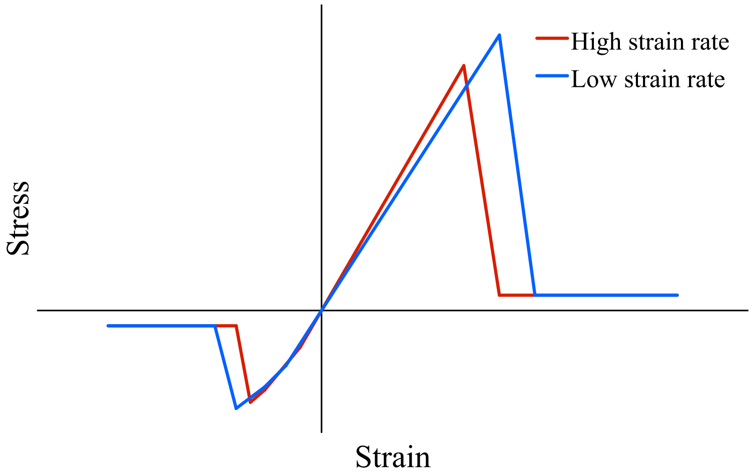

Figure 5.1: Comparison of constitutive law in the fibre direction for high and low strain rate.

$$\begin{aligned} E_{22}^{s} &= \begin{cases} E_{22}^{0} & , \quad d_{22} < 0 \\ \left(1 - d_{22}\right) E_{22}^{0} & , \quad d_{22} \geq 0 \end{cases} \\ G_{12}^{s} &= G_{12}^{0} \left(1 - d_{12}\right) \end{aligned} \tag{5.7}$$

Two irreversible energetic threshold values that describe the damage state of the material with respect to the material direction (see section 2.1.3.2) are defined as follows:

$$Y_{12}(t) = \max\left\{\sqrt{\frac{\sigma_{12}(\tau)}{2G_{12}^{0}\left(1-d_{12}(\tau)\right)^{2}} + b\frac{\max\left(\sigma_{22}(\tau),0\right)^{2}}{2E_{22}^{0}\left(1-d_{22}(\tau)\right)^{2}}} \quad , \quad \tau \leq t\right\} \tag{5.8}$$

and

$$Y_{22}(t) = \max\left\{\sqrt{\frac{\max\left(\sigma_{22}(\tau),0\right)^{2}}{2E_{22}^{0}\left(1-d_{22}(\tau)\right)^{2}}} \quad , \quad \tau \leq t\right\} \tag{5.9}$$

These energetic threshold variables are then used in the computation of the damage parameters for the shear and transverse direction.

$$d_{12}(t) = \begin{cases} \dfrac{\max\left(Y_{12}(t) - Y_{12}^{0}\sqrt{1+D_{12}\left|\dot{\varepsilon}_{12}\right|},0\right)}{Y_{12}^{C}\sqrt{1+D_{12}\left|\dot{\varepsilon}_{12}\right|}} & , \quad d_{12}(t) < d_{max} \wedge Y_{12} < Y_{12}^{U} \wedge Y_{22} < Y_{22}^{U} \\ d_{max} & , \quad d_{12}(t) > d_{max} \vee Y_{12} > Y_{12}^{U} \vee Y_{22} > Y_{22}^{U} \end{cases} \tag{5.10}$$

and

$$d_{22}(t) = \begin{cases} \dfrac{\max\left(Y_{22}(t) - Y_{22}^{0}\sqrt{1+D_{22}\left|\dot{\varepsilon}_{22}\right|},0\right)}{Y_{22}^{C}\sqrt{1+D_{22}\left|\dot{\varepsilon}_{22}\right|}} & , \quad d_{22}(t) < d_{max} \wedge Y_{12} < Y_{12}^{U} \wedge Y_{22} < Y_{22}^{U} \\ d_{max} & , \quad d_{22}(t) > d_{max} \vee Y_{12} > Y_{12}^{U} \vee Y_{22} > Y_{22}^{U} \end{cases} \tag{5.11}$$

The strain rate dependence of the transverse and shear moduli is then expressed as:

$$\begin{aligned} E_{22} &= E_{22}^{s}\left(1+D_{22}\left|\dot{\varepsilon}_{22}\right|\right) \\ G_{12} &= G_{12}^{s}\left(1+D_{12}\left|\dot{\varepsilon}_{12}\right|\right) \end{aligned} \tag{5.12}$$

The inelastic part of the response is incorporated via a Hills-type criterion with isotropic hardening (see section 2.1.3.3). The yield surface is:

$$\sqrt{\left(\frac{\sigma_{12}}{1-d_{12}}\right)^2 + A\left(\frac{\max\left(\sigma_{22},0\right)}{1-d_{22}} + \min\left(\sigma_{22},0\right)\right)^2} - \left[R_0\left(1+D_R\left|\dot{\varepsilon}_R\right|\right) + \beta\left(\bar{\varepsilon}^p\right)^m\right] = 0 \tag{5.13}$$

Here A is the coupling factor between transverse and shear direction, R_0 is the initial yield stress, β and m are the parameters of the power law describing the yielding behaviour of the material and $\bar{\varepsilon}^p$ is the equivalent plastic strain. Figures 5.2 and 5.3 illustrate the uni-axial material response for the transverse and the shear material direction for different stain rates. In the transverse direction an increasing strain rate leads to a lower failure strength while the stiffness of the material remains constant. In contrast, higher stresses are achieved for the material under shear loading.

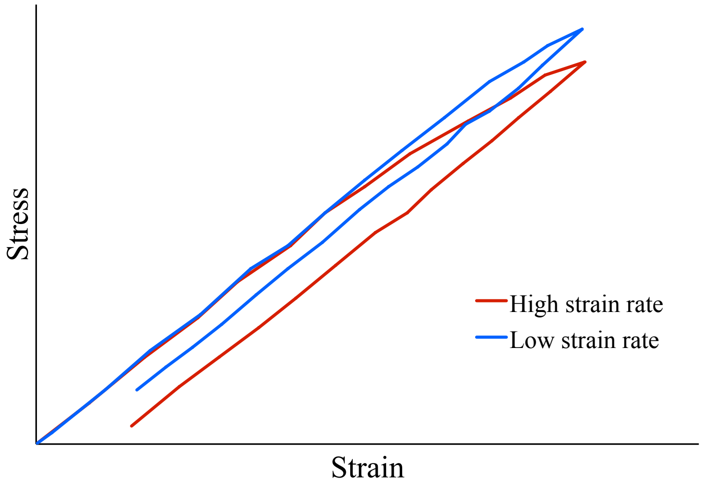

Figure 5.2: Comparison of constitutive law in the transverse direction for high and low strain rate.

5.1.2 Out-of-plane damage model

Delamination damage is incorporated in the model using cohesive interfaces as implemented via the tied interface option in Pam-Crash™ [197]. When cohesive interfaces are used, degrees of freedom of nodes on opposite sides of the interface are related via a force-displacement law as follows:

$$\begin{aligned} t_I &= f\left(\Delta u_I\right) \\ t_{II} &= g\left(\Delta u_{II}\right) \end{aligned} \tag{5.14}$$

where t_I and t_{II} are the forces related to the mode I and II displacements. In a three dimensional analysis the total number of relations is three, with two identical

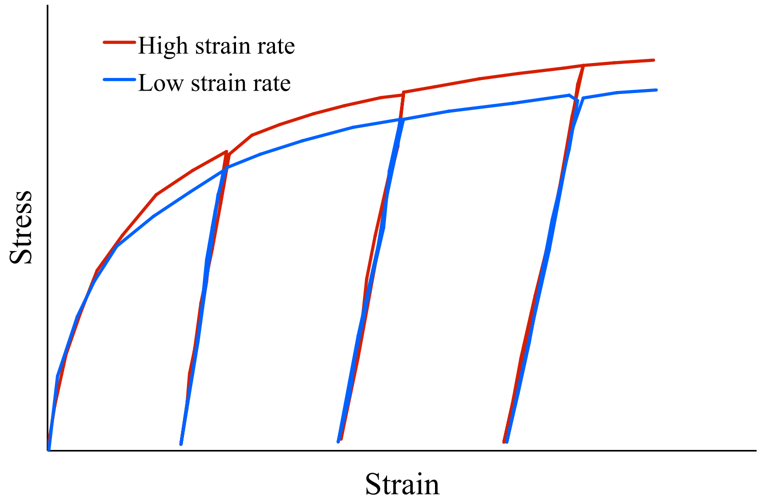

Figure 5.3: Comparison of constitutive law in the shear direction for high and low strain rate.

components in the shear directions and one in the normal direction. A bi-linear material law [111] is followed in this work:

$$\begin{aligned} \sigma_I &= (1 - d_I)\, E_{22}^0 \varepsilon_I \\ \sigma_{II} &= (1 - d_{II})\, G_{12}^0 \varepsilon_{II} \end{aligned} \tag{5.15}$$

where

$$d_I = \begin{cases} \dfrac{\varepsilon_I - \varepsilon_I^i}{\varepsilon_I^u - \varepsilon_I^i} & , \quad \varepsilon_I^i < \varepsilon_I \leq \varepsilon_I^u \\ 0 & , \quad \varepsilon_I \leq \varepsilon_I^i \end{cases} \tag{5.16}$$

and

$$d_{II} = \begin{cases} \left| \dfrac{\varepsilon_{II} - \varepsilon_{II}^i}{\varepsilon_{II}^u - \varepsilon_{II}^i} \right| & , \quad |\varepsilon_{II}^i| < |\varepsilon_{II}| \leq |\varepsilon_{II}^u| \\ 0 & , \quad |\varepsilon_{II}| \leq |\varepsilon_{II}^i| \end{cases} \tag{5.17}$$

Here σ_I, σ_{II}, d_I, d_{II}, ε_I and ε_{II} are the stress, damage parameter and strain values in mode I and II respectively. Equations 5.15-5.17 imply that damage starts in each direction when an elastic energy limit is exceeded. This limit is defined for each mode as:

$$\begin{aligned} G_I^0 &= \frac{\sigma_I^{max^2}}{2E_{22}^0} \\ G_{II}^0 &= \frac{\sigma_{II}^{max^2}}{2G_{12}^0} \end{aligned} \tag{5.18}$$

where G_I^0 and G_{II}^0 corresponds to the initial energy threshold values for crack propagation (see also figure 6.6). Furthermore σ_I^{max} and σ_{II}^{max} are the fracture initiation threshold stresses in mode I and II respectively. Failure propagates gradually from that point until an ultimate energy limit (G_I^u and G_{II}^u for mode I and II respectively) is reached. This limit corresponds to the ultimate strains of the interface

$$\begin{aligned} \varepsilon_I^u &= \frac{2G_I^u}{\sigma_I^{max}} \\ \varepsilon_{II}^u &= \frac{2G_{II}^u}{\sigma_{II}^{max}} \end{aligned} \tag{5.19}$$

over which the interface is deactivated. For mixed mode loading the initiation and completion of damage are calculated using the following law:

$$\frac{G_I}{G_I^u} + \frac{G_{II}}{G_{II}^u} = G_{cont} \tag{5.20}$$

Here parameter G_{cont} governs the magnitude of the mixed mode loading and allows the coupling of the two modes. Figure 5.4 shows a typical bi-linear interface response (see also figure 6.6). The area under the curve is equivalent to the value of energy release rate. The crack initiation and propagation for the interface model is defined via a corresponding stress value for mode I and II (see section 5.2.1.2).

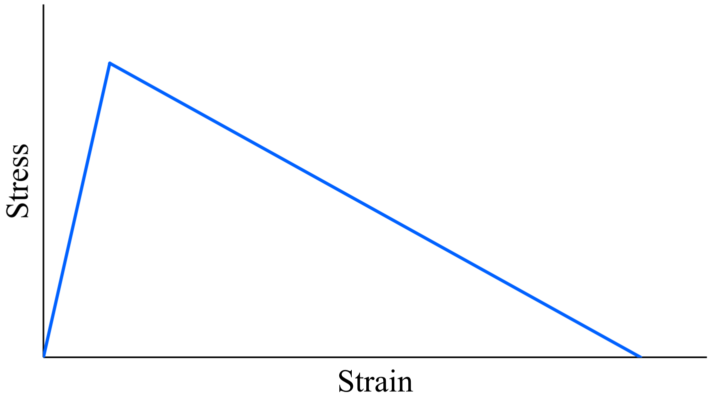

Figure 5.4: Schematic evolution of the cohesive interface model.

5.2 Material model parameter identification

This section addresses the different methods used to identify the parameters required for the use of material models in finite element analysis. At first the conventional method, as recommended by the published literature for this model [8, 9, 197], is followed. In addition to this method two different approaches were developed. In both methods the task of identifying the parameters was defined as an inverse problem. Therefore the material model was implemented in different development environments. The first alternative approach uses a gradient-based solver while the second procedure addresses the problem with a Markov Chain Monte Carlo simulation. Solutions from all three techniques are compared in the end of this chapter. Throughout the following sections the procedures of extracting the parameters from the specific experimental data via the different methods is demonstrated on the basis of only one representative experiment. Experimental data of the reference laminate are used for this purpose. However, results from the whole data sets are presented in the final section of this chapter.

5.2.1 Conventional parameter identification method

5.2.1.1 In-plane properties

Fibre direction

For the determination of elastic and failure properties of composites in the fibre direction the specimens are uniformly loaded until failure occurs. By definition stresses and strains for this material direction are related to the recorded data as follows:

$$\begin{Bmatrix} \sigma_{11} \\ \sigma_{22} \\ \sigma_{12} \end{Bmatrix} = \begin{Bmatrix} \sigma_L \\ 0 \\ 0 \end{Bmatrix} \quad \text{and} \quad \begin{Bmatrix} \varepsilon_{11} \\ \varepsilon_{22} \\ 2\varepsilon_{12} \end{Bmatrix} = \begin{Bmatrix} \varepsilon_L \\ \varepsilon_T \\ 0 \end{Bmatrix} \tag{5.21}$$

Here σ_{11}, σ_{22} and σ_{12} are the stress components in the material coordinate system, whereas σ_L is the longitudinal stress of the global coordinate frame, which coincides with the data acquisition system. Similarly ε_{11}, ε_{22} and ε_{12} are the strain in the material coordinate system and ε_L, ε_T are the longitudinal and transverse strains in the global frame. In order to determine the undamaged elastic modulus in the fibre direction E_1^{0t} an extraction region is defined using 50% and 10% of the tensile failure stress σ_i^{ft}[183, 208]. Hence the undamaged elastic modulus is calculated as follows:

$$E_{11}^{0t} = \frac{\sigma_{11}'' - \sigma_{11}'}{\varepsilon_{11}'' - \varepsilon_{11}'} \tag{5.22}$$

Here ε_{11}'' and ε_{11}' are the strains at 50% (σ_{11}'') and 10% (σ_{11}') of the tensile failure stress. Figure 5.5 illustrates the experimental curve and indicates the highlighted data points which were used to determine the undamaged elastic modulus in this material direction. Furthermore the undamaged value for the Poisson's ratio is determined using the definition:

$$\nu_{12}^0 = -\frac{\varepsilon_{22}}{\varepsilon_{11}} \tag{5.23}$$

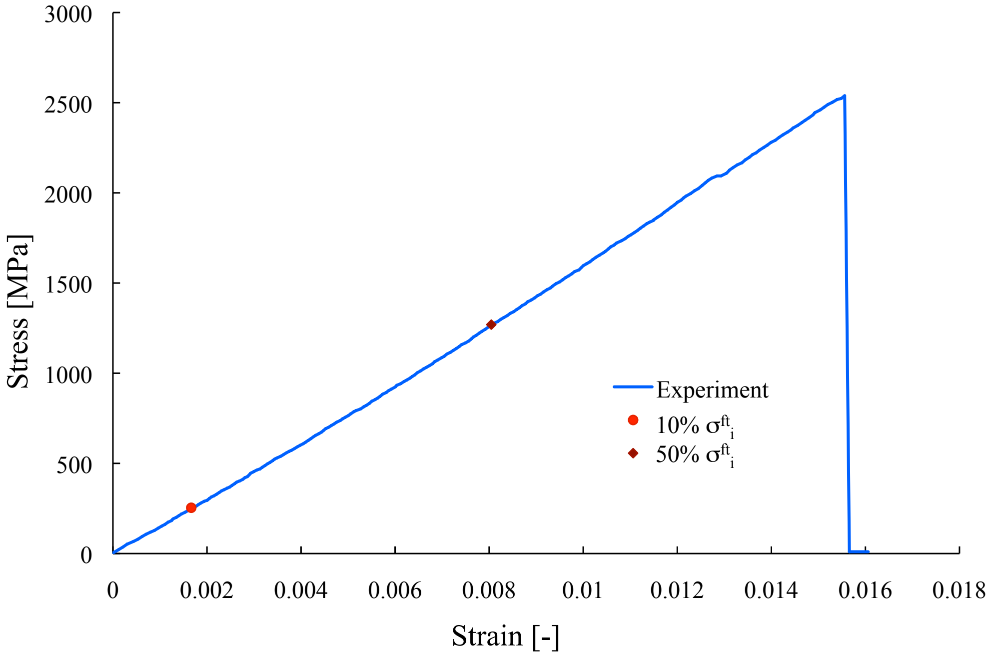

Figure 5.5: Stress-strain curve for tension in the fibre direction.

The rest of the properties influence the failure and post damage behaviour in the fibre direction. The remaining portion of the stress-strain data is used to extract these values graphically. The initial tensile failure strain ε_i^{ft} corresponds to the maximum stress value of the stress-strain curve while the ultimate failure strain ε_u^{ft} and the damage parameter d_u^{ft} that is used to degrade the undamaged elastic modulus are extracted from the data corresponding to the post failure behaviour of the material. The resulting parameter set controlling model behaviour in the fibre direction under tensile loading for one experiment on the reference laminate is listed in table 5.1. Similarly to the tensile material model, properties for the compressive fibre direction are determined directly from the stress-strain data. Here the compressive elastic modulus is calculated from two points within the initial part

Property	Unit	Value
E_{11}^{0t}	GPa	159.2
ν_{12}^{0}	–	0.29
ε_i^{ft}	–	1.56E-02
ε_u^{ft}	–	1.57E-02
d_u^{ft}	–	1

Table 5.1: Material properties in fibre direction for tensile loading.

of the average stress-strain curve [184, 209] as follows:

$$E_{11}^{0c} = \frac{\sigma_{11}'' - \sigma_{11}'}{\varepsilon_{11}'' - \varepsilon_{11}'} \tag{5.24}$$

Here σ_C'' corresponds to the stress value at $\varepsilon_C'' = 0.25\%$ strain and σ_C' is the stress value at $\varepsilon_C' = 0.05\%$ strain. Properties governing the post failure behaviour are deduced from the load drop. Hence, the initial and ultimate compressive failure strains ε_i^{fc} and ε_u^{fc} define the range in which the material becomes incapable of carrying further load. The ultimate compression damage d_u^{fc} is then chosen according to the material post failure behaviour. A correction parameter γ is introduced to address the nonlinear compressive behaviour due to fibre crimp and micro-buckling. This parameter is calculated using an arbitrary point, picked from the higher strain region, for which the tangent modulus E_1^{γ} is computed and applied as follows

$$\gamma = \frac{E_{11}^{0c} - E_{11}^{\gamma}}{E_{11}^{\gamma} E_{11}^{0c} \left|\varepsilon_{11}\right|} \tag{5.25}$$

Table 5.2 lists the parameters of the material model, extracted from the experimental data shown in figure 5.6.

Property	Unit	Value
E_{11}^{0c}	GPa	129.3
ε_i^{fc}	–	9.3E-03
ε_u^{fc}	–	9.4E-03
d_u^{fc}	–	1
γ	–	6.4E-02

Table 5.2: Material properties in the fibre direction for compressive loading.

Cyclic tensile test on $[\pm 45°]_{2s}$ specimens

The cyclic shear tests on $[\pm 45°]_{2s}$ coupons are used to extract shear damage evolution, plasticity and failure data. The variables describing these phenomena are the shear modulus, the thermodynamic shear damage variables, the initial yield stress and the hardening coefficients. The recorded data are transformed into the fibre frame using the following definition:

$$\left\{ \begin{array}{c} \sigma_{11} \\ \sigma_{22} \\ \sigma_{12} \end{array} \right\} = \left\{ \begin{array}{c} 0 \\ 0 \\ \dfrac{\sigma_L}{2} \end{array} \right\} \quad \text{and} \quad \left\{ \begin{array}{c} \varepsilon_{11} \\ \varepsilon_{22} \\ 2\varepsilon_{12} \end{array} \right\} = \left\{ \begin{array}{c} 0 \\ 0 \\ \varepsilon_L - \varepsilon_T \end{array} \right\} \tag{5.26}$$

The undamaged shear modulus in 1-2 plane is calculated from the initial slope using

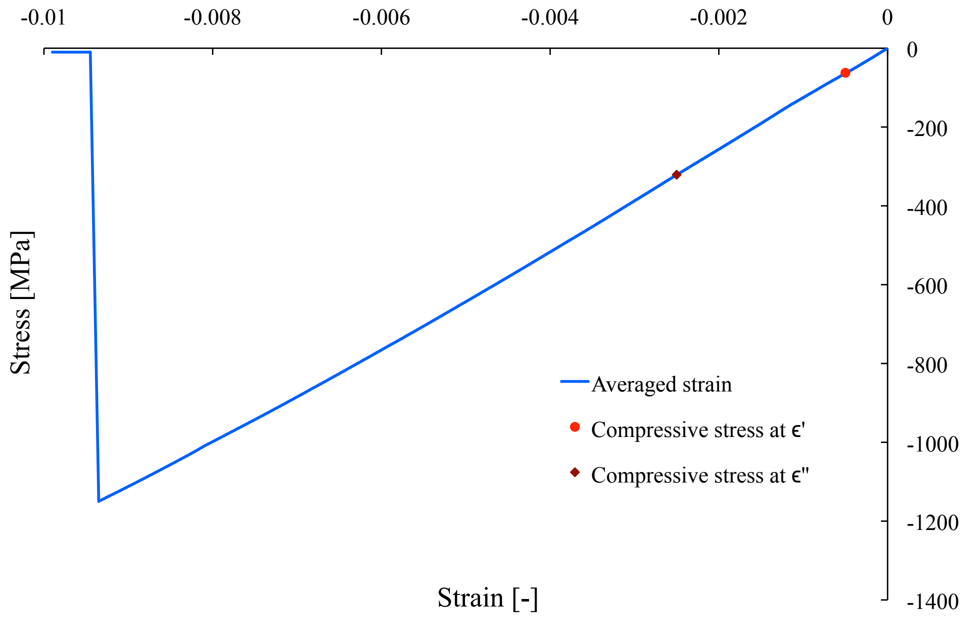

Figure 5.6: Average compressive stress-strain curve with marks at the points used to determine the compressive modulus.

the shear stress and engineering shear strain.

$$G_{12}^{0} = \frac{\sigma_{12}}{2\varepsilon_{12}} \tag{5.27}$$

Shear damage is given by the change of slope of the cyclic shear modulus G_{12}^{i} and plasticity by the growth of ε^{p^i} for each loading cycle. The stresses and strains of the cycle points are identified as illustrated in figure 5.7. At each cycle the stiffness loss is given by the shear modulus reduction. Hence the magnitude of the shear damage d_{12} is given by the relationship:

$$d_{12}^{i} = 1 - \frac{G_{12}^{i}}{G_{12}^{0}} \tag{5.28}$$

The resulting stiffness loss and damage values, using equation 5.28, are listed in table 5.3. The material model uses the term Y_{12}, which is derived from the stored energy of a single ply (see section 2.1.3.2), to characterise the damage progress. Considering only the stored energy for shear, the thermodynamic force at each cycle is given by:

$$Y_{12}^{i} = \sqrt{\frac{1}{2} G_{12}^{0} (2\varepsilon_{12}^{e^i})^2} \tag{5.29}$$

Using the information provided by the cycle points and equation 5.29 it is possible to compute the thermodynamic force as function of shear damage. The results are illustrated in figure 5.8. The damage follows a linear behaviour for small strains with

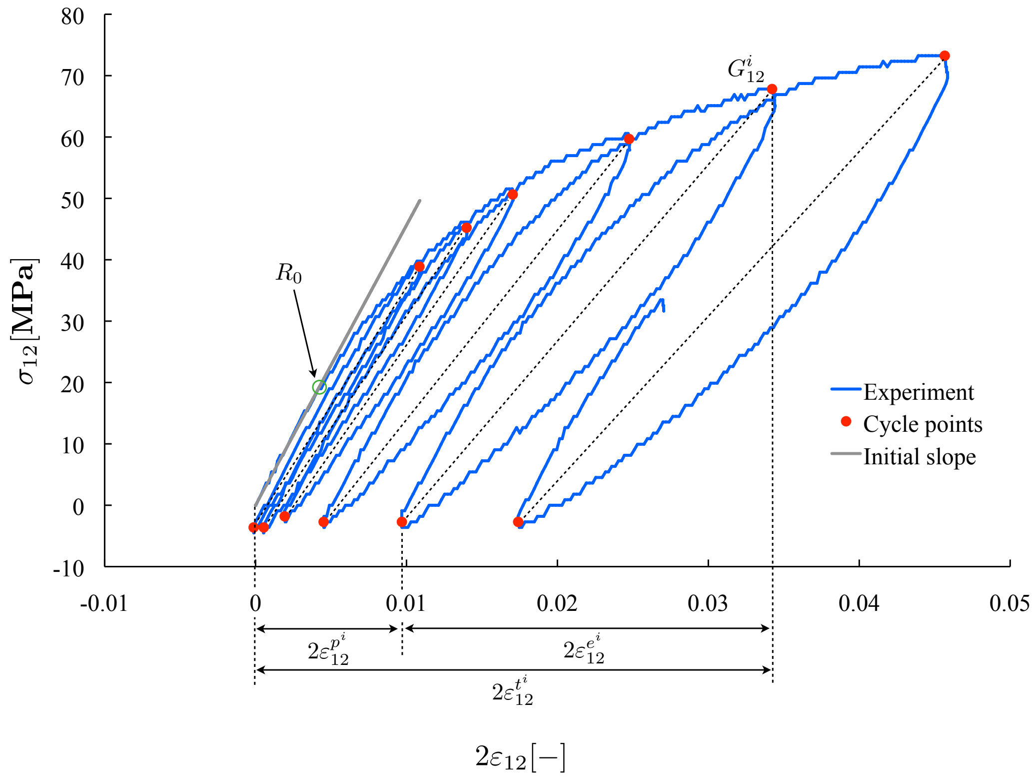

Figure 5.7: Stress-strain response of $[\pm 45°]_{2s}$ specimens under cyclic loading.

an increasing slope close to failure. The finite element solver used [197] provides a choice of functions that can be fitted against the data points. Exponential, curve and linear functions are available. The linear function was chosen in this work as the extracted data points were adequately represented by the following function:

$$\hat{Y} = Y_{12}^C d_{12} + Y_{12}^0 \tag{5.30}$$

Here Y_{12}^0 is the intercept and Y_{12}^C the slope of the linear function. An additional parameter corresponding to the the shear damage maximum is determined as

$$Y_{12}^U = \max Y_{12}^i \tag{5.31}$$

Table 5.4 lists the shear damage parameters for a linear evolution curve.
The inelastic deformation is described by a plasticity law which couples transverse and shear terms only (see section 2.1.3.3). Three more parameters are required to achieve this. The initial yield stress R_0 can be extracted directly from the stress strain curve as illustrated in figure 5.7. The yield stress is identified as the stress value at which the experimental curve diverts from the linear curve drawn using the undamaged shear modulus. From this value onwards the yielding process is representable using a power law with two hardening coefficients β and m which

Cycle	G_{12}^i [GPa]	d_{12}^i [−]
0	4.56	0
1	3.87	0.152
2	3.63	0.204
3	3.47	0.239
4	3.08	0.324
5	2.88	0.369
6	2.69	0.411

Table 5.3: Stiffness loss at each cycle.

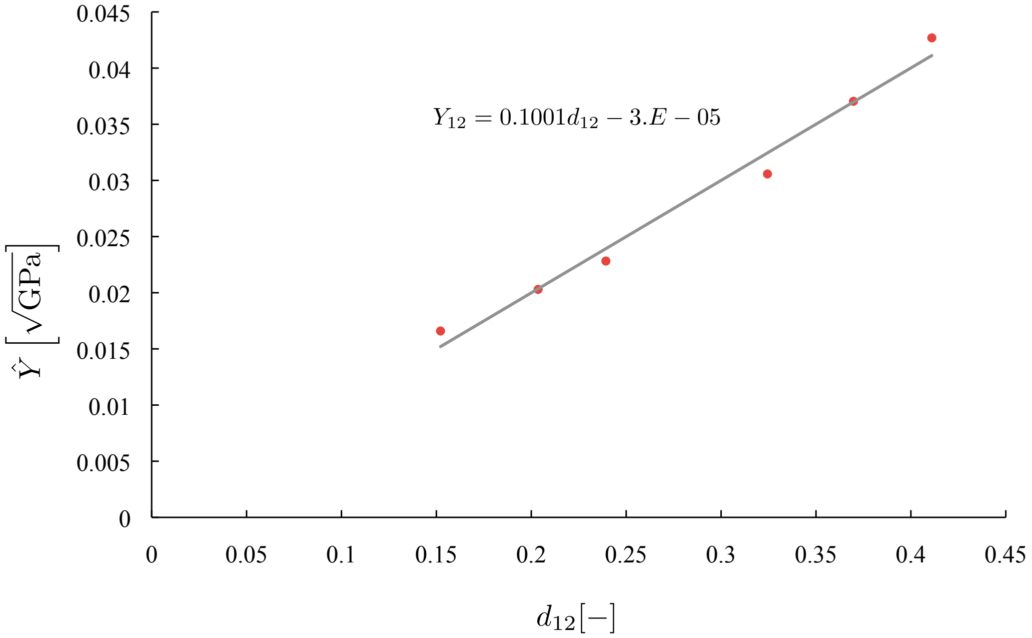

Figure 5.8: Curve fitting for the thermodynamic forces depending on shear.

define the shape of the plasticity curve as follows:

$$R^j = \beta \left(\bar{\varepsilon}_{12}^{pj}\right)^m \tag{5.32}$$

To determine these two parameters, the yield stress evolution is plotted based on the damage information of the experiment using the following relation.

$$R^i = \frac{\sigma_{12}^i}{(1 - d_{12}^i)} - R_0 \tag{5.33}$$

However, the power law introduced in equation 5.32 uses the effective plastic strain as an independent variable. Therefore the effective plastic strain $\bar{\varepsilon}_{12}^{pj}$ is calculated

Property	Unit	Value
Y_{12}^{0}	$\sqrt{\text{GPa}}$	-3.24E-05
Y_{12}^{C}	$\sqrt{\text{GPa}}$	0.1
Y_{12}^{U}	$\sqrt{\text{GPa}}$	4.27E-02

Table 5.4: Energetic shear threshold values.

using the following relations:

$$\tilde{\varepsilon}_{12}^{p^i} = \int_{\varepsilon_{12}^{p^{i-1}}}^{\varepsilon_{12}^{p^i}} (1 - d_{12}^{i}) d\varepsilon_{12}^{p} \tag{5.34}$$

and

$$\bar{\varepsilon}_{12}^{p^j} = \sum_{i=1}^{i=j} \tilde{\varepsilon}_{12}^{p^i} \tag{5.35}$$

Figure 5.9 presents the graphical illustration of equation 5.34. The areas under the damage progress versus plastic engineering shear strain curve are calculated. The

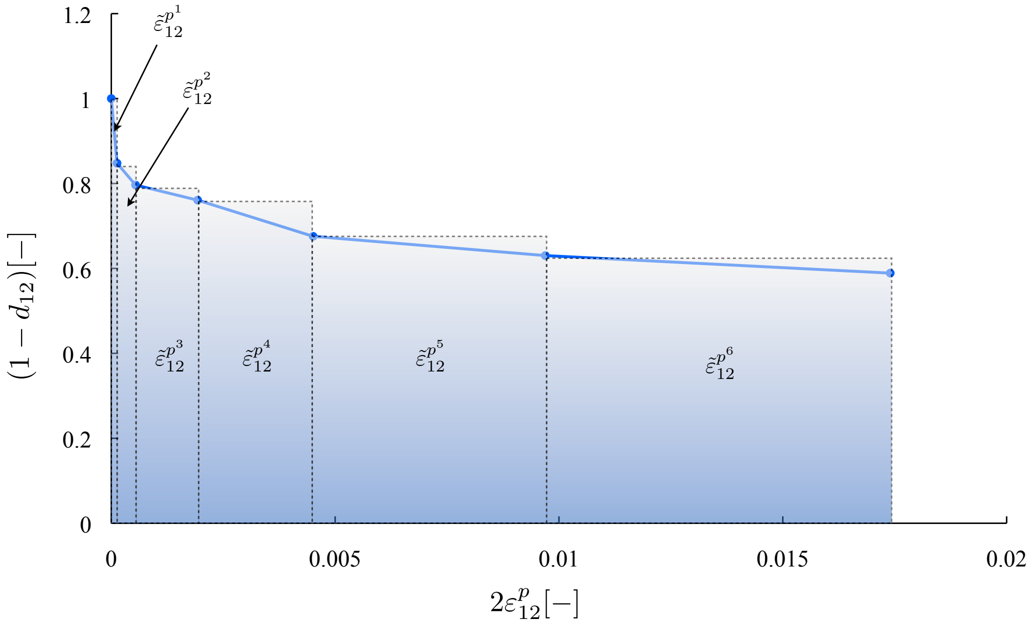

Figure 5.9: Plot of damage evolution versus engineering plastic strain.

Property	Unit	Value
R_0	GPa	2.2E-02
β	$-$	0.39
m	$-$	0.35

Table 5.5: Yield parameters from single shear experiment.

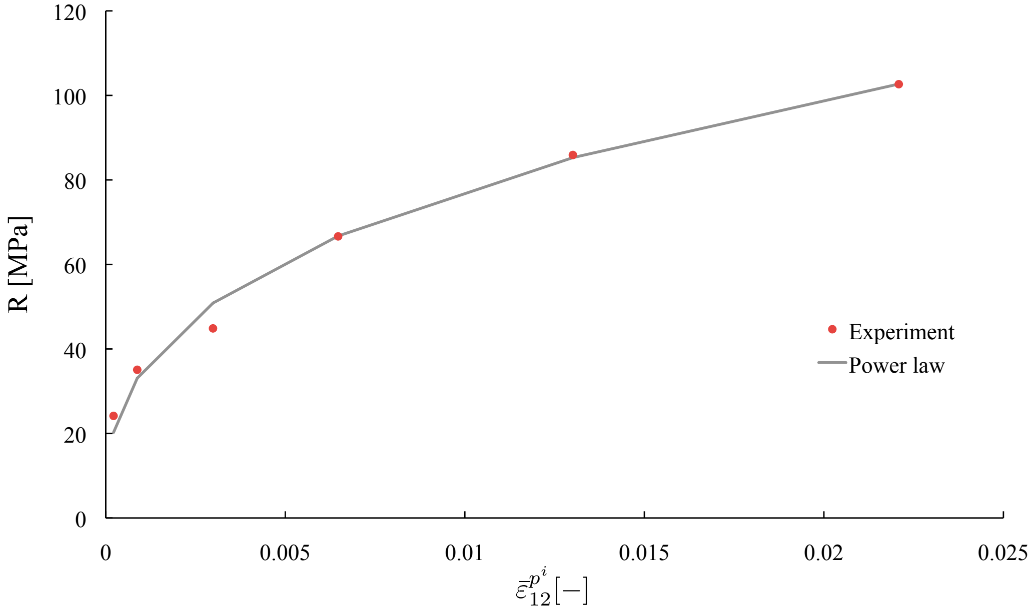

Figure 5.10: Curve fitting for the yield stress power law.

progressive sum of these areas leads to the current effective plastic strain that is used as an input for the power law (see equation 5.32). Hence, parameters β and m are chosen to achieve the best fit between equations 5.32 and 5.33. This fitting procedure can be performed within Microsoft Excel using the gradient-based solver implementation [207] with an error minimisation objective. The result of this procedure is show in figure 5.10. The values obtained for the plasticity model are listed in table 5.5.

Cyclic tensile test on$[+45°]_8$ coupons

Coupons with a $[+45°]_8$ layup are subjected to cyclic loading with increasing load levels. This experiment is designed to extract two more parameters for the material model:

- the coupling factor between transverse and shear plastic strains A
- the transverse modulus E_{22}^0

The stress measured and the longitudinal and transverse strain values are transformed into the material frame using the following expressions:

$$\left\{ \begin{array}{c} \sigma_{11} \\ \sigma_{22} \\ \sigma_{12} \end{array} \right\} = \left\{ \begin{array}{c} 0 \\ \frac{\sigma_L}{2} \\ \frac{\sigma_L}{2} \end{array} \right\} \quad \text{and} \quad \left\{ \begin{array}{c} \varepsilon_{11} \\ \varepsilon_{22} \\ 2\varepsilon_{12} \end{array} \right\} = \left\{ \begin{array}{c} 0 \\ \varepsilon_L + \varepsilon_T \\ \varepsilon_L - \varepsilon_T \end{array} \right\} \tag{5.36}$$

This transformation allows to plot the synchronised transverse and shear response of the material. The initial transverse modulus can be obtained from the initial linear slope of the transverse material response. Thereafter, the damage factor in the transverse direction is defined for each cycle by the drop in stiffness as described in the following relation:

$$d_{22}^{i} = 1 - \frac{E_{22}^{i}}{E_{22}^{0}} \tag{5.37}$$

The shear damage parameter at each cycle is also required for the identification of the coupling factor. This parameter is deduced from the shear response of the material using equation 5.28. Together with the transverse and shear plastic strains the coupling factor is calculated for each cycle using the following expression:

$$A^{i} = \frac{\left(\varepsilon_{22}^{p^{i}} - \varepsilon_{22}^{p^{i-1}}\right) \cdot \left(1 - d_{22}^{i}\right)^{2}}{\left(2\varepsilon_{12}^{p^{i}} - 2\varepsilon_{12}^{p^{i-1}}\right) \cdot \left(1 - d_{12}^{i}\right)^{2}} \tag{5.38}$$

The final value for the couping parameter is calculated as the average of all individual data. The values for the undamaged transverse modulus and the coupling factor for this single experiment are listed in table 5.6.

Property	Unit	Values
E_{22}^{0}	GPa	9.6
A	–	6.3E-02

Table 5.6: Parameters obtained from [+45°] specimen.

Cyclic tensile test on $[\pm 67.5°]_{2s}$ specimen

The final set of parameters for the material model is determined from cyclic loading experiments on $[\pm 67.5°]_{2s}$ coupons. Here the energetic threshold values for the transverse direction and the coupling factor between transverse and shear damage b are determined.

A laminate with this stacking sequence is used due to the fact that interlaminar stresses are relatively small and therefore do not cause damage initiation or failure. Furthermore, a bi-axial stress state with respect to the principal material coordinates is achieved which allows to probe coupling effects [63].

The data from the experiments are translated to the material frame by using the expressions.

$$\left\{ \begin{array}{c} \sigma_{11} \\ \sigma_{22} \\ \sigma_{12} \end{array} \right\} = \left\{ \begin{array}{c} B \\ (1 - B) \\ -\frac{1}{2cs}\left(B\left(1 - 2c^{2}\right) + c^{2}\right) \end{array} \right\} \sigma_{L} \tag{5.39}$$

and

$$\begin{Bmatrix} \varepsilon_{11} \\ \varepsilon_{22} \\ 2\varepsilon_{12} \end{Bmatrix} = \begin{bmatrix} c^2 & s^2 & cs \\ s^2 & c^2 & -cs \\ -2cs & 2cs & c^2 - s^2 \end{bmatrix} \begin{Bmatrix} \varepsilon_L \\ \varepsilon_T \\ 0 \end{Bmatrix} \tag{5.40}$$

For abbreviation purposes c and s are substituted for $\cos\Theta$ and $\sin\Theta$ respectively, where Θ is the ply angle. Furthermore, the coefficient B is expressed as follows:

$$B = \left[\frac{c^2\left(2c^2-1\right) + 4c^2s^2 \frac{G_{12}^0}{E_{22}^0}\left(\frac{E_{22}^0}{E_{11}^0}\nu_{12}^0 + 1\right)}{4c^2s^2\frac{G_{12}^0}{E_{22}^0}\left(\frac{E_{22}^0}{E_{11}^0} + 2\frac{E_{22}^0}{E_{11}^0}\nu_{12}^0 + 1\right) + \left(2c^2-1\right)\left(c^2-s^2\right)} \right] \tag{5.41}$$

It should be noted that the moduli for the shear, transverse and fibre direction have to be known in order to calculate this value with a constant ply angle Θ. However, in case of materials where $E_1 \gg E_2$ this term can be simplified as follows:

$$B_a = \left[\frac{c^2\left(2c^2-1\right) + 4c^2s^2\frac{G_{12}^0}{E_{22}^0}}{4c^2s^2\frac{G_{12}^0}{E_{22}^0} + \left(2c^2-1\right)\left(c^2-s^2\right)} \right] \tag{5.42}$$

For comparison the values of B and B_a calculated from the results presented in the previous section are 0.180617 and 0.180527 respectively.

The shear and transverse material response can be extracted from this experiment similar to the $[+45°]_8$ laminate. The elastic strains are used to calculate the thermodynamic variables as follows (also see equations 2.22 and 2.23):

$$Z_{22} = \frac{1}{2}E_{22}^0\left(\nu_{12}^0\varepsilon_{11}^{e^i} + \varepsilon_{22}^{e^i}\right) \tag{5.43}$$

$$Z_{12} = \frac{1}{2}G_{12}^0\left(2\varepsilon_{12}^{e^i}\right)^2 \tag{5.44}$$

The data obtained are used to calculate the corresponding coupling factors in addition to the previously determined shear threshold values Y_{12}^C and Y_{12}^0:

$$b_i = \frac{Y_{12}^C d_{12}^i + Y_{12}^0 - Z_{12}^i}{Z_{22}^i} \tag{5.45}$$

Constant b can be determined from a best fit of all available experimental data for this particular test.

The same approach as followed previously for the shear direction to determine the energetic threshold values for the transverse direction is applied here. Experimental points for the curve fitting procedure on the energy threshold values are calculated from the elastic strain information of the cyclic transverse material response using the following relation.

$$Y_{22}^{i} = \sqrt{\frac{1}{2} E_{22}^{0} (\varepsilon_{22}^{ei})^{2}} \tag{5.46}$$

These data points are plotted against the damage values, in the transverse direction for each cycle using equation 5.37 (see figure 5.11). The energetic parameters determined are the two parameters of a linear expression:

$$\hat{Y} = Y_{22}^{C} d_{22} + Y_{22}^{0} \tag{5.47}$$

Figure 5.11 shows the results of this procedure. The brittle damage threshold value for the fibre/matrix interface is calculated as the maximum of the data set produced using equation 5.46.

$$Y_{22}^{U} = \max Y_{22}^{i} \tag{5.48}$$

Values obtained from the described procedures are listed in table 5.7.

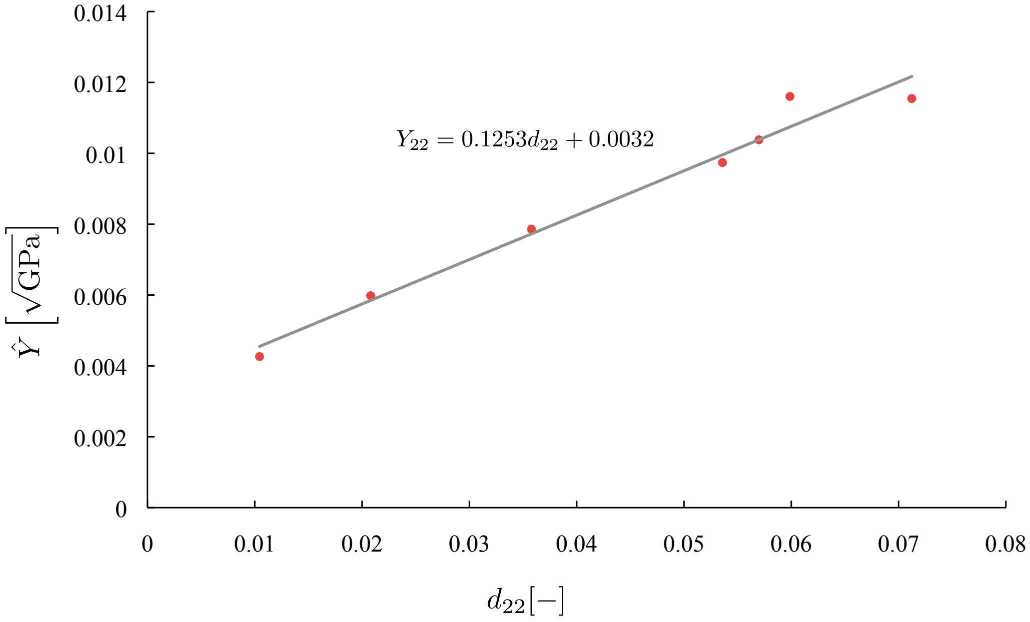

Figure 5.11: Best fit for transverse energetic threshold values.

5.2.1.2 Out-of-plane properties

In its basic form the model governing the out-of-plane behaviour follows a tri-linear curve as illustrated in figure 5.12. An initial curve with a linear slope allows the interface to withstand the load up to a defined stress level corresponding to the crack initiation. Thereafter the crack propagation behaviour of the model is governed by

Property	Unit	Value
Y_{22}^0	$\sqrt{\text{GPa}}$	3.2E-03
Y_{22}^C	$\sqrt{\text{GPa}}$	0.13
Y_{22}^U	$\sqrt{\text{GPa}}$	1.16E-02
b	–	8.07E-02

Table 5.7: Threshold values for transverse direction and coupling factor for transverse and shear damage from $[\pm 67.5°]_{2s}$ specimen.

a propagation stress and the numerical parameter NCYCLE. In total the model requires the input of ten parameters and follows the description provided in section 5.1.2. The critical energy release rates for mode I and II were calculated using a Microsoft Excel spreadsheet implementation of equations 3.1 and 3.4 introduced in section 3.3.2.

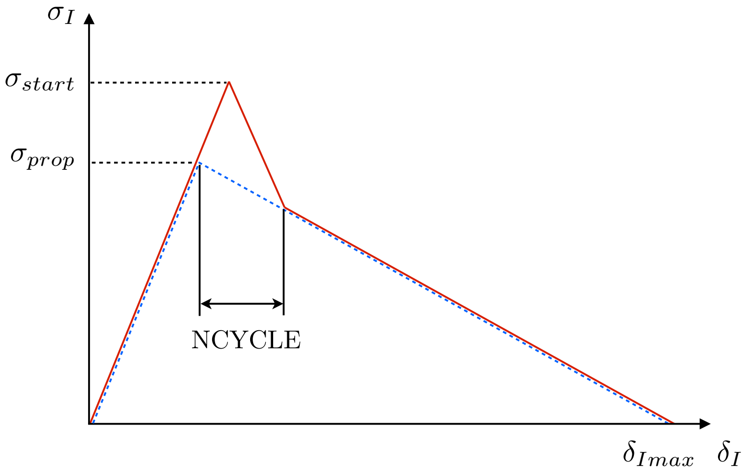

Figure 5.12: Optional schematic shape of the tied interface for mode I (Mode II analogous).

The contact thickness h_{cont} required to calculate the strains from the nodal displacement (see equation 6.1) is a FE model specific setting which requires knowledge of the geometrical distance between two linked bodies. In order to calculate the effective stresses in the normal and tangent direction (see equation 5.15) the out-of-plane model requires the undamaged moduli in the transverse and shear direction which are already identified in the characterisation of the in-plane properties. Four more material parameters are required, namely the start and propagation stress values for normal and shear for the two propagation modes respectively. The use of a tri-linear curve is appropriate for a variety of possible applications for this interface model. However, for a composite material on a macro-scale level the use of a bi-linear model provides sufficient accuracy. Therefore, the curve is shaped to follow a bi-linear behaviour. This is achieved by using identical initiation and propagation values. In general the parameter NCYCLE can be used to define the curve shape after crack initiation as shown in figure 5.12. However, this parameter is purely a FE solver specific property defined for numerical reasons. Hence a default value for this parameter was chosen.

It should also be noted that the stress values for crack initiation and propagation do not represent the true physical conditions as they would be present during DCB or ELS experiments. However, these values could have a physical meaning when the element size was in the magnitude of the crack influence zone. This could be the case when modelling on the micro-scale level. The accuracy of these values is of secondary importance [111, 210] as the energy based definition of the model relies on the surface area (see section 6.2.2). Nonetheless, values for the stress initiation and propagation were deduced from the transverse and shear response failure stress of the $[\pm 67.5°]_{2s}$ laminate. These values match with values presented in the literature [111, 211].

Table 5.8 lists the model parameters. Here the values for mode I and II fracture toughness were taken from DCB and ELS tests while the remaining are determined from in-plane experiments.

Property	Unit	Value
$\sigma_{start/prop}$	GPa	5.2E-02
G_I^u	$^{J}/_{mm^2}$	4.325E-04
$\tau_{start/prop}$	GPa	2.6E-02
G_{II}^u	$^{J}/_{mm^2}$	4.631E-04
h_{cont}	mm	0.1375

Table 5.8: Parameter overview for tied interface from single experiment.

5.2.2 Improved identification method using a gradient-based error minimisation procedure

The identification of model parameters given a set of experimental data is a classic inverse problem. Inverse problems, such as this parameter identification, are very often ill-posed. Generally ill-posed problems violate the postulates of Hadamard [212] which define well-posed problems. Three conditions characterise well-posed problems, namely that (a) a solution exists, (b) the solution is unique and (c) the solution depends continuously on the experimental data.

In the case of the parameter estimation for the composite damage models the postulate for a unique solution is violated. An alternative method to identify the parameters for the in and out-of-plane material models was developed here. The

concept of this method is based on an error minimisation approach where the model response is fitted against the experimental data by varying the model parameters. The material model was implemented in a Microsoft Excel environment via Visual Basic for Applications (VBA) to achieve this (see appendix B).
Experimental data is supplied as pairs of strain and stress values. The strain time series acts as an input for the material model, while the stresses computed are used to calculate the error between experimental data and model response. The following error function was used in order to estimate the model parameters.

$$Err_{acc} = \sum_{i}^{n} \left| \sigma_i^{exp} - \sigma_i^{mod} \right| \tag{5.49}$$

The error function sums the absolute differences between model results $\left(\sigma_i^{mod}\right)$ and experimental data (σ_i^{exp}) for a specific strain in a similar fashion as presented in [213]. The parameters in the solution vector are then modified using the robust and well-documented Generalised Reduced Gradient Nonlinear Optimisation method available in Microsoft Excel [207] with the objective of minimising Err_{acc} for each material test. In the context of this work the initial solution vector was provided by the values obtained from the conventional parameter identification method. However, values provided in the literature for similar models could also be used as an initial guess.

5.2.2.1 Parameter results for in-plane material model

Five parameters govern the behaviour of the model under tensile loading. Besides the undamaged elastic modulus and the strain values for initiation and ultimate failure the value for ultimate damage were obtained. The results are presented in table 5.9.

Property	Unit	Value
E_{11}^{0t}	GPa	160.9
ε_i^{ft}	–	1.56E-02
ε_u^{ft}	–	1.57E-02
d_u^{ft}	–	0.99

Table 5.9: Material properties in the fibre direction for tensile loading.

The determination of the initial Poisson's ratio was not included in this solution as only the strain field in the 11-direction was used to generate the model response. The graphical representation of the model response and a comparison with the experiment for the reference laminate is illustrated in figure 5.13. The model response using the parameters obtained follows closely the experimental curve. Here the error was minimised by the solver and a value of 0.018 $^{\mathrm{GPa}}/_{\text{data point}}$ was obtained. Following the same approach the model parameters in the fibre direction under compressive loading were estimated as listed in table 5.10. The elastic modulus for compression and the correction parameter to address the non-linear behaviour due to fibre-crimp and micro-buckling are determined in addition to the parameters related to the failure behaviour. After the minimisation process an average error of 0.004 $^{\mathrm{GPa}}/_{\text{data point}}$ was obtained. Figure 5.14 illustrates the result of the fitting. As previously for the tensile direction the material model response follows the experimental data curve very closely.

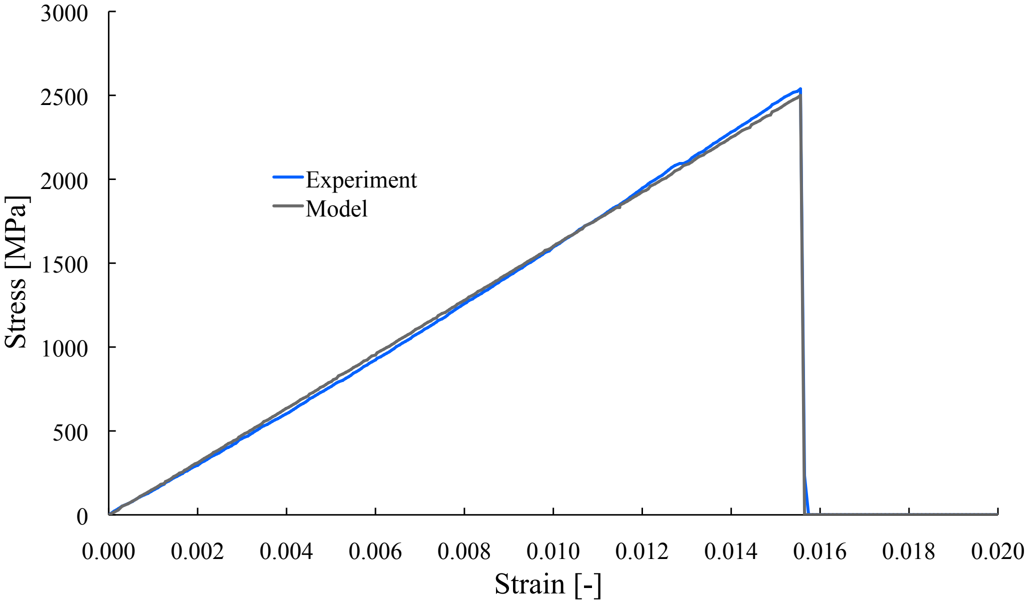

Figure 5.13: Material parameter fitting in the fibre direction under tension via gradient-based error minimisation using experimental data from reference laminate test 7.

Property	Unit	Value
E_{11}^{0c}	GPa	132.8
γ	–	7.59
ε_i^{fc}	–	9.36E-03
ε_u^{fc}	–	9.5E-03
d_u^{fc}	–	0.99

Table 5.10: Material properties in the fibre direction for compressive loading.

The fit for the parameters in shear and transverse direction involves the variation of a larger parameter set. Furthermore, the experimental data incorporates larger magnitudes of non-linearity. This is especially the case for the shear direction. The

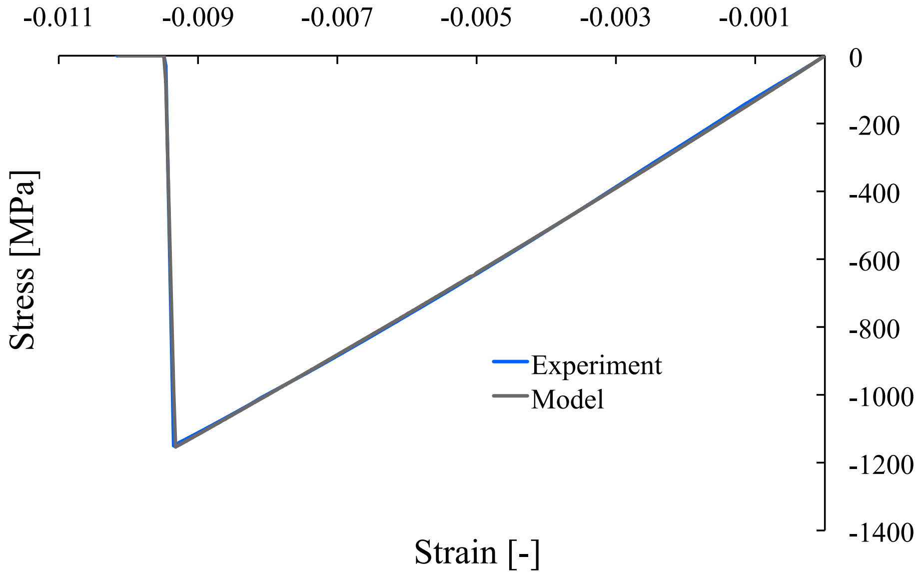

Figure 5.14: Fitting result from a gradient-based error minimisation for compressive fibre direction with experimental data from reference laminate experiment 5.

gradient-based minimisation method was applied to a single experimental shear data set in order to determine the parameters. The initial elastic modulus and the energetic threshold values for the damage evolution in shear and the parameters governing the inelastic behaviour are listed in table 5.11. The response using the identified parameter set is shown in figure 5.15. Here the value for the average accumulated error is 0.005 $^{\text{GPa}}/_{\text{data point}}$.

Property	Unit	Value
G_{12}^0	GPa	4.6
Y_{12}^0	$\sqrt{\text{GPa}}$	1E-8
Y_{12}^C	$\sqrt{\text{GPa}}$	7.62E-02
Y_{12}^U	$\sqrt{\text{GPa}}$	4.27E-02
d_{max}	–	0.41
R_0	GPa	1.E-8
β	–	0.37
m	–	0.35

Table 5.11: Model parameters for the shear direction determined using the gradient-based solving method.

The experimental data of a single cyclic experiment performed on a $[90°]_8$ coupon is used in the error minimisation method. Tests in the transverse direction provide the values for the initial transverse modulus and the energetic threshold values defining the damage behaviour in transverse direction. Figure 5.16 shows the plots of experimental data and the transverse model response using the set of parameters shown in table 5.12. Here a very good agreement was achieved yielding to a final

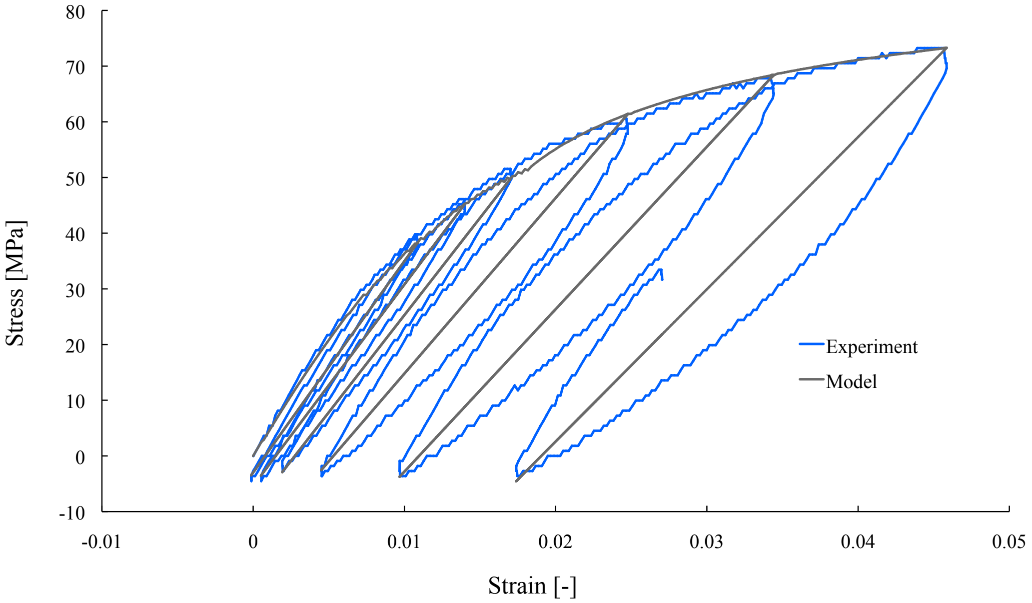

Figure 5.15: Fit of shear response from reference material test 4 obtained using the gradient-based minimisation method.

Property	Unit	Value
E_{22}^{0}	GPa	9.45
Y_{22}^{0}	$\sqrt{\text{GPa}}$	5.32E-03
Y_{22}^{C}	$\sqrt{\text{GPa}}$	0.159
Y_{22}^{U}	$\sqrt{\text{GPa}}$	2.59E-02
b	–	1.49
A	–	0.33

Table 5.12: Parameters set obtained from single transverse experiment via gradient-based solving method.

value for the averaged accumulated error of 0.0004 $^{\text{GPa}}/_{\text{data point}}$.

However, with the current implementation error minimisation method the two coupling parameters for transverse and shear direction b and A show hardly any sensitivity as the transverse and shear responses are observed independently. Thus, the implementation needs to be modified so that the shear and transverse direction are coupled explicitly. Furthermore the use of shear and transverse responses obtained from experiments on $[+45°]_8$ and $[\pm 67.5°]_{2s}$ coupons can be used for this purpose.

5.2.2.2 Parameter sensitivity analysis

The behaviour of a model will depend critically on dominant parameters while other parameters only have a weak influence. A sampling-based sensitivity analysis [145, 214] was carried out for the material model shown for the single shear experiment which is used throughout this work to demonstrate the different parameter

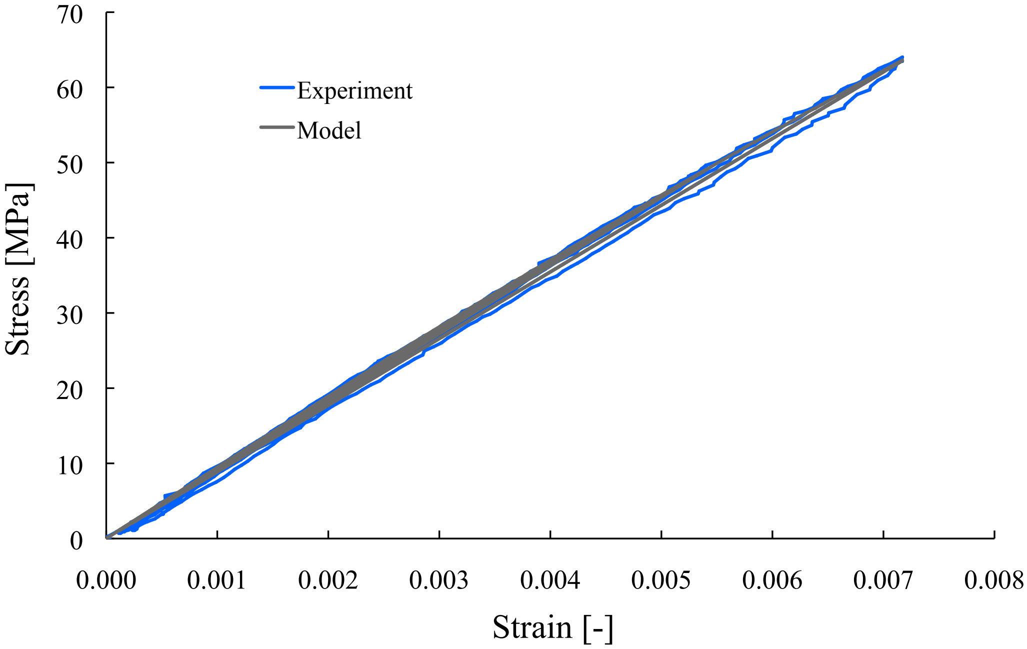

Figure 5.16: Fit of transverse response from reference material test 3 obtained using the gradient-based minimisation method.

identification methods. Furthermore the information obtained from a sensitivity analysis can also be used to define bounds for parameter estimation. In this approach the model is executed repeatedly for each parameter value while the output in form of the error function defined in equation 5.49 is monitored. The generated output is then used to assess the sensitivity of a parameter. Thereby parameters with high sensitivity are expected to have narrow error bounds whilst parameters with very low sensitivity are expected to have large error bounds in respect to parameter estimation. The dependence of input and output can be quantified by the normalised parameter sensitivity [215]. This is defined as the change in the output of the model for a given fractional change in each parameter.

$$Sens = \frac{\dfrac{\Delta Err_{acc}}{Err_{acc}\left(\Theta_{prior}\right)}}{\dfrac{\Delta\Theta}{\Theta_{prior}}} \tag{5.50}$$

Here the numerator is the normalised change in the output using the error function defined in 5.49 whilst the denominator is the normalised change of a parameter value Θ relative to its prior value. However higher parameter sensitivity does not necessarily lead to better parameter estimates as parameter sensitivity does not take into account the correlation between parameters which can influence parameter estimation drastically.

Exemplary figures 5.17 and 5.18 illustrate the resulting plots of the sensitivity for the undamaged shear modulus and the initial yield stress as an evolution plot for the parameter change. The flatter the slope of the evolution plot of $Sens$ at the location of the prior the lower the sensitivity to a parameter is whilst a steeper gradient indicates a higher sensitivity. The plot of the undamaged shear modulus illustrated in figure 5.17 indicates that this parameter is of higher sensitivity. On the other hand the results for the initial yield stress shown in figure 5.18 suggest a lower parameter sensitivity.

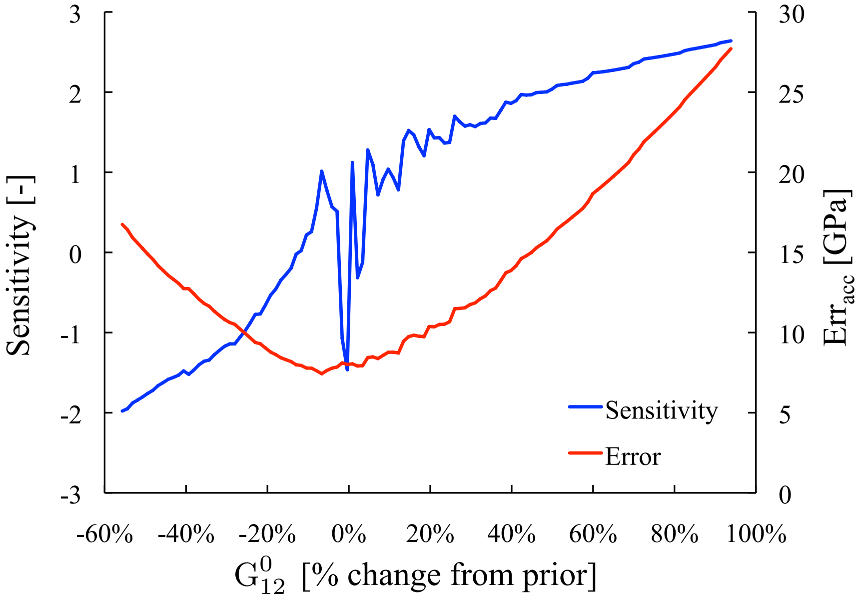

Figure 5.17: Sensitivity and error plot for undamaged shear modulus G^0_{12}

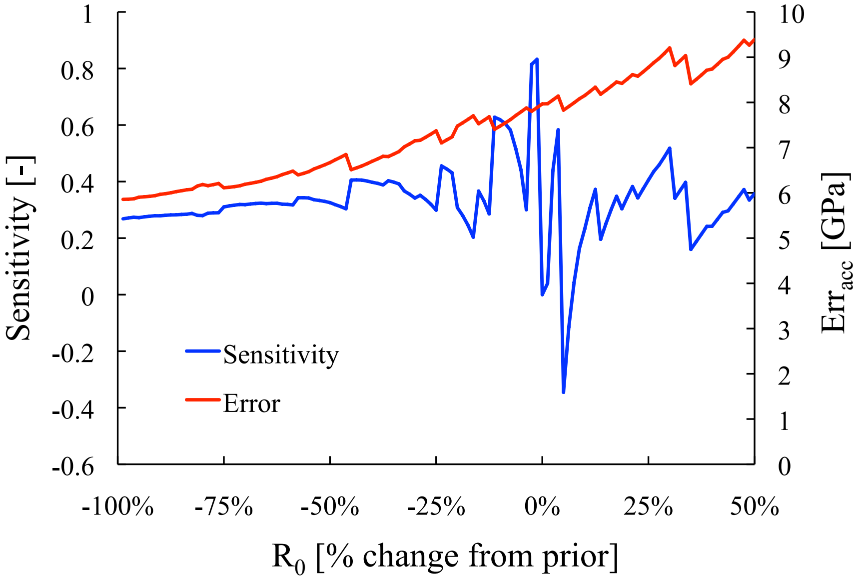

Figure 5.18: Sensitivity and error plot for initial yield stress R_0.

A simple method of determining the parameter sensitivity is to calculate the output percent difference when varying one input parameter from its minimum value to its maximum value in the form of the sensitivity index (SI) [215].

$$SI = \frac{Err_{acc}^{max} - Err_{acc}^{min}}{Err_{acc}^{max}} \tag{5.51}$$

The results of the sensitivity analysis are enlisted in table 5.13 and show the parameters related to the shear response of the material model. Here the initial shear damage threshold value Y_{12}^{0} shows very little sensitivity while the variation of the ultimate shear damage limit Y_{12}^{U} and the initial yield stress R_0 show moderate sensitivity. The remaining parameters correspond to high sensitivity. In addition to the normalised parameter sensitivity and the sensitivity index, scatter plots were generated to obtain an understanding of how the model response varies as a function of different parameter input values.

Property	Unit	Prior	SI	Sens at -20%	Sens at 20%
G_{12}^{0}	GPa	4.64	73%	-0.66	1.53
d_{max}	–	0.411	80%	-1.97	-0.25
Y_{12}^{0}	$\sqrt{\text{GPa}}$	1.0E-08	1.1E-14%	5.45E-7	5.45E-7
Y_{12}^{C}	$\sqrt{\text{GPa}}$	7.62E-02	71%	0.47	1.88
Y_{12}^{U}	$\sqrt{\text{GPa}}$	4.27E-02	17%	-1.67E-15	1.67E-15
R_0	GPa	2E-02	38%	0.31	0.34
β	–	0.37	81%	1.35	2.51
m	–	0.35	82%	-3.77	-1.4

Table 5.13: Results for sensitivity analysis enlisted for each parameter.

Figure 5.19 shows a scatter plot of the resulting error value for a given pair of the ultimate damage threshold Y_{12}^{U} and the initial yield stress R_0. Here a global minimum can be found for lower values of R_0 and higher values of Y_{12}^{0}. Hence the importance of the search constraints, especially for R_0, is shown as the gradient-based method tends to minimise the error towards the global minimum while this would lead to a physically unrealistic result. Figure 5.20 illustrates the error surface for the parameter couple β and m which are used to define the shape of the power law controlling the evolution of the yield stress. The plot shows a narrow band of possible parameter couples.

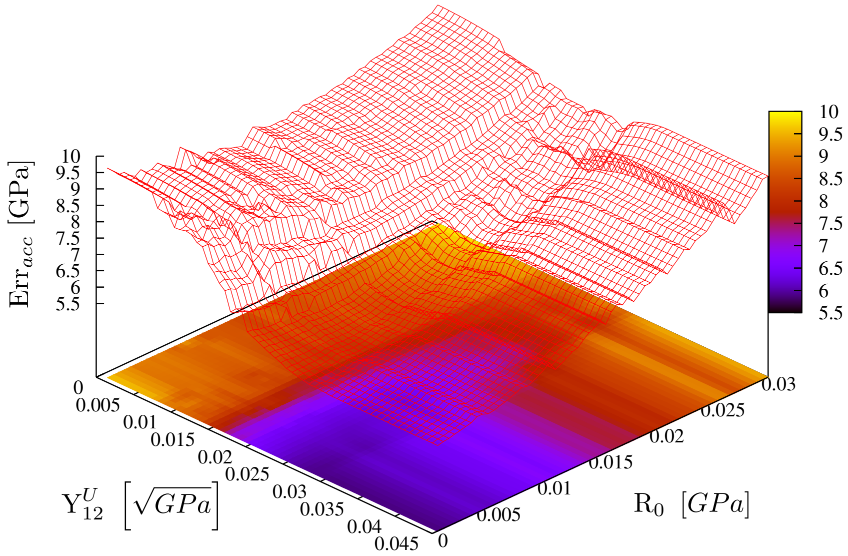

Figure 5.19: Scatter plot of error output for ultimate shear damage limit versus initial yield stress.

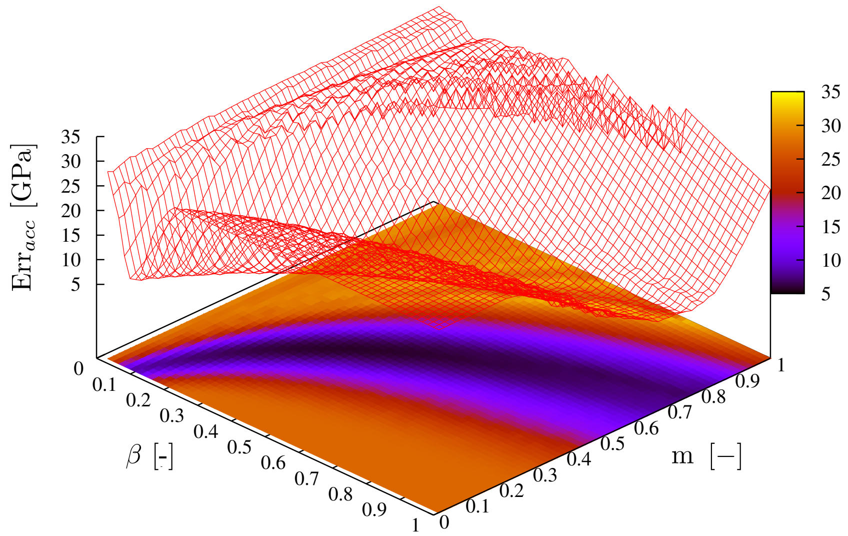

Figure 5.20: Scatter plot of error output depending on yield stress evolution parameters.

5.2.2.3 Model stability

As the material model was implemented via a forward difference scheme it relies on a critical step size. To identify this critical step size the original set of experimental data points was gradually reduced resulting in a larger step size and the influence on the response was investigated. Besides finding the critical step size, results of this study can also be used to minimise the amount of data points while guaranteeing that the model is able to calculate an accurate response, leading to an improvement in model runtime.

The stability test was undertaken on the same data sets used for the parameter identification. The number of data points was halved each time and the reduced strain time series were used as an input for the material model.

A very stable model behaviour was found for the fibre and transverse direction. For the fibre direction under tension and compression the original number of data points recorded during the test was 244 and 397 respectively, while the cyclic transverse experiment contained 981 points. The average strain increment for the initial tension, compression and transverse data set was 1E-04, 1E-05 and 1E-05 respectively. All tests underwent five reduction cycles while the stability of the model was still maintained. However, it should be noted that the nature of these tests is dominated by a linear behaviour; this is especially the case for the fibre direction. In shear however, the model is exposed to a extended non-linear behaviour. Similarly to the studies for the other directions the data points were reduced up to five times, starting from an average strain increment of 2E-04 and halving the number of data points during each cycle. From the results shown in figure 5.21 it is evident that the model is still able to simulate an adequate response after the third reduction process using only one eighth of the original data points (172 vs. 1375). However, the model shows the first signs of instability after the next iteration, the model response differs significantly in comparison to the original set. The discrepancy between model and experiment are manifested at the turning points of the unloading and loading cycles where the gradient changes within a very small data range.

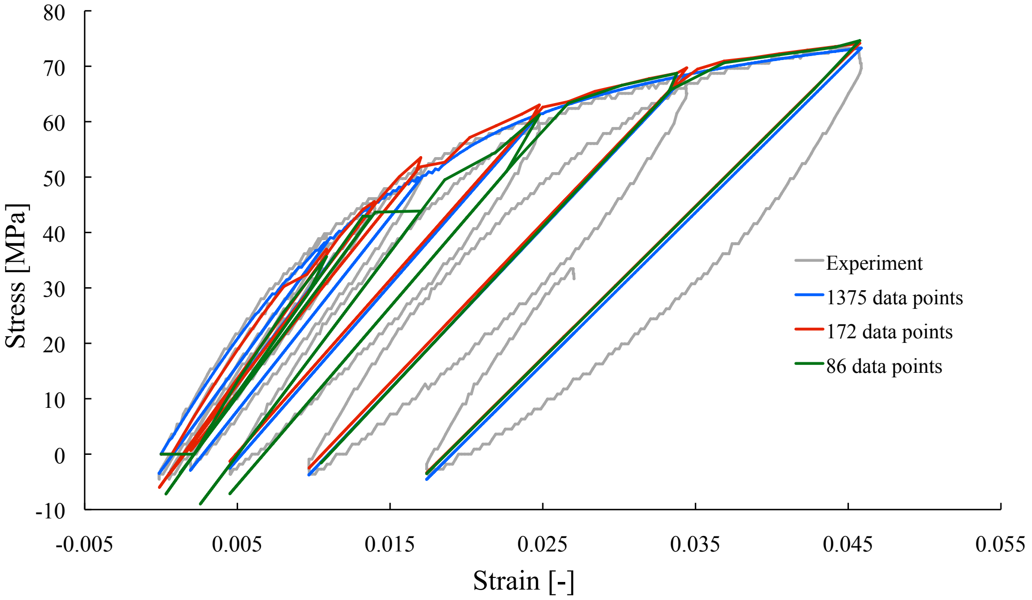

Figure 5.21: Illustration of the material model response for shear in dependency of the strain step size.

5.2.2.4 Results for out-of-plane parameters

In-plane experiments provide strain-stress pairs which are directly used to calculate the model response and error. In contrast, delamination experiments are given in a triple format of toughness versus crack length and cross head displacement. The experimental information needs to be translated to estimate the values for the stresses for crack propagation and the toughness in mode I and II respectively for the cohesive material model (see also equations 6.1 and 6.2). Equations 5.52 and 5.53, based on beam theory, are used to calculate the sliding crack opening displacement relative to the initial crack length for mode I and II respectively [216]:

$$\Delta_I = \frac{3d}{a^3}\left[\frac{a\left(a-a_0\right)^2}{2} - \frac{\left(a-a_0\right)^3}{6}\right] \tag{5.52}$$

$$\Delta_{II} = \frac{2da^3h}{3a^3+L^3}\left[\frac{3}{a} - \frac{3a_0^2}{a^3}\right] \tag{5.53}$$

Here d is the cross head displacement and a the crack length from the experimental data sets. The initial crack length is given by a_0 , h is the specimen half thickness and L the length of the specimen.

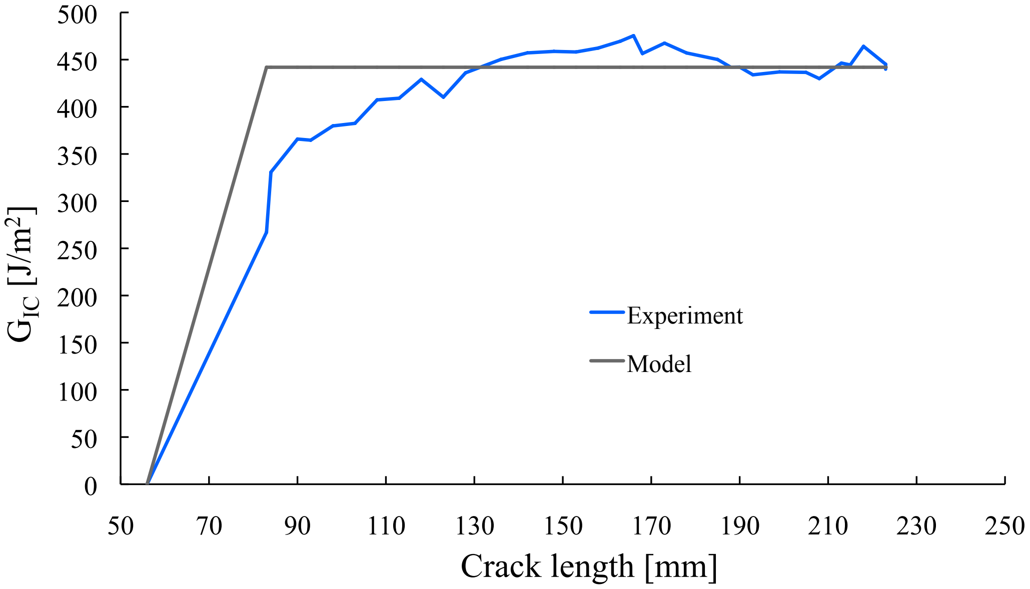

Figure 5.22: Result from parameter estimation via gradient-based method for mode I.

The strains in the normal and transverse directions are calculated by dividing the sliding opening displacements for mode I and II by the contact thickness h_{cont}. For a shell based finite element model the value for h_{cont} can be approximated as the virtual element thickness when using equally thick pairs of elements.

The accumulated error between the toughness data of experiment and the model response was minimised using the gradient-based method. The parameters, which are modified by the gradient-based solver are the propagation stresses as well as the energy release rates for mode I and II. Further parameters such as the interface thickness and the undamaged transverse and shear moduli are additional necessary inputs for the cohesive material model. The interface thickness is a finite element model specific value (in this example $h_{cont} = 0.1375$), while the moduli in the transverse and shear directions were already determined for the in-plane model. These parameter values are reported in tables 5.12 and 5.11.

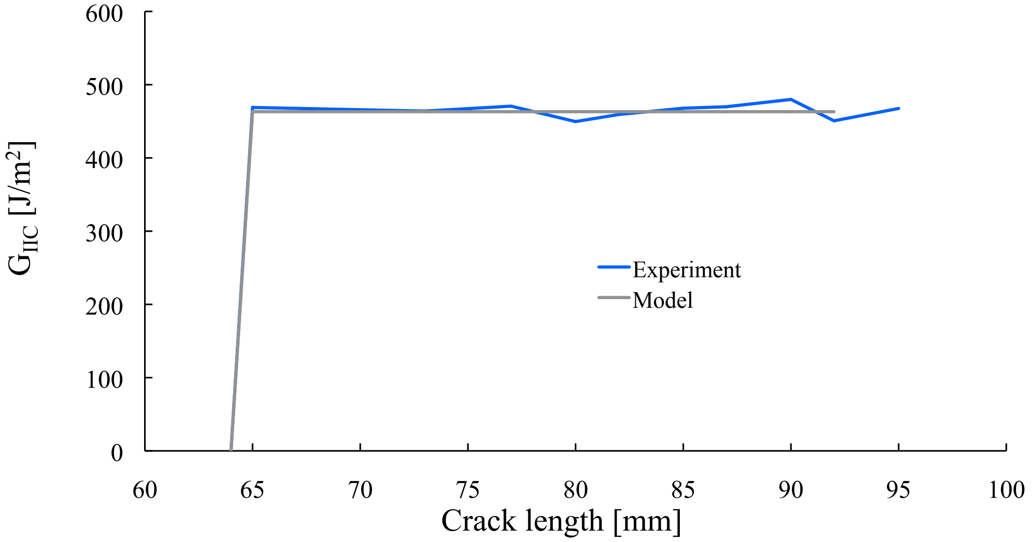

Figure 5.23: Results of parameter estimation via the gradient-based method for mode II.

The initiation values for the unknown parameters were taken from the conventional parameter identification method as listed in table 5.8. Figures 5.22 and 5.23 illustrate the results from the parameter estimation method using the gradient-based error minimisation method. The fit for mode I shows close agreement with the experimental data where a constant value for the mode I fracture toughness is determined as the best fit with the whole data series.

Property	Unit	Value
$\sigma_{start/prop}$	GPa	0.15
G_I^u	J/mm²	4.412E-04
$\tau_{start/prop}$	GPa	0.025
G_{II}^u	J/mm²	4.653E-04

Table 5.14: Parameter overview for tied interface.

The fitting of the mode II fracture toughness shows excellent agreement with the data set. Here it is also evident that the mode II data set is more uniform and is represented well by the constant fracture toughness value. The resulting parameters are listed in table 5.14. The sum of errors after the solution vector was identified were 1.0E-03 $^{\mathrm{J}}/_{\mathrm{mm}^2}$ and 7.2E-05 $^{\mathrm{J}}/_{\mathrm{mm}^2}$ for mode I and II respectively.

5.2.3 Enhanced identification method

An alternative to the methods previously described is provided by the Markov Chain Monte Carlo technique (see section 2.2.2). A variety of MCMC algorithms exists and can be tailored to solve a range of problems. This techniques utilises the concept of conditional probabilities with respect to experimental data and theoretical data generated by a model. By iteratively varying material parameters to generate different theoretical data and comparing the outcome to the experiment, the algorithm is capable of producing probability density functions for each parameter which converge to the target distribution. The approximation of the target distribution is improved during the runtime of the algorithm. In this work the Random walk Metropolis-Hastings algorithm (see section 2.2) is used to infer the in-plane and out-of-plane parameters for the material models described in section 5.1.

5.2.3.1 General implementation of the Random walk Metropolis-Hastings algorithm

This section describes the general implementation of the Random walk Metropolis-Hastings algorithm as it is used in the context of this work. The complete code for the VBA and C++ implementations is attached in appendix B and C.

Choice of prior, proposal calculation and use of transformations

Finding appropriate initial values is often a problem when applying the MCMC method, however, as discussed in [166] there are many valid approaches. On one hand values for a prior distribution can be determined from simpler models or can be chosen from an acceptable data range. For many parameters in the constitutive material model used in this work, such as the elastic moduli, a certain choice for the initial values can be made easily.

With respect to model efficiency and accuracy it can be useful to apply transformation rules to the distributions; this can lead to a reduction in computation time by factor of 10 to 40 [166, 217]. The natural logarithm of the parameter was used in the implemented algorithm, which leads to numerical improvements when calculating the likelihood and prior distributions as described in [154, 218, 219].

Symmetric proposal distributions are used for the random walk. Therefore the proposed parameter set for each iteration can be determined using a noise term ε^j

which is applied to the prior parameter set as follows:

$$\Theta_i^j = \Theta_{i-1}^j + \varepsilon^j \quad \text{with} \quad \varepsilon^j \sim N\left(0, \sigma_{\varepsilon^j}\right) \tag{5.54}$$

Here the random noise value is drawn from a normal distribution with a mean value of 0 and a standard deviation σ_{ε^j} corresponding to each parameter.

Calculation of the acceptance probability

As part of the Metropolis-Hastings algorithm it is necessary to determine the posterior distribution for the acceptance probability. Following Bayes' theorem the posterior distribution can be calculated as follows (see also equation 2.34):

$$p\left(F\left(\Theta\right)|Y\right) = \frac{p\left(Y|F\left(\Theta\right)\right) \cdot p\left(\Theta\right)}{p\left(Y\right)} \tag{5.55}$$

Here $p\left(F\left(\Theta\right)|Y\right)$ is the posterior, $p\left(Y|F\left(\Theta\right)\right)$ the likelihood and $p\left(\Theta\right)$ the prior distribution. As the marginal distribution $p\left(Y\right)$ acts only as a scaling factor the expression can be rewritten, describing a proportionality relation of the posterior on the likelihood and prior (see also equation 2.35)

$$p\left(F\left(\Theta\right)|Y\right) \propto p\left(Y|F\left(\Theta\right)\right) \cdot p\left(\Theta\right) \tag{5.56}$$

As shown in this expression it is possible to calculate the acceptance probability on the basis of the likelihood and prior using the logarithmic values of Θ_i and Θ_{i-1} for each iteration i:

$$\alpha = \min\left\{1, \frac{p\left(Y|F\left(\exp\left\{\Theta_i\right\}\right)\right) \cdot p\left(\Theta_i\right)}{p\left(Y|F\left(\exp\left\{\Theta_{i-1}\right\}\right)\right) \cdot p\left(\Theta_{i-1}\right)}\right\} \tag{5.57}$$

In this context Y represents the stress values obtained from experiments while $F\left(\exp\Theta\right)$ is the material model response using the transformed parameters.

The joint likelihood is computed from the experimental and theoretical data points. In the case of the in-plane model the strain field is used as an input to generate the stress response of the material model, while the out-of-plane model uses the crack length to compute the energy release rate values. Thus, the exact number of data points are generated and employed as follows:

$$\begin{aligned} p\left(Y|F\left(\exp\Theta\right)\right) &= \prod_{k=1}^{l} p\left(Y_k|F_k\left(\exp\left\{\Theta\right\}\right)\right) \\ &= \prod_{k=1}^{l} N\left(Y_k; F_k\left(\exp\left\{\Theta\right\}, \sigma\right)\right) \\ &= \sum_{k=1}^{l} \ln\left\{N\left(Y_k; F\left(\exp\left\{\Theta\right\}, \sigma\right)\right)\right\} \end{aligned} \tag{5.58}$$

The joint likelihood incorporates all the distributions which are calculated with the experimental data point Y_k using a normal distribution with the theoretical value $F_k\left(\exp\left\{\Theta\right\}\right)$ as mean and a standard deviation σ. The likelihood can be interpreted as a Gaussian error function (see also figure 5.27). The standard deviation is one of the MCMC tuning parameters and needs to be adjusted appropriately.

The joint prior is calculated in a similar fashion. A choice for an appropriate distribution describing the parameter best is often difficult to select, thus a generic choice is given by applying a normal distribution [220, 221].

$$\begin{aligned} p\left(\Theta\right) &= \prod_{m=1}^{n} N\left(\Theta^m; 0, \sigma_{\Theta^m}\right) \\ &= \sum_{m=1}^{n} \ln\left\{N\left(\Theta^m; 0, \sigma_{\Theta^m}\right)\right\} \end{aligned} \tag{5.59}$$

Similarly to the likelihood, the standard deviations σ_{Θ^j} act as tuning parameters for the algorithm and need to be selected for each parameter. Again the logarithm was employed to take advantage of the simplification while maintaining accuracy of the expression. With the applied logarithmic transformation the acceptance probability can be computed as the sum of the joint likelihoods and priors. Thereafter the exponential function is applied to the calculated sum which yields the following expression:

$$\alpha = \min\left\{1, \exp\left\{p\left(Y|F\left(\exp\left\{\Theta_i\right\}\right)\right) + p\left(\Theta_i\right) - p\left(Y|F\left(\exp\left\{\Theta_{i-1}\right\}\right)\right) - p\left(\Theta_{i-1}\right)\right\}\right\} \tag{5.60}$$

MCMC tuning

In the MCMC algorithm the standard deviations operate as tuning parameters and need to be adjusted accordingly. When using the Random walk Metropolis-Hastings algorithm, three categories of standard deviations are employed:

1. The standard deviation σ used in the likelihood term is assigned with a rel-

atively small value as this parameter assesses the quality of the theoretical response [219].

2. The value for the standard deviation used in the computation of the prior distribution σ_{Θ^j} is set to a large value. In literature this approach is referred as informal prior distribution [166, 222]. By assigning a larger value the algorithm is able to explore a larger parameter region.

3. The standard deviations σ_{ε^j} allows to limit or increase the noise level ε^j which determines the sampling behaviour of a sequence [163, 223].

The choice of these standard deviations affects the acceptance probability. The algorithm should be tuned based on the empirical studies so that an acceptance probability of around 25% for a high-dimensional model and 50% for models of one or two dimensions is reached [163]. However, for heavily correlated target densities the optimal acceptance probability for high-dimensional models can be very different[224]. Furthermore, it is rarely a sensible idea to fine tune the algorithm too carefully since good mixing behaviour can be achieved from algorithms with acceptance probabilities in the range of 15-50% [225]. Therefore, any tuning process should be carried out as a pilot sample analysis only. As a result, any efficiency gain from excessive fine-tuning is usually lost in the time spent carrying out pilot studies [224].

For a manually controlled Random walk Metropolis-Hastings algorithm, a useful approach is to fix the values for σ and σ_Θ and start with a large value for σ_{ε^j}, approximately $^1/_{10}$ of the prior uncertainty of that parameter [143]. A number of short sequences are generated by varying one value of σ_ε at a time. If the acceptance probability is too high the MCMC sampling behaviour is too conservative (value for σ_{ε^j} is too small) and the chain is limited to an unrepresentative region of the parameter space failing to explore the full space. Hence, increasing the standard deviation allows the sequence to explore a larger region of the parameter space. On the contrary, if the acceptance probability is too low the sampling behaviour is too vigorous and unable to identify a modal region.

5.2.3.2 Single parameter implementation

For initial investigations the Random walk Metropolis-Hastings algorithm was implemented and tested using a simple model with only one parameter. Therefore Hooke's law with

$$\sigma = E\varepsilon \tag{5.61}$$

was chosen where the elastic modulus is the only model parameter required to generate a material model response. Data points from a linear stress-strain curve were used for the simulation. The strain series acts as an input to generate the stress response of the constitutive law. Hence two stress values, from model and experiment, correspond to a given strain value.

At first the algorithm was implemented in R [226], a free software environment for statistical computing. Thus, a second implementation in Microsoft Excel could be easily verified and validated. The implementation path via Microsoft Excel was chosen as the material models presented in 5.1 were available through VBA as part of the gradient-based solution development (see section 5.2.2).

A single chain was set up to run for 1000 iterations starting from an initial value of 6 GPa. The standard deviation for the likelihood distribution defining the Gaussian error between experimental and theoretical value was set to 0.005 GPa. In order to induce an informal prior distribution a standard deviation of 10 GPa was chosen for the applied noise level. A number of short sequences were simulated to tune the standard deviation for the sample noise level. An acceptance probability of 48% was achieved using a standard deviation of 1.3 GPa.

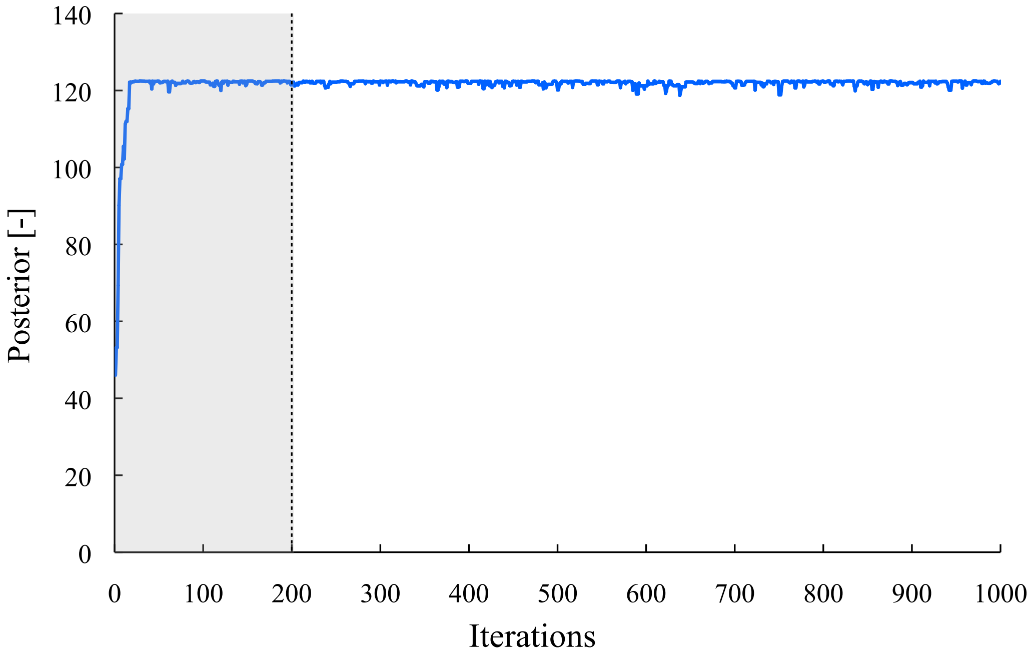

Figure 5.24: Convergence assessment via posterior distribution plot for a single parameter problem.

When dealing with a problem that is aimed to infer one or two parameters a simple solution to assess the convergence of the chain is to observe the evolution of the posterior distribution [165]. Figure 5.24 shows the evolution of the posterior. Here the first 200 iterations are highlighted to indicate the burn-in region. This region defines the region of disregarded data points due to initial mode finding. In fact the algorithm is able to find a mode after just 17 iterations, hence the burn-in zone is rather over-sized and could be reduced for runtime optimisation purposes.

By observing figure 5.24 carefully it becomes clear how this algorithm works. The algorithm tries to maximise the value for the posterior density but allows reduction steps occasionally in order to extend the sample range [227]. The sampling behaviour of the chain can be observed by plotting the parameter evolution (see figure 5.25). Again disregarded values within the burn-in zone are highlighted in this plot. Starting from the initial value of 6 GPa the chain is quickly able to generate samples which lead to the maximisation of the posterior. Due to the nature of the Random walk Metropolis-Hastings algorithm the values within the stationary sequence are highly correlated. With the aid of the auto-correlation function (ACF) in R the step size for thinning the sequence can be determined. Consequently the resulting sample vector contains uncorrelated values which were gathered from the stationary sequence and were used to determine the parameter value [228, 229].

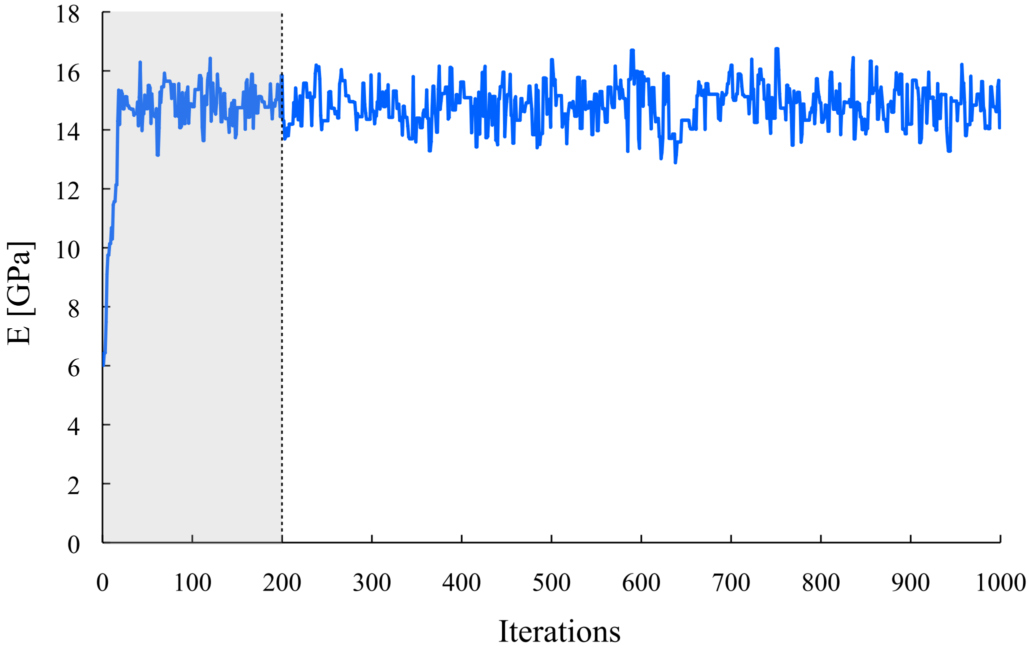

Figure 5.25: Sampling behaviour for a single chain parameter inference.

Here, the sequence ended with an acceptance ratio of 49% and was thinned by using every tenth value. The elastic modulus is then computed as the posterior mean value using the data from the thinned chain and results in 14.8±1 GPa. Sometimes, it is advisable to use the posterior median with the 95% confidence region instead of the mean value and standard deviation to disregard outliers [157]. Here a median value of 14.9±1 GPa was obtained. For the in- and out-of-plane model used in the subsequent sections it was shown that the use of the median value leads to more reliable results. In addition the data generated from the thinned sequence can be used to plot the probability density for the parameter as shown in figure 5.26.

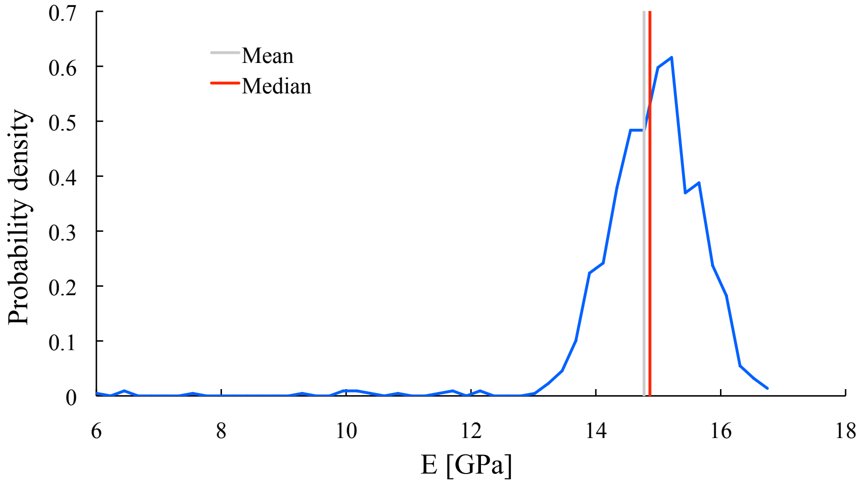

Figure 5.26: Probability density plot for the single parameter problem.

Figure 5.27 illustrates the material model response using the identified elastic modulus. Furthermore, this illustration incorporates a schematic graphical representation of the likelihood function which evaluates the error between experimental data and model response. The model is able to generate a reasonable response that is in agreement with the experimental data.

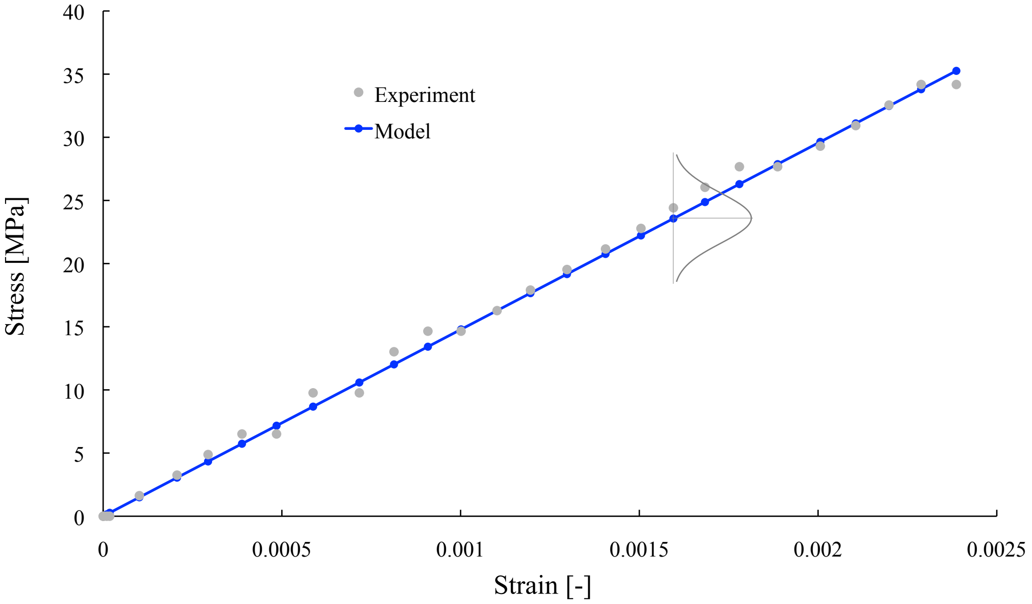

Figure 5.27: Data fitting result for a linear problem using MCMC.

5.2.3.3 Multiple parameter implementation

A total of 32 parameters need to be provided for the material models described in section 5.1. However, the strain rate parameters D_{11}, D_{11}^{R}, D_{22}, D_{12}, D_R can be excluded from the parameter estimation due to the quasi-static conditions that were applied during testing. Hence, the parameter set is reduced to a total of 27 parameters. For the identification of these parameters via the MCMC method the available implementation of the material models from the gradient-based solver approach was used. Hence the above MCMC implementation via VBA for a single parameter was modified and the constitutive model was replaced.

Similarly to the single parameter implementation, a single chain is used to generate the data. However, with an increasing number of parameters it becomes more difficult to assess the convergence of a chain [166]. Furthermore, a single chain might get trapped in a local optimum similarly to a gradient-based minimisation method. Hence it is difficult to decide whether the results obtained can actually represent the target distribution when relying only on the evolution of the posterior distribution and the acceptance ratio. The implementation of other convergence assessment methods in the VBA environment showed to be cumbersome.

A further drawback of the VBA implementation was the CPU runtime. In an attempt to reduce the duration of the MCMC simulation the amount of data points was reduced in conjunction with the results from the model stability investigation presented in section 5.2.2.3. Furthermore, the automatic screen update option in Excel was disabled for the duration of the simulation and the chain output was reduced by writing out every tenth value. However, a significant reduction of CPU runtime was not achieved. The average duration of a simulation with a single chain of 1,000,000 iterations was 112 hrs : 40 min [1].

To overcome these problems and to allow more flexibility for further extensions to the algorithm such as automated convergence assessment, use of multiple chains and parallel tempering the algorithm was implemented in C++. The algorithm was verified with the help of the VBA implementation. While using the same algorithm, experimental data sets and tuning setup the CPU runtime was reduced to an average of 2 hrs : 30 min[2].

When dealing with a large set of parameters it is recommended to run multiple chains, that eventually explore different or larger regions of the parameter space. Thereafter the results of the simulation are deduced using the data generated from

---

[1] Using VBA and Excel 2003 on a 32 bit architecture with a 3.4 GHz Intel Pentium D processor and 3.25 GB RAM.

[2] Compiled with GCC4.2 for x86_64 architecture, running on a 2.4 GHz Intel Core 2 Duo processor with 4 GB RAM.

all chains. The advantage of multiple chains can also be employed in a different way. Instead of running a single chain for a large number of iterations, shorter chains can run in parallel [166]. However, supporters of the single chain approach argue that samples drawn from a longer chain are likely to be closer to the target distribution [165].

Property	Unit	Apriori 1	Apriori 2	Apriori 3	Apriori 4
E_{11}^{0c}	GPa	128.9	128.8	128.9	128.6
E_{11}^{0t}	GPa	159.9	159.6	159.2	159.1
γ	–	0.1485	0.1499	0.1491	0.1485
ε_i^{fc}	–	9.32E-03	9.36E-03	9.46E-03	9.33E-03
ε_u^{fc}	–	9.54E-03	9.72E-03	9.74E-03	9.68E-03
ε_i^{ft}	–	1.56E-02	1.55E-02	1.55E-02	1.55E-02
ε_u^{ft}	–	1.57E-02	1.58E-02	1.58E-02	1.58E-02
d_u^{fc}	–	0.94	0.96	0.96	0.97
d_u^{ft}	–	0.95	0.96	0.95	0.96
E_{22}^{0}	GPa	9.47	9.56	9.49	9.48
G_{12}^{0}	GPa	4.55	4.54	4.57	4.56
b	–	8.1E-02	8.3E-02	8.1E-02	8.2E-02
Y_{22}^{0}	$\sqrt{\text{GPa}}$	5.35E-03	5.41E-03	5.39E-03	5.28E-03
Y_{12}^{0}	$\sqrt{\text{GPa}}$	9.93E-09	9.93E-09	9.91E-09	9.93E-09
Y_{22}^{C}	$\sqrt{\text{GPa}}$	0.159	0.161	0.159	0.161
Y_{12}^{C}	$\sqrt{\text{GPa}}$	9.92E-02	9.93E-02	9.96E-02	9.99E-02
Y_{22}^{U}	$\sqrt{\text{GPa}}$	2.55E-02	2.53E-02	2.64E-02	2.62E-02
Y_{12}^{U}	$\sqrt{\text{GPa}}$	4.39E-02	4.35E-02	4.23E-02	4.27E-02
d_{max}	–	0.402	0.407	0.412	0.409
A	–	6.4E-02	6.2E-02	6.1E-02	6.3E-02
R_0	GPa	2.18E-02	2.24E-02	2.23E-02	2.17E-02
β	–	0.391	0.385	0.388	0.392
m	–	0.352	0.357	0.355	0.352
G_I^u	$^{\mathrm{J}}/_{\mathrm{mm}^2}$	4.27E-04	4.29E-04	4.32E-04	4.33E-04
$\sigma_{start/prop}$	GPa	8.06E-03	8.15E-03	8.09E-03	7.94E-03
G_{II}^u	$^{\mathrm{J}}/_{\mathrm{mm}^2}$	4.58E-04	4.61E-04	4.62E-04	4.59E-04
$\tau_{start/prop}$	GPa	2.47E-02	2.52E-02	2.50E-02	2.52E-02

Table 5.15: Initial vectors for the sequences.

Besides, the potential advantage of reducing the number of iterations, multiple chains also allow the application of convergence assessment criteria. A variety of convergence criteria for MCMC simulations are freely available as outcome of open source projects or are straightforward to implement. However, the assessment tools provided are often algorithm specific and imply further assumptions. In general it is difficult to declare the convergence of a MCMC simulation hence a combination of different methods is recommended [165]. The method presented in [168] was used in this work (see also section 2.2.2.2). This method takes advantage of multiple chains and calculates an estimated posterior variance for each parameter. These values are computed from the between-chain and within-chain variances after each iteration. In addition to the posterior variance, the evolution plots of the posterior distribution and the parameters were inspected.

Property	Unit	Std. Dev. 1	Std. Dev 2	Std. Dev. 3	Std. Dev. 4
E_{11}^{0c}	GPa	0.01	0.01	0.01	0.1
E_{11}^{0t}	GPa	7E-03	7E-03	7E-03	7E-03
γ	–	0.5	0.25	0.18	0.35
ε_i^{fc}	–	1.8E-03	3.E-03	3.E-03	2.5E-03
ε_u^{fc}	–	1.5E-03	1.2E-03	6E-05	1.4E-03
ε_i^{ft}	–	6E-04	8E-04	8E-04	8E-04
ε_u^{ft}	–	1.1E-03	1E-03	6.5E-04	8E-04
d_u^{fc}	–	2.5E-02	2.5E-02	2.5E-02	2.5E-02
d_u^{ft}	–	8E-03	8E-03	8E-03	8E-03
E_{22}^0	GPa	1.3E-03	1.3E-03	1.3E-03	1.3E-03
G_{12}^0	GPa	2E-04	2E-04	2E-04	2E-04
b	–	2E-03	2E-03	2E-03	2E-03
Y_{22}^0	$\sqrt{\text{GPa}}$	0.05	0.06	0.05	0.05
Y_{12}^0	$\sqrt{\text{GPa}}$	2E-03	2E-03	2E-03	2E-03
Y_{22}^C	$\sqrt{\text{GPa}}$	0.025	0.022	0.025	0.025
Y_{12}^C	$\sqrt{\text{GPa}}$	1.8E-04	1.8E-04	1.8E-04	1.8E-04
Y_{22}^U	$\sqrt{\text{GPa}}$	2E-03	2E-03	2E-03	2E-03
Y_{12}^U	$\sqrt{\text{GPa}}$	2E-03	2E-03	2E-03	2E-03
d_{max}	–	0.9	0.9	0.9	0.9
A	–	2E-03	2E-03	2E-03	2E-03
R_0	GPa	3E-04	3E-04	3.5E-04	3.5E-04
β	–	8E-05	8E-05	8E-05	8E-05
m	–	6E-05	6E-05	6E-05	6E-05
G_I^u	$^{\text{J}}/_{\text{mm}^2}$	1.1E-02	1.1E-02	1.1E-02	1.1E-02
$\sigma_{start/prop}$	GPa	0.12	0.12	0.12	0.12
G_{II}^u	$^{\text{J}}/_{\text{mm}^2}$	1E-02	1E-02	1E-02	1E-02
$\tau_{start/prop}$	GPa	2.2	2.2	2.2	2.2

Table 5.16: Standard deviations for parallel sequences in logarithmic domain.

A MCMC simulation with four parallel chains and data sets from single experiments was set up for the comparative study on the different identification methods . The initial value vectors (see table 5.15) and standard deviations (see table 5.16) for the simulation were set up in such a way so that the priors were over dispersed, while overlapping of the distributions was maintained. Furthermore, the chains were tuned to achieve an acceptance probability between 20% and 50% to achieve a good mixing behaviour of the sequence. The four parallel chains were set up to run for 4,000,000 iterations with a burn-in zone of 1,000,000 iterations to ensure sequence stationarity. It should be noted that the definition of the burn-in zone only affects the on-line calculations of the chain, such as convergence assessment and computation of updated mean values. However, the complete output is written to text files so that additional post-processing is possible via alternative tools such as R.

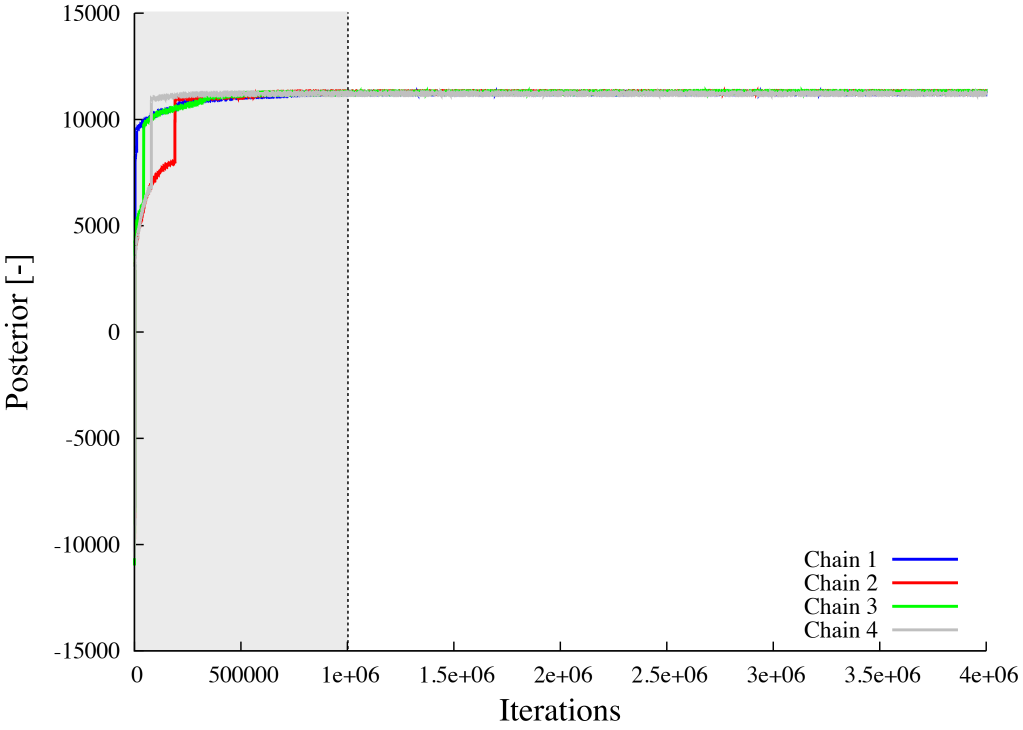

Figure 5.28: Posterior distribution plot corresponding to the neutral chains of each MCMC simulation.

For this setup a CPU runtime of 37 hrs : 17 min was recorded. Figure 5.28 illustrates the evolution plots for the posterior. The acceptance ratios of the chains were in the range of 43-48%. The post-processing of this simulation showed that the burn-in zone could be reduced to 55,000 iterations. The data generated from all chains were thinned so that only uncorrelated samples were used for the parameter estimation. Probability density plots are very useful when evaluating the result of the estimated parameter as they provide information about the explored range. Figure 5.29 illustrates the density plot for the tensile modulus in the fibre direction. The shape of the density plot for this parameter resembles a Gaussian distribution. Here the median value of the undamaged elastic modulus was computed as 161.2±0.4 GPa while all sequences started with initial values in the range of 159.06 - 159.85 GPa.

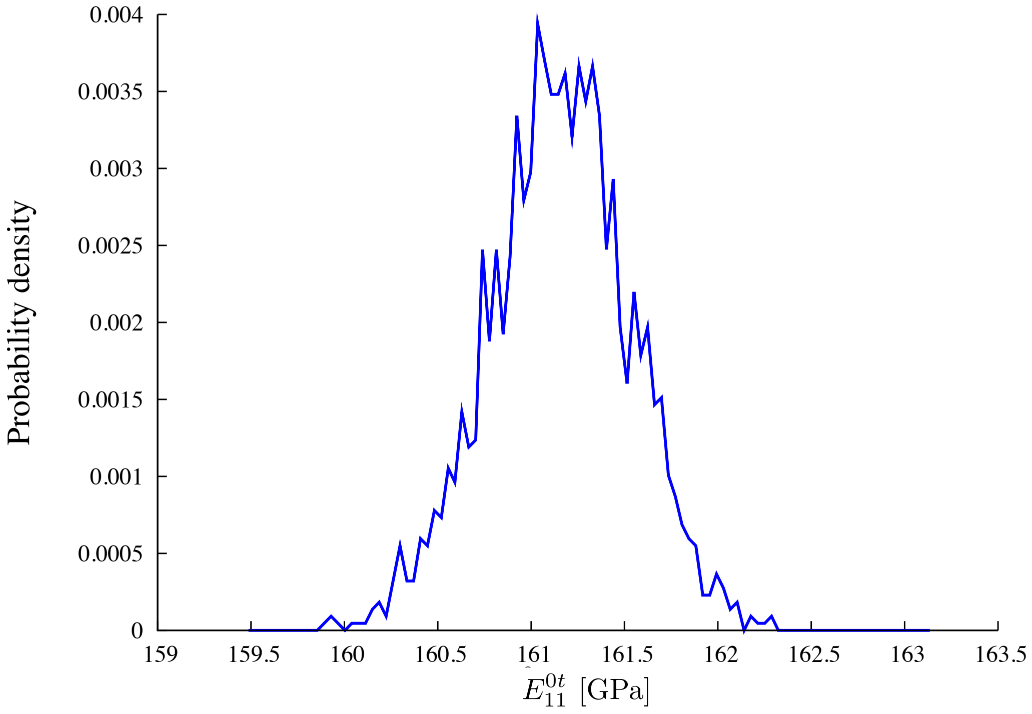

Figure 5.29: Probability density for the tensile modulus in the fibre direction.

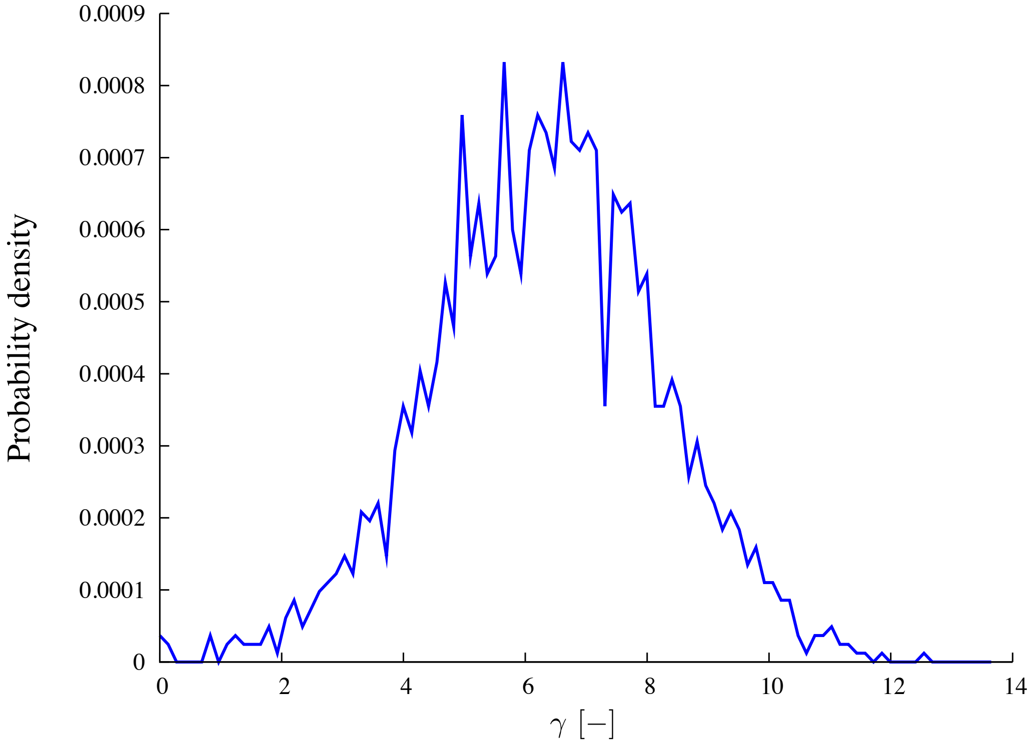

Figure 5.30: Probability density plot for the compressive correction parameter.

Figure 5.30 shows the probability density plot for the compressive correction parameter. Here a mean value of 6.3±1.8 was obtained while the initial values for this parameter, as identified by the conventional identification method, were in the range of 0.1485 - 0.1499. Again the density plot for this parameter resembles a normal distribution closely. Besides the verification of the mean or median of a parameter the density plot can also be used to draw further conclusions. In the case of the exponential parameter of the plastic hardening law a multi modal density plot with other regions of significant probability was obtained (see figure 5.31). Additional modes do have an influence on the determination of the mean value (0.357) while the median value (0.359) is less affected by possible outliers. However, the main advantage nonetheless is that such a density plot reveals these circumstances, where other methods do not allow a quality assessment in a similar form. The whole result vector from this simulation is listed in table 5.17 together with the results from the conventional and gradient-based method.

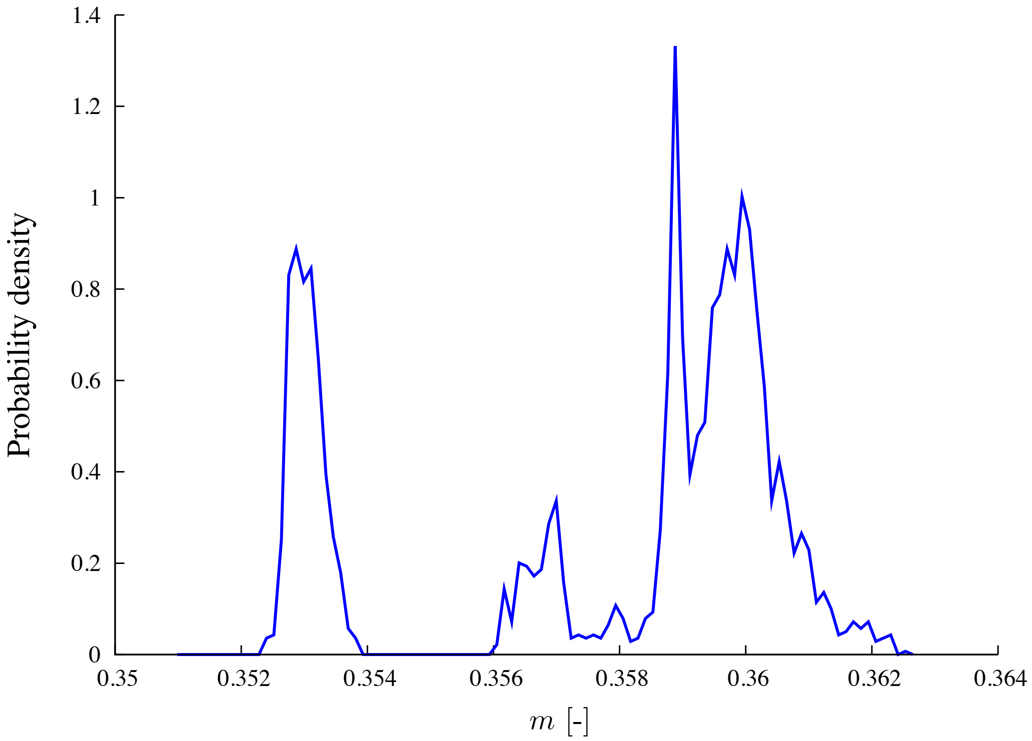

Figure 5.31: Probability density plot for the coupling factor of transverse and shear plastic strains.

A meaningful visualisation of a high-dimensional simulation is difficult due to the high parameter interaction. Nonetheless figure 5.32 illustrates samples in the parameter space in the fibre direction for compressive loading. The parameter space is spanned by the compressive elastic modulus in the fibre direction, the compressive correction factor and the initial compressive failure strain.

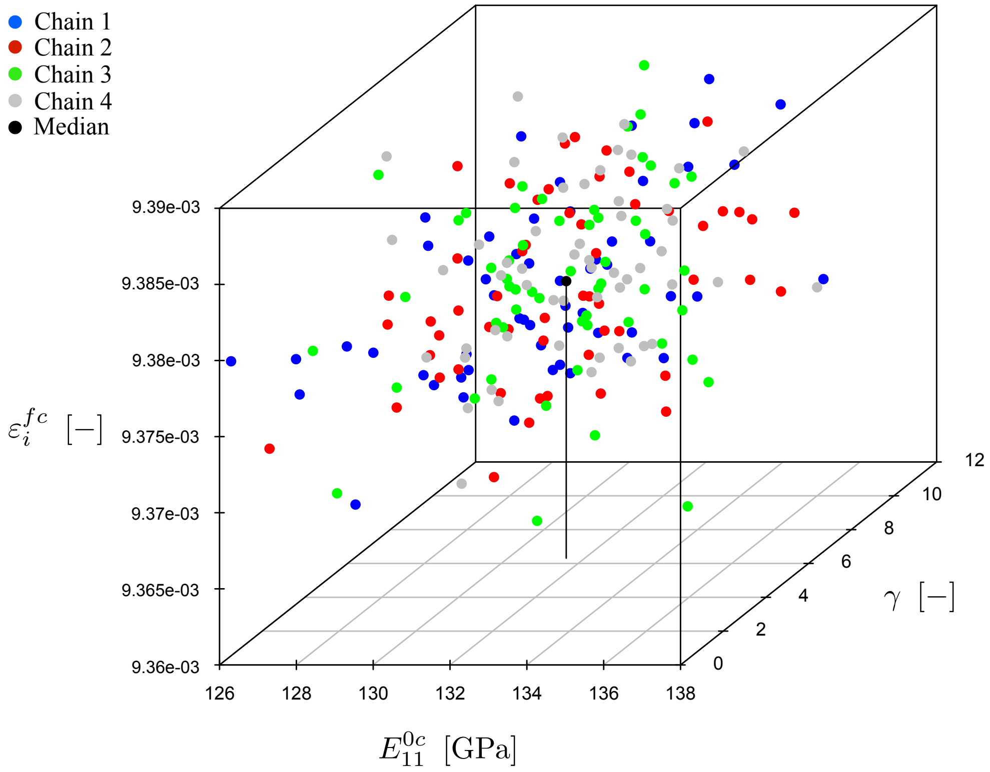

Figure 5.32: Domain plot for primary compressive parameters.

The samples from each chain were reduced by a factor 100 and plotted in the parameter space. The samples form a cloud around the combined median value which is located at [131.6, 6.4, 9.4E-03].

5.2.3.4 Application of parallel tempering

For complex models is it possible that a chain can be trapped in a mode or local optima. To overcome this problem parallel tempering can be applied (see section 2.2.2.3). The algorithm described previously was extended with the parallel tempering option. A different tempering parameter in the range of 1 to 0 was assigned to each individual chain. The lower the tempering parameter the higher the chance of a proposed parameter set to be accepted. Ultimately this leads to a higher acceptance probability for that sequence and allows the exploration of a larger parameter region.

The simulation was carried out for 4,000,000 iterations using parallel tempering and a burn-in range of 1,000,000 iterations was defined. Figure 5.33 illustrates the evolutions of the posterior for each chain. The downside of using parallel tempering is that only one chain, namely the one with the neutral tempering parameter, can be used for the final analysis. The remaining chains are only used to spur on the neutral sequence in case it gets trapped in a mode. The acceptance probabilities for chains 1 to 4 were 37%, 49% , 58% and 62%.

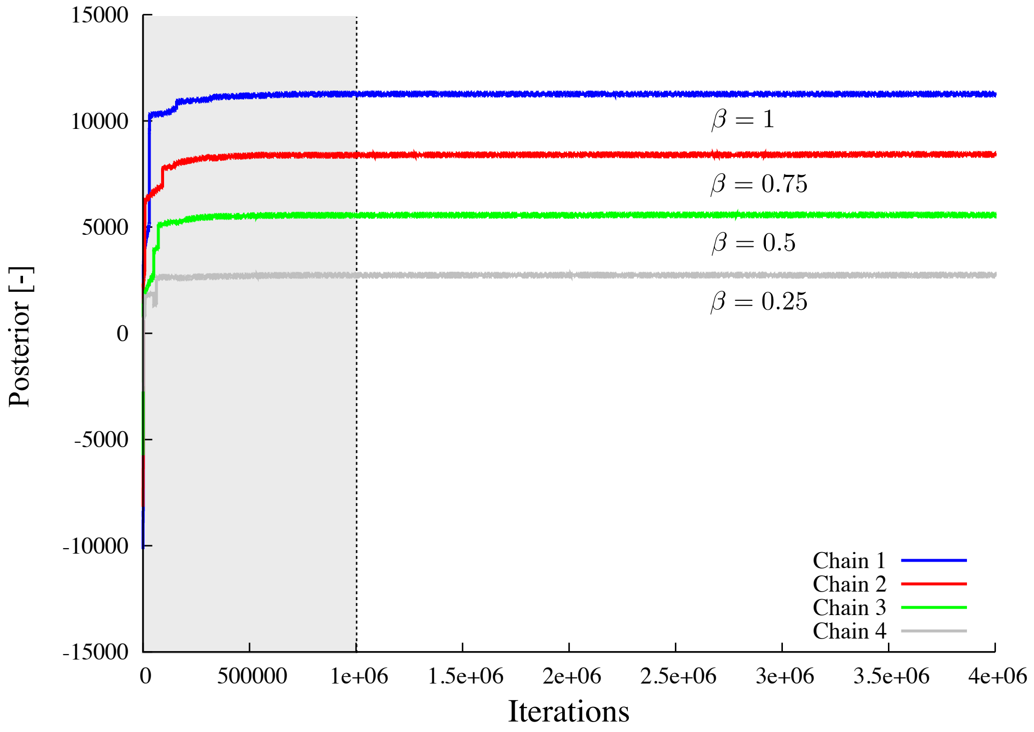

Figure 5.33: Probability density plot for the critical energetic threshold value in shear.

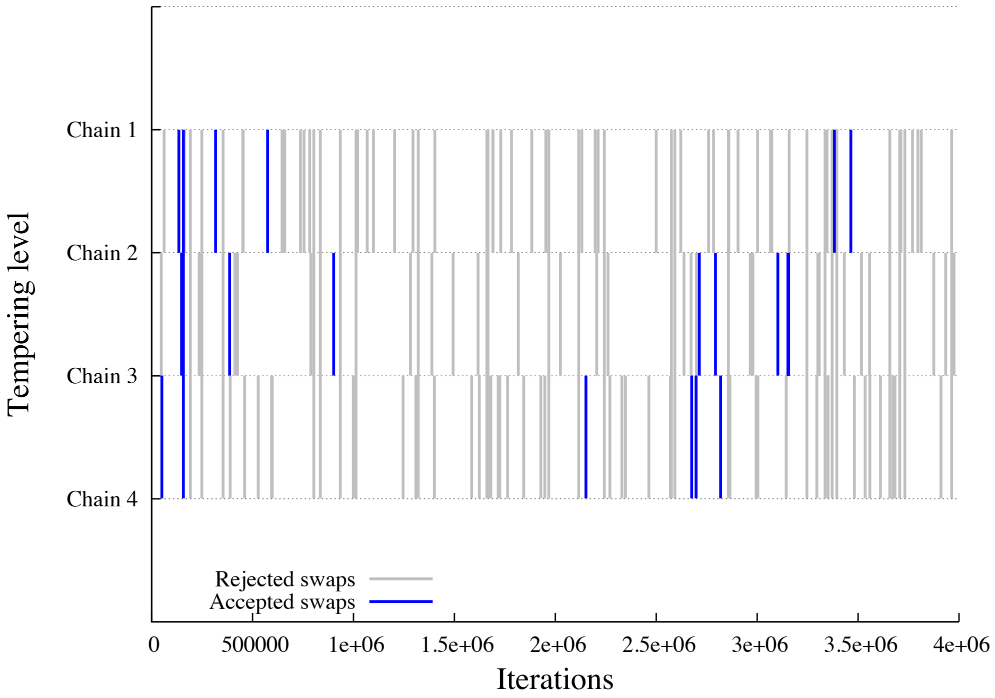

Figure 5.34: Plot of accepted and rejected parameter exchange.

The parallel tempering algorithm repetitively proposes a parameter vector exchange between a randomly picked pair of chains after a fixed number of iterations. Figure 5.34 shows the proposed and executed parameter exchanges between chains at different tempering levels. Here, values of the tempering parameter of 1, 0.75, 0.5 and 0.25 were assigned to chains 1 to 4 respectively.

5.2.4 Comparison of identification techniques

The results obtained from the three parameter identification methods are compared in this section. The results from a single experiment in the respective direction are presented first. Hence the material model responses can be plotted over the experimental data using the different parameter results and the accuracy of the results can be evaluated.The parallel tempering algorithm repetitively proposes a parameter vector exchange between a randomly picked pair of chains after a fixed number of iterations. Figure 5.34 shows the proposed and executed parameter exchanges between chains at different tempering levels. Here, values of the tempering parameter of 1, 0.75, 0.5 and 0.25 were assigned to chains 1 to 4 respectively.
All parameters listed in the tables of this section use the units that correspond to the finite element solution described in the next chapter (mm, kg, ms and °K). For consistency this set results in GPa for the moduli, $\sqrt{\text{GPa}}$ for the energetic threshold values and $^{\text{J}}/_{\text{mm}^2}$ for the energy release rated in mode I and II respectively.

5.2.4.1 Single specimen results for the reference laminate

Table 5.17 reports the results from the three identification techniques for the reference laminate using a single test in each case. Here the outcome from the conventional and gradient-based solver methods result into a single value whilst the nature of the MCMC technique provides the median value of all the generated samples with the corresponding standard deviation. The comparison of the identification methods is especially interesting under the point of view of the coupling parameters and energetic threshold values. Results from the conventional and gradient-based solution already showed significant differences for the compressive correction parameter and the initial yield stress. Further judgement about these values can be made with the aid of the results from the MCMC simulation. The model responses using the identified material parameters from each method for the different test directions are plotted in the following for a single experiment. The material responses are plotted first alongside the underlying experimental data for the tensile direction (see figure 5.35). All methods show very good agreement with the experimental data with no particularly outstanding performance for any method. Figure 5.36 illustrates the

Property	Unit	Value (a)	Value (b)	Value (c)		
E_{11}^{0t}	GPa	159.17	160.98	161.18	±	0.38
ε_{i}^{ft}	–	1.561E-02	1.561E-02	1.567E-02	±	2.20E-05
ε_{u}^{ft}	–	1.572E-02	1.573E-02	1.574E-02	±	4.93E-05
d_{u}^{ft}	–	1	0.998	0.997	±	2.82E-03
E_{11}^{0c}	GPa	129.31	132.82	131.66	±	1.84
ε_{i}^{fc}	–	9.3E-03	9.4E-03	9.4E-03	±	5.30E-06
ε_{u}^{fc}	–	9.4E-03	9.5E-03	9.5E-03	±	5.53E-06
d_{u}^{fc}	–	1	0.998	1	±	8.87E-03
γ	–	0.064	7.59	6.37	±	1.86
G_{12}^{0}	GPa	4.56	4.64	4.06	±	0.14
d_{max}	–	0.411	0.411	0.9	±	1.87
Y_{12}^{0}	$\sqrt{\text{GPa}}$	-3.24E-05	1.0E-08	5.02E-05	±	2.76E-03
Y_{12}^{C}	$\sqrt{\text{GPa}}$	0.1	7.62E-02	7.44E-02	±	6.13E-03
Y_{12}^{U}	$\sqrt{\text{GPa}}$	4.27E-02	4.27E-02	5.11E-02	±	3.62E-02
R_0	GPa	2.2E-02	1E-08	1.97E-02	±	5.05E-04
β	–	0.39	0.37	0.39	±	1.18E-02
m	–	0.35	0.35	0.36	±	2.98E-03
E_{22}^{0}	GPa	9.64	9.45	9.64	±	9.57E-02
A	–	0.063	0.063	0.26	±	1.51E-02
Y_{22}^{0}	$\sqrt{\text{GPa}}$	3.2E-03	5.3E-03	6.57E-05	±	1.89E-03
Y_{22}^{C}	$\sqrt{\text{GPa}}$	0.125	0.159	0.198	±	1.91E-02
Y_{22}^{U}	$\sqrt{\text{GPa}}$	1.16E-02	2.59E-02	4.22E-02	±	1.97E-02
b	–	8.07E-02	8.07E-02	5.5E-03	±	1.16
$\sigma_{start/prop}$	GPa	0.052	0.15	1.82E-04	±	5.09E-06
G_{I}^{u}	J/mm^2	4.33E-04	4.33E-04	4.41E-04	±	1.87E-06
$\tau_{start/prop}$	GPa	2.6E-02	2.5E-02	5.5E-02	±	4.12E-02
G_{II}^{u}	J/mm^2	4.63E-04	4.63E-04	4.64E-04	±	1.67E-06

Table 5.17: Result vector comparison for different parameter identification methods obtained from the analysis of single coupon experiments, (a) conventional, (b) gradient-based solution and (c) MCMC.

results for compression in the fibre direction. A significant difference is visible in the high stress region. This range is sensitive to the parameter γ which governs the non-linear behaviour due to fibre buckling. Here the gradient-based solver and MCMC method are able to match the experimental data equally well, while the stress response obtained with the conventional result vector shows hardly any non-linearity. Both advanced techniques started with a value of 0.064 which was determined by the conventional method. However, significantly higher values are computed with both methods. Figure 5.30 illustrates the probability density of this parameter and shows that the values computed by the gradient-based (7.6) and by the MCMC method (6.4±1.9) lie in the high probability region of the density plot.

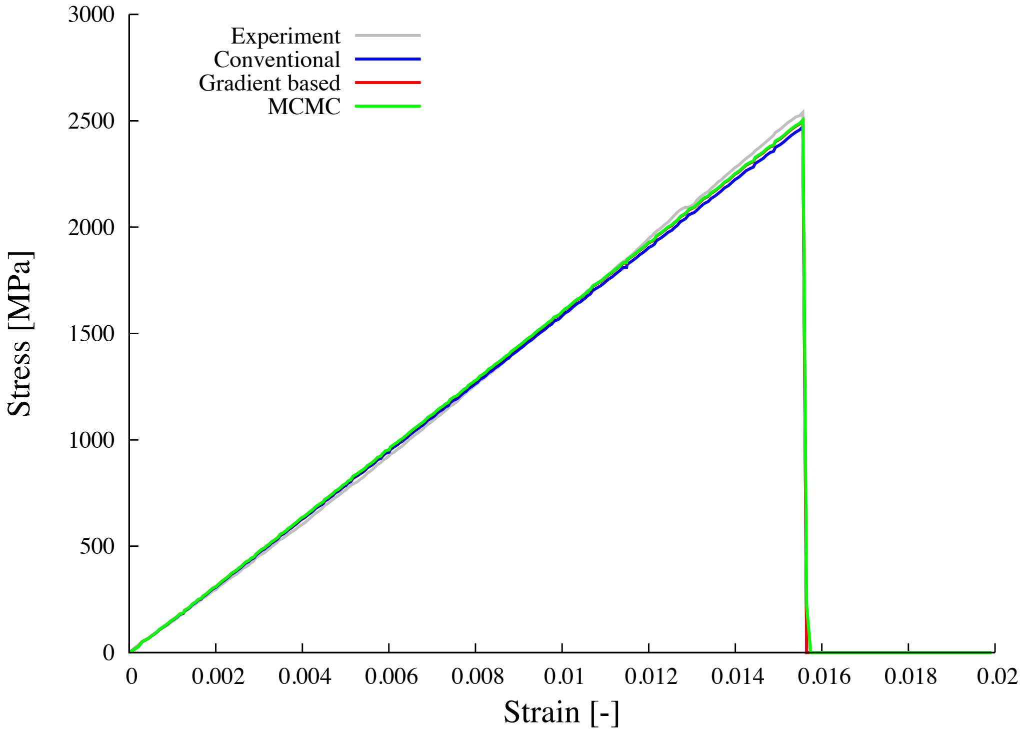

Figure 5.35: Comparison of model responses in fibre tension for a single experiment on the reference laminate.

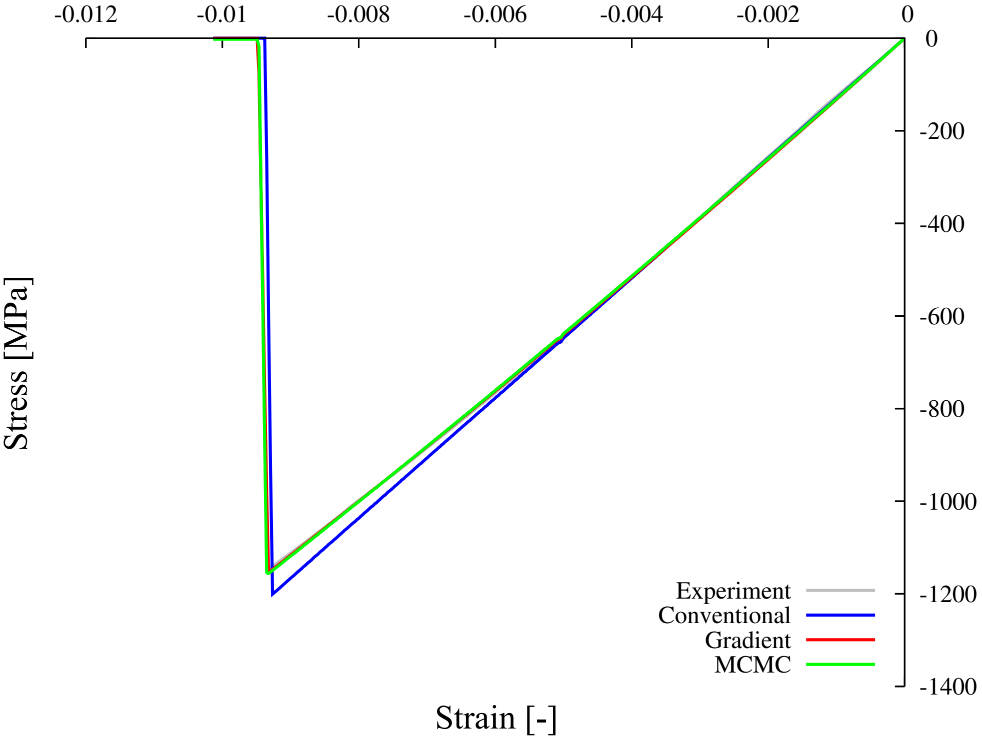

Figure 5.36: Material responses in fibre compression for a single experiment on the reference laminate.

Substantial differences were observed for the shear experiment illustrated in figure 5.37. The result from the conventional method over predicts the stress response and fails to match the experimental data in the later stage of the experiment. The automated methods are capable to match the yield evolution closely. Furthermore the gradient-based solution provides the best fitting result, while the MCMC solution vector fails to conform with the lower stress levels.

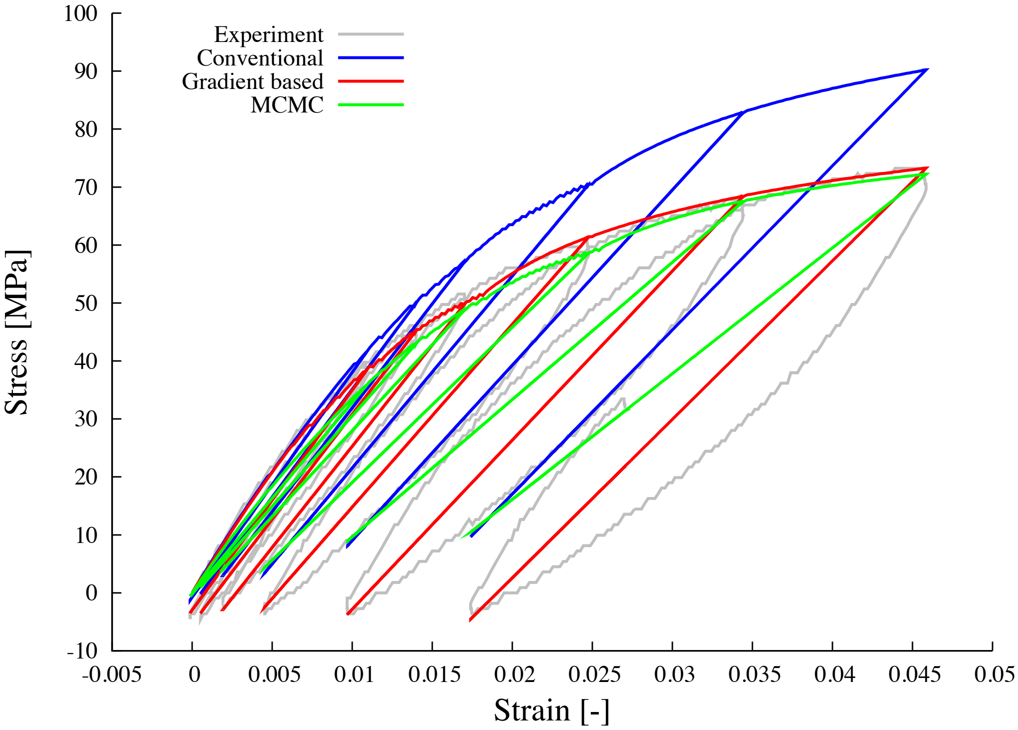

Figure 5.37: Comparative plot for a single shear test on the reference laminate, using parameters from conventional, gradient-based minimisation and MCMC method.

However, the value identified for the initial yield stress R_0 has a great influence on this plot. This parameter can be identified with significant confidence via the conventional method directly from the shear data plot (see figure 5.7), which leads to 0.022 GPa for the initial yield stress. The gradient-based method however, infers a value of 1E-08 GPa while the MCMC method results in a value of 0.019±5.05E-04 GPa. Figure 5.38 illustrates the probability density for this parameter. The underlying noise level in an experimental data set can lead to scatter in the final result. However, the value for the initial yield stress as determined by the gradient-based solution is unrealistically low. Furthermore, when replacing the value of the yield stress in the MCMC solution vector the material response coincides with the gradient-based solution. Hence the MCMC solution can be interpreted as a compromise between the conventional and gradient-based method. This is an excellent example where the gradient-based minimisation method identifies a local optimum and fails to explore other regions with the aim for a global optimum.

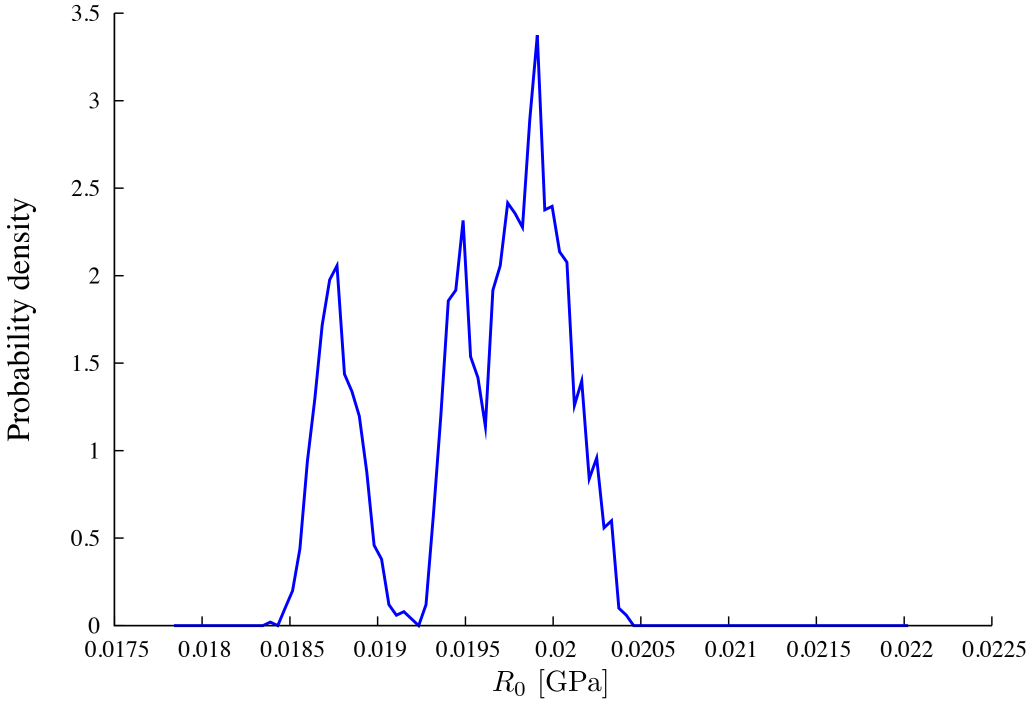

Figure 5.38: Probability density plot for the critical energetic threshold value in shear.

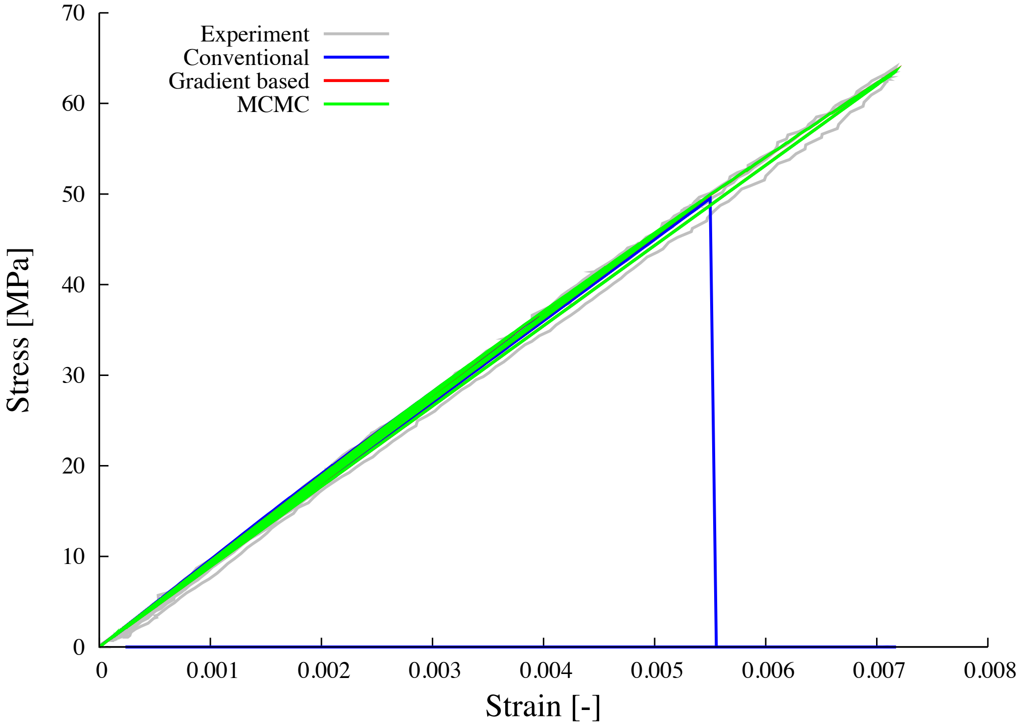

Figure 5.39: Plot of transverse model response using the parameters identified with conventional, gradient-based and MCMC methods.

Here the advantage of the MCMC method is also visible, as it overcomes this problem on the basis of the prior information and the sampling behaviour of the chains. It should be noted that the hysteresis effect within the experimental data can be explained with inter-ply friction and fibre hooking [9, 210]. Such effects are not considered and cannot be represented by the in-plane material model.

The results from the stress responses in the transverse direction are shown in figure 5.39. Here the stress responses generated from the automated methods perform equally well. They show very good agreement with the experimental data throughout the test, while stresses determined with the conventional vector only show a good agreement until the value for maximum damage of the material is reached. After this point the material is completely damaged and is unable to carry further load. In numerical terms this is equivalent to generating a zero stress response for the rest of the experiment. The responses for the delamination model in mode I show only little difference in the plateau region as illustrated in figure 5.40. The plateau describes the crack propagation region which the material model considers constant. Considerable differences however, were observed for the initiation. Here, the result vector determined with the MCMC simulation provides the best fit. In mode II the model responses match with the experimental data equally well (see figure 5.41).

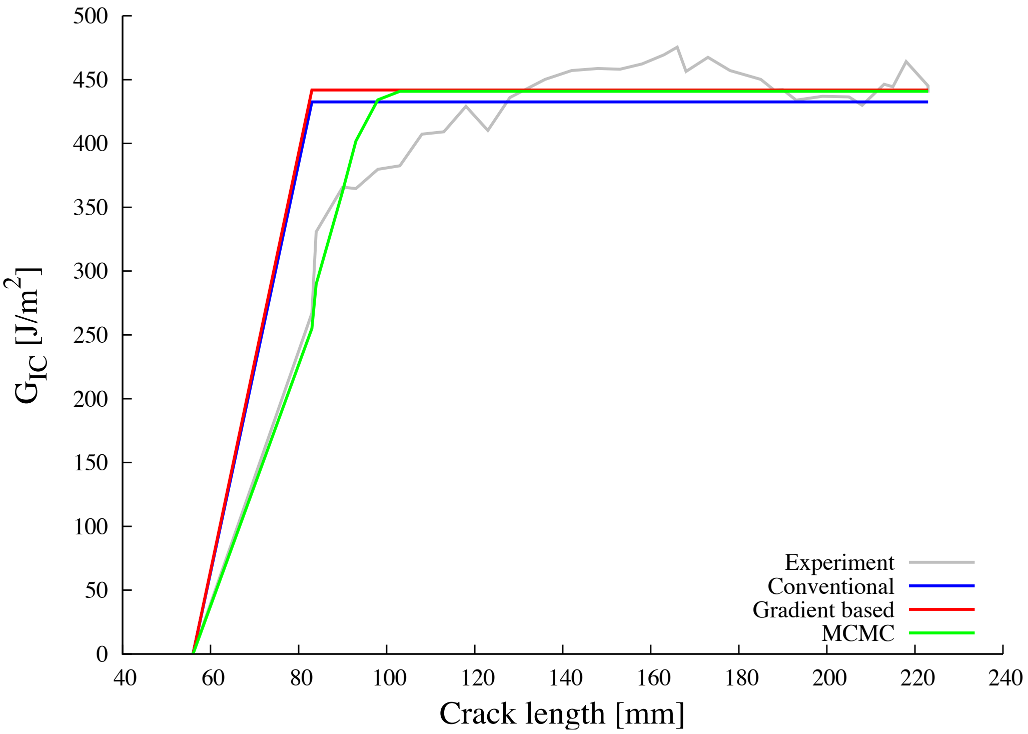

Figure 5.40: Experimental resistance curve and model responses for mode I delamination generated from different methods.

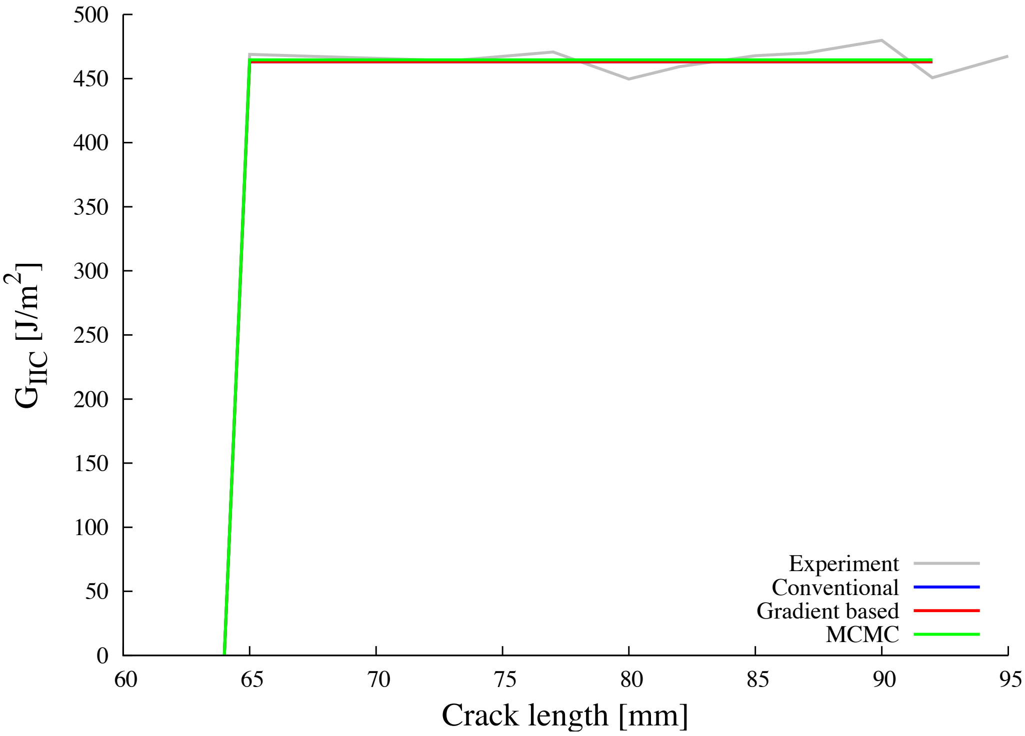

Figure 5.41: Resistance plot for single mode II delamination experiment over layed with model responses from different parameter sets.

Similarly to mode I delamination the plateau region is represented by a constant value. Both delamination models depend on the input of the elastic moduli in transverse (mode I) and shear (mode II) direction which effectively link these models with the in-plane transverse and shear tests. The MCMC method is capable of taking these model linking effects into account.

5.2.4.2 Test programme results

Inhomogeneously bindered preform material

The material parameters extracted from the test programme on inhomogeneously bindered material at the preform stage are presented in table 5.18. In the fibre direction the conventional and MCMC method lead to similar results of 141 GPa while the gradient-based solution results to 138 GPa. For the initial damage and failure strain in the fibre direction, slight differences were observed. The total damage value was determined as 1 for all the different methods. In the shear direction differences in the material properties were observed for the total damage, the critical energetic threshold and the initial yield stress value. While the gradient-based and MCMC methods gave similar results for the total damage of 0.56 and 0.64 respectively; the conventional method lead to a lower result of 0.073. The parameters for the critical threshold value differ for all the methods. In the case of the initial yield stress the values estimated via the conventional and MCMC method have similar magnitudes of about 1.4E-03 GPa which are significantly higher than the gradient method result of 3.59E-04 GPa.

Property	Unit	Value (a)			Value (b)			Value (c)		
E_{11}^{0t}	GPa	141.05	±	10.58	137.87	±	5.44	141.74	±	0.35
ε_i^{ft}	–	1.278E-02	±	9.E-04	1.281E-02	±	8.E-04	1.197E-02	±	1.84E-05
ε_u^{ft}	–	1.287E-02	±	9E-04	1.283E-02	±	7.7E-03	1.42E-02	±	3.05E-05
d_u^{ft}	–	1	±	-	1	±	-	0.99	±	7.8E-03
G_{12}^0	GPa	2.11	±	0.09	2.11	±	0.12	2.18	±	0.034
d_{max}	–	0.073	±	0.074	0.56	±	0.057	0.64	±	0.07
Y_{12}^0	$\sqrt{\text{GPa}}$	1.08E-03	±	9.51E-05	1.08E-03	±	9.51E-05	1.09E-03	±	2.86E-05
Y_{12}^C	$\sqrt{\text{GPa}}$	-1.262E-03	±	8.E-03	5.36E-03	±	1.78E-04	1.60E-05	±	1.95E-06
Y_{12}^U	$\sqrt{\text{GPa}}$	1.31E-03	±	2.89E-04	1.31E-03	±	2.89E-04	1.23E-03	±	9.51E-05
R_0	GPa	1.39E-03	±	1.52E-04	3.59E-04	±	5.07E-04	1.43E-03	±	1.02E-05
β	–	0.27	±	0.01	0.27	±	0.01	0.27	±	9.01E-03
m	–	0.73	±	0.02	0.73	±	0.02	0.71	±	0.015
E_{22}^0	GPa	0.083	±	0.006	17.99	±	-	0.037	±	0.005
A	–		±		0.21	±	-	0.14	±	0.2
Y_{22}^0	$\sqrt{\text{GPa}}$	1.08E-03	±	-	5.74E-02	±	-	4.82E-06	±	1.31E-04
Y_{22}^C	$\sqrt{\text{GPa}}$	1.3E-03	±	-	0.17	±	-	2.61E-03	±	3.85E-04
Y_{22}^U	$\sqrt{\text{GPa}}$	1.16E-03	±	-	2.59E-02	±	-	1.81E-03	±	2.09E-04
b	–		±		0.79	±	-	9.36E-02	±	4.92E-03

Table 5.18: Comparison of parameter vectors for the inhomogeneously bindered material obtained from test programme, (a) conventional, (b) gradient-based solver and (c) MCMC method.

Although three experiments in the transverse direction were undertaken the results

from one experiment were used for the identification of the full transverse parameter set. However, the other valid experiment for this direction allowed the extraction of the initial elastic modulus in the transverse direction via the conventional method. For the initial transverse modulus the MCMC method resulted in the lowest value (0.037 GPa), whilst the conventional method yields a value approximately 100% higher. An unrealistically high value of 18 GPa was obtained using the gradient-based method. Significant differences were observed for the energetic threshold values in the transverse direction.
The coupling factors A and b were estimated via the gradient-based and MCMC method. The conventional method was too prone to the noise level in the data. Here a value of 0.21 versus 0.14 for the coupling factor between transverse and shear plastic strains A was obtained from the MCMC and the gradient-based method respectively. A bigger difference was observed for the coupling factor between transverse and shear damage b, where the gradient-based solver results to a value of 0.79 and the outcome of the MCMC method is a value of 9.4E-02.

Homogeneously bindered preform material

The improved material properties of the homogeneously bindered preform material lead to improvements in the characterisation process (see table 5.19). Similar results were obtained with the conventional and gradient-based solution method in the fibre direction, whilst the initial modulus determined via the MCMC is 17 GPa lower than the other two methods. Furthermore, slightly higher values for the initial and ultimate failure strain were identified by the MCMC in comparison to the two other methods. The application of the DIC system also allowed to determine the undamaged Poisson's ratio (0.28±0.08). This parameter is necessary for the material model input, however, it was not included in the unconventional identification methods. Differences for the parameters in the shear experiment were observed. While the conventional and gradient-based solution have similar results for the shear modulus and the ultimate damage, the MCMC differs and provides a lower modulus but higher ultimate damage value. Further dissimilarities were observed for the energetic threshold values, where the conventional method results in a negative value for the initial threshold. Slight differences were also observed in the parameter set governing inelastic deformation. Here the initial yield stress determined by the MCMC has a lower value than the two other methods. The yield power law factor β was determined as 0.24, 0.12 and 0.18 for the conventional, gradient-based and MCMC methods respectively. The exponent of the power law has a similar value for all these methods.

Property	Unit	Value (a)	Value (b)	Value (c)
E_{11}^{0t}	GPa	136.31 ± 8.49	136.64 ± 9.3	119.04 ± 0.39
ε_i^{ft}	–	6.349E-03 ± 6.58E-04	6.386E-03 ± 6.73E-04	7.08E-03 ± 6.62E-06
ε_u^{ft}	–	6.402E-03 ± 6.63E-04	6.479E-03 ± 6.66E-04	7.31E-03 ± 7.90E-06
d_u^{ft}	–	0.99 ± 1.95E-08	0.99 ± 1.59E-08	1 ± 0.01
G_{12}^0	GPa	0.24 ± 0.04	0.26 ± 0.099	0.18 ± 0.4
d_{max}	–	0.64 ± 0.081	0.61 ± 0.395	0.95 ± 0.038
Y_{12}^0	$\sqrt{\text{GPa}}$	-3.12E-03 ± 4.13E-03	4.17E-04 ± 3.92E-04	6.75E-05 ± 0.11
Y_{12}^C	$\sqrt{\text{GPa}}$	1.367E-02 ± 8.52E-03	2.67E-03 ± 3.46E-03	3.95E-03 ± 2.86E-03
Y_{12}^U	$\sqrt{\text{GPa}}$	7.44E-03 ± 2.4E-03	5.49E-03 ± 4.55E-03	3.29E-03 ± 2.44E-02
R_0	GPa	2.38E-04 ± 3.58E-05	2.33E-04 ± 1.83E-04	4.47E-05 ± 3.68E-04
β	–	0.24 ± 0.08	0.12 ± 0.11	0.18 ± 0.45
m	–	0.97 ± 0.06	0.99 ± 0.04	0.99 ± 0.05
E_{22}^0	GPa	0.5 ± 0.1	0.49 ± 0.09	0.85 ± 0.047
A	–	0.41 ± 7.2E-02	0.14 ± 0.19	0.6 ± 0.76
Y_{22}^0	$\sqrt{\text{GPa}}$	1.06E-03 ± 2.75E-04	2.84E-04 ± 2.18E-04	2.60E-05 ± 7.18E-05
Y_{22}^C	$\sqrt{\text{GPa}}$	2.03E-03 ± 2.15E-04	1.84E-03 ± 7.77E-05	1.39E-03 ± 9.51E-05
Y_{22}^U	$\sqrt{\text{GPa}}$	1.52E-03 ± 1.9E-04	1.42E-03 ± 0	1.83E-03 ± 4.43E-04
b	–	1.71 ± 0.43	0.65 ± 0.73	5.38E-04 ± 1.44
$\sigma_{start/prop}$	GPa	8.74E-04 ± 2.36E-04	1.26E-02 ± 8.87E-03	2.64E-02 ± 9E-03
G_I^u	$^{\text{J}}/_{\text{mm}^2}$	1.71E-04 ± 6.11E-05	1.71E-04 ± 6.11E-05	1.72E-04 ± 7.67E-07
$\tau_{start/prop}$	GPa	9.63E-04 ± 5.39E-04	6.1E-03 ± 5.63E-03	1.71E-03 ± 4.05E-05
G_{II}^u	$^{\text{J}}/_{\text{mm}^2}$	1.07E-04 ± 6.15E-05	1.07E-04 ± 6.15E-05	1.52E-04 ± 3.79E-06

Table 5.19: Comparison of parameter vector obtained from different methods for the homogeneously bindered material programme, (a) conventional, (b) gradient-based solver and (c) MCMC.

Differences were observed for the energetic thresholds in the transverse material direction, which define the evolution of the inelastic strain due to damage. All three methods come up with a different set for the linear law. The result for the brittle transverse damage limit of the fibre/matrix interface determined via the gradient-based minimisation method are particularly interesting. Here, a standard deviation of $\pm 0 \sqrt{\mathrm{GPa}}$ corresponding to this parameter was determined, which leads to the conclusion that this parameter was not varied in any of the simulation throughout the test programme set. The ultimately threshold set is also influenced by the initial elastic modulus and the coupling parameters. Whilst the conventional and gradient-based method lead to similar values of 0.5 GPa and standard deviations for the elastic modulus, the MCMC method yields to a larger value of 0.85±0.047 GPa. In terms of the coupling parameters A and b the results differ across the different methods. The conventional method yields a value of 0.41 with a small standard deviation of 7.2E-02 for A. The other methods show a lower and higher value with a higher deviation. For parameter b the MCMC technique indicates a very low coupling of the transverse and shear damage, while the other two methods imply a more significant coupling effect.

The mode I fracture toughness was determined as 1.7E-04 $^{\mathrm{J}}/_{\mathrm{mm}^2}$ throughout the different methods whereas the MCMC methods established a slightly higher value for the mode II fracture toughness with 1.52E-04 versus 1.07E-04 $^{\mathrm{J}}/_{\mathrm{mm}^2}$ for the conventional and gradient-based method. Different values where determined from the identification methods for both crack initiation stresses.

Reference laminate

A full test programme was carried out including compression experiments in the fibre direction for the reference laminate. The results of all methods are listed in table 5.20. Starting with the tensile parameters in the fibre direction, the three identification methods show good agreement while the undamaged initial modulus in the fibre direction identified via the MCMC method is 2 GPa lower in comparison to the other methods. Similarly to the homogeneously bindered material the DIC equipment was used with the reference laminate to determine the Poisson's ratio from the longitudinal and transverse deformation. A value of 0.31±0.024 was estimated for this material.

The initial modulus under compression in the fibre direction varies around 130 GPa where the conventional method provides the smallest value of 128 GPa versus 131 and 133 GPa for the gradient-based and MCMC methods respectively. The initial and ultimate fibre failure strains as determined by the conventional and gradient-based method correlate well, whereas the MCMC finds a lower initial and a larger ultimate value. Similarly to the single experiment analysis the correction factor for non-linear fibre compression differs. A value of 0.15 is obtained from the conventional method, while significantly larger values are determined via the other techniques. The gradient-based method yields a value of 7.32 whilst the MCMC simulation results in a value of 3.34. The shear direction results show differences for the energetic threshold values and the yield function parameters.

Property	Unit	Value (a)	Value (b)	Value (c)
E_{11}^{0t}	GPa	156.97 ± 2.61	156.72 ± 3.06	154.34 ± 0.17
ε_i^{ft}	–	1.436E-02 ± 1.26E-03	1.454E-02 ± 1.25E-03	1.458E-02 ± 1.76E-06
ε_u^{ft}	–	1.446E-02 ± 1.26E-03	1.471E-02 ± 1.33E-03	1.468E-02 ± 1.42E-06
d_u^{ft}	–	1 ± -	1. ± 2.85E-03	0.92 ± 1.88E-03
E_{11}^{0c}	GPa	128.34 ± 10.18	131.05 ± 13.81	133.12 ± 10.61
ε_i^{fc}	–	8.294E-03 ± 9.2E-04	8.297E-03 ± 9.24E-04	7.11E-03 ± 9.83E-04
ε_u^{fc}	–	8.395E-03 ± 9.2E-04	8.432E-03 ± 9.28E-04	9.51E-03 ± 4.01E-03
d_u^{fc}	–	1 ± -	0.99 ± 9.28E-04	1 ± 0.9
γ	–	0.15 ± 0.035	7.32 ± 4.6	3.34 ± 15.76
G_{12}^0	GPa	4.77 ± 0.16	4.68 ± 0.09	4.17 ± 0.21
d_{max}	–	0.45 ± 0.06	0.41 ± 0.08	0.51 ± 0.06
Y_{12}^0	$\sqrt{\text{GPa}}$	7.12E-04 ± 3.96E-03	4.34E-03 ± 1.25E-03	2.50E-05 ± 9.64E-06
Y_{12}^C	$\sqrt{\text{GPa}}$	9.54E-02 ± 1.11E-02	4.59E-02 ± 1.3E-02	8.46E-02 ± 5.94E-03
Y_{12}^U	$\sqrt{\text{GPa}}$	4.68E-02 ± 6.9E-03	2.38E-02 ± 7.7E-03	4.57E-02 ± 5.92E-02
R_0	GPa	1.67E-02 ± 4.2E-03	6.82E-02 ± 1.3E-02	1.46E-02 ± 7.23E-04
β	–	0.4 ± 0.05	0.53 ± 0.11	0.39 ± 1.69E-02
m	–	0.32 ± 0.03	0.71 ± 0.03	0.33 ± 7.63E-03
E_{22}^0	GPa	9.64 ± 0.22	9.2 ± 0.16	8.84 ± 0.28
A	–	0.24 ± 0.09	0.33 ± 0.02	0.31 ± 0.11
Y_{22}^0	$\sqrt{\text{GPa}}$	5.9E-03 ± 2.6E-03	4.33E-02 ± 0.0215	3.78E-03 ± 1.50E-03
Y_{22}^C	$\sqrt{\text{GPa}}$	0.137 ± 3.28E-02	0.173 ± 7.8E-03	0.182 ± 1.33E-02
Y_{22}^U	$\sqrt{\text{GPa}}$	1.51E-02 ± 4.4E-03	2.59E-02 ± 0	1.52E-02 ± 1.15E-03
b	–	8.07E-02 ± 7.74E-02	8.07E-02 ± 0	7.61E-03 ± 1.71
$\sigma_{start/prop}$	GPa	5.97E-02 ± 8.2E-03	5.06E-02 ± 8.61E-02	2.43E-04 ± 8.00E-06
G_I^u	J/mm^2	3.51E-04 ± 1.29E-04	3.51E-04 ± 1.29E-04	3.7E-04 ± 1.14E-06
$\tau_{start/prop}$	GPa	6.3E-02 ± 3.2E-02	2.4E-02 ± 2.E-03	1.69E-02 ± 2.98E-04
G_{II}^u	J/mm^2	4.31E-04 ± 5.99E-05	4.31E-04 ± 5.99E-05	4.46E-04 ± 8.84E-07

Table 5.20: Comparison of parameter vector from different methods from reference material test programme, (a) conventional, (b) gradient-based solver and (c) MCMC.

The values determined via the conventional and MCMC approach are close, whereas the gradient-based results are higher or lower. Similarly to the single experiment analysis, the initial yield stress and power law exponent determined via the gradient-based solver deviate from the other techniques. In both cases the gradient-based solution leads to higher values.

The parameters for the transverse direction show differences in the energetic threshold values. However, good agreement was found for the initial and critical energetic threshold values. Furthermore the values for the brittle transverse damage limit show very good agreement for the conventional and the MCMC method. For the gradient-based method, however, the parameter remains unchanged for all experiments. The same behaviour is also observed for the coupling factor between transverse and shear damage b. The conventional method leads to a value of 8.1E-02 versus 7.6E-03 for the MCMC method. The initiation value of 8.1E-02 remained unchanged in the case of the gradient-based method, which yields a value of 8.1E-02±0.

In the case of the out-of-plane properties only slight variations were observed for the energy release rate values. Values of about 5E-02 GPa were obtained for the propagation stress in mode I from the conventional and gradient-based method, whereas the MCMC yields a value of 2E-04 GPa. The gradient-based and MCMC methods result in similar values for the propagation stress in mode II of about 2E-02 GPa, while the result of 6E-02 from the conventional method is three times larger.

Bindered laminate

The tests preformed with the bindered laminate material were analysed and the results are listed in table 5.21. Good agreement between parameters determined via the three identification methods was found for the fibre direction for both tension and compression. Disagreements were only observed for the compressive non-linear correction factor, which showed values of 0.15 and 0.72 for the conventional and MCMC methods respectively. The gradient-based method found a much higher value of 11. The Poisson's ratio for this material is similar to the reference laminate with a value of 0.31±0.035. The parameter sets for the shear experiments from the MCMC and conventional method showed great similarities, whereas the gradient-based solution differed especially on the maximal damage parameter, elementary shear damage fracture limit, initial yield stress and power law exponent. For the shear damage fracture limit the gradient-based solution remains unchanged throughout the whole programme, whereas the initial yield stress value and power law exponent are roughly 30% higher than the values determined with the other methods.

Property	Unit	Value (a)			Value (b)			Value (c)		
E_{11}^{0t}	GPa	125.61	±	0.78	126.39	±	0.29	126.52	±	0.18
ε_i^{ft}	–	1.748E-02	±	3.44E-04	1.623E-02	±	4.09E-04	1.616E-02	±	2.93E-05
ε_u^{ft}	–	1.754E-02	±	3.46E-04	1.636E-02	±	4.5E-04	1.705E-02	±	1.94E-05
d_u^{ft}	–	1	±	-	1	±	7.42E-04	1	±	6.49E-03
E_{11}^{0c}	GPa	126.46	±	16.18	127.14	±	14.19	124.84	±	1
ε_i^{fc}	–	4.93E-03	±	1.82E-04	4.93E-03	±	1.79E-04	4.83E-03	±	7.21E-05
ε_u^{fc}	–	5.01E-03	±	1.94E-04	5.07E-03	±	1.93E-04	4.95E-03	±	2.89E-04
d_u^{fc}	–	0.99	±	-	0.99	±	1.93E-04	0.64	±	0.28
γ	–	0.15	±	0.17	10.88	±	7.65	0.72	±	2.2
G_{12}^0	GPa	2.49	±	0.32	1.96	±	0.24	2.26	±	0.13
d_{max}	–	0.47	±	0.2	0.37	±	0.1	0.48	±	0.25
Y_{12}^0	$\sqrt{\text{GPa}}$	-1.08E-02	±	1.64E-02	0.05764	±	0.1301	8.91E-08	±	2.77E-06
Y_{12}^C	$\sqrt{\text{GPa}}$	6.67E-02	±	3.5E-02	4.3E-02	±	3.28E-02	5.5E-02	±	5.81E-03
Y_{12}^U	$\sqrt{\text{GPa}}$	2.17E-02	±	1.1E-02	2.17E-02	±	0	2.82E-02	±	2.94E-03
R_0	GPa	6.5E-03	±	2.91E-03	9.02E-03	±	3.66E-03	6.18E-03	±	2.67E-04
β	–	0.58	±	0.22	0.52	±	0.12	0.55	±	4.04E-02
m	–	0.58	±	0.12	0.73	±	0.03	0.57	±	1.54E-02
E_{22}^0	GPa	6.02	±	0.2	5.57	±	0.08	5.5	±	0.15
A	–	0.37	±	0.11	0.33	±	4.71E-09	0.34	±	1.83E-02
Y_{22}^0	$\sqrt{\text{GPa}}$	6.41E-03	±	1.29E-03	3.99E-03	±	2.43E-03	7.98E-03	±	3.92E-04
Y_{22}^C	$\sqrt{\text{GPa}}$	3.83E-02	±	1.39E-02	4.35E-02	±	1.33E-02	1.95E-03	±	9.69E-03
Y_{22}^U	$\sqrt{\text{GPa}}$	1.11E-02	±	2.15E-03	1.13E-02	±	2.11E-03	9.24E-03	±	6.76E-04
b	–	6.79E-02	±	3.91E-03	1.49	±	1.88E-08	0.49	±	0.42
$\sigma_{start/prop}$	GPa	3E-02	±	6.86E-03	9E-02	±	6E-02	1.3E-02	±	1.47E-03
G_I^u	$^{\text{J}}/_{\text{mm}^2}$	1.02E-04	±	4.69E-4	6.36E-04	±	2.34E-05	6.99E-04	±	6.52E-06
$\tau_{start/prop}$	GPa	2.4E-02	±	1.1E-02	5.6E-02	±	4.3E-02	1.31E-02	±	2.73E-04
G_{II}^u	$^{\text{J}}/_{\text{mm}^2}$	8.21E-04	±	2.58E-05	8.27E-04	±	2.53E-05	8.11E-04	±	1.20E-06

Table 5.21: Comparison of parameter vector from different methods for the bindered composite test programme, (a) conventional, (b) gradient-based solver and (c) MCMC.

In the transverse direction set all techniques lead to similar values for the undamaged modulus and coupling factor between transverse and shear plastic strains. However, only small differences were observed for the threshold values of the linear damage law. Notable differences were observed for the coupling factor between transverse and shear damage b, where a value of 6.8E-02 is determined with the conventional method, whereas the other methods find a higher coupling effect between the two directions. The MCMC method leads to a value of 0.49 and the gradient-based minimisation method results in a value of 1.49.

The values for the mode II fracture toughness are determined with a very good agreement for all methods whereas the fracture toughness for mode I shows significant differences. The automated techniques yield values of 6.4E-04 and 7E-04 $^{\mathrm{J}}/_{\mathrm{mm}^2}$ for the gradient-based and MCMC method respectively with low standard deviations. The value determined via the conventional methods is 1E-04 $^{\mathrm{J}}/_{\mathrm{mm}^2}$. Nonetheless the corresponding standard deviation of 4.7E-04 $^{\mathrm{J}}/_{\mathrm{mm}^2}$ is high and reaches into the range of the values determined with the automated methods. Similarly to the reference material, the propagation stresses as determined via the MCMC method are lower than those estimated using the other two techniques. The gradient-based solver leads to higher stress values in comparison to those determined via the conventional method.

6 Finite element modelling

This chapter describes the implementation of the material models, as introduced in section 5.1, and the finite element simulations. The material parameter sets as obtained for the respective material type via the MCMC method are used in the finite element models. The material and finite element behaviour is validated using the experimental findings from three-point bending tests on laminated material. A further FE model addresses the behaviour of the preform material under impact loading for validation purposes. A set of simulations investigates the performance of a helicopter component under the perspective of fibre angle shear due to the manufacturing process is presented in the final section of this chapter. The influence of the fibre orientations on the overall performance of the component is evaluated. Therefore nominal orientations chosen from a design perspective are compared to the results from draping simulations, which are based on the draping process.

6.1 Modelling strategy

The modelling strategy followed in this work is based on using shell elements in combination with cohesive zone elements as illustrated in figure 6.1. Multi-layered

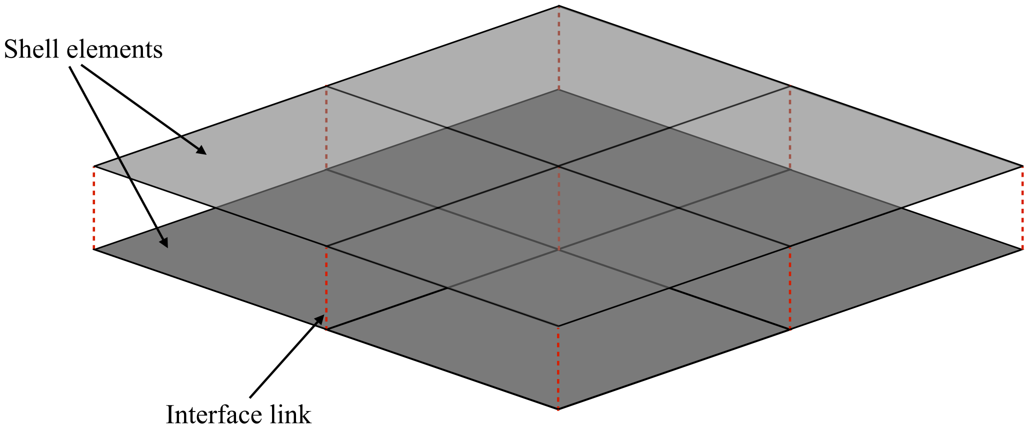

Figure 6.1: Finite element modelling strategy.

shell elements allow the representation of multiple plies, which may differ in fibre angle orientation and ply thickness. A continuum damage model that covers the in-plane damage effects can be assigned to each layer of the multi-layered shell element via the material definition card. Throughout the virtual thickness of the shell element the number of plies and their orientations are defined in the element section.

However, multi-layered shell elements alone are unable to display delaminations as the assigned continuum damage model only addresses in-plane damage. Therefore cohesive interfaces are used to incorporate delamination damage. The shell elements represent two sub-laminates of a symmetric composite, while the cohesive interface elements are located in the symmetry plane where delamination effects are most likely to appear.

The disadvantage of using a shell based model is linked to the loss of precision when investigating through thickness effects. However, the use of shell elements is motivated by the runtime efficiency when dealing with larger structures, while delamination damage can be addressed with the use of cohesive interfaces.

6.2 Finite element environment

The explicit finite element solver Pam-Crash™ is used for the FE simulations presented in the subsequent sections. The solver provides an implementation of multi-layered shell elements via material type 131 [197]. To address the occurrence of delamination damage cohesive interfaces can be selected via material type 303. The material data obtained for the preform and laminate material via the MCMC method are presented in section 5.2.4 and used in the subsequent simulations.

6.2.1 Material type 131

For the representation of the sub-laminates the shell element is located in the mid-plane while the unidirectional plies are stacked up from the bottom to the top throughout the virtual thickness as shown in figure 6.2.

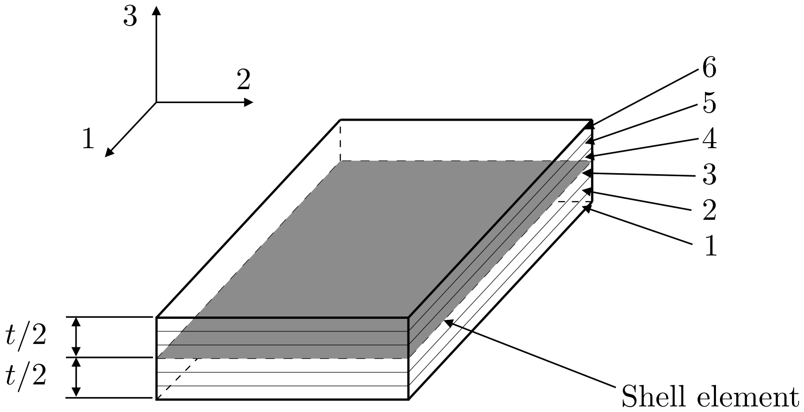

Figure 6.2: Multi-layered shell element as implemented in Pam-Crash™.

The number of plies within the laminate that are represented by the element is defined by parameter NOPLY (see figure 6.3).

```
$           IDMAT    MATYP             RHO    ISINT     ISHG  ISTRAT    IFROZ
MATER /         2      131        1.8E-006        0        0        0        0
...
$ TITLE
NAME Composite_pm45_8s
$     SDMP1      SLFACM      NOPLY        HGM        HGW        HGQ        As
        0.1          0.          8       0.01       0.01       0.01    0.8333
$#    IDPLY       THKPL      ANGPL
          1      0.1375        45.
          1      0.1375       -45.
...
          1      0.1375        45.
...
$  PLY   VAR   PLY   VAR   PLY   VAR   PLY   VAR   PLY   VAR   PLY   VAR   PLY   VAR
     1    11     1    12     1    13     1    14     1    15     2    11     2    12
...
```

Figure 6.3: Material definition for multi-layered shell element.

In the example shown in figure 6.3, eight plies (NOPLY) are represented by the multi-layered element where each ply has an orientation angle (ANGPL) of 45° or -45°. The finite element solver expects the same number of lines with the ply information as declared by parameter NOPLY. Besides the fibre orientation angle, the ply information includes the ply database and thickness assigned to each layer via parameters IDPLY and THKPL respectively. Here all plies have the same thickness of 0.1375 mm. Additional result posting is optional via the auxiliary output definition section in the lower part of figure 6.3. In this example, variables 11 − 15 are written to the solver output file. These variables stand for the model specific shear damage d_{12}, transverse damage d_2, plastic transverse strain ε^p_{22} , plastic shear strain ε^p_{12} and the strain rate $\dot{\varepsilon}$. The composite ply database with the respective material parameters for the multi-layered shell element is selected through the parameter IDPLY. The value 1 under IDPLY refers to the material data set which is assigned to the ply. Figure 6.4 shows the underlying ply data definition card.

```
$          IDPLY    ITYP             RHIFAIL_INP
PLY   /        1       1        1.6E-006       0
$ TITLE
NAME Ply_Data
$    E1_0t      E2_0
    154.34      8.84
$    G12_0     G23_0     G13_0    NU12_0 ...
      4.17      4.17                0.31
...
```

Figure 6.4: Extract from ply definition in Pam-Crash™.

The type of material model is chosen by parameter ITYP. This parameter is set to 1 which indicates the selection of the Ladevèze material model (see section 5.1.1). The remaining section of the ply data contains the material parameters which are required for the selected material model via ITYP.

6.2.2 Material type 303

The interface model implemented in material type 303 is able to represent detachable links between two parts. Figure 6.5 shows the kinematics of the tied interface. A distinct layer, for example the symmetry plane, is chosen to represent the delamination area. A penalty method is used to represent the link between slave nodes and a master segment. The displacement vector $\bar{\delta}$ is decomposed into a normal δ_I (mode I) and tangent δ_{II} (mode II) component by using the master segment normal vector $\bar{n}$ (see figure 6.5).

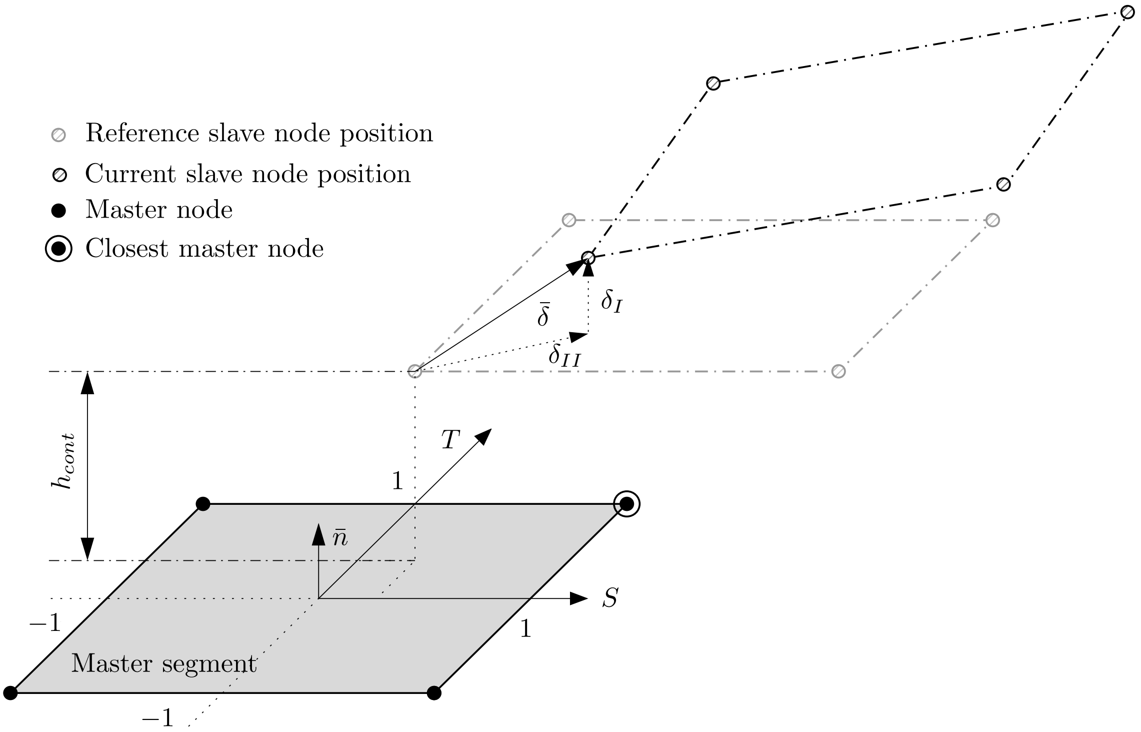

Figure 6.5: Kinematics of the delamination model MATER 303 in Pam-Crash™.

The strains in the normal and transverse directions ε_i are deduced from the displacement vector components of nodes δ_i in relation to the contact thickness h_{cont} for the representation of the delamination behaviour as follows:

$$\varepsilon_i = \frac{\delta_i}{h_{cont}} \tag{6.1}$$

Using equation 6.1 the stress vector is calculated using the following expression:

$$\begin{Bmatrix} \sigma_I \\ \sigma_{II} \end{Bmatrix} = \begin{bmatrix} E_0 & 0 \\ 0 & G_0 \end{bmatrix} \begin{Bmatrix} \varepsilon_I \\ \varepsilon_{II} \end{Bmatrix} \tag{6.2}$$

where E_0 and G_0 are the initial moduli in the transverse and shear direction, which are determined from the in-plane experiments and are matrix dominated properties. ε_I and ε_{II} are the normal and tangent components of the strain vector which are used to determine the related stresses (σ_I and σ_{II}). Equation 6.2 shows a linear-elastic relation for the delamination interface which is valid until reaching the fracture initiation threshold stress σ_I^{max} (see figure 6.6). The moduli are then degraded using the damage model described in section 5.1.2. The interface response behaves in accordance with the experimentally determined energy release rate which corresponds to the area under the bi-linear curve.

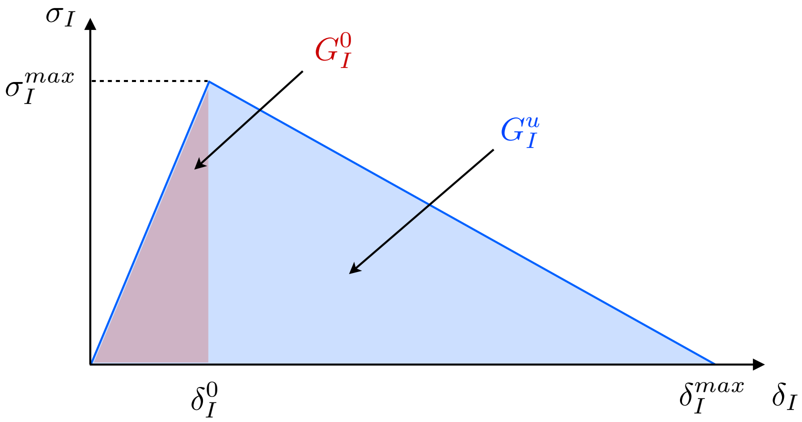

Figure 6.6: Stress-crack-opening diagram for mode I delamination (similar for mode II).

6.2.3 Contact algorithms

In the context of finite element simulations a contact algorithm is used to treat the interaction between contacting bodies [13]. Therefore the bodies which could potentially interact with each other need to be defined in a contact table. The following classification is used for a non-symmetric contact problem with two bodies:

Master-segments which are defined as the penetrable body in the contact pair. Therefore the segment surface is computed from the master-nodes.

Slave-segments which are defined as the contact body which penetrates the master segments via the slave-nodes.

Often non-symmetric contacts are defined to save CPU runtime. Therefore it is important to define the master and slave contacts in accordance to the above definitions. However, the extension to a symmetric contact algorithm is straightforward. The advantage of using a symmetric algorithm is the additional check for possible penetrations on both contact surfaces. Such an algorithm can be separated into two steps. In a first step the contact search algorithm tries to identify potential contact pairs, whereas the second step investigates the present contact condition. Depending on the penetration level a contact force is introduced in order to generate a physical behaviour of the touching contact bodies. Figure 6.7 illustrates the general principle of the contact algorithm. To ensure an efficient contact search algorithm the following points should be considered [197]:

- The master-segment should be discretised with a coarser mesh than the slave-segment.
- The surface areas of the two segments should not differ by more than factor 4.

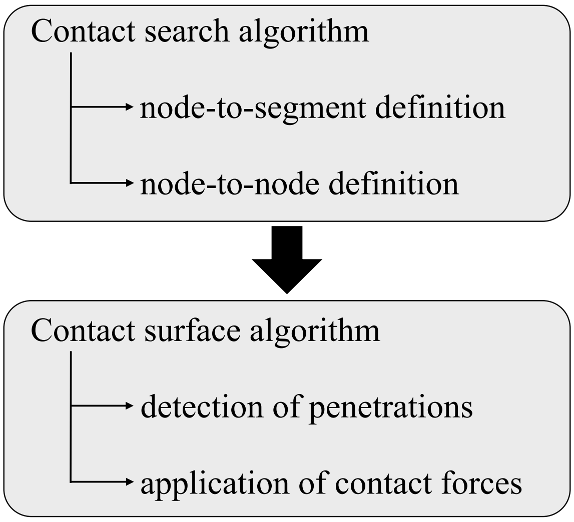

Figure 6.7: Contact algorithm.

The contact types described in the following use the penalty method to generate the contact forces. The magnitude of these forces are proportional to the penetration depth.

6.2.3.1 Master-slave contact - type 34

The contact type 34 is a symmetric algorithm which examines both predefined bodies for possible interactions. In the case of penetration a penalty force is applied to prevent perforation. Therefore a search box is defined around each master segment as illustrated in figure 6.8. If no further information is provided in the contact definition card the search box is generated using the contact thickness of the shell element.

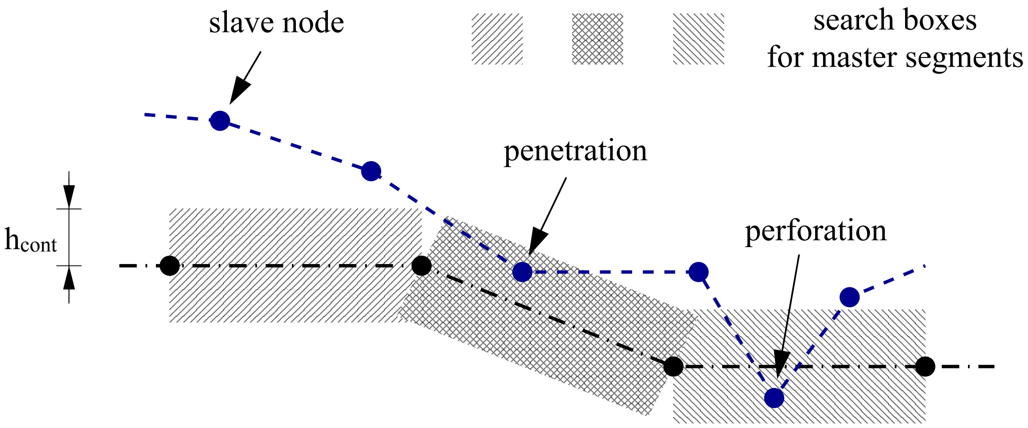

Figure 6.8: Illustration of master-slave contact.

6.2.3.2 Self-penetration contact - type 36

This contact type can be applied when the large deformation or separation of a part may lead to a penetration to itself. This contact type requires only the definition of a slave-segment. This contact type is computationally expensive, hence it should be applied to restricted areas, nonetheless, it might be advantageous for the model runtime to use only a single self-penetration contact instead of several symmetric master-slave pairs.

6.3 Finite element analysis

6.3.1 Model validation via three point bending test

The three point bending test was chosen to validate the modelling concept in combination with the laminate data set obtained via the MCMC method as described in the previous chapter. This test combines good reproducibility while providing a set of information that can easily be compared with the results obtained from a finite element solution Furthermore, this model allows to test the material response with respect to the identified material parameters for the reference material via the MCMC method as described in the previous chapter.

Figure 6.9 illustrates the general assembly of the finite element model. The model comprises four different parts and includes a total of 10191 nodes connecting 9760 elements. The number of elements was fixed as a result of a mesh sensitivity study. Two fixed support cylinders are located underneath the laminate and a third cylinder

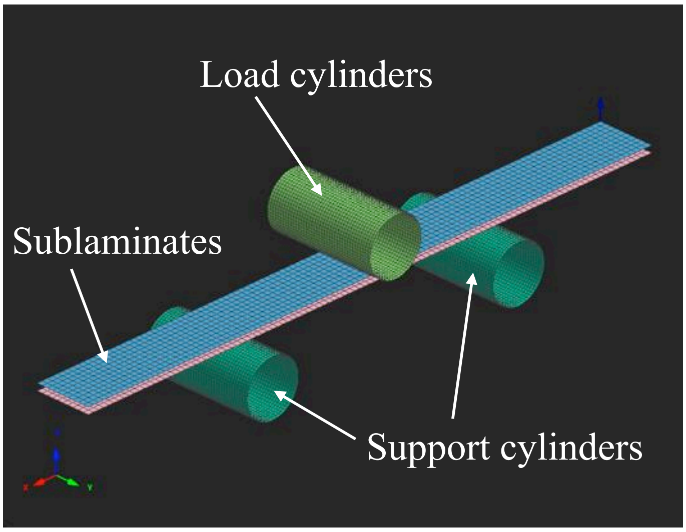

Figure 6.9: Model assembly for three point bending simulation.

is used to introduce the load from the top of the laminate. The laminate has the dimensions of 110×10×2.4 mm and is conceptually designed of two separated parts, where each of them represents a sub-laminate of 12 UD layers with a virtual thickness of 1.2 mm. As both sub-laminates have the same properties the material card can be assigned to each ply of both parts via element type 131.

A set of contact definitions are applied to the model in order to maintain physically realistic behaviour. A self-penetration contact of type 36 (see section 6.2.3.2) is defined between the two sub-laminates. Two further symmetric contacts of type 34, as described in section 6.2.3.1, are defined between laminate, support cylinders and loading cylinder respectively. In contrast to the self-penetration contact where part ID numbers were used to specify the contact pair, node and element IDs where used in the symmetric contact. Hence numerical efficiency is maintained as the contact search algorithm can be limited to a restricted region.

Two centre of gravity (COG) points were defined in the laminate symmetry plane above and underneath the cylinders as shown in figure 6.10. These COGs are also used in the rigid body definition of the cylinders. Moreover the boundary conditions are applied to these points. Hence all degrees of freedom are constrained for the lower COG which is connected to the support cylinders. The top COG only allows movements in the z-direction and a linear displacement function is assigned to it. In the definition of the displacement function a maximum displacement of 6 mm is reached after 80 ms. Furthermore, this COG node acts as the reference node for the load introduction cylinder.

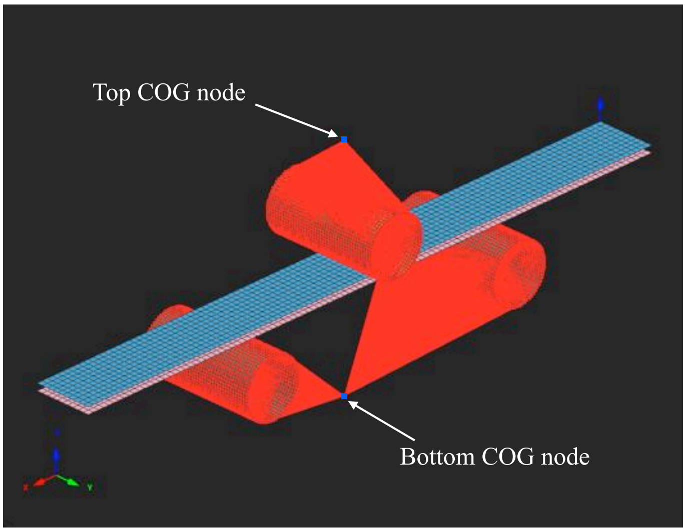

Figure 6.10: Rigid body definition in three point bending simulation.

A time-history-plot (THP) node was defined in the model symmetry plane (see figure 6.11) to generate a load versus deflection plot that can be compared with the experimental results. The load versus deflection plot is generated using the contact force between the support cylinder and the laminate, whereas the displacement information is provided by the THP node.

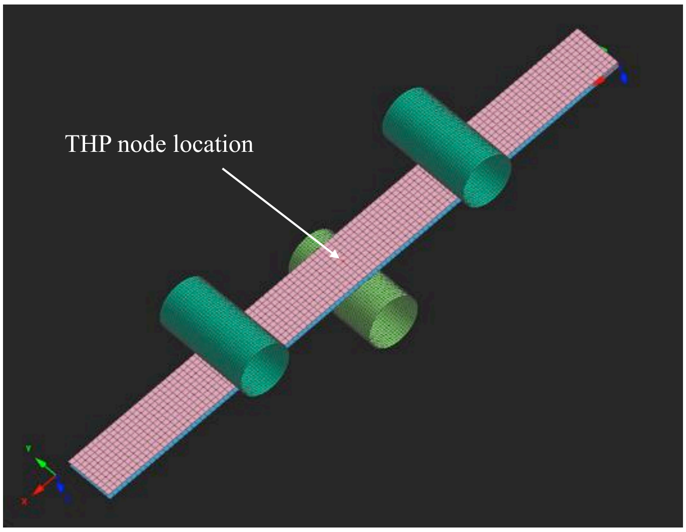

Figure 6.11: Location of Time History Plot (THP) node in the three point bending simulation.

Figure 6.12 illustrates the results from the finite element simulation. The load versus deflection curve obtained is in good agreement with the experimental data of the more compliant responses. The calculated flexural modulus of 135 GPa is very similar to the result of test 1 and 4 (133 and 135 GPa respectively).

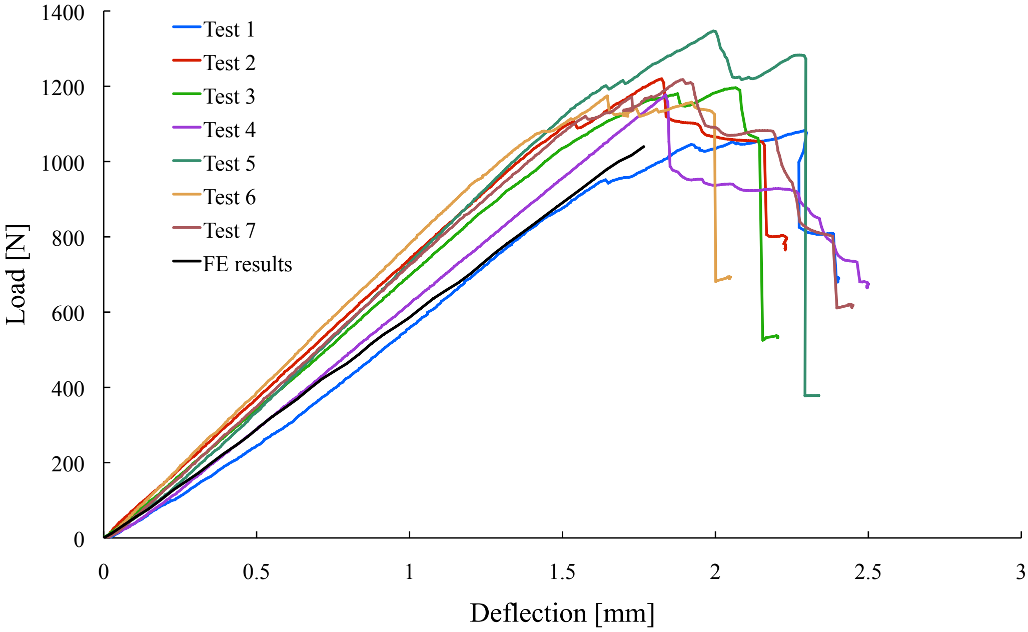

Figure 6.12: Comparison between three point bending experiments and result from finite element simulation.

The failure part of the curve, as observed in the experimental data, is not generated by the finite element solver. The simulation stops at a maximum force of 1040 N with a displacement of 1.8 mm as too many elements failed and were deleted. However, there is a small non-linearity that indicates damage development just before the run termination.

6.3.2 Preform spar section impact

An impact scenario was proposed to assess the robustness of the preform spar section component. The spar section was modelled with the $[0°/90°]_{2s}$ layup as described in section 3.2.3.2. The spar section FE model comprises two separated shell based parts, with each representing four layers of a symmetric layup. Here, the shell elements have a virtual thickness of 0.5 mm and are located in the mid-plane of the respective sub-preform. The overall dimensions of the FE model agree with the dimensions of the manufactured part (144×158×78 mm). The preform was discretised using a constant mesh seed with an element size of 2.5×2.5 mm. Hence, 13806 nodes and 13456 elements, resulting from a mesh sensitivity study, were used for the discretisation of the preform.

The in-plane continuum damage model described in section 6.2.1 is used to simulate the in-plane material behaviour, while delamination effects are addresses with the out-of-plane material model described in section 6.2.2. A cohesive interface is defined between the two sub-preform parts in the symmetry plane of the stack. The material parameter set for the homogeneously bindered preform material obtained via the MCMC method was used in the context of this model. This material data set does not contain the parameters for the compressive behaviour in the fibre direction. Hence, the compressive elastic modulus in fibre direction was set to 70% of the tensile elastic modulus. The correction factor for non-linear fibre compression was set to 0, while the initial and ultimate failure strains were defined as 40% of the tensile values.

6.3.2.1 Model assembly

Figure 6.13 illustrates the model for the impact scenario. A local coordinate system was generated and a support plane was defined with an offset of 0.75 mm from the outer sub-preform side surface of the preform component. The offset is determined from the virtual thickness of the shell elements (1 mm for support elements and 0.5 mm for sub-preform elements) to ensure a touching surface. The generated support plane has dimensions of 200×224 mm and is discretised with 7200 shell elements and 7371 nodes.

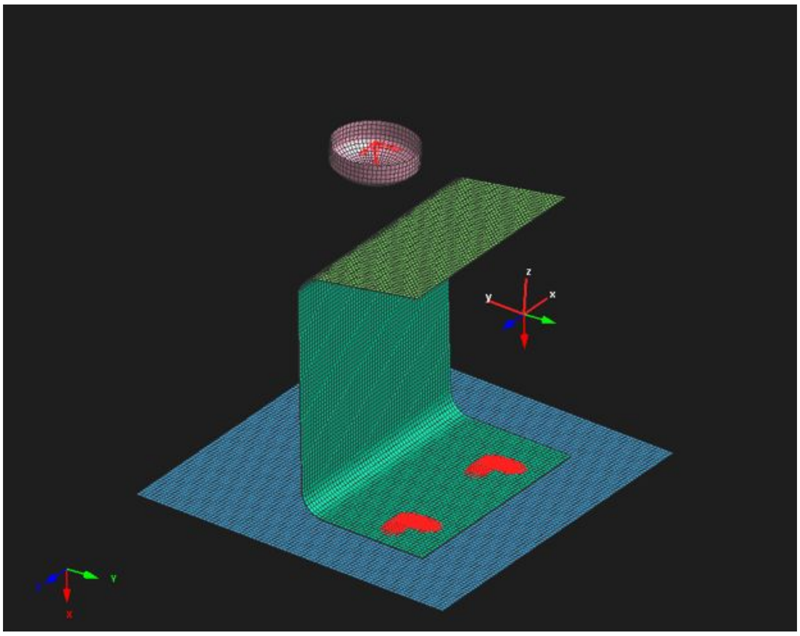

Figure 6.13: Assembled model for preform spar section impact.

A spherical impactor is modelled relative to the local coordinate system to ensure a perpendicular alignment with respect to the support plane. Figure 6.14 shows the impactor representing the head used in the experiments. The total height of the head is 20 mm with a diameter of 50 mm. The impactor head merges from a cylinder into a spherical shape. This profile is rotated around its symmetry axis to generate a meshable surface above the preform model.

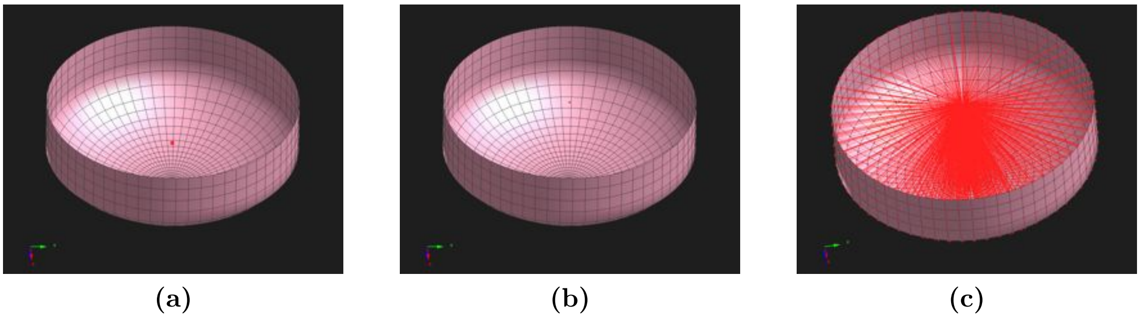
(a) **(b)** **(c)**

Figure 6.14: Impactor head with (a) visualisation of localised mass, (b) highlighted COG and (c) rigid body definition link to COG and mass point.

Three additional nodes were added to the model, hence a total number of 22693 nodes and 22167 elements are used within this model. Two of the additional nodes are located above the impactor head while the remaining node is positioned underneath the support plane. Two of these nodes act as COGs and are used to define the rigid body property for impactor head and support respectively. These nodes are linked with the respective COGs to employ the boundary conditions. In order to prohibit any movement of the support plane all degrees of freedom are blocked via the bottom COG. To allow the movement of the impactor head the related COG is only free to move in the z-direction of the local coordinate system. Furthermore, an initial velocity of -4.4 $^{m}/_{s}$ in the z-direction of the local coordinate system is assigned to the COG located above the impactor head. The other node positioned above the impactor head is also included in the rigid body definition of the impactor head and acts as a localised mass point. A mass of 3 kg was assigned to this node. These conditions result into a starting energy of 29.9 J which corresponds to the target energy of the experiment.

An additional set of boundary conditions is applied to the preform directly to represent the clamps that hold the preform in position during the experiment as shown in figure 6.13. Therefore nodes of the inner sub-laminate, which are located in the region of the clamps are blocked in all degrees of freedom.

A self-penetration contact of type 36 was defined for the preform parts and symmetric contacts of type 34 were defined for the rigid bodies and the preform part respectively.

6.3.2.2 Model results

Figures 6.15 and 6.16 show two states within the impact scenario while comparing the footage of the experiment with the simulation. The initial state of the impact is shown in figure 6.15. The impactor strikes the area of the fillet segment and causes the structure to bend in the symmetry plane of the top surface. The corresponding simulation shows the in-plane damage map at the initial contact between impactor

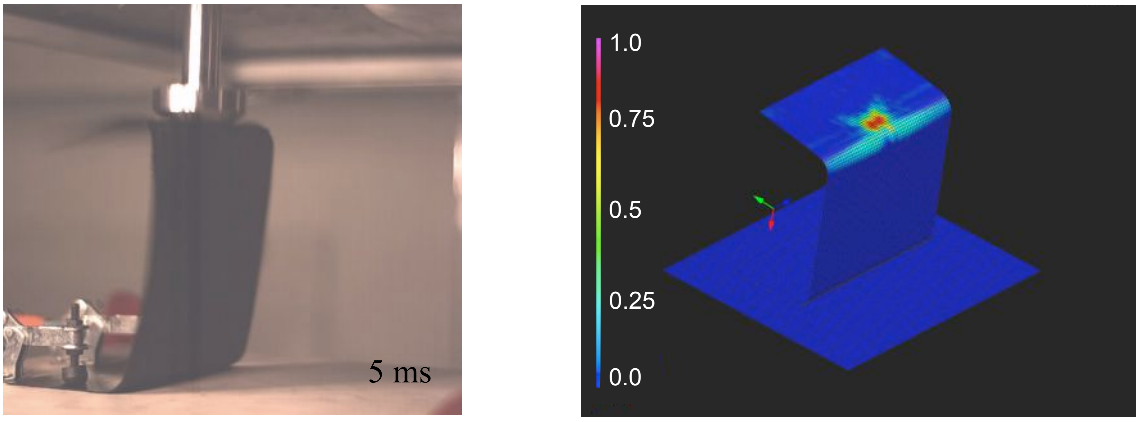

(a) (b)

Figure 6.15: Impact event prior to support touch, (a) high speed camera footage of test 4 and (b) in-plane total damage map from FE simulation.

head and component. Only localised damage can be observed under the removed rigid body.

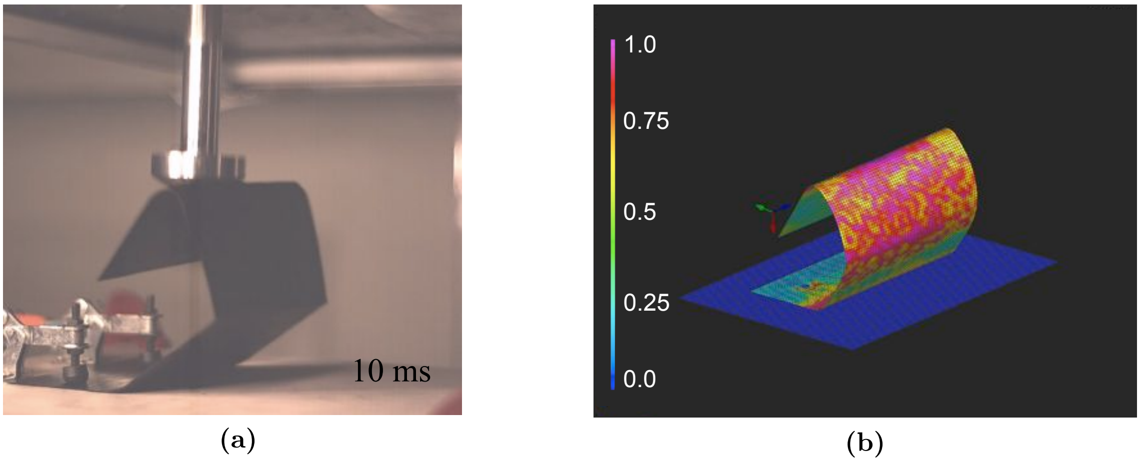

(a) **(b)**

Figure 6.16: Impactor rebound from support, (a) video footage of test 4 and (b) corresponding in-plane total damage map from FE simulation.

Figure 6.16 corresponds to a later stage of the impact. Here the high speed footage shows the deformed component where the leg segment is bent inwards and the top surface is buckled in the symmetry plane at the location of the initial bending. The simulation is capable of representing the corresponding experimental state very closely. The deformation of the component and the in-plane damage map shown provide realistic results, especially in the symmetry plane of the top surface where total damage is indicated.

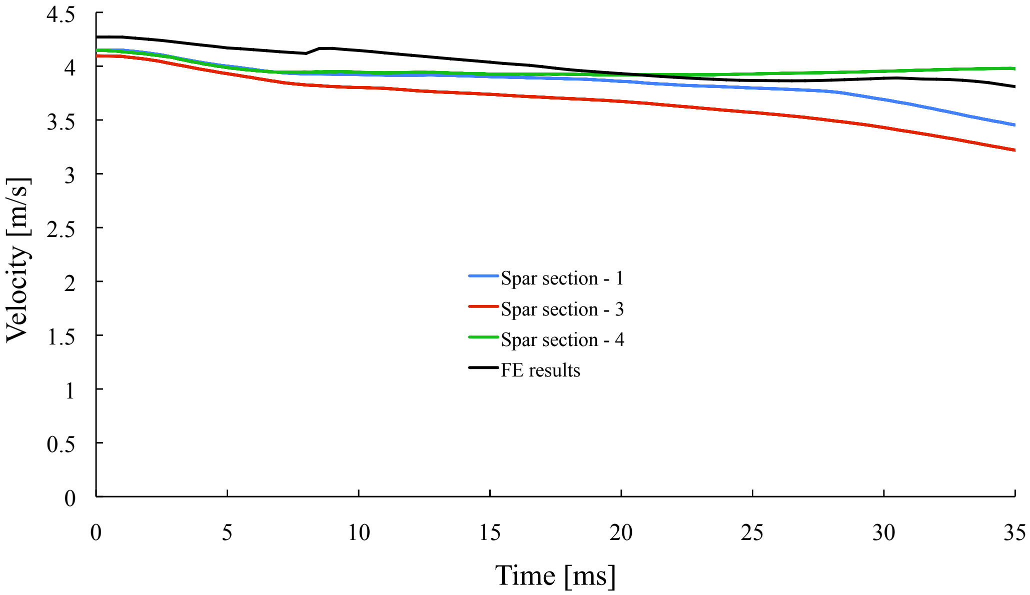

Figure 6.17: Comparison of experimental and simulated impactor velocities for the preform impact scenario.

Besides the damage maps the simulation also provides the velocity profile of the impactor head which allows a direct comparison to the experimental data as shown in figure 6.17. Here the impactor head starts with an initial velocity of 4.4 m/s whereas the experiments start with velocities in the vicinity of 4.1 m/s. The velocity profile resembles closely the one recorded in test 4 throughout the duration of the impact. Similarly to the experiment the striker is slowed down by the damping effect caused by the component. Similarly to test 4 the component is pushed aside by the impactor (see figure 4.43), hence the impactor is not slowed down as much as the experimental data shows for case of test 1 and 3. The influence of the component being crushed underneath the striker head is particularly interesting for the time range prior to the impactor/support contact where the compacted preform helps to absorb the impact energy.

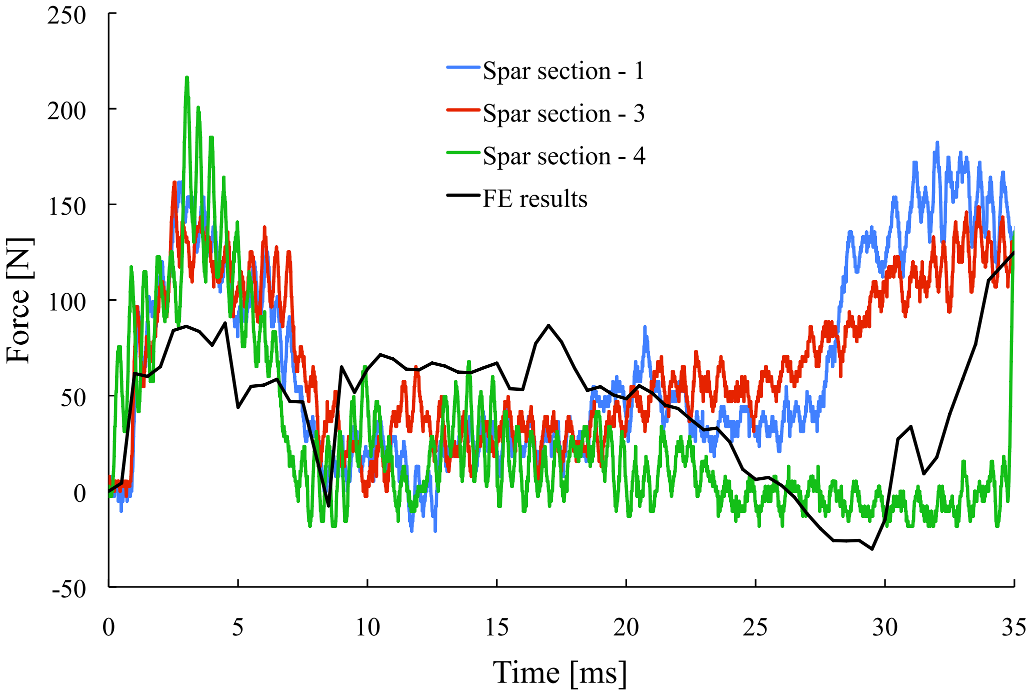

Figure 6.18: Force history plots of experimental data and finite element simulation for the preform impact.

The force profile of the impactor can be deduced from the acceleration of the impactor head COG shown in figure 6.14. Figure 6.18 illustrates the result and allows the comparison with the experimental data. The model is capable of representing the force evolution for the scenario. The initial contact between the impactor head and the preform lasting up to 8 ms is reproduced very well. The simulation shows a lower initial force level of around 90 N while the corresponding forces from the experimental observations indicate forces between 160 to 215 N. However, the experimental curves contain a significant amount of noise. In the second section (8 -

20 ms) the component deforms underneath the impactor head which slides above the component and causes relatively low forces in the case of the experiments. For the same region, the simulation shows higher forces which could be related to the unverified friction coefficient of 0.3. In the last part of the curve the experimental curves of test 1 and 3 differ to number 4 due to the deformation of the component under the striker head (compare figures 4.42 and 4.43). In test 4 the component is not crushed by the impactor head, hence no contact force between the head and the component is present until the impactor reaches the support plane. The simulation is acting in a similar manner.

The energy profile of the simulation the same characteristics as the experimental curves (see figure 6.19). The initial part of the curves evolve in a similar fashion while the latter part shows close resemblance with test 4 and differs from test 1 and 3 due to the deformation of the component in the later part of the experiment.

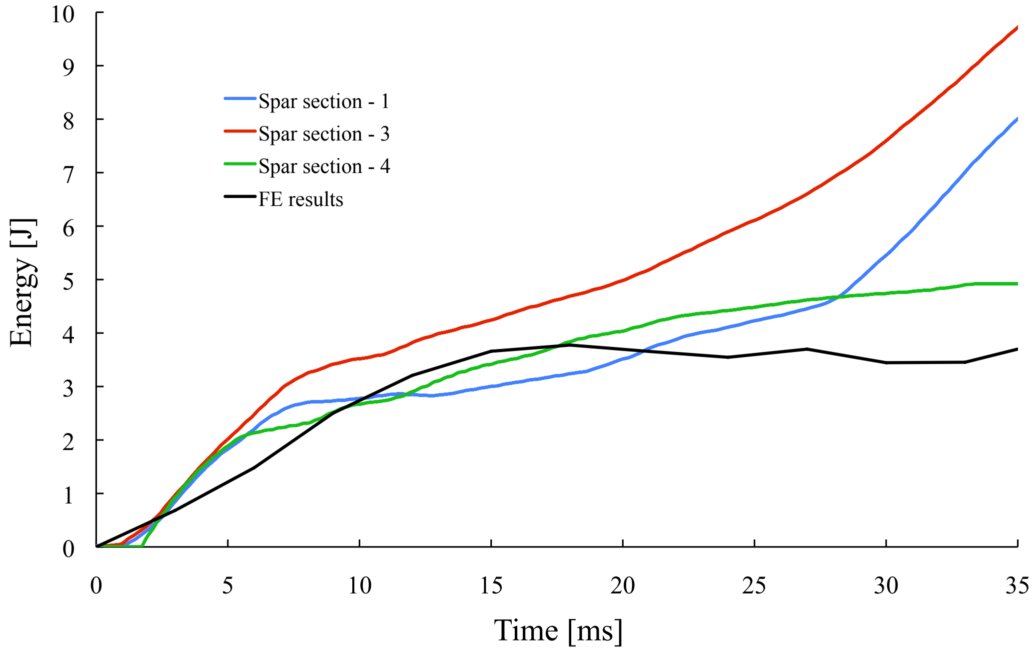

Figure 6.19: Comparison of energy evolution plots for experimental and simulated preform impact scenario.

6.3.3 Exploratory simulation on a helicopter component

This section describes the simulations performed on a helicopter pitch horn. The motivation for these simulations is to investigate the influence of fibre shear due to the manufacturing process on the mechanical performance of the component. Such local changes are generally not considered in the design process where the nominal fibre orientation is used. The shear of the material depends on one hand on the

drapability and formability of the material itself but also on the draping parameters, such as starting point and roll out direction. Optimised draping strategies can be developed to minimise the shear of the material with the aid of software tools.
Hence three models of the helicopter component are compared in the result section of this part. The first simulation follows the usual approach by using the nominal fibre orientation from a design perspective, while the second and third simulation incorporate the local fibre orientations from two different draping strategies. The second model uses the fibre shear information which results from current manufacturing process while the third model uses the fibre shear information determined from a drape optimisation via a genetic algorithm (GA). This optimisation was not part of this work and is therefore not described here.

6.3.3.1 Description of the pitch horn component

The information with respect to geometry, layup and load cases for a large scale component was provided by the PreCarBi project partner Eurocopter. The pitch horn is located at the end of a rotor blade as illustrated in figure 6.20. The purpose of this part is to introduce the inclination angle of the rotor blade. Furthermore, damper attachments are fitted on this part to eliminate vibrations from the blade, which could propagate through the rotor shaft and lead to unsatisfactory flight characteristics. The reference axis is pointing in the rotor direction. This axis is also later referred to in the assembly of the FE model where the fibre orientation is set relative to the reference frame.

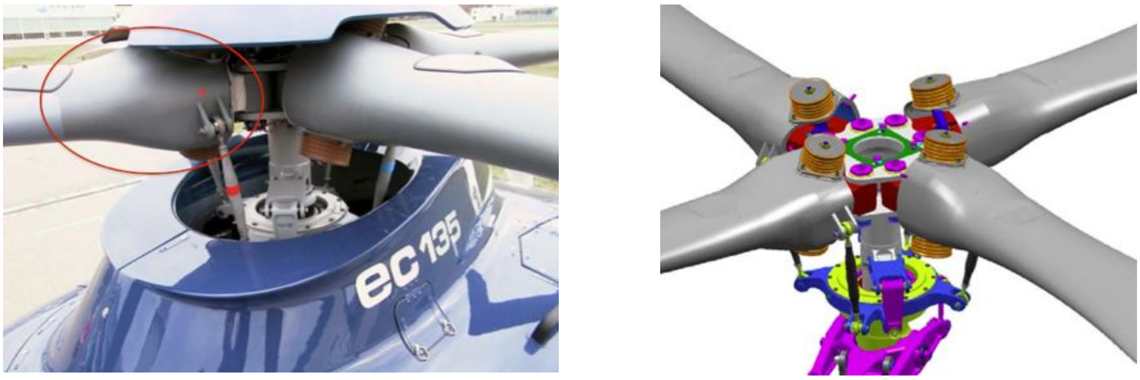

(a)

(b)

Figure 6.20: Location of the pitch horn component (a) assembly within the rotor head and (b) CAD illustration.

Currently the manufacturing process of this component involves different steps before it is finally merged from two separately hand manufactured parts. Each part is layed up as a separate shell on two tools. The tools can be differentiated into two sections. A box-shaped racetrack profile that blends to an oval segment is attached to the rotor blade. After the draping procedure is finished the fabrics are trimmed. The next manufacturing step includes the positioning of the pitch lever profiles which transfer a force onto one side of the component. Therefore a 100 mm long and 8 mm wide slot is cut through the shell under a 22° angle in order to place a U shape insert while a second L shaped lever profile is placed on top of the exterior skin. Subsequently the half-shells are pressed together in a tool with a sacrificial layer of glass fibre for the damper contact on the top and bottom side. In a final step the part is placed in the tool and then cured in an autoclave. Figure 6.22 illustrates the load case used for the simulations. The load case, as provided by the project partner Eurocopter, indicates the location of the assigned forces. Here two normal forces F_Z located on the top and bottom surfaces of the component represent the damper related loads, while pitch lever force F_{ST} is applied under an angle of 22° on the side of the component. Furthermore, these forces have a predefined ratio.

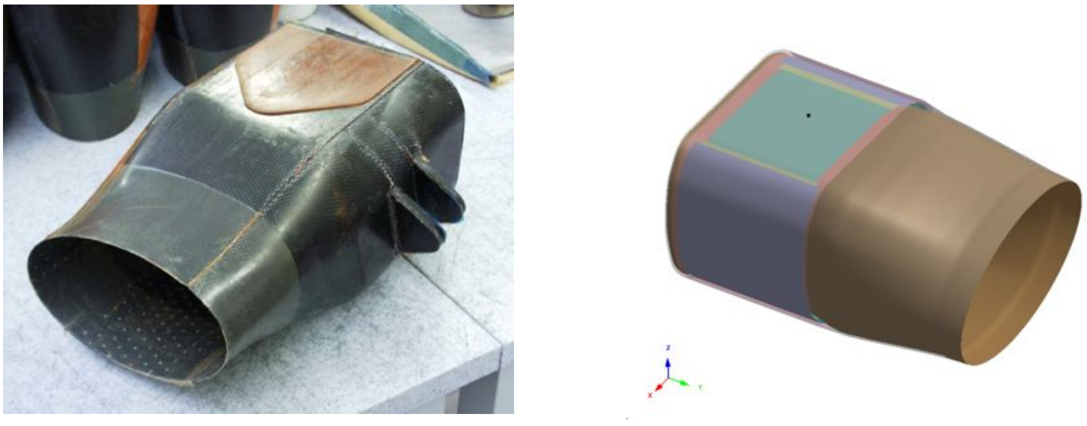

(a) (b)

Figure 6.21: Pitch horn component, (a) isolated part and (b) FE base model.

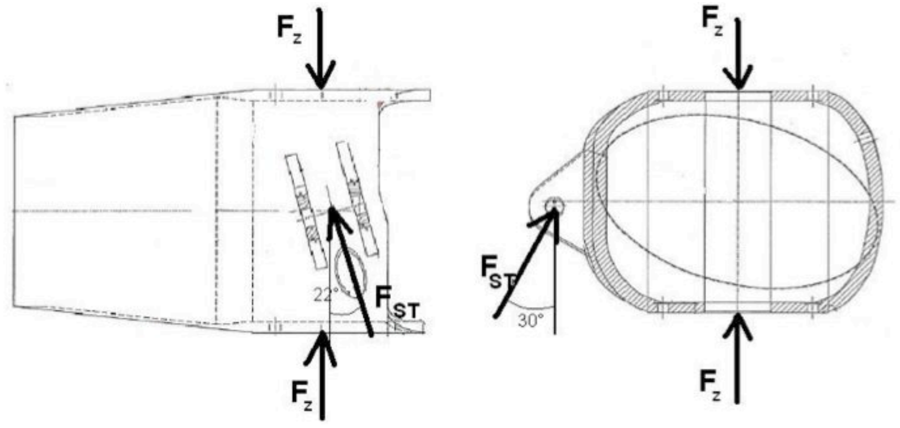

Figure 6.22: Load cases for the rotor component.

6.3.3.2 Design model assembly

The base model comprises six different parts where the exterior and interior skins follow a symmetric $[\pm 45°]_{4s}$ layup. The remaining four parts correspond to unidirectional (UD) fillers. The symmetry plane for the $[\pm 45°]_{4s}$ arrangement is located between the interior and exterior skin. The information related to the fibre orientation for a part is defined in the material definition card of material type 131 (see section 6.2.1).

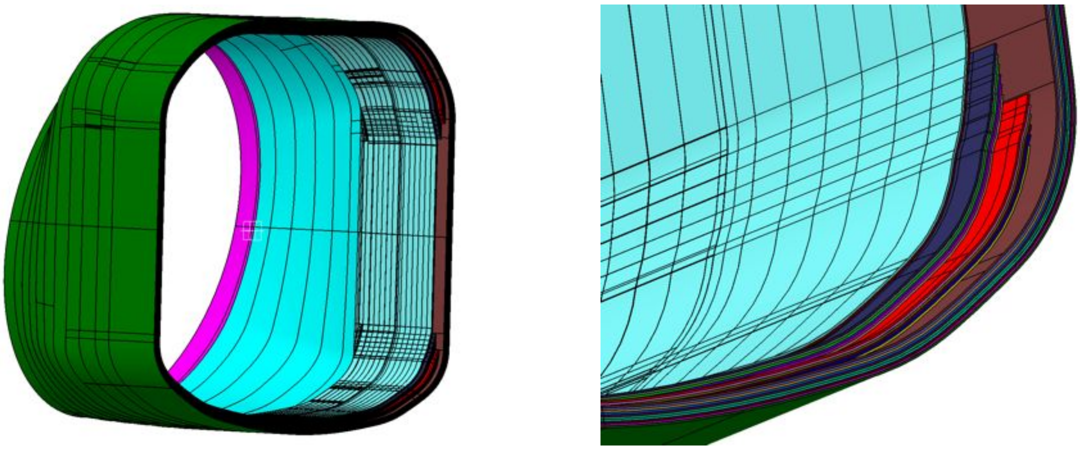
(a) **(b)**

Figure 6.23: Manufacturing details of the ply layup, (a) view from race track side and (b) close up with detailed information.

Figure 6.23 illustrates the ply layup of the design including the filler saddles on both ends of the race track profile. The discretisation of the filler arrangement for the FE model is illustrated in figure 6.24c.

The interior and exterior skin are represented by a single layer of multi-layered shell elements. The joint between the two shell components which occurs due to the manufacturing process is not considered in the model. The interior and exterior skins are modelled as continuous parts using one layer of shell elements with the layup of $[45°, -45°]_4$ and $[45°, -45°]_4$ respectively. Similarly to the internal and exterior skin the filler sets are represented by a single layer of shell elements (figure 6.24c). A total of 31873 nodes and 31045 elements are used to discretise the component in the finite element model. The average element size is 5×5 mm.

The individual parts are connected via cohesive interfaces. The connectivity between these parts is established by using a node-to-element definition. Figure 6.25 illustrates the interface definition on the basis of the two innermost UD filler sets. To avoid the occurrence of self-penetration all parts in the FE model are included in a contact definition of type 36 (see section 6.2.3.2). Nodes located at the elliptical section of the interior skin are fully constrained in translational and rotational degrees of freedom as shown in figure 6.26.

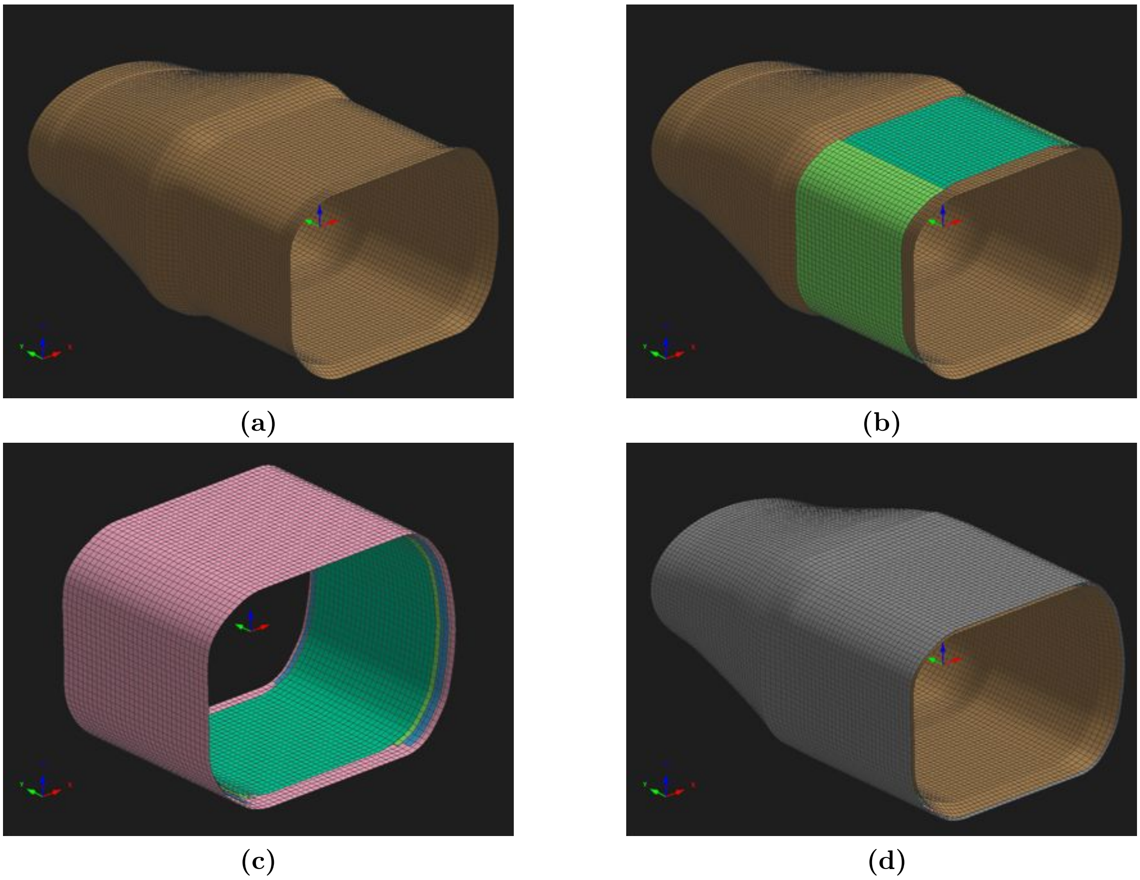

(a)

(b)

(c)

(d)

Figure 6.24: Model assembly of the component, (a) interior skin, (b) interior skin with UD filler arrangements, (c) UD filler sets, (d) assembled component.

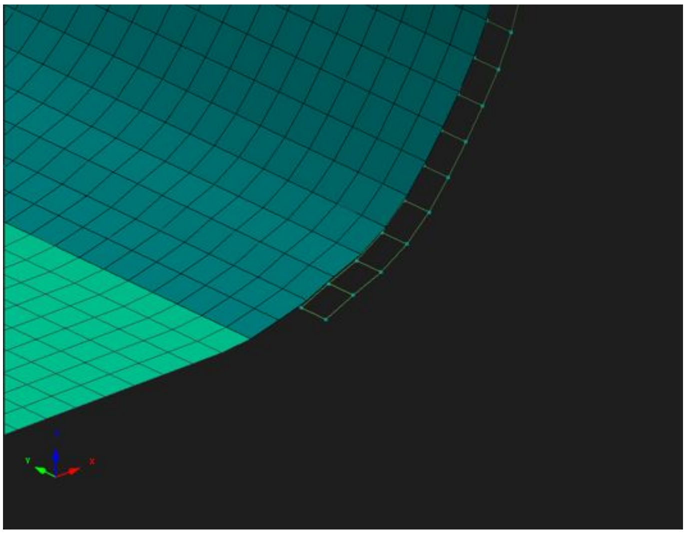

Figure 6.25: Delamination interface (Node-to-Element) illustrated for the the UD filler section.

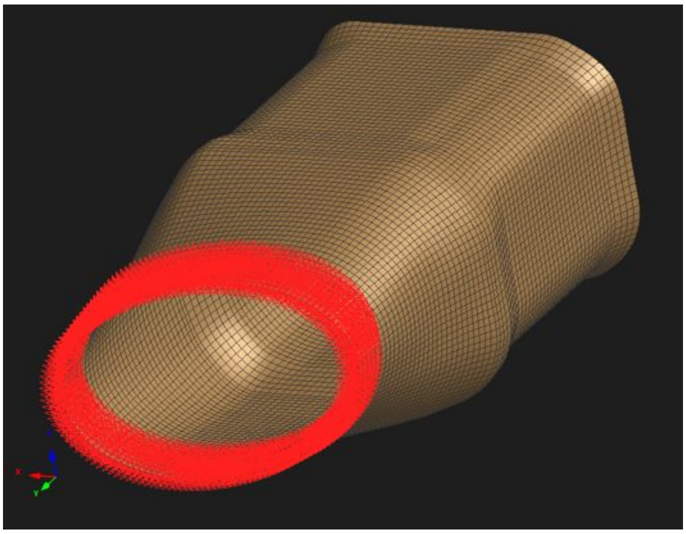

Figure 6.26: Boundary condition on the elliptical end of the interior skin.

Three centre of gravity (COG) nodes are located in distinct positions for the application of load functions via rigid body definitions (see figure 6.27). Compressive forces with a maximum value of 6 kN act on the COG located at the top and bottom side of the race track section. In addition, a second force with of a magnitude of 16.8 kN is applied to the COG node located on the side. The direction of this force is defined via a local coordinate system which is tilted by 22° in order to represent the conditions present at the pitch lever profiles. As the pitch lever profiles are not modelled explicitly all nodes in the respective area that are affected by the profiles are used for the rigid body link definition. In the case of the L shaped lever, which is located towards the box-shaped side of the component, only nodes of the exterior skin are selected. For the U shaped profile all nodes from all parts within the corresponding area are selected as the lever is placed through the component. All three

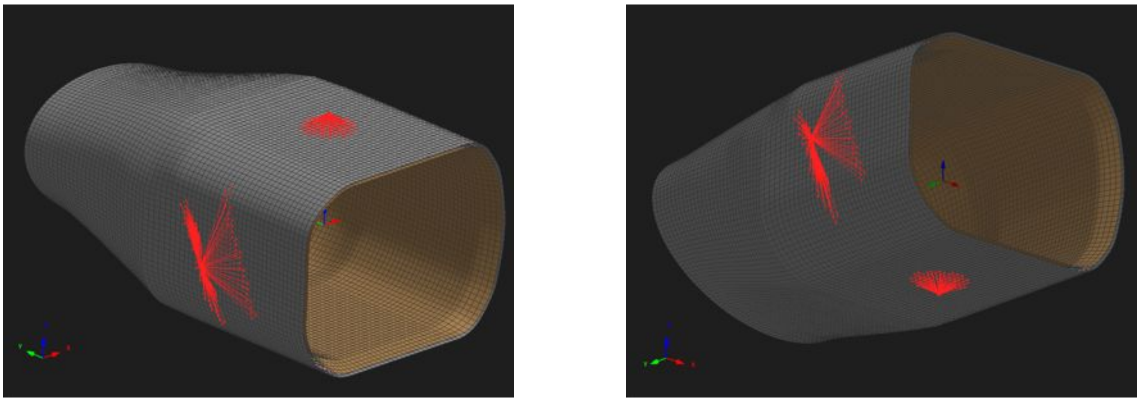

(a) **(b)**

Figure 6.27: Load application, (a) top view, (b) bottom view.

applied forces are defined via a linear function which reaches the maximum value at the end of the simulation after 5 ms.

6.3.3.3 Drape model assembly

The fibre orientation of the exterior and interior skin results from the manufacturing process and are determined via the drape simulation software Pam-Quickform [230]. Two sets of fibre angles are used for the drape models, (a) fibre shear from the draping strategy of the current manufacturing process and (b) fibre orientation obtained from an optimised draping strategy as identified through a GA with the objective of shear angle minimisation. The optimisation task was not part of this work, however, the fibre shear data was provided through the work presented in [231]. In that work it was observed that minimum shear occurs in the race track profile section of the component in the vicinity of the centre line. Shear maximises towards the joint line of the two shell components. The shear angle distribution reflects the slight asymmetry of the component. The average maximum shear angles obtained are 32° and 16° following the current and optimised draping strategy respectively.

Conceptually the drape model is based on the design model which is described in the previous section, however, as the data related to the fibre orientation are stored in the material definition card, which again is linked to the part definition, it is necessary to decompose the outer and interior skin in such a way so that each element is defined as a separate part (see figure 6.28). Instead of six different parts, as for the design model, the drape model comprises 18832 parts which are included in the contact definition table.

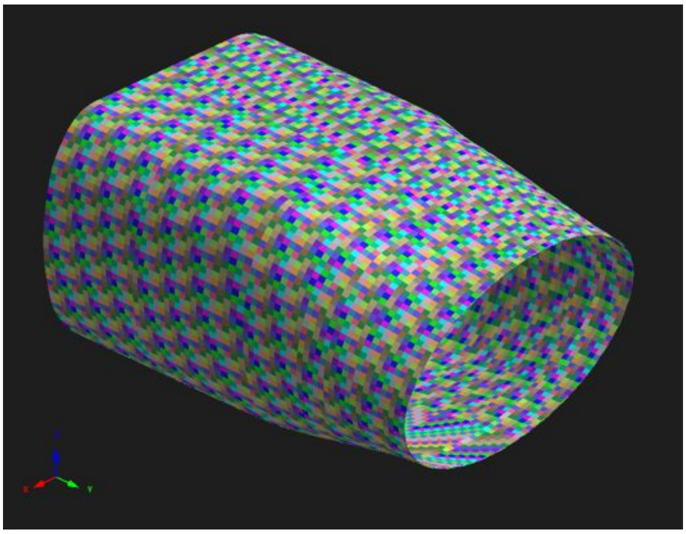

Figure 6.28: Drape model assembly with decomposed external and internal skins.

6.3.3.4 Model results for nominal fibre angle model

Figures 6.29a and 6.29b show the damage maps of the in-plane and shear damage at the end of the design model simulation. The simulation indicates the first instance of a totally damaged element occurs after 3.5 ms, which corresponds to force values of 4.2 kN for the compressive loads from the top and bottom race track profile and 11.8 kN for the lug force.

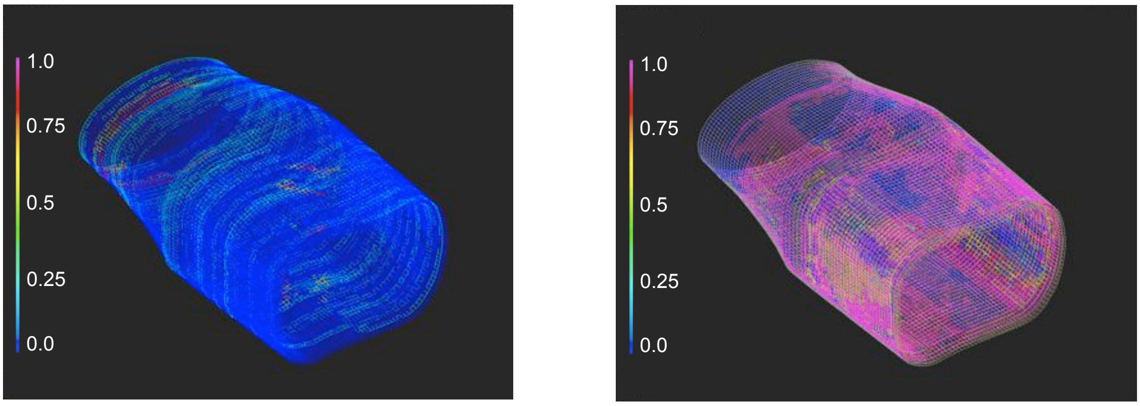

(a) (b)

Figure 6.29: Damage maps for the pitch horn component with nominal fibre angles, (a) in-plane and (b) out-of-plane shear damage.

The model shows an area of maximum damage close to the elliptical section where the skins have their maximum deflection. This segment of the model also corresponds to the fixed boundary condition at the interior skin. Besides this segment the overall damage remains mainly localised to the oval end of the component and the lug section. Areas experiencing complete shear damage, as extracted from the cohesive interfaces, can be found in the fillet sections of the component, while other levels of shear damage are widely spread over the component.

6.3.3.5 Model results for base drape model

The base drape model uses the fibre angle information of the current draping process. Figures 6.30a and 6.30b show the damage maps for the in-plane and out-of-plane shear damage respectively. For the in-plane damage map the area indicating total damage that is located close to the oval section is slightly smaller than for the design model, however, the damaged region has a similar size compared to the design model but shows slightly lower damage values. When comparing the in-plane damage distribution of design and base drape model throughout the whole component slightly higher values can be seen for the drape model. This effect can also be found when comparing the out-of-plane damage map. The areas with failed interfaces resemble those of the design model. The model indicates that total in-plane damage occurs first after 3.4 ms. This corresponds to a compressive top and bottom force of 4.1 kN and a lug force of 11.42 kN.

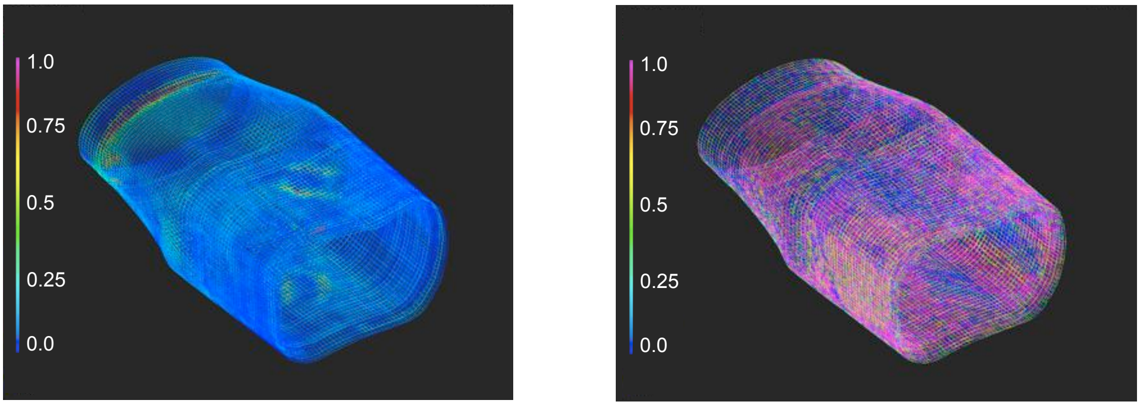

(a) (b)

Figure 6.30: Damage maps for the pitch horn component with the base drape fibre orientations, (a) in-plane and (b) out-of-plane shear damage.

6.3.3.6 Model results for optimised drape model

The optimised drape model contains the draped fibre angles which are the output of the drape optimisation via the genetic algorithm. Similarly to the base drape model the main damage areas are restricted to the oval section and the top and bottom compression areas on the race track profile (see figure 6.31a). A similar in-plane damage value distribution to the base drape model is observed, whilst the out-of-plane map shown in figure 6.31b comprises slightly larger damaged areas on the sides of the component. The remaining areas show low damage values comparable

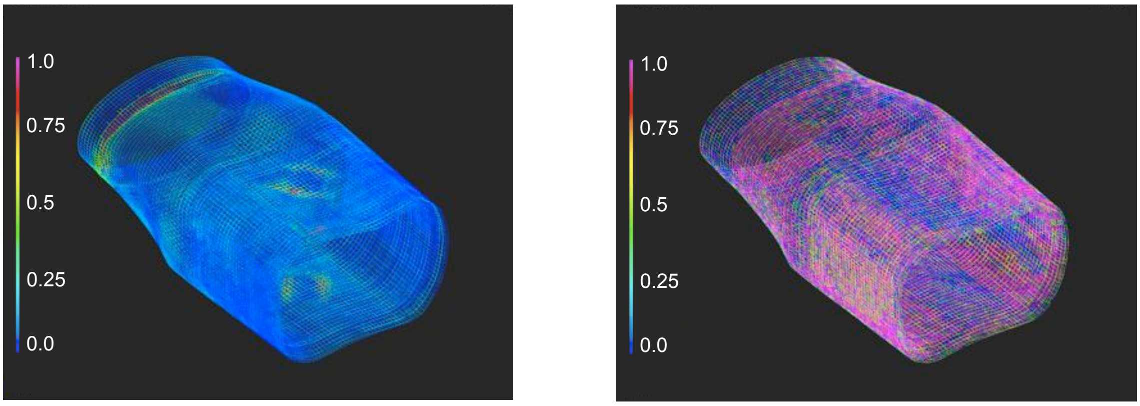

(a) (b)

Figure 6.31: Damage maps for the drape optimised pitch horn component, (a) in-plane and (b) out-of-plane shear damage.

to the base drape model. Sudden failure of the component occurs after 3.3 ms which corresponds to a force of 3.9 kN which is applied to both race track stamps and a force of 11 kN applied to the lugs on the side of the component.

6.3.3.7 Comparison of pitch horn models

To compare the mechanical performance of the three models, the in-plane damage evolution was extracted from two elements which are located in areas with high shear angles. The first element in location A is part of the interior skin while the second element in location B belongs to the exterior skin (see figure 6.32).

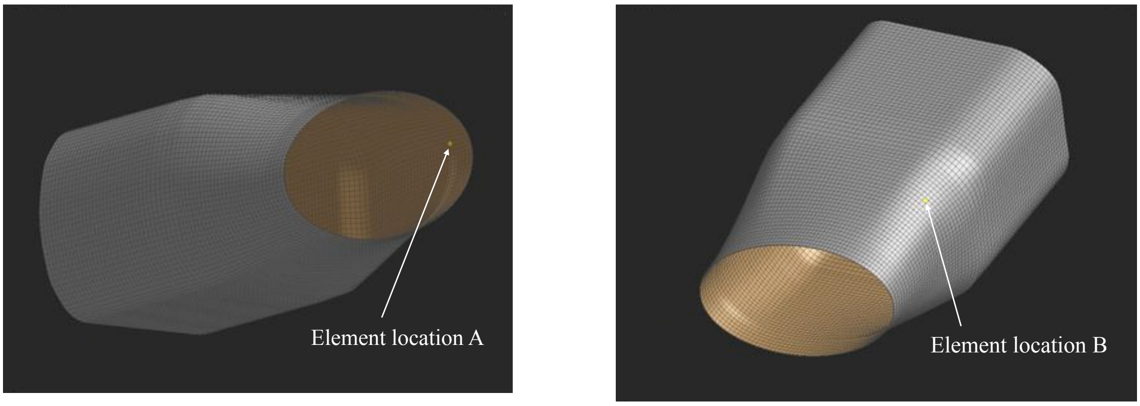

(a)

(b)

Figure 6.32: Location of elements used for the total damage plots (a) location A within interior skin and (b) location B as part of the exterior skin.

For location A the in-plane damage evolution is shown in figure 6.33. The damage curve obtained from the design model can be divided into three different sections. In the first section the damage value increases slowly and reaches a value of 0.1 at 3.6 ms. In the second section the damage value increases rapidly to 0.6 which corresponds to the sudden failure of the component. Subsequently the damage increases further and reaches a maximum value of 0.9 at the time of 5 ms. The base and optimised drape models provide similar evolution curves with four characteristic sections. Similarly to the design model the initial damage curve shows slow growth. The next section of the curve shows a high gradient damage increase followed by a plateau region with a constant value of 0.5. The final section incorporates a rapid damage increase with a maximum damage value of 0.9 and 0.95 for the base and optimised drape model respectively.

In case of location B, as part of the exterior skin, the design model shows again a slightly better performance compared to the draped models. However, all models follow the same characteristic shape with an initially low damage region followed by a rapid increase to reach the final in-plane damage state.

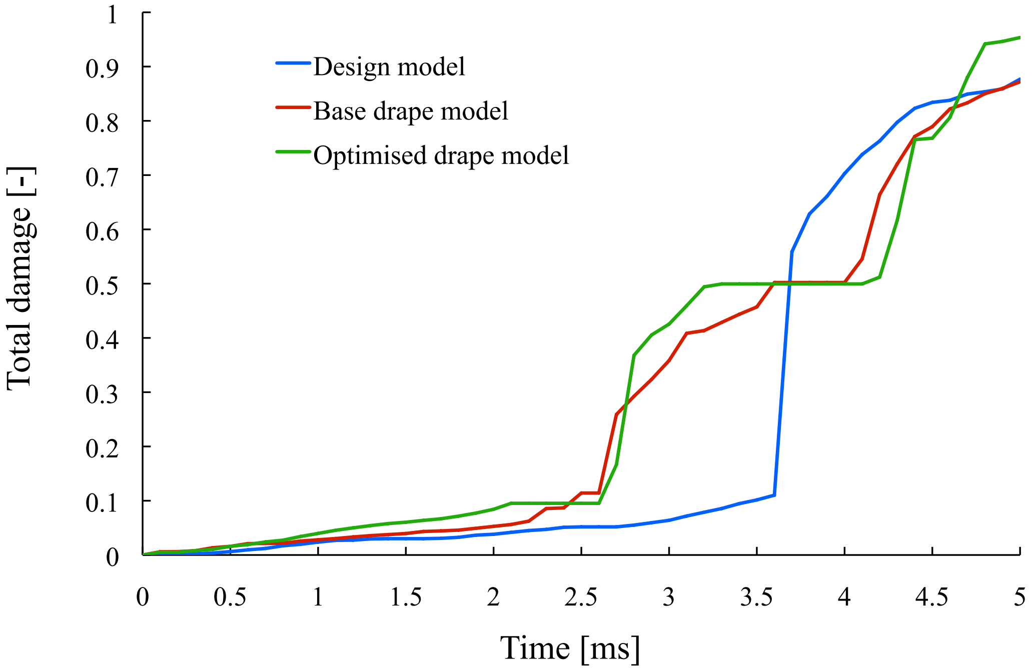

Figure 6.33: In-plane damage evolution extracted from location A.

Both drape models show closely matching maps for the in and out-of-plane damage. However, in the damage evolution plots for both elements the base drape model shows moderately better performance than the optimised model in respect to the initial low damage section. Here lower damage values can be maintained for a longer duration.

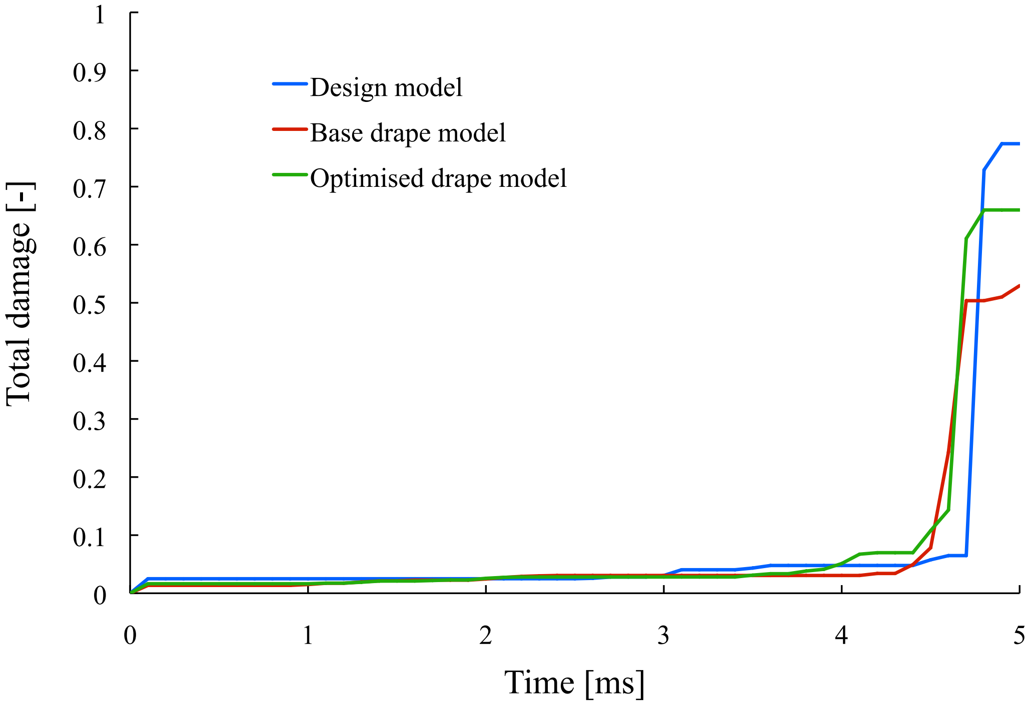

Figure 6.34: In-plane damage evolution extracted from location B.

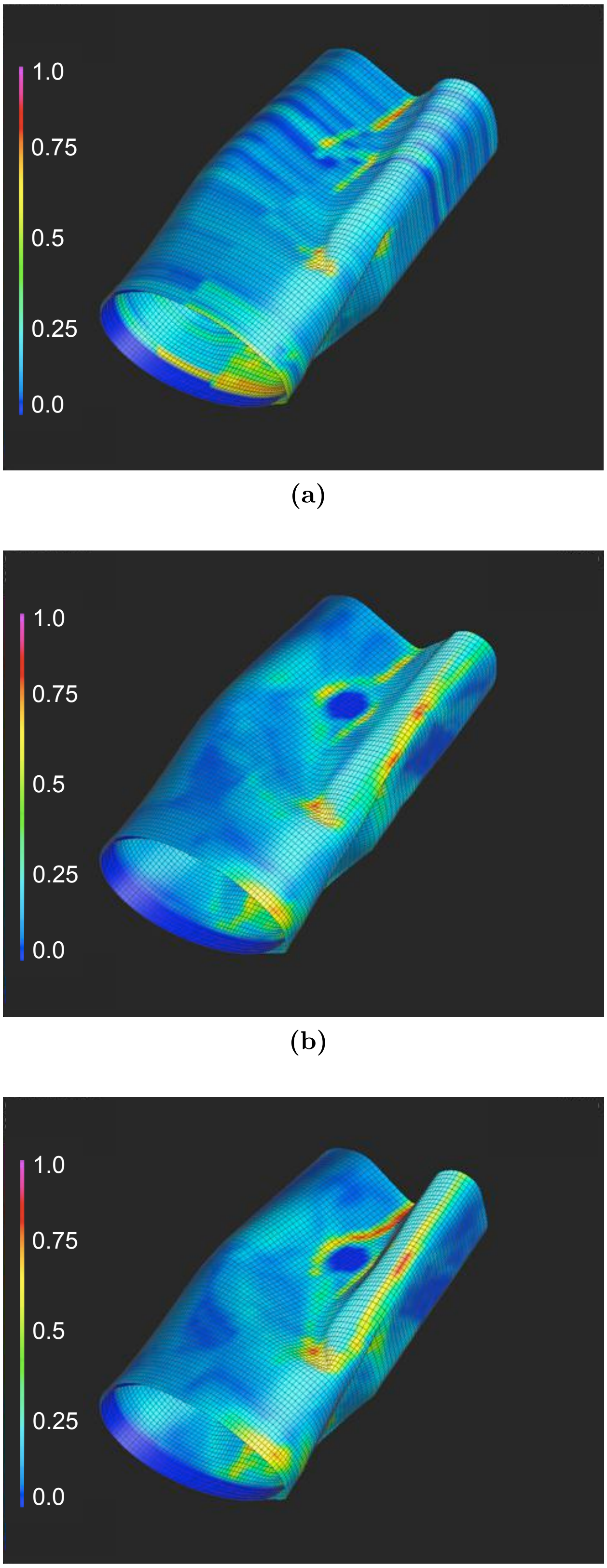

(a)

(b)

(c)

Figure 6.35: Final deformation and in-plane damage states for models with (a) nominal fibre angles, (b) fibre shear from current draping strategy and (c) fibre orientations resulting from drape optimisation.

Figure 6.35 shows the final deformation in combination with the in-plane damage map of each model at the end of the runtime. Here the design model with the nominal fibre directions shows the least deformation. When comparing the two drape models it is also noticeable that the model with the fibre orientations obtained from the optimised drape strategy has the largest deformation of all the three models. In conjunction with the in-plane and out-of-plane damage maps shown in figures 6.29, 6.30 and 6.31 it is obvious that the design model shows the best mechanical performance. In case of the drape models similar performance was observed. However, it is inevitable that the fibre shear due to the manufacturing process has a significant influence on the performance of the component and that results differs a great deal from the design component. This effect is critical given that nominal fibre orientation results in a more robust behaviour and thus leads to an overestimation of the performance.

7 Overall discussion

This chapter summarises and comments on the main outcomes of the work and discusses potential implications in current and future technology. The relevant discussion is around issues of manufacturing using bindered preforms, mechanical properties, material parameter estimation and finite element modelling.

7.1 Improving materials and manufacturing processes for bindered preforms

A manufacturing process to produce laminates based on homogeneously bindered carbon fibres was identified. The first step in the manufacturing process involves a low pressure activation of the binder coated carbon fibres to avoid excessive consolidation and to ensure the existence of flow channels within the preform. The infusion process using VARTM was also modified to avoid the reactivation of the binder particles. Hence the infusion with RTM6 was undertaken at 80°C (40°C lower than normal) to prohibit further compaction of the preform prior to the actual resin infusion.

Throughout this work a tow alignment tool was used to manufacture preform and laminate panels with UD plies. The quality of the material achieved in terms of fibre alignment was excellent while nylon place holding stitching was unnecessary. Furthermore the layup showed to be very consistent and allowed significant improvements in time and accuracy for non-UD arrangements, such as ±45° and ±67.5°.

7.2 Experimental work

For the characterisation of the preform material the test protocol suggested for laminates was followed. The preform material showed sufficient robustness to perform these experiments. The standard test protocol consists of experiment in the fibre direction for tension and compression as well as cyclic loading for ±45°, +45° and

±67.5°. The latter two experiments are also used for the extraction of the transverse material properties. However, in the case of the +45° experiment the transverse response generated showed a high noise level, whereas the shear response was usable for the material parameter identification. Hence the additional experiments on 90° specimens, which are not part of the original experimental programme, allowed extracting the transverse parameters.

The observed differences between the failure strain and strength values in fibre tension for the homogeneously and inhomogeneously bindered material may be explained by the difference in the shear moduli of the two materials. A shear modulus of 2.11 GPa for the inhomogeneously bindered material was obtained whilst the homogeneously bindered material had a value of 0.24 GPa. The higher value for the shear modulus indicates that the inhomogeneously bindered material is capable of producing a more uniform and laminate-like stress field throughout the specimen. Thus load from single fibre failure is redistributed over the remaining cross-section area while the homogeneously bindered material suffers from stress localisation.

For a reduced characterisation programme it is possible to avoid experiments on +45° specimens as the necessary data can also be provided by the experiments on the ±67.5°. In the test programme proposed the initial transverse modulus is determined using the transverse responses of both, +45° and ±67.5°, experiments. However, it was observed that the values obtained from +45° specimens are higher than those obtained from pure transverse experiment on 90° coupons, while the ±67.5° tests tend to provide lower values. Thus, when the originally proposed test programme is followed the use of both data sets leads to values similar to those obtained from pure transverse experiments on 90° coupons. However, the +45° specimens are relatively easy to manufacture and the experimental data set can be increased significantly when including +45° coupons.

As a result of the moderate compaction of the preform material the fibre volume content was lower compared to the reference material. Hence lower in-plane properties were observed, however, the preform laminates showed consistently higher out-of-plane properties compared to the reference laminate. With a fixed formulation of the binder coated carbon fibres this manufacturing process could be optimised with respect to the out-of-plane properties.

The use of a digital image correlation system for the strain field measuring enhanced the test analysis profoundly. Besides the strain field information such a system provides additional information, which can be used to check the evolution of the experiment. While the algorithm used in the system correlates the speckled pattern on the specimen surface from one state image to the following, the system can be used for high speed applications as well; provided the image capturing system is able to record the images in a high enough frequency. Thus the system could be employed for the preform spar section impact. The acquired deformation animation can then be mapped and compared with the results of finite element analysis. However, a negative aspect of this system was observed during the experimental programme. The surface condition influences the results of the system to a great extent hence any negative effects, such as splintered carbon fibres as shown in figure 7.1, introduce noise to the strain field measurement as the algorithm is unable to correlate a covered speckle to the previous state image.

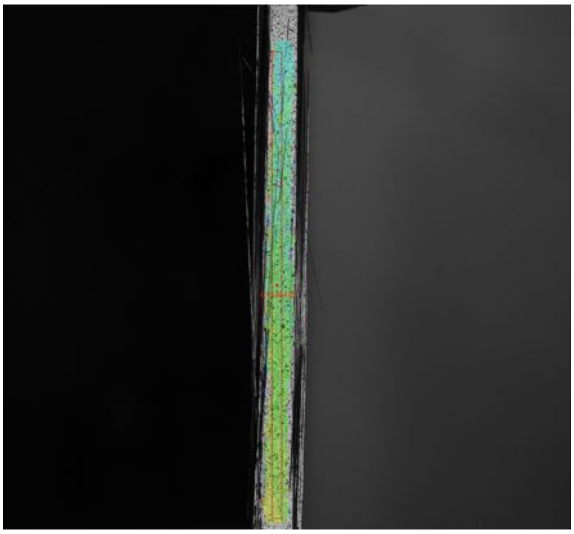

Figure 7.1: Decomposition of the test specimen surface at high deformation.

7.3 Parameter identification

Results from the conventional identification method show that the parameters determined lead to a material response, which overestimates the stress values. In particular this is the case for the shear direction where the sensitive energetic threshold values may result in significant differences in the material response. It may be possible to address this issue with the additional damage state fitting curves that are available in the recent versions of the FE solver used in this study. However, this feature was not examined in the context of this work.

Further general improvements of the results obtained via the gradient-based solver error minimisation method could be achieved by improving the coupling of the material directions explicitly. The coupling factors A and b do not show any sensitivity when tested in the pure shear and transverse material directions, and the data used from ±45° and 90° are uncoupled from the phenomena that should be covered by these parameters. Hence a coupling of the transverse and shear responses of the +45° and ±67.5° can lead to improved results. This implementation could still be accomplished in the Microsoft Excel environment; however, it would be advantageous to utilise a faster programming language, such as C or C++. This would also imply the use of an alternative implementation of a gradient-based solver. The current implementation of this method is not able to overcome the ill-posed nature of this inverse problem. Hence it is not certain whether the vector found represents a global solution. For this reason a regularisation method needs to be applied so that the smoothness or bounds of the solution space is ensured. This can be in the form of a priory information for some of the material constants and the incorporation of a penalty term in the minimisation functional that ensures proximity of the solution to prior estimates. This type of regularisation overcomes non-uniqueness problems with regards to the inverse solution.

The issue related to the coupling factors A and b, as observed with the implementation of the gradient-based solution, is overcome by the MCMC method as all parameters are taken into account by the posterior distribution. However, the main advantage of the MCMC method, compared to the other methods in addition to its regularising character is that probability densities are generated for all parameters. Although the mean or median value is generally used in an automated analysis of the MCMC output, the probability density plots provide information of different solutions to the inverse problem, which are not available when using the other methods. With such an output this method can also be used in the context of stochastic simulation that will enable incorporation of uncertainty information in models of the mechanical and damage response of composite components and preforms. This feature becomes of critical importance as design methodologies in the aerospace industry pay more attention to damage tolerance as well as the concept of fail safe structures.

The standard deviations listed in table 5.18, 5.19, 5.20 and 5.21 are of different nature. While the standard deviations for the conventional and gradient-based method display the error originating from the difference in experimental data the standard deviations for the MCMC method are generated from the probability density function of each parameter and provide further information about the certainty of each parameter in respect to the behaviour of the material model. As the MCMC method is able to generate a direct material parameter driven comparison between theoretical and experimental data whist considering parameter correlation it seems likely that the results for this method provide a better reflection of the parameter value.

The main motivation for using the MCMC method is the information provided by the output data. Improvements on the MCMC runtime can be achieved by addressing the following aspects. The program could be re-implemented in a more efficient manner by capitalising on more programming language specific features, such as object orientation and the usage of multiple threads to take advantage of multiple CPUs. Furthermore modern graphic cards can be used for solving number processing intensive operations. Therefore the iterative process could be run on the graphic cards GPU instead of the computers CPU. However, currently such operations are restricted to certain graphic card models [232]. Besides the usage of programming and machine related improvements, the algorithm could be altered in such a way so that block updating (variation of multiple parameters within a single iteration) is enabled [233]. However, by enabling this feature the sequence also becomes more difficult to tune manually. Therefore the implementation of an automated tuning algorithm [143] is beneficial. Such an algorithm will have a negative effect on the overall runtime of the chain as the burn-in region is extended significantly. The number of iterations needed in the automated tuning procedure depends on how quickly the underlying model enables the chain to produce samples from a stationary distribution. Thus an improvement is gained with respect to the tuning procedure. The tuning process is completely automated and does not require the lengthy manual tuning runs. On the other hand block updating allows changing similar parameters within the same iteration, which reduces the overall number of iterations. While these suggestions only address runtime improvements it is also possible to improve the results of the MCMC simulation. By introducing an additional noise term to the posterior distribution as described in [143, 218, 229] the algorithm is capable of interpreting experimental data, which cannot be expressed by the model, as noise. In the context of this work the constitutive material model cannot cover the hysteresis curves present in the shear experiments, which affects the overall result of the MCMC simulation.

For both automated parameter identification methods used in this work the undamaged Poisson's ratio in 1,2-direction was removed from the parameter vector, as the determination of this parameter is straightforward and did not justify the increase in runtime caused by the additional data sets. However, the methods can be extended to analyse the transverse strain data from the fibre tension tests which are provided by the digital image correlation system.

7.4 Modelling approaches

The simulation of three point bending was used to validate the material model and the shell element cohesive interface combination based modelling concept. The modelling approach showed good agreement with the experimental data. The result from the finite element solution lead to a similar flexural modulus as deduced from the experimental data.

For the preform spar section impact the simulation also showed good agreement with the experimental findings. The findings also show that the underlying constitutive material models are capable of representing the preform material in impact situations. This development sets the basis for quantitative modelling of preform behaviour and robustness under situations of storage, transport and handling, a step necessary for the consideration of binder coated tow preforms as an alternative raw material for advanced composites processing.

The set of simulations carried out on the pitch horn component to investigate the influence of fibre shear on the mechanical performance and to demonstrate the capabilities of the modelling strategy selected in designing real scale and high complexity industrial composite components. Therefore three models were assembled. The first model incorporated the nominal fibre angles, which were set from a design perspective while the two other models used the fibre angle orientations from the current and an optimised draping strategy. Here optimisation was carried out with the objective of minimising the overall fibre shear. It should be noted that current design practice is based on usage of nominal fibre orientations, an assumption that may result in overestimation of failure loads. As expected the model with the nominal fibre angles performed best while the other models showed only little differences. However, the modelling approach established could be applied in the context of multi-objective optimisation, which takes the fibre shear into account while improving the mechanical performance of the component. Thus an optimal draping strategy could be identified while taking into account the influence on mechanical performance.

8 Conclusions and suggestions for further investigation

8.1 Conclusions

The main outcomes of this work are summarised in the following:

Experimental work

- An experimental programme for the characterisation of the damage behaviour of preforms is feasible by modifying the programme used for laminates with the exception of compression tests in the fibre direction.
- The inhomogeneously bindered preform is more robust than the homogeneous material. However, the inhomogenity of the material affects the reproducibility of the experiments while this effect is weaker in the homogeneously bindered preform. This effect can be seen in the experimental results of the transverse experiments shown in figure 4.3 and 4.12 for the inhomogeneously and homogeneously bindered material.
- The bindered composites achieved significantly better out-of-plane properties due to the lower fibre volume content, which resulted in interleaving, while the in-plane properties were similar or lower compared to the reference laminate.
- An alternative curing cycle for the epoxy system used in this study (Hexcel RTM6) involved infusing at 80°C instead of 120°C and allowed satisfactory infusion of homogeneously bindered preforms.

Model parameter identification

- The parameter vector as identified using the conventional method showed good agreement with the experimental data, however, the stress values for the shear tests were over predicted while the transverse response lead to early failure.
- The gradient-based method is a relatively robust approach for the identification of damage model parameters. The fit achieved was very good, however, the results depend highly on defined bounds, which restrict the search space.

- The Markov Chain Monte Carlo method provided a material data set, which resulted in excellent agreement with the experiments. In the case of shear tests the parameter set did not lead to the best fit compared to the results of the gradient-based method. However, the MCMC parameter set presents a good compromise between the over predicting character of the conventional method and the unrealistic, yet best fit, of the gradient-based error minimisation method.

- The Markov Chain Monte Carlo method results in estimation of the correlated probability distributions of the unknown variables. The results obtained for the damage models of this study showed significant variations for most parameters with some of them (R_0, m, β) following multimodal distributions.

Finite element analysis

- The finite element representation of bindered preforms using an assembly of shell elements, representing sub-laminates, connected with cohesive interface elements offers a valid simulation of the mechanical and damage response. This was demonstrated via comparison with results form a spar section impact experiment.

- The shell/cohesive finite element representation of composite laminates follows closely experimental damage response results. A model of this type offers adequate representation of in-plane and delamination damage at low computing cost. Use of such a model in the context of component design was demonstrated for a helicopter pitch horn component.

8.2 Suggestions for further investigation

Application for the binder coated carbon fibres could be used to enhance the toughness of the system. The binder formulation could be modified to incorporate toughening agents. This approach would allow infusing the preform with a low viscosity resin, which would be modified by the binder upon activation.

The difference of failure strain and strength in fibre direction for the preform materials should be investigated further. The properties of the inhomogeneously bindered preform indicate laminate-like behaviour with respect to fibre tensile and shear modulus. A repetition of the tensile experiments on the inhomogeneously bindered material using the digital image correlation system could provide further information about the stress distribution of the specimen during the test.

Further investigations need to address the combination of optimal binder distribution and content to ensure a satisfactory infusion results. The optimal combination of these parameters will allow the creation of flow paths in the resin possibly via the existence of controlled inhomogeneties.

The gradient-based error minimisation method showed great runtime efficiency in combination with excellent results. The downside of this method is the incapability to overcome the ill-posedness of the inverse problem. A regularisation term would be a valuable extension to improve the identification of global optima.

The results from the MCMC method provide a variety of information in addition to estimators of the material constants. These are in the form of multivariate probability distributions incorporating correlation between variables. This type of information can be the basis stochastic simulations of the mechanical and damage response of both preforms and laminates.

The finite element model developed for preforms showed excellent agreement with the experimental data. This model can find application in the context of the design of preforms that are robust under conditions of storage and transport.

The established shell/interface based modelling strategy with the inclusion of actual fibre orientations showed robust behaviour and could be utilised in the context of multiobjective optimisation. The objectives of drape shear minimisation and best mechanical performance could be addressed in such a scheme.

References

[1] PreCarBi project. `www.esi-group.com/corporate/alliances/projects/precarbi/precarbi`.

[2] J Fan and J Zhang. In-situ damage evolution and micro/macro transition for laminated composites. *Composites Science and Technology*, 47:107–118, 1993.

[3] A Puck and H Schürmann. Failure analysis of FRP laminates by means of physically based phenomenological models. *Composites Science and Technology*, 58:1045–1067, 1998.

[4] A Puck, J Kopp and M Knops. Guidelines for the determination of the parameters in Puck's action plane strength criterion. *Composites Science and Technology*, 62:371–378, 2002.

[5] M Brünig. A framework for large strain elastic-plastic damage mechanics based on metric transformations. *International Journal of Engineering Science*, 39: 1033–1056, 2001.

[6] M Brünig. An anisotropic ductile damage model based on irreversible thermodynamics. *International Journal of Plasticity*, 19:1679–1713, 2003.

[7] LM Kachanov. Rupture time under creep conditions. *International Journal of Fracture*, 97:11–18, 1999.

[8] P Ladevèze and E Le Dantec. Damage modelling of the elementary ply for laminated composites. *Composites Science and Technology*, 43:257–267, 1992.

[9] P Ladevèze, O Allix, JF Deü and D Lévêque. A mesomodel for localisation and damage computation in laminates. *Computer Methods in Applied Mechanics and Engineering*, 183:105–122, 2000.

[10] P Ladevèze, G Lubineau and D Violeau. A computational damage micromodel of laminated composites. *International Journal of Fracture*, 137:139–150, 2006.

[11] A Al-Rub, K Rashid and GZ Voyiadjis. On the coupling of anisotropic damage and plasticity models for ductile materials. *International Journal of Solids and Structures*, 40:2611–2643, 2003.

[12] JC Simo and TJR Hughes. *Computational Inelasticity.* Springer, 1998.

[13] T Belytschko, WK Liu and B Moran. *Nonlinear Finite Elements for Continua and Structures.* John Wiley & Sons Ltd, 2005.

[14] J Lubliner. *Plasticity Theory.* Pearson Education Inc, 2006.

[15] A Al-Rub, K Rashid and GZ Voyiadjis. A finite strain plastic-damage model for high velocity impact using combined viscosity and gradient localization limiters: Part I - theoretical formulation. *International Journal of Damage Mechanics*, 15:293–334, 2006.

[16] J Bielski, JJ Skrzypek and H Kuna-Ciskal. Implementation of a model of coupled elastic-plastic unilateral damage material to finite element code. *International Journal of Damage Mechanics*, 15:5–39, 2006.

[17] JL Chaboche. Anisotropic creep damage in the framework of continuum damage mechanics. *Nuclear Engineering and Design*, 79:309–319, 1984.

[18] JL Chaboche. Constitutive equations for cyclic plasticity and cyclic viscoplasticity. *International Journal of Plasticity*, 5:247–302, 1989.

[19] JL Chaboche and G Cailletaud. Integration methods for complex plastic constitutive equations. *Computer Methods in Applied Mechanics and Engineering*, 133:125–155, 1996.

[20] YY Zhu and S Cescotto. A fully coupled elasto-visco-plastic damage theory for anisotropic materials. *International Journal of Solids and Structures*, 32: 1607–1641, 1995.

[21] JF Maire and JL Chaboche. A new formulation of continuum damage mechanics (CDM) for composite materials. *Aerospace Science and Technology*, 4: 247–257, 1997.

[22] GZ Voyiadjis and B Deliktas. A coupled anisotropic damage model for the inelastic response of composite materials. *Computer Methods in Applied Mechanics and Engineering*, 183:159–199, 2000.

[23] J Lemaitre. Coupled elasto-plasticity and damage constitutive equations. *Computer Methods in Applied Mechanics and Engineering*, 51:31–49, 1985.

[24] M Alves, JL Yu and N Jones. On the elastic modulus degradation in continuum damage mechanics. *Computers and Structures*, 76:703–712, 2000.

[25] CL Chow and J Wang. An anisotropic theory of continuum damage mechanics for ductile fracture. *Engineering Fracture Mechanics*, 27:547–558, 1987.

[26] TJ Lu and CL Chow. On constitutive equations of inelastic solids with anisotropic damage. *Theoretical and Applied Fracture Mechanics*, 14:187–218, 1990.

[27] GZ Voyiadjis and PI Kattan. A plasticity-damage theory for large deformation of solids. I - theoretical formulation. *International Journal of Engineering Science*, 30:1089–1108, 1992.

[28] K Saanouni, C Forster and F Ben Hatira. On the inelastic flow with damage. *International Journal of Damage Mechanics*, 3:140–169, 1994.

[29] J Lemaitre. Coupled elasto-plasticity and damage constitutive equations. *Computer Methods in Applied Mechanics and Engineering*, 51:31–49, 1985.

[30] JL Chaboche. Continuum damage mechanics: Present state and future trends. *Nuclear Engineering and Design*, 105:19–33, 1987.

[31] JC Simo and JW Ju. Strain- and stress-based continuum damage models - I. Formulation. *International Journal of Solids and Structures*, 23:821–840, 1987.

[32] JC Simo and JW Ju. Strain- and stress-based continuum damage models - II. Computational aspects. *International Journal of Solids and Structures*, 23: 841–869, 1987.

[33] NR Hansen. A thermodynamically consistent framework for theories of elastoplasticity coupled with damage. *International Journal of Solids and Structures*, 31:359–389, 1994.

[34] GZ Voyiadjis and T Park. Local and interfacial damage analysis of metal matrix composites using the finite element method. *Engineering Fracture Mechanics*, 56:483–511, 1997.

[35] K Hayakawa, S Murakami and YC Liu. An irreversible thermodynamics theory for elastic-plastic-damage materials. *European Journal of Mechanics - A/Solids*, 17:13–32, 1998.

[36] R Hill. A self-consistent mechanics of composite materials. *Journal of the Mechanics and Physics of Solids*, 13:213–222, 1965.

[37] Q Yang, X Chen, and WY Zhou. On the structure of anisotropic damage yield criteria. *Mechanics of Materials*, 37:1049–1058, 2005.

[38] J Lemaitre, R Desmorat and M Sauzay. Anisotropic damage law of evolution. *European Journal of Mechanics - A/Solids*, 19:187–208, 2000.

[39] JJ Skrzypek, AW Ganczarski, F Rustichelli and H Egner. *Advanced Materials and Structures for Extreme Operating Conditions.* Springer, 2008.

[40] NR Hansen and HL Schreyer. Thermodynamically consistent theories for elastoplasticity coupled with damage. *International Journal of Solids and Structures*, 31:359–389, 1994.

[41] M Cegielski and A Ganczarski. Effect of continuous damage deactivation on yield and failure surfaces. *Acta Mechanica et Automatica*, 1:15–18, 2007.

[42] A Ganczarski and L Barwacz. Low cycle fatigue based on unilateral damage evolution. *International Journal of Damage Mechanics*, 16:159–177, 2007.

[43] N Challamel, C Lanos and C Casandjian. Strain-based anisotropic damage modelling and unilateral effects. *International Journal of Mechanical Sciences*, 47:459–473, 2005.

[44] VA Lubarda and D Krajcinovic. Damage tensors and the crack density distribution. *International Journal of Solids and Structures*, 30:2859–2877, 1993.

[45] VA Lubarda, D Krajcinovic and S Mastilovic. Damage model for brittle elastic solids with unequal tensile and compressive strengths. *Engineering Fracture Mechanics*, 49:681–697, 1994.

[46] VA Lubarda and D Krajcinovic. Some fundamental issues in rate theory of damage-elastoplasticity. *International Journal of Plasticity*, 11:763–797, 1995.

[47] S Murakami and K Kamiya. Constitutive and damage evolution equations of elastic-brittle materials based on irreversible thermodynamics. *International Journal of Mechanical Sciences*, 39:473–486, 1997.

[48] JW Ju. On energy-based coupled elastoplastic damage theories: Constitutive modeling and computational aspects. *International Journal of Solids and Structures*, 25:803–833, 1989.

[49] JL Chaboche. Damage induced anisotropy: On the difficulties associated with the active/passive unilateral condition. *International Journal of Damage Mechanics*, 1:148–171, 1992.

[50] JL Chaboche. Development of continuum damage mechanics for elastic solids sustaining anisotropic and unilateral damage. *International Journal of Damage Mechanics*, 2:311–332, 1993.

[51] D Halm and A Dragon. A model of anisotropic damage by mesocrack growth unilateral effect. *International Journal of Damage Mechanics*, 5:384–402, 1996.

[52] J Lemaitre. Anisotropic damage law of evolution. *European Journal of Mechanics - A/Solids*, 19:187–208, 2000.

[53] MHJW Paas, PJG Schreurs and WAM Brekelmans. A continuum approach to brittle and fatigue damage - theory and numerical procedures. *International Journal of Solids and Structures*, 30:579–599, 1993.

[54] NR Hansen and HL Schreyer. Damage deactivation. *International Journal of Applied Mechanics*, 62:450–458, 1995.

[55] J Lemaitre. *A Course on Damage Mechanics*. Springer, 1992.

[56] J Lemaitre and JP Sermage. One damage law for different mechanisms, 1997.

[57] P Ladevèze. A damage computational method for composite structures. *WCCM - World Congress of Computational Mechanics, Stuttgart, Germany, August 27-31*, 1990.

[58] MJ Hinton, AS Kaddour, and PD Soden. A comparison of the predictive capabilities of current failure theories for composite laminates, ... *Composites Science and Technology*, 2002.

[59] M Hinton, PD Soden and AS Kaddour. *Failure Criteria in Fibre-Reinforced-Polymer Composites*. Elsevier Science, 2004.

[60] O Allix, P Ladevèze and E Vittecoq. Modelling and identification of the mechanical behaviour of composite laminates in compression. *Composites Science and Technology*, 51:35–42, 1994.

[61] JL Chaboche, S Kruch, JF Maire and T Pottier. Towards a micromechanics based inelastic and damage modeling of composites. *International Journal of Plasticity*, 17:411–439, 2001.

[62] HT Hahn and SW Tsai. *Introduction to Composite Materials.* Technomic Publishing Company, 1980.

[63] CT Herakovich. *Mechanics of Fibrous Composites.* John Wiley & Sons, Inc., 1997.

[64] AJM Spencer. *Continuum Theory of the Mechanics of Fibre-Reinforced Composites.* Springer, 1984.

[65] M Andrews and R Massabo. Delamination in flat sheet geometries with material imperfections and thickness variations. *Composites Part B: Engineering*, 39:139–150, 2008.

[66] SN Chatterjee, WA Dick and RB Pipes. Mixed-mode delamination fracture in laminated composites. *Fibre Science and Technology*, 25:49–67, 1986.

[67] OO Ochoa and A Moore. A parametric study on strain energy release rates of compression members. *Composite Structures*, 11:151–163, 1989.

[68] S Lim and S Li. Energy release rates for transverse cracking and delaminations induced by transverse cracks in laminated composites. *Composites Part A: Applied Science and Manufacturing*, 36:1467–1476, 2005.

[69] JL Rebière and D Gamby. A decomposition of the strain energy release rate associated with the initiation of transverse cracking, longitudinal cracking and delamination in cross-ply laminates. *Composite Structures*, 84:186–197, 2008.

[70] J Andersons and M König. Dependence of fracture toughness of composite laminates on interface ply orientations and delamination growth direction. *Composites Science and Technology*, 64:2139–2152, 2004.

[71] AJ Brunner and P Flüeler. Prospects in fracture mechanics of “engineering” laminates. *Engineering Fracture Mechanics*, 72:899–908, 2005.

[72] *BS ISO 15024 - Fiber-reinforced plastic composites - Determination of mode I interlaminar fracture toughness, G_{IC}, for unidirectionally reinforced materials.* British Standards Institution, London, 2001.

[73] C Henaff-Gardin, MC Lafarie-Frenot and D Gamby. Doubly periodic matrix cracking in composite laminates. Part 2: Thermal biaxial loading. *Composite Structures*, 36:131–140, 1996.

[74] SL Bazhenov. Interlaminar and intralaminar fracture modes in 0/90 cross-ply glass/epoxy laminate. *Composites*, 26:125–133, 1995.

[75] CT Sun and S Zheng. Delamination characteristics of double-cantilever beam and end-notched flexure composite specimens. *Composites Science and Technology*, 56:451–459, 1996.

[76] KD Cowley and PWR Beaumont. The interlaminar and intralaminar fracture toughness of carbon-fibre/polymer composites: The effect of temperature. *Composites Science and Technology*, 57:1433–1444, 1997.

[77] C Baxevanakis, D Jeulin, B Lebon and J Renard. Fracture statistics modeling of laminate composites. *International Journal of Solids and Structures*, 35: 2505–2521, 1998.

[78] T Okabe, H Sekine, J Noda, M Nishikawa and N Takeda. Characterization of tensile damage and strength in GFRP cross-ply laminates. *Materials Science & Engineering A*, 383:381–389, 2004.

[79] *ASTM D5528 - Standard Test Method for Mode I Interlaminar Fracture Toughness of Unidirectional Fiber Reinforced Polymer Matrix Composites.* ASTM International, United States, 2001.

[80] *Fiber-reinforced plastic composites - Determination of apparent Mode II interlaminar fracture toughness, G_{IIC}, for unidirectionally reinforced materials.* European Structural & Integrity Society (ESIS), Version 01-04-02, Task Committee 4 (TC4) on fracture of composites and polymers, 2002.

[81] BRK Blackman, AJ Kinloch and M Paraschi. The determination of the mode II adhesive fracture resistance, G_{IIC}, of structural adhesive joints: An effective crack length approach. *Engineering Fracture Mechanics*, 72:877–897, 2005.

[82] BRK Blackman, AJ Brunner and JG Williams. Mode II fracture testing of composites: A new look at an old problem. *Engineering Fracture Mechanics*, 73:2443–2455, 2006.

[83] JM Hodgkinson. *Mechanical Testing of Advanced Fibre Composites.* Woodhead Publishing Ltd, 2000.

[84] EF Rybicki and MF Kanninen. A finite element calculation of stress intensity factors by a modified crack closure integral. *Engineering Fracture Mechanics*, 9:931–938, 1977.

[85] IS Raju. Calculation of strain-energy release rates with higher order and singular finite elements. *Engineering Fracture Mechanics*, 28:251–274, 1987.

[86] R Krueger. The virtual crack closure technique: History, approach and application. *NASA/CR-2002-211628 CASE Report No. 2002-10*, 2002.

[87] S Li, S Reid, and Z Zou. Modelling damage of multiple delaminations and transverse matrix cracking in laminated composites due to low velocity lateral impact. *Composites Science and Technology*, 66:827–836, 2006.

[88] Z Petrossian and MR Wisnom. Prediction of delamination initiation and growth from discontinuous plies using interface elements. *Composites Part A: Applied Science and Manufacturing*, 29:503–515, 1998.

[89] PP Camanho, CG Dávila and DR Ambur. Numerical simulation of delamination growth in composite materials. *NASA/TP—2001–211041*, 2001.

[90] ST Pinho, L Iannucci and P Robinson. Formulation and implementation of decohesion elements in an explicit finite element code. *Composites Part A: Applied Science and Manufacturing*, 37:778–789, 2006.

[91] WG Jiang, SR Hallett, BG Green and MR Wisnom. A concise interface constitutive law for analysis of delamination and splitting in composite materials and its application to scaled notched tensile specimens. *International Journal for Numerical Methods in Engineering*, 69:1982–1995, 2006.

[92] ST Pinho, P Robinson, and L Iannucci. Fracture toughness of the tensile and compressive fibre failure modes in laminated composites. *Composites Science and Technology*, 66:2069–2079, 2006.

[93] VK Goyal and ER Johnson. Predictive strength-fracture model for composite bonded joints. *Composite Structures*, 82:434–446, 2008.

[94] DS Dugdale. Yielding of steel sheets containing slits. *Journal of the Mechanics and Physics of Solids*, 8:100–104, 1960.

[95] GI Barenblatt. The mathematical theory of equilibrium cracks in brittle fracture. *Advances in Applied Mechanics*, 7:55–129, 1962.

[96] VK Goyal, ER Johnson and CG Dávila. Irreversible constitutive law for modeling the delamination process using interfacial surface discontinuities. *Composite Structures*, 65:289–305, 2004.

[97] A Hillerborg, M Modeer and PE Petersson. Analysis of crack formation and crack growth in concrete by means of fracture mechanics and finite elements. *Cement and Concrete Research*, 6:773–782, 1976.

[98] JCJ Schellenkens and R De Borst. A non-linear finite element approach for the analysis of mode I free edge delamination in composites. *International Journal of Solids and Structures*, 30:1239–1253, 1993.

[99] MR Wisnom, ZJ Petrossian and MI Jones. Interlaminar failure of unidirectional glass/epoxy due to combined through thickness shear and tension. *Composites Part A: Applied Science and Manufacturing*, 27:921–929, 1996.

[100] O Allix and P Ladevèze. Interlaminar interface modelling for the prediction of delamination. *Composite Structures*, 22:235–242, 1992.

[101] PP Camanho, CG Davila and M Moura. Numerical simulation of mixed-mode progressive delamination in composite materials. *Journal of Composite Materials*, 37:1415–1438, 2003.

[102] C Balzani and W Wagner. An interface element for the simulation of delamination in unidirectional fiber-reinforced composite laminates. *Engineering Fracture Mechanics*, 75:2597–2615, 2008.

[103] I Guiamatsia, JK Ankersen, GAO Davies and L Iannucci. Decohesion finite element with enriched basis functions for delamination. *Composites Science and Technology*, 69:2616–2624, 2009.

[104] N Hu, Y Zemba, T Okabe, C Yan, H Fukunaga and AM Elmarakbi. A new cohesive model for simulating delamination propagation in composite laminates under transverse loads. *Mechanics of Materials*, 40:920–935, 2008.

[105] DH Allen. Homogenization principles and their application to continuum damage mechanics. *Composites Science and Technology*, 61:2223–2230, 2001.

[106] A Corigliano. Formulation, identification and use of interface models in the numerical analysis of composite delamination. *International Journal of Solids and Structures*, 30:2779–2811, 1993.

[107] Y Mi, MA Crisfield, GAO Davies and HB Hellweg. Progressive delamination using interface elements. *Journal of Composite Materials*, 32:1246–1272, 1998.

[108] M Wisheart and MOW Richardson. The finite element analysis of impact induced delamination in composite materials using a novel interface element. *Composites Part A: Applied Science and Manufacturing*, 29:301–313, 1998.

[109] PH Geubelle and JS Baylor. Impact-induced delamination of composites: a 2D simulation. *Composites Part B: Engineering*, 29:589–602, 1998.

[110] PP Camanho, CG Davila and MF De Moura. Numerical simulation of mixed-mode progressive delamination in composite materials. *Journal of Composite Materials*, 37:1415–1438, 2003.

[111] L Greve and AK Pickett. Delamination testing and modelling for composite crash simulation. *Composites Science and Technology*, 66:816–826, 2006.

[112] L Greve and AK Pickett. Modelling damage and failure in carbon/epoxy non-crimp fabric composites including effects of fabric pre-shear. *Composites Part A: Applied Science and Manufacturing*, 37:1983–2001, 2006.

[113] SR Hallett, WG Jiang, B Khan and MR Wisnom. Modelling the interaction between matrix cracks and delamination damage in scaled quasi-isotropic specimens. *Composites Science and Technology*, 68:80–89, 2008.

[114] D Bruno, F Greco and P Lonetti. A coupled interface-multilayer approach for mixed mode delamination and contact analysis in laminated composites. *International Journal of Solids and Structures*, 40:7245–7268, 2003.

[115] R Krueger and TK O'Brien. A shell/3D modeling technique for the analysis of delaminated composite laminates. *Composites Part A: Applied Science and Manufacturing*, 32:25–44, 2001.

[116] O Allix and L Blanchard. Mesomodeling of delamination: towards industrial applications. *Composites Science and Technology*, 66:731–744, 2006.

[117] F Aymerich, F Dore and P Priolo. Simulation of multiple delaminations in impacted cross-ply laminates using a finite element model based on cohesive interface elements. *Composites Science and Technology*, 69:1699–1709, 2009.

[118] MFSF de Moura and JPM Gonçalves. Modelling the interaction between matrix cracking and delamination in carbon-epoxy laminates under low velocity impact. *Composites Science and Technology*, 64:1021–1027, 2004.

[119] M Nishikawa, T Okabe and N Takeda. Numerical simulation of interlaminar damage propagation in CFRP cross-ply laminates under transverse loading. *International Journal of Solids and Structures*, 44:3101–3113, 2007.

[120] H Sol, H Hua, J De Visscher, J Vantomme and WP De Wilde. A mixed numerical/experimental technique for the nondestructive identification of the stiffness properties of fibre reinforced composite materials. *NDT and E International*, 30:85–91, 1997.

[121] L Le Magorou, F Bos and F Rouger. Identification of constitutive laws for wood-based panels by means of an inverse method. *Composites Science and Technology*, 62:591–596, 2002.

[122] WG Knauss. Perspectives in experimental solid mechanics. *International Journal of Solids and Structures*, 37:251–266, 2000.

[123] SW Doebling, CR Farrar and MB Prime. A summary review of vibration-based damage identification methods. *Shock and Vibration Digest*, 30:91–105, 1998.

[124] LX Yang, W Steinchen, M Schuth and G Kupfer. Precision measurement and nondestructive testing by means of digital phase shifting speckle pattern and speckle pattern shearing interferometry. *Measurement*, 16:149–160, 1995.

[125] M Grediac. The use of full-field measurement methods in composite material characterization: interest and limitations. *Composites Part A: Applied Science and Manufacturing*, 35:751–761, 2004.

[126] K Mai, E Mäder and M Mühle. Interphase characterization in composites with new non-destructive methods. *Composites Part A: Applied Science and Manufacturing*, 29:1111–1119, 1998.

[127] KH Ip, PC Tse and TC Lai. Material characterization for orthotropic shells using modal analysis and Rayleigh-Ritz models. *Composites Part B: Engineering*, 29:397–409, 1998.

[128] AK Bledzki, A Kessler, R Rikards and A Chate. Determination of elastic constants of glass/epoxy unidirectional laminates by the vibration testing of plates. *Composites Science and Technology*, 59:2015–2024, 1999.

[129] AL Araujo, CM Mota Soares and MJ Moreira de Freitas. Characterization of material parameters of composite plate specimens using optimization and

experimental vibrational data. *Composites Part B: Engineering*, 27:185–191, 1996.

[130] PS Frederiksen. Parameter uncertainty and design of optimal experiments for the estimation of elastic constants. *International Journal of Solids and Structures*, 35:1241–1260, 1998.

[131] AL Araujo, CM Mota Soares, MJ Moreira de Freitas, P Pedersen and J Herskovits. Combined numerical-experimental model for the identification of mechanical properties of laminated structures. *Composite Structures*, 50:363–372, 2000.

[132] C Maletta and L Pagnotta. On the determination of mechanical properties of composite laminates using genetic algorithms. *International Journal of Mechanics and Materials in Design*, 1:199–211, 2004.

[133] RH Iding, KS Pister and RL Taylor. Identification of nonlinear elastic solids by a finite element method (stress constitutive modeling). *Computer Methods in Applied Mechanics and Engineering*, 4:121–142, 1974.

[134] F Daghia, S de Miranda, F Ubertini and E Viola. Estimation of elastic constants of thick laminated plates within a Bayesian framework. *Composite Structures*, 80:461–473, 2007.

[135] WB Walton. Parameter estimation for nonlinear models-convergence, data and parameter uncertainty, and constraints on parameter changes. *Mathematical and Computer Modelling*, 12:181–192, 1989.

[136] TC Lai and KH Ip. Parameter estimation of orthotropic plates by Bayesian sensitivity analysis. *Composite Structures*, 34:29–42, 1996.

[137] K Balasubramaniam and NS Rao. Inversion of composite material elastic constants from ultrasonic bulk wave phase velocity data using genetic algorithms. *Composites Part B: Engineering*, 29:171–180, 1998.

[138] GR Liu, X Han and KY Lam. A combined genetic algorithm and nonlinear least squares method for material characterization using elastic waves. *Computer Methods in Applied Mechanics and Engineering*, 191:1909–1921, 2002.

[139] M Mitchell. *An introduction to genetic algorithms.* The MIT Press, 1998.

[140] J Vishnuvardhan, CV Krishnamurthy and K Balasubramaniam. Genetic algorithm reconstruction of orthotropic composite plate elastic constants from

a single non-symmetric plane ultrasonic velocity data. *Composites Part B: Engineering*, 38:216–227, 2007.

[141] SF Hwang, JC Wu and RS He. Identification of effective elastic constants of composite plates based on a hybrid genetic algorithm. *Composite Structures*, 90:217–224, 2009.

[142] Y Li, R He and Y Guo. Faster genetic algorithm for network paths. *The Sixth International Symposium on Operations Research and Its Applications (ISORA'06), China*, 2006.

[143] PC Gregory. *Bayesian Logical Data Analysis for the Physical Sciences: A Comparative Approach with Mathematica Support.* Cambridge University Press, 2005.

[144] M Bayes and M Price. An essay towards solving a problem in the doctrine of chances. *Philosophical Transactions*, 1763.

[145] A Gelman, JB Carlin, HS Stern and DB Rubin. *Bayesian Data Analysis.* Chapman & Hall, 2003.

[146] N Metropolis, AW Rosenbluth, MN Rosenbluth, AH Teller and E Teller. Equation of state calculations by fast computing machines. *The Journal of Chemical Physics*, 21:1087–1092, 1953.

[147] N Metropolis. The beginning of the Monte Carlo method. *Los Alamos Science*, pages 125–130, 1987.

[148] WK Hastings. Monte Carlo sampling methods using Markov chains and their applications. *Biometrika*, 57:97–109, 1970.

[149] DP Landau and K Binder. *A Guide to Monte Carlo Simulations in Statistical Physics.* Cambridge University Press, 2005.

[150] C Robert and G Casella. A history of Markov Chain Monte Carlo–subjective recollections from incomplete data–, 2008. URL http://arxiv.org/abs/0808.2902v5.

[151] J Geweke. Bayesian inference in econometric models using Monte Carlo integration. *Econometrica*, 57:1317–1339, 1989.

[152] J Geweke. Using simulation methods for Bayesian econometric models: inference, development,and communication. *Econometric Reviews*, 18:1–73, 1999.

[153] WR Gilks, S Richardson and DJ Spiegelhalter. *Markov Chain Monte Carlo in Practive.* Chapman & Hall, 1995.

[154] J Gyarmati-Szabó and L Markus. A hierarchical bayesian model to predict belatedly reported claims in insurances. *Recent Advances In Stochastic Modeling And Data Analysis*, pages 137–145, 2007.

[155] C Andrieu and CP Robert. Controlled MCMC for optimal sampling. *Technical Report*, 2001.

[156] C Andrieu, N de Freitas, A Doucet and MI Jordan. An introduction to MCMC for machine learning. *Machine Learning*, 50:5–43, 2003.

[157] EF Eastoe. A hierarchical model for non-stationary multivariate extremes: a case study of surface-level ozone and no_x data in the UK. *Environmetrics*, 20: 428–444, 2009.

[158] J Gyarmati-Szabó, HE Chen and LV Bogachev. Multivariate extreme value modelling of air pollution concentrations and analysis of traffic and meteorological impact. Technical report, University of Leeds, 2010.

[159] J Wang and N Zabaras. A Bayesian inference approach to the inverse heat conduction problem. *International Journal of Heat and Mass Transfer*, 2004.

[160] J Wang and N Zabaras. Using Bayesian statistics in the estimation of heat source in radiation. *International Journal of Heat and Mass Transfer*, 48: 15–29, 2005.

[161] TD Fadale, AV Nenarokomov and AF Emery. Uncertainties in parameter estimation: the inverse problem. *International Journal of Heat and Mass Transfer*, 38:511–518, 1995.

[162] S Chib and E Greenberg. Understanding the metropolis-hastings algorithm. *The American Statistician*, 49:327–335, 1995.

[163] GO Roberts, A Gelman and WR Gilks. Weak convergence and optimal scaling of random walk Metropolis algorithms. *The Annals of Applied Probability*, 7: 110–120, 1997.

[164] V Prokaj. Proposal selection for MCMC simulation. *The XIII International Conference - Applied Stochastic Models and Data Analysis*, 2009.

[165] MK Cowles and BP Carlin. Markov Chain Monte Carlo convergence diagnostics: a comparative review. *Journal of the American Statistical Association*, 91:883–904, 1996.

[166] RE Kass, BP Carlin, A Gelman and RM Neal. Markov Chain Monte Carlo in practice: A roundtable discussion. *The American Statistician*, 52:93–100, 1998.

[167] C Robert and G Casella. *Introducing Monte Carlo Methods with R*. Springer, 2010.

[168] A Gelman and DB Rubin. Inference from iterative simulation using multiple sequences. *Statistical Science*, 7:457–472, 1992.

[169] S Kirkpatrick, CD Gelatt and MP Vecchi. Optimization by simulated annealing. *Science*, 220:671–680, 1983.

[170] CJ Geyer and EA Thompson. Annealing Markov Chain Monte Carlo with applications to ancestral inference. *Journal of the American Statistical Association*, 90:909–920, 1995.

[171] RH Swendsen and JS Wang. Replica Monte Carlo simulation of spin-glasses. *Physical Review Letters*, 57:2607–2609, 1986.

[172] RM Neal. Sampling from multimodal distributions using tempered transitions. *Statistics and Computing*, 6:353–366, 1996.

[173] K Hukushima and K Nemoto. Exchange Monte Carlo method and application to spin glass simulations. *Journal of the Physical Society of Japan*, 65:1604–1608, 1996.

[174] DJ Earl and MW Deem. Parallel tempering: Theory, applications, and new perspectives. *Physical Chemistry Chemical Physics*, 7:3910–3916, 2005.

[175] AB Adib. The theory behind tempered Monte Carlo methods. *Technical Report*, 2005.

[176] *Delivery programme and characteristics for Tenax® HTA/HTS filament yarn*. Toho Tenax Europe GmbH, Germany, 2008.

[177] M Asareh. *Processing and performance of composite reinforcement preforms using binder coated carbon fibre tows*. PhD thesis, Cranfield University, in preparation.

[178] *Product Data Sheet for HexFlow® RTM 6.* Hexcel, United Kingdom, 2002.

[179] *Product data sheet for Araldite® 420 AB.* Huntsman Advanced Materials, Switzerland, 2004.

[180] Richmond Aerovac. `www.richmondaircraft.com`.

[181] Inc. Schnee-Morehead. `www.schneemorehead.com`.

[182] VAC Innovation Ltd. `www.vacinnovation.co.uk`, .

[183] *ASTM D3039/3039M - Standard Test Method for Tensile Properties of Polymer Matrix Composite Materials.* ASTM International, United States, 2005.

[184] *ASTM D3410/D3410M-03 - Standard Test Method for Compressive Properties of Polymer Matrix Composite Materials with Unsupported Gage Section by Shear Loading.* ASTM International, United States, 2003.

[185] *ASTM - D3518/D3518M-01 - Standard Test Method for In-Plane Shear Response of Polymer Matrix Composite Materials by Tensile Test of a ±45° Laminate.* ASTM International, United States, 2001.

[186] A Salomi, T Garstka, K Potter, A Greco and A Maffezzoli. Spring-in angle as molding distortion for thermoplastic matrix composite. *Composites Science and Technology*, 68:3047–3054, 2008.

[187] N Ersoy, T Garstka, K Potter, MR Wisnom, D Porter and G Stringer. Modelling of the spring-in phenomenon in curved parts made of a thermosetting composite. *Composites Part A: Applied Science and Manufacturing*, 2009.

[188] AC Lang. *Composites Forming Technologies.* Woodhead Publishing Ltd, 2007.

[189] Instron Material testing solutions. `http://www.instron.us/`.

[190] Limess Messtechnik & Software GmbH. `http://www.limess.com`.

[191] Tokyo Sokki Kenkyujo Co. Ltd. `http://www.tml.jp`, .

[192] National Instruments LabVIEW. `http://www.ni.com/labview/`.

[193] Electronic Instrument Research. `http://www.e-i-r.com/`.

[194] Zwick material testing. `http://www.zwick.com/`.

[195] DDR Cartié. *Effect of Z-fibres™ on the delamination behaviour of carbon-fibre/epoxy laminates.* PhD thesis, Cranfield University, 2000.

[196] S Hashemi, AJ Kinloch and JG Williams. The analysis of interlaminar fracture in uniaxial fibre-polymer composites. *Proceedings of the Royal Society of London Series A*, 427:173–199, 1990.

[197] *Pam-Crash™, Virtual Performance Solution 2008 - Explicit Solver Notes Manual, Explicit Solver Reference Manual.* ESI Group, France, 2008.

[198] *ASTM D790M - 93 - Standard Test Methods for Flexural Properties of Unreinforced and Reinforced Plastics and Electrical Insulating Materials (Metric).* ASTM International, United States, 1993.

[199] Photron Ltd. `www.photron.com`, .

[200] PreCarBi Project Deliverable 3.2.1. New testing methods to characterise "tack" and "robustness" properties of binder yarns and preforms. Technical report, April 2007.

[201] V Altstädt, D Gerth, M Stängle and HG Recker. Interlaminar crack growth in third-generation thermoset prepreg systems. *Polymer*, 34:907–909, 1993.

[202] O Ishai, H Rosenthal, N Sela and E Drukker. Effect of selective adhesive interleaving on interlaminar fracture toughness of graphite/epoxy composite laminates. *Composites*, 19:49–54, 1988.

[203] A Aksoy and LA Carlsson. Crack tip yield zone estimates in mode II interlaminar fracture of interleaved composites. *Engineering Fracture Mechanics*, 39:525–534, 1991.

[204] A Aksoy and LA Carlsson. Interlaminar shear fracture of interleaved graphite/epoxy composites. *Composites Science and Technology*, 43:55–69, 1992.

[205] N Sela, O Ishai and L Banks-Sills. The effect of adhesive thickness on interlaminar fracture toughness of interleaved cfrp specimens. *Composites*, 20: 257–264, 1989.

[206] S Singh and IK Partridge. Mixed-mode fracture in an interleaved carbon-fibre/epoxy composite. *Composites Science and Technology*, 55:319–327, 1995.

[207] D Fylstra, L Lasdon, J Watson and A Warren. Design and use of the Microsoft Excel Solver. *Interfaces*, 28:29–55, 1998.

[208] *ISO 527-5:1997 - Plastics – Determination of tensile properties – Part 5: Test conditions for unidirectional fibre-reinforced plastic composites.* International Organization for Standardization, Switzerland, 1997.

[209] *ISO 14126:1999 - Fibre-reinforced plastic composites – Determination of compressive properties in the in-plane direction.* International Organization for Standardization, Switzerland, 1999.

[210] AK Pickett and MRC Fouinneteau. Material characterisation and calibration of a meso-mechanical damage model for braid reinforced reinforced composites. *Composites Part A: Applied Science and Manufacturing*, 2006.

[211] AF Johnson, AK Pickett and P Rozycki. Computational methods for predicting impact damage in composite structures. *Composites Science and Technology*, 61:2183–2192, 2001.

[212] J Hadamard. Sur les problèmes aux dérivées partielles et leur signification physique type. *Princeton University Bulletin*, 13:49–52, 1902.

[213] WT Wang and TY Kam. Material characterization of laminated composite plates via static testing. *Composite Structures*, 50:347–352, 2000.

[214] JC Helton, JD Johnson, CJ Sallaberry and CB Storlie. Survey of sampling-based methods for uncertainty and sensitivity analysis. *Reliability Engineering & System Safety*, 91:1175 – 1209, 2006.

[215] DM Hamby. A review of techniques for parameter sensitivity analysis of environmental models. *Environmental Monitoring and Assessment*, 32:135–154, 1994.

[216] JK Lander. *Designing with Z-pins: locally reinforced composite structures.* PhD thesis, Cranfield University, 2008.

[217] A Andrade-Campos, S Thuillier, P Pilvin and F Teixeira-Dias. On the determination of material parameters for internal variable thermoelastic-viscoplastic constitutive models. *International Journal of Plasticity*, 23:1349–1379, 2007.

[218] TD Fadale, AV Nenarokomov and AF Emery. Uncertainties in parameter estimation: the inverse problem. *International Journal of Heat and Mass Transfer*, 1995.

[219] RC Aster, B Borchers and CH Thurber. *Parameter estimation and inverse problems.* 2005.

[220] A Gelman, AH El-Shaarawi, and WW Piegorsch. Prior distribution. *Encyclopedia of Environmetrics*, 3:1634–1637, 2002.

[221] J Hawthorne. Confirmation theory. *Philosophy of Statistics, Handbook of the Philosophy of Science*, 7, 2008.

[222] P Gustafson, D Aeschliman and AR Levy. A simple approach to fitting Bayesian survival models. *Lifetime Data Analysis*, 9:5–19, 2003.

[223] A Gelman, GO Roberts and MB Giles. Efficient Metropolis jumping rules. *Bayesian Statistics*, 5:599–607, 1996.

[224] GO Roberts and JS Rosenthal. Markov Chain Monte Carlo: some practical implications of theoretical results. *The Canadian Journal of Statistics*, 26: 5–31, 1998.

[225] GO Roberts, JS Rosenthal and PO Schwartz. Convergence properties of perturbed Markov chains. *Journal of Applied Probability*, 35:1–11, 1998.

[226] The R Project for Statistical Computing. `www.r-project.org`.

[227] CJ Geyer. Practical Markov Chain Monte Carlo. *Statistical Science*, 7:473–511, 1992.

[228] R Fedele, G Maier and M Whelan. Stochastic calibration of local constitutive models through measurements at the macroscale in heterogeneous media. *Computer Methods in Applied Mechanics and Engineering*, 195:4971–4990, 2006.

[229] AF Emery, E Valenti and D Bardot. Using Bayesian inference for parameter estimation when the system response and experimental conditions are measured with error and some variables are considered as nuisance variables. *Measurement Science and Technology*, 18:19–29, 2007.

[230] *Pam-Quickform™, Reference Manual.* ESI Group, France, 2008.

[231] I Sitaras and AA Skordos. Drape optimisation using GAs. *34 month PreCarBi progress meeting, Ried im Innkreis, Austria, July 6-7*, 2009.

[232] A Lee, C Yau, MB Giles, A Doucet and CC Holmes. On the utility of graphics cards to perform massively parallel simulation of advanced monte carlo methods. *Arxiv preprint*, 2009. URL `http://arxiv.org/abs/0905.2441v3`.

[233] M Hurn, H Rue, and NA Sheehan. Block updating in constrained markov chain monte carlo sampling. *Statistics & Probability Letters*, 41:353–361, 1999.

A - List of publications

Accepted

- C. Knipprath, A.A. Skordos and A.K. Pickett. A simplified discrete finite element modelling approach for non-crimped fabric composites. *Cranfield Multi-Strand Conference, Cranfield, United Kingdom*, May 6 - 7, 2008
- C. Knipprath, A.A. Skordos and A.K. Pickett. A simplified discrete finite element model for non-crimped fabric composites. *13th European Conference on Composite Materials, Stockholm, Sweden*, June 2 - 5, 2008
- K. Scobbie, P. Tsotra, J. Hoge, P. Christou, C. Knipprath, A.A. Skordos, S. Nilsson, L. E. Asp and A.K. Pickett. Development of high toughness epoxy resins for liquid composite moulding. *17th International Conference on Composite Materials, Edinburgh, United Kingdom*, July 27 - 31, 2009

In preparation

- C. Knipprath, A.A. Skordos. Material model parameter identification using the Markov Chain Monte Carlo technique. *International Journal for Numerical Methods in Engineering*
- C. Knipprath, A.A. Skordos. An experimental and modelling approach for preform robustness determination. *Composites Part A: Applied Science and Manufacturing*

B - Visual Basic source code

In-plane damage model

```
Function Y_12(E_2_0, G_12_0, b, Y_12_U, d_max, dam_12, dam_22, sig_12, sig_22, _
        Y_12_prev)
If dam_12 < d_max And dam_22 < d_max Then
    Y_12 = Sqr(sig_12 ^ 2 / (2 * G_12_0 * (1 - dam_12)) + b * _
        (maxim(sig_22, 0) ^ 2 / (2 * E_2_0 * (1 - dam_22))))
    If Y_12 < Y_12_prev Then Y_12 = Y_12_prev
Else
    Y_12 = Y_12_U
End If
End Function
```

```
Function Y_22(E_2_0, Y_22_U, d_max, dam_22, sig_22, Y_22_prev)
If dam_22 < d_max Then
    Y_22 = Sqr(maxim(sig_22, 0) ^ 2 / (2 * E_2_0 * (1 - dam_22)))
    If Y_22 < Y_22_prev Then Y_22 = Y_22_prev
Else
    Y_22 = Y_22_U
End If
End Function
```

```
Function dam_12(Y_12, Y_22, Y_12_0, Y_12_C, Y_22_U, Y_12_U, d_max, _
        D_12, epsrat_12)
Dim Ydyn_12_0 As Double, Ydyn_12_C As Double
Ydyn_12_0 = Y_12_0 * (1 + D_12 * Abs(epsrat_12))
Ydyn_12_C = Y_12_C * (1 + D_12 * Abs(epsrat_12))
If Y_12 < Y_12_U And Y_22 < Y_22_U Then
    dam_12 = maxim(Y_12 - Ydyn_12_0, 0) / Ydyn_12_C
End If
If Y_12 >= Y_12_U Or Y_22 >= Y_22_U Or dam_12 > d_max Then
    dam_12 = d_max
End If
End Function
```

```
Function dam_22(Y_12, Y_22, Y_22_0, Y_22_C, Y_22_U, Y_12_U, d_max, _
        D_22, epsrat_22)
Dim Ydyn_22_0 As Double, Ydyn_22_C As Double
Ydyn_22_0 = Y_22_0 * (1 + D_22 * Abs(epsrat_22))
Ydyn_22_C = Y_22_C * (1 + D_22 * Abs(epsrat_22))
If Y_12 < Y_12_U And Y_22 < Y_22_U Then
    dam_22 = maxim(Y_22 - Ydyn_22_0, 0) / Ydyn_22_C
End If
If Y_12 >= Y_12_U Or Y_22 >= Y_22_U Or dam_22 > d_max Then
```

```
    dam_22 = d_max
End If
End Function
```

```
Function E_2(eps_22_e, epsrat_22, dam_22, E_2_0, D_22)
Dim E_2_s As Double
If eps_22_e < 0 Then E_2_s = E_2_0
If eps_22_e >= 0 Then E_2_s = E_2_0 * (1 - dam_22)
E_2 = E_2_s * (1 + D_22 * Abs(epsrat_22))
End Function
```

```
Function G_12(dam_12, epsrat_12, G_12_0, D_12)
Dim G_12_s As Double
G_12_s = G_12_0 * (1 - dam_12)
G_12 = G_12_s * (1 + D_12 * Abs(epsrat_12))
End Function
```

```
Function sig_eps_12(sig_12_prev, eps_12_p_prev, p_12_prev, eps_12, epsrat_12, _
        eps_12_e_prev, deps_12, dam_12, dam_12_prev, G_12_0, D_12, R_0, _
        D_R, beta, m)
Dim dG_12 As Double, dsig_12 As Double, sig_12 As Double, eps_12_p As Double
Dim eps_12_e As Double, p_12 As Double
Dim R0dyn As Double, R As Double
Dim aux(1 To 4) As Variant
dG_12 = G_12(dam_12, epsrat_12, G_12_0, D_12) - _
        G_12(dam_12_prev, epsrat_12, G_12_0, D_12)
dsig_12 = deps_12 * G_12(dam_12, epsrat_12, G_12_0, D_12) + _
                          dG_12 * eps_12_e_prev
sig_12 = sig_12_prev + dsig_12
R0dyn = R_0 * (1 + D_R * Abs(epsrat_12))
R = R0dyn + beta * Abs(p_12_prev) ^ m
If dam_12 < 1 Then
    If Abs(sig_12 / (1 - dam_12)) - R <= 0 Then
        eps_12_e = sig_12 / G_12(dam_12, epsrat_12 + deps_12, G_12_0, D_12)
        eps_12_p = eps_12_p_prev
        p_12 = p_12_prev
    Else
        sig_12 = (1 - dam_12) * R
        eps_12_e = sig_12 / G_12(dam_12, epsrat_12 + deps_12, G_12_0, D_12)
        eps_12_p = eps_12 - eps_12_e
        p_12 = p_12_prev + 2 * (1 - dam_12) * deps_12
    End If
Else
    sig_12 = 0
    eps_12_e = 0
    eps_12_p = eps_12 - eps_12_e
    p_12 = p_12_prev + 2 * (1 - dam_12) * deps_12
End If
aux(1) = sig_12
aux(2) = eps_12_p
aux(3) = eps_12_e
aux(4) = p_12
sig_eps_12 = aux
End Function
```

```
Function sig_eps_22(sig_22_prev, eps_22_p_prev, p_22_prev, eps_22, epsrat_22, _
                    eps_22_e_prev, deps_22, dam_22, dam22_prev, E_2_0, D_22, R_0, _
                    D_R, beta, m, a)
Dim dE_2 As Double, dsig_22 As Double, sig_22 As Double, eps_22_p As Double, _
    eps_22_e As Double, p_22 As Double
Dim R0dyn As Double, R As Double
Dim aux(1 To 4) As Variant
dE_2 = E_2(eps_22_e_prev, epsrat_22, dam_22, E_2_0, D_22) - _
       E_2(eps_22_e_prev, epsrat_22, dam22_prev, E_2_0, D_22)
dsig_22 = deps_22 * E_2(eps_22_e_prev, epsrat_22, dam_22, E_2_0, D_22) + _
                         dE_2 * eps_22_e_prev
sig_22 = sig_22_prev + dsig_22
R0dyn = R_0 * (1 + D_R * Abs(epsrat_22))
R = R0dyn + beta * Abs(p_22_prev) ^ m
If dam_22 < 1 Then
    If Abs(a) * Abs(maxim(sig_22, 0) / (1 - dam_22) + minim(sig_22, 0)) _
        - R <= 0 Then
        eps_22_e = sig_22 / E_2(eps_22_e_prev, epsrat_22, dam_22, E_2_0, D_22)
        eps_22_p = eps_22_p_prev
        p_22 = p_22_prev
    Else
        sig_22 = (1 - dam_22) * R / a
        eps_22_e = sig_22 / E_2(eps_22_e_prev, epsrat_22, dam_22, E_2_0, D_22)
        eps_22_p = eps_22 - eps_22_e
        p_22 = p_22_prev + a * (1 - dam_22) * deps_22
    End If
Else
    sig_22 = 0
    eps_22_e = 0
    eps_22_p = eps_22 - eps_22_e
    p_22 = p_22_prev + a * (1 - dam_22) * deps_22
End If
aux(1) = sig_22
aux(2) = eps_22_p
aux(3) = eps_22_e
aux(4) = p_22
sig_eps_22 = aux
End Function
```

Out-of-plane model

```
Function Mode_I(E_0, t_max_n, G_u_n, eps_n, hcont)
Dim eps_i As Double, eps_u As Double
eps_n = eps_n * hcont
eps_i = t_max_n / E_0 * hcont
eps_u = 2 * G_u_n / t_max_n
If eps_n > 0 Then
    If Abs(eps_n) < eps_i Then
        Mode_I = 1 / 2 * E_0 * eps_n ^ 2
    Else
        If Abs(eps_n) < eps_u Then
            Mode_I = 1 / 2 / E_0 * t_max_n ^ 2 * hcont + _
                    (eps_n ^ 2 / 2 - (eps_i) ^ 2 / 2) * t_max_n / (eps_i - eps_u) _
```

```
                    - (eps_n - eps_i) * eps_u * t_max_n / (eps_i - eps_u)
            Else
                Mode_I = G_u_n
        End If
    End If
End If
If 1 / 2 / E_0 * t_max_n ^ 2 * hcont > G_u_n Then Mode_I = 100
End Function
```

```
Function Mode_II(G_0, t_max_s, G_u_s, eps_s, hcont)
Dim eps_i As Double, eps_u As Double
eps_s = eps_s * hcont
eps_i = t_max_s / G_0 * hcont
eps_u = 2 * G_u_s / t_max_s
If Abs(eps_s) < eps_i Then
    Mode_II = 1 / 2 * G_0 * eps_s ^ 2
Else
    If Abs(eps_s) < eps_u Then
        Mode_II = 1 / 2 / G_0 * t_max_s ^ 2 * hcont + _
                (eps_s ^ 2 / 2 - (eps_i) ^ 2 / 2) * t_max_s / (eps_i - eps_u) _
                - (eps_s - eps_i) * eps_u * t_max_s / (eps_i - eps_u)
        Else
            Mode_II = G_u_s
    End If
End If
If 1 / 2 / G_0 * t_max_s ^ 2 * hcont > G_u_s Then Mode_II = 100
End Function
```

Markov Chain Monte Carlo implementation

```
Private Sub MCMC()
Dim n As Integer, i As Integer, j As Integer, s As Integer, datarange As Integer
Dim i_start As Integer, stepsize As Double
Dim sigma As Double, ups As Double, sigma_theta As Double
Dim theta_cur As Double, theta_new As Double, theta_mean As Double
Dim Y As Double, Ftheta_new As Double, Ftheta_cur As Double
Dim Arg1 As Double, Arg2 As Double, Arg3 As Double, Arg4 As Double, Arg5 As Double
Dim Sum1 As Double, Sum2 As Double
Dim alpha As Double, apost As Double, ranuni As Double
Dim epsilon As Double, count As Double
Application.ScreenUpdating = False
Sheets("MCMC␣Output").Select
Range("A2:H40000").Select
Selection.ClearContents
datarange = Application.WorksheetFunction.count(Worksheets("Data␣&␣Model")._
        Range("A:A"))
datarange = datarange
sigma = Worksheets("Data␣&␣Model").Cells(14, 15)
sigma_theta = Worksheets("Data␣&␣Model").Cells(15, 15)
ups = Worksheets("Data␣&␣Model").Cells(16, 15)
n = Worksheets("Data␣&␣Model").Cells(17, 15)
i_start = Worksheets("Data␣&␣Model").Cells(18, 15)
stepsize = Worksheets("Data␣&␣Model").Cells(19, 15)
```

```
theta_cur = Worksheets("Data␣&␣Model").Cells(21, 15)
For i = 1 To n
    Worksheets("MCMC␣Output").Cells(i + 1, 5) = Application.WorksheetFunction._
        NormInv(Rnd, 0, ups)
    Worksheets("MCMC␣Output").Cells(i + 1, 6) = Rnd
    epsilon = Worksheets("MCMC␣Output").Cells(i + 1, 5)
    theta_new = theta_cur + epsilon
    Worksheets("Data␣&␣Model").Cells(2, 15) = theta_cur
    Worksheets("Data␣&␣Model").Cells(2, 14) = theta_new
    Sheets("Data␣&␣Model").Select
    ActiveSheet.Calculate
    Sum1 = 0
    Sum2 = 0
    j = 2
    Do While j <= datarange
        Y = Worksheets("Data␣&␣Model").Cells(j, 2)
        Ftheta_new = Worksheets("Data␣&␣Model").Cells(j, 9)
        Ftheta_cur = Worksheets("Data␣&␣Model").Cells(j, 10)
        Arg1 = Application.WorksheetFunction.Ln(Application.WorksheetFunction._
                NormDist(Y, Ftheta_new, sigma, False))
        Arg2 = Application.WorksheetFunction.Ln(Application.WorksheetFunction._
                NormDist(Y, Ftheta_cur, sigma, False))
        Sum1 = Sum1 + Arg1
        Sum2 = Sum2 + Arg2
        j = j + 1
    Loop
    Arg3 = Application.WorksheetFunction.Ln(Application.WorksheetFunction._
        NormDist(theta_new, 0, sigma_theta, False))
    Arg4 = Application.WorksheetFunction.Ln(Application.WorksheetFunction._
        NormDist(theta_cur, 0, sigma_theta, False))
    alpha = Min(1, Exp(1) ^ (Sum1 - Sum2 + Arg3 - Arg4))
    Worksheets("MCMC␣Output").Cells(i + 1, 8) = alpha
    ranuni = Worksheets("MCMC␣Output").Cells(i + 1, 6)
    If alpha > ranuni Then
        theta_cur = theta_new
        s = 1
        Worksheets("Data␣&␣Model").Cells(2, 15) = theta_cur
        Sheets("Data␣&␣Model").Select
        ActiveSheet.Calculate
        apost = 0
        j = 2
        Do While j <= datarange
            Y = Worksheets("Data␣&␣Model").Cells(j, 2)
            Ftheta_cur = Worksheets("Data␣&␣Model").Cells(j, 10)
            Arg5 = Application.WorksheetFunction.Ln(Application.WorksheetFunction._
                NormDist(Y, Ftheta_cur, sigma, False))
            apost = apost + Arg5
            j = j + 1
        Loop
        apost = apost + Application.WorksheetFunction.Ln( _
            Application.WorksheetFunction.NormDist(theta_cur, 0, sigma_theta,_
                False))
    Else
        theta_cur = theta_cur
        s = 0
        apost = Sum2 + Arg4
    End If
```

```
    Worksheets("MCMC Output").Cells((i + 1), 1) = s
    Worksheets("MCMC Output").Cells((i + 1), 2) = apost
    Worksheets("MCMC Output").Cells((i + 1), 3) = theta_cur
Next
theta_mean = 0
count = 0
For i = i_start To n Step stepsize
    theta_mean = theta_mean + Worksheets("MCMC Output").Cells((i + 1), 3)
    count = count + 1
Next
theta_mean = theta_mean / count
Worksheets("Data & Model").Cells(2, 16) = theta_mean
Sheets("Data & Model").Select
ActiveSheet.Calculate
Application.ScreenUpdating = True
End Sub
```

C - C++ source code

Markov Chain Monte Carlo implementation

```
int main(){
    unsigned long int i, j, k;
    unsigned long int n;
    double **theta_cur;
    theta_cur = (double **) malloc((nChains)*sizeof(double *));
    if (theta_cur != NULL) {
        for (k=0; k<(nParameters); k++) {
            theta_cur[k] = (double *) malloc(nParameters * sizeof(double *));
            if (theta_cur[k] == NULL) {
                printf("Memory␣allocation␣failed.␣Exiting....");
                return 1;
            }
        }
    } else {
        printf("Memory␣allocation␣failed.␣Exiting....");
        return 1;
    }
    double **theta_new; {...}
    {...}
    double **sj2; {...}
    double *Sum1 = new double[nChains];
    {...}
    int *meanStepCount = new int[nChains];
    double *psiBarDotDot = new double[nParameters];
    {...}
    double *R = new double[nParameters];
    double psiBarDotDotApost, BApost, WApost, RApost;
    {...}
    double sigma_theta, sigmaTens, sigmaComp, sigmaTrans, sigmaShear;
    double sigmaModelI, sigmaModelII;
    MTRand MersenneTwister;
    unsigned long int burnInRange;
    int meanStepLength;
    bool enableParTemp = true;
    int nsParTemp = 30;
    double parTempU1 = ((double) 1./nsParTemp);
    int nsParTempCounter = 0;
    double delta = (1-0.001)/nChains;
    betaParTemp[0] = 1.;
    for (j=1; j!=nChains; j++) {betaParTemp[j] = betaParTemp[j-1] - delta;}
    ofstream outfile1("output1.txt");
    {...}
    ofstream outfileHisto1("output_Histogram_input1.txt");
```

```
    {...}
    outfile1 << "i\t␣s\t␣apost␣\t␣alpha␣\t␣E_1_0c␣\t␣E_1_0t␣\t␣gamma␣\t␣eps_i_fc
␣␣␣␣␣␣␣␣\t␣eps_u_fc␣␣\t␣eps_i_ft␣\t␣eps_u_ft␣\t␣d_u_fc␣\t␣d_u_ft␣\t␣D_11␣\t␣D_11_R
␣␣␣␣␣␣␣␣\t␣E_2_0␣\t␣G_12_0␣\t␣b␣\t␣Y_22_0␣\t␣Y_12_0␣\t␣Y_22_C␣\t␣Y_12_C
␣␣␣␣␣␣␣␣\t␣Y_22_U␣\t␣Y_12_U␣\t␣dmax␣\t␣D_22␣\t␣D_12␣\t␣a␣\t␣R_0␣\t␣D_R␣\t␣beta
␣␣␣␣␣␣␣␣\t␣m␣\t␣GIu␣\t␣sigImax␣\t␣GIIu␣\t␣sigIImax" << endl;
    {...}
    const char *fileNameSetTen1, *fileNameSetComp1, *fileNameSetTrans1;
    const char *fileNameSetShear1, *fileNameSetModelI1, *fileNameSetModelII1;
    fileNameSetTen1 = "data_Tension1.txt";
    dimSetTen1 = getDim(fileNameSetTen1);
    double (*dataSetTen1)[inPlaneDataArrayWidth] = new double[dimSetTen1]
        [inPlaneDataArrayWidth];
    getData(fileNameSetTen1, dimSetTen1, dataSetTen1);
    fileNameSetComp1 = "data_Compression1.txt";
    {...}
    fileNameSetTrans1 = "data_Transverse1.txt";
    {...}
    fileNameSetShear1 = "data_Shear45_1.txt";
    {...}
    fileNameSetModelI1 = "data_DCB_1.txt";
    dimSetModelI1 = getDim(fileNameSetModelI1);
    double (*dataSetModelI1)[outPlaneDataArrayWidth] =new double[dimSetModelI1]
        [outPlaneDataArrayWidth];
    getData3Columns(fileNameSetModelI1, dimSetModelI1, dataSetModelI1);
    fileNameSetModelII1 = "data_ELS_1.txt";
     {...}
    theta_cur[0][0]  =  135.6053378;
    theta_cur[0][1]  =  166.5764595;
    theta_cur[0][2]  =  0.153487795;
    theta_cur[0][3]  =  0.009593106;
    theta_cur[0][4]  =  0.009840742;
    theta_cur[0][5]  =  0.015498758;
    theta_cur[0][6]  =  0.015872407;
    theta_cur[0][7]  =  0.942750323;
    theta_cur[0][8]  =  1.004606247;
    theta_cur[0][9]  =  1.01E-14;
    theta_cur[0][10] =  1.00E-14;
    theta_cur[0][11] =  9.712413991;
    theta_cur[0][12] =  4.331598146;
    theta_cur[0][13] =  0.051483421;
    theta_cur[0][14] =  0.002679217;
    theta_cur[0][15] =  0.004513456;
    theta_cur[0][16] =  0.153243527;
    theta_cur[0][17] =  0.043213706;
    theta_cur[0][18] =  0.018807773;
    theta_cur[0][19] =  0.019438298;
    theta_cur[0][20] =  0.398555465;
    theta_cur[0][21] =  9.69E-15;
    theta_cur[0][22] =  9.82E-15;
    theta_cur[0][23] =  0.237898239;
    theta_cur[0][24] =  0.071918718;
    theta_cur[0][25] =  9.90E-15;
    theta_cur[0][26] =  0.476475647;
    theta_cur[0][27] =  0.738793689;
    theta_cur[0][28] =  0.000415385;
    theta_cur[0][29] =  0.007738246;
```

```
theta_cur[0][30] = 0.000447237;
theta_cur[0][31] = 0.023835519;
theta_cur[1][0]  = {...}
theta_cur[2][0]  = {...}
theta_cur[3][0]  = {...}
sigma_epsilon[0][0]  =      0.0009  ;
sigma_epsilon[0][1]  =      0.0006  ;
sigma_epsilon[0][2]  =      0.001  ;
sigma_epsilon[0][3]  =      0.0006  ;
sigma_epsilon[0][4]  =      0.0008  ;
sigma_epsilon[0][5]  =      0.0008  ;
sigma_epsilon[0][6]  =      0.0002  ;
sigma_epsilon[0][7]  =      0.0009  ;
sigma_epsilon[0][8]  =      0.0009  ;
sigma_epsilon[0][9]  =      0.000001;
sigma_epsilon[0][10] =      0.000001;
sigma_epsilon[0][11] =      0.0009  ;
sigma_epsilon[0][12] =      0.0003  ;
sigma_epsilon[0][13] =      0.007  ;
sigma_epsilon[0][14] =      0.006  ;
sigma_epsilon[0][15] =      0.004  ;
sigma_epsilon[0][16] =      0.004  ;
sigma_epsilon[0][17] =      0.003  ;
sigma_epsilon[0][18] =      0.007  ;
sigma_epsilon[0][19] =      0.004  ;
sigma_epsilon[0][20] =      0.001;
sigma_epsilon[0][21] =      0.000001;
sigma_epsilon[0][22] =      0.000001;
sigma_epsilon[0][23] =      0.0003  ;
sigma_epsilon[0][24] =      0.004  ;
sigma_epsilon[0][25] =      0.000001;
sigma_epsilon[0][26] =      0.004  ;
sigma_epsilon[0][27] =      0.001  ;
sigma_epsilon[0][28] =      0.001  ;
sigma_epsilon[0][29] =      0.006  ;
sigma_epsilon[0][30] =      0.009  ;
sigma_epsilon[0][31] =      0.005  ;
sigma_epsilon[1][0]  = {...}
sigma_epsilon[2][0]  = {...}
sigma_epsilon[3][0]  = {...}
n = 200000;
burnInRange = n/2;
meanStepLength = 10;
enableScreenOutput = false;
sigma_theta = 10.;
sigmaTens = 0.05;
sigmaComp = 0.05;
sigmaTrans = 0.005;
sigmaShear = 0.005;
sigmaModelI = 0.05;
sigmaModelII = 0.05;
{...}
for (j=0; j != nChains; j++) {
    {...}
}
for (i = 0 ; i <= n ; i++){
    for (j=0; j!=nChains; j++) {
```

```
            Sum1[j] = 0.;
            Sum2[j] = 0.;
            Sum3[j] = 0.;
            Sum4[j] = 0.;
            ranuni[j] = MersenneTwister.rand();
            for (k=0; k!=nParameters; k++) {
                epsilon[j][k] = normalInv(MersenneTwister.rand(), 0,
                        sigma_epsilon[j][k]);
                theta_new[j][k] = theta_cur[j][k] + epsilon[j][k];
            }
            LadevezeTenComp(dataSetTen1, dimSetTen1, theta_cur, theta_new,
                sigmaTens, Sum1, Sum2, j);
                {...}
            LadevezeTenComp(dataSetComp1, dimSetComp1, theta_cur, theta_new,
                sigmaComp, Sum1, Sum2, j);
                {...}
            LadevezeTrans(dataSetTrans1, dimSetTrans1, theta_cur, theta_new,
                sigmaTrans, Sum1, Sum2, j);
                {...}
            LadevezeShear(dataSetShear1, dimSetShear1, theta_cur, theta_new,
                sigmaShear, Sum1, Sum2, j);
                {...}
            ModelICalc(dataSetModelI1, dimSetModelI1, theta_cur, theta_new, hcont,
                sigmaModelI, Sum1, Sum2, j);
                {...}
            ModelIICalc(dataSetModelII1, dimSetModelII1, theta_cur, theta_new, hcont,
                h, L, sigmaModelII, Sum1, Sum2, j);
                {...}
            for (k=0; k!=nParameters; k++) {
                Sum3[j] += log(normDist(theta_new[j][k], 0, sigma_theta));
                Sum4[j] += log(normDist(theta_cur[j][k], 0, sigma_theta));
            }
            if (enableParTemp && nChains >1) {
                alpha[j] = min(1., exp(piParTemp(Sum3, Sum1, betaParTemp, j, j) -
                        piParTemp(Sum4, Sum2, betaParTemp, j, j)));
            } else {
                alpha[j] = min(1., exp(Sum1[j] - Sum2[j] + Sum3[j] - Sum4[j]));
            }
            if (alpha[j] > ranuni[j]){
                for (k=0; k!=nParameters; k++) {
                    theta_cur[j][k] = theta_new[j][k];
                }
                acceptFlag[j] = 1;
                acceptCount[j]++;
                if (enableParTemp && nChains > 1) {
                    apost[j] = piParTemp(Sum3, Sum1, betaParTemp, j, j);
                }else {
                    apost[j] = Sum1[j] + Sum3[j];
                }
            }
            else{
                acceptFlag[j] = 0;
                if (enableParTemp && nChains > 1) {
                    apost[j] = piParTemp(Sum4, Sum2, betaParTemp, j, j);
                }else {
                    apost[j] = Sum2[j] + Sum4[j];
                }
```

```
            }
            if (i > burnInRange){
                if (meanStepCount[j] == meanStepLength){
                    meanCount[j]++;
                    for (k = 0; k!=nParameters; k++) {
                        theta_delta[j][k] = exp(theta_cur[j][k]) - theta_mean[j][k];
                        theta_mean[j][k] += theta_delta[j][k] / meanCount[j];
                        theta_M2[j][k] += theta_delta[j][k] * (exp(theta_cur[j][k])-
                                theta_mean[j][k]);
                        if (meanCount-1 == 0) {
                            theta_variance[j][k] = 0.;
                        } else {
                            theta_variance[j][k] = theta_M2[j][k]/(meanCount[j]-1);
                        }
                        theta_stddev[j][k] = sqrt(theta_variance[j][k]);
                    }
                    meanStepCount[j] = 0;
                }
                meanStepCount[j]++;
                if (nChains > 1) {
                    for (k = 0; k!=nParameters; k++) {
                        psiBarDotJ_delta[j][k] = exp(theta_cur[j][k]) -
                                psiBarDotJ[j][k];
                        psiBarDotJ[j][k] += psiBarDotJ_delta[j][k]/(i-burnInRange);
                        psiBarDotJ_M2[j][k] += psiBarDotJ_delta[j][k] *
                                (exp(theta_cur[j][k]) - psiBarDotJ[j][k]);
                        if ((i-burnInRange)-1 == 0) {
                            sj2[j][k] = 0.;
                        } else {
                            sj2[j][k] = psiBarDotJ_M2[j][k]/((i-burnInRange)-1);
                        }
                    }
                    if (i > burnInRange) {
                        psiBarDotJApost_delta[j] = apost[j] - psiBarDotJApost[j];
                        psiBarDotJApost[j] += psiBarDotJApost_delta[j] /
                                (i-burnInRange);
                        psiBarDotJApost_M2[j] += psiBarDotJApost_delta[j] *
                                (apost[j] - psiBarDotJApost[j]);
                        if ((i-burnInRange)-1 == 0) {
                            sj2Apost[j] = 0.;
                        } else {
                            sj2Apost[j] = psiBarDotJApost_M2[j]/((i-burnInRange)-1);
                        }
                    }
                }
            }
        }
        if (nChains>1 && i > burnInRange) {
            for (k=0; k!=nParameters; k++) {
                psiBarDotDot[k] = 0.;
                B[k] = 0.;
                W[k] = 0.;
                for (j=0; j!=nChains; j++) {
                    psiBarDotDot[k] += psiBarDotJ[j][k];
                }
                for (j=0; j!=nChains; j++) {
                    B[k] += pow((psiBarDotJ[j][k] - psiBarDotDot[k] / nChains), 2.);
```

```
                    W[k] += sj2[j][k];
                }
                B[k] = B[k] * ((double) (i-burnInRange)/(nChains-1));
                W[k] = W[k] / nChains;
                R[k] = sqrt((((double) ((i-burnInRange)-1)/(i-burnInRange))*W[k] +
                        ((double) 1./(i-burnInRange))*B[k])/W[k]);
            }
            psiBarDotDotApost = 0.;
            BApost = 0.;
            WApost = 0.;
            for (j=0; j!=nChains; j++) {
                psiBarDotDotApost += psiBarDotJApost[j];
            }
            for (j=0; j!=nChains; j++) {
                BApost += pow((psiBarDotJApost[j] - psiBarDotDotApost /
                        nChains), 2.);
                WApost += sj2Apost[j];
            }
            BApost = BApost * ((double) (i-burnInRange)/(nChains-1));
            WApost = WApost / nChains;
            RApost = sqrt((((double) ((i-burnInRange)-1)/(i-burnInRange))*WApost +
                ((double) 1./(i-burnInRange))*BApost)/WApost);
        }
        outfile1 << i << "\t" << acceptFlag[0] << "\t" << apost[0] << "\t" <<
                alpha[0] << "\t";
        {...}
        if (i > burnInRange) {outfileConvergenceR << i << "\t" << RApost << "\t";}
        for (k=0; k!=nParameters; k++) {
            outfile1 << exp(theta_cur[0][k]) << "\t";
            {...}
            outfileHisto1 << exp(theta_cur[0][k]) << "\t";
            {...}
        }
        outfile1 << endl;
        {...}
        outfileHisto1 << endl;
        {...}
        if (enableParTemp && nsParTempCounter == nsParTemp && nChains>1) {
            if (MersenneTwister.rand() <= parTempU1) {
                iParTemp = MersenneTwister.randInt(nChains-1);
                ipl1ParTemp = iParTemp + 1;
                if (ipl1ParTemp >= nChains) {ipl1ParTemp = 0;}
                pi_Xipl1_Betai = piParTemp(acceptFlag[ipl1ParTemp]==1 ? Sum3 : Sum4,
                        acceptFlag[ipl1ParTemp]==1 ? Sum1 : Sum2, betaParTemp,
                ipl1ParTemp, iParTemp);
                pi_Xi_Betaipl1 = {...}
                pi_Xi_Betai = {...}
                pi_Xipl1_Betaipl1 = {...}
                rParTemp = min(1., exp(pi_Xipl1_Betai + pi_Xi_Betaipl1-pi_Xi_Betai-
                        pi_Xipl1_Betaipl1));
                if (MersenneTwister.rand()<=rParTemp) {
                    for (k=0; k!=nParameters; k++) {
                        swapParTempMem = theta_cur[iParTemp][k];
                        theta_cur[iParTemp][k] = theta_cur[ipl1ParTemp][k];
                        theta_cur[ipl1ParTemp][k] = swapParTempMem;
                    }
                    {...}
```

```
                } else {
                    {...}
                }
            }
            {...}
        }
        if (enableParTemp && nChains>1) {nsParTempCounter++;}
    }
    resultSummaryOutfile << "Acceptance␣ratio(s):" << endl;
    for (j=0; j!=nChains; j++) {
        resultSummaryOutfile << "Chain␣" << j << ":␣\t" <<
                ((double) acceptCount[j]/n) << endl;
    }
    resultSummaryOutfile << "Solution␣vector(s):" << endl;
    for (k=0; k!=nParameters; k++) {
        for (j=0; j!=nChains; j++) {
            resultSummaryOutfile << theta_mean[j][k] << "\t␣+/-␣\t"<<
                 theta_stddev[j][k] << "\t";
        }
        resultSummaryOutfile << endl;
    }
    free(theta_cur);
    {...}
    theta_cur = NULL;
    {...}
    delete [] Sum1;
    {...}
    return 0;
}
```

```
double piParTemp(double *pXI, double *pDXI, double *betaI, int pIndex,
        int betaIndex){
    return (pXI[pIndex] + betaI[betaIndex] * pDXI[pIndex];);
}
```

```
void getData(const char *filename, unsigned long int count, double (*array)
        [inPlaneDataArrayWidth]){
    ifstream infile;
    unsigned long int i;
    if (!infile){cerr << "Cannot␣open␣file␣" << endl;}
    infile.open(filename);
    for (i = 0; i != count; i++){infile >> array[i][0] >> array[i][1];}
    infile.close();
}
```

```
void getData3Columns(const char *filename, unsigned long int count, double (*array)
        [outPlaneDataArrayWidth]){
    ifstream infile;
    unsigned long int i;
    if (!infile){cerr << "Cannot␣open␣file␣" << endl;}
    infile.open(filename);
    for (i = 0; i != count; i++){infile >> array[i][0] >> array[i][1] >>
        array[i][2];}
    infile.close();
}
```

```
void LadevezeTenComp(double (*array)[inPlaneDataArrayWidth], unsigned long int dim,
        double **theta_cur, double **theta_new, double sigma, double *Sum1,
        double *Sum2,   unsigned long int j){
    unsigned long int i;
    double epsrat_11;
    double *simStressCur = new double[dim];
    double *simStressNew = new double[dim];
    simStressCur[0]=0.;
    simStressNew[0]=0.;
    epsrat_11=0.;
    for (i=1; i < (dim-1); i++){
        simStressCur[i] = sig_11(simStressCur[i-1], epsrat_11, array[i][0],
        array[i+1][0]-array[i][0], exp(theta_cur[j][0]),
        exp(theta_cur[j][1]), exp(theta_cur[j][2]), exp(theta_cur[j][3]),
        exp(theta_cur[j][4]), exp(theta_cur[j][5]), exp(theta_cur[j][6]),
        exp(theta_cur[j][7]), exp(theta_cur[j][8]), exp(theta_cur[j][9]),
        exp(theta_cur[j][10]));
        simStressNew[i] = sig_11(simStressNew[i-1], epsrat_11, array[i][0],
        array[i+1][0]-array[i][0], exp(theta_new[j][0]), exp(theta_new[j][1]),
        exp(theta_new[j][2]), exp(theta_new[j][3]), exp(theta_new[j][4]),
        exp(theta_new[j][5]), exp(theta_new[j][6]), exp(theta_new[j][7]),
        exp(theta_new[j][8]), exp(theta_new[j][9]), exp(theta_new[j][10]));
        Sum1[j] += log(normDist(array[i][1], simStressNew[i], sigma));
        Sum2[j] += log(normDist(array[i][1], simStressCur[i], sigma));
    }
    delete [] simStressCur;
    delete [] simStressNew;
}
```

```
void LadevezeTrans(double (*array)[inPlaneDataArrayWidth], unsigned long int dim,
        double **theta_cur, double **theta_new, double sigma, double *Sum1,
        double *Sum2, unsigned long int j){
    unsigned long int i;
    double epsrat_12, epsrat_22;
    double *simStressCur = new double[dim];
    {...}
    double *p_22_New = new double[dim];
    simStressCur[0]=0.;
    {...}
    p_22_New[0] = 0.;
    epsrat_12=0.;
    epsrat_22=0.;
    for (i=1; i < dim; i++){
        Y12Cur[i] = Y_12(exp(theta_cur[j][11]), exp(theta_cur[j][12]),
                exp(theta_cur[j][13]), exp(theta_cur[j][19]), exp(theta_cur[j][20]),
        dam12Cur[i-1], dam22Cur[i-1], 0, simStressCur[i-1], Y12Cur[i-1]);
        Y22Cur[i] = Y_22(exp(theta_cur[j][11]), exp(theta_cur[j][18]),
                exp(theta_cur[j][20]),dam22Cur[i-1],simStressCur[i-1],Y22Cur[i-1]);
        dam12Cur[i] = dam_12(Y12Cur[i], Y22Cur[i],exp(theta_cur[j][15]),
                exp(theta_cur[j][17]), exp(theta_cur[j][18]), exp(theta_cur[j][19]),
        exp(theta_cur[j][20]), exp(theta_cur[j][22]), epsrat_12);
        dam22Cur[i] = dam_22(Y12Cur[i], Y22Cur[i], exp(theta_cur[j][14]),
                exp(theta_cur[j][16]), exp(theta_cur[j][18]), exp(theta_cur[j][19]),
        exp(theta_cur[j][20]), exp(theta_cur[j][21]), epsrat_22);
        sig_eps_22(simStressCur[i-1],eps_22_p_Cur[i-1],p_22_Cur[i-1],array[i][0],
                epsrat_22, eps_22_e_Cur[i-1],array[i][0] - array[i-1][0],dam22Cur[i],
```

```
        dam22Cur[i-1], exp(theta_cur[j][11]), exp(theta_cur[j][21]),
        exp(theta_cur[j][24]), exp(theta_cur[j][25]), exp(theta_cur[j][26]),
        exp(theta_cur[j][27]), exp(theta_cur[j][23]), &simStressCur[i],
        &eps_22_e_Cur[i], &eps_22_p_Cur[i], &p_22_Cur[i]);
        Y12New[i] = Y_12(exp(theta_new[j][11]), exp(theta_new[j][12]),
                exp(theta_new[j][13]), exp(theta_new[j][19]), exp(theta_new[j][20]),
        dam12New[i-1], dam22New[i-1], 0, simStressNew[i-1], Y12New[i-1]);
        Y22New[i] = Y_22(exp(theta_new[j][11]), exp(theta_new[j][18]),
                exp(theta_new[j][20]),dam22New[i-1],simStressNew[i-1],Y22New[i-1]);
        dam12New[i] = dam_12(Y12New[i], Y22New[i], exp(theta_new[j][15]),
                exp(theta_new[j][17]), exp(theta_new[j][18]), exp(theta_new[j][19]),
        exp(theta_new[j][20]), exp(theta_new[j][22]), epsrat_12);
        dam22New[i] = dam_22(Y12New[i], Y22New[i], exp(theta_new[j][14]),
                exp(theta_new[j][16]), exp(theta_new[j][18]), exp(theta_new[j][19]),
        exp(theta_new[j][20]), exp(theta_new[j][21]), epsrat_22);
        sig_eps_22(simStressNew[i-1], eps_22_p_New[i-1], p_22_New[i-1],
                array[i][0],epsrat_22,eps_22_e_New[i-1],array[i][0]-array[i-1][0],
        dam22New[i], dam22New[i-1], exp(theta_new[j][11]),
        exp(theta_new[j][21]), exp(theta_new[j][24]), exp(theta_new[j][25]),
        exp(theta_new[j][26]), exp(theta_new[j][27]), exp(theta_new[j][23]),
        &simStressNew[i], &eps_22_e_New[i], &eps_22_p_New[i], &p_22_New[i]);
        Sum1[j] += log(normDist(array[i][1], simStressNew[i], sigma));
        Sum2[j] += log(normDist(array[i][1], simStressCur[i], sigma));
    }
    delete [] simStressCur;
    {...}
}
```

```
void LadevezeShear(double (*array)[inPlaneDataArrayWidth], unsigned long int dim,
        double **theta_cur, double **theta_new, double sigma, double *Sum1,
        double *Sum2, unsigned long int j){
    unsigned long int i;
    double epsrat_12, epsrat_22;
    double *simStressCur = new double[dim];
    {...}
    double *p_12_New = new double[dim];
    simStressCur[0]=0.;
    {...}
    p_12_New[0] = 0.;
    epsrat_12=0.;
    epsrat_22=0.;
    for (i=1; i < dim; i++){
        Y12Cur[i] = Y_12(exp(theta_cur[j][11]), exp(theta_cur[j][12]),
                exp(theta_cur[j][13]), exp(theta_cur[j][19]), exp(theta_cur[j][20]),
        dam12Cur[i-1], dam22Cur[i-1], simStressCur[i-1], 0, Y12Cur[i-1]);
        Y22Cur[i] = Y_22(exp(theta_cur[j][11]), exp(theta_cur[j][18]),
                exp(theta_cur[j][20]), dam22Cur[i-1], 0, Y22Cur[i-1]);
        dam12Cur[i] = dam_12(Y12Cur[i], Y22Cur[i], exp(theta_cur[j][15]),
                exp(theta_cur[j][17]), exp(theta_cur[j][18]), exp(theta_cur[j][19]),
        exp(theta_cur[j][20]), exp(theta_cur[j][22]), epsrat_12);
        dam22Cur[i] = dam_22(Y12Cur[i], Y22Cur[i], exp(theta_cur[j][14]),
                exp(theta_cur[j][16]),exp(theta_cur[j][18]),exp(theta_cur[j][19]),
        exp(theta_cur[j][20]), exp(theta_cur[j][21]), epsrat_22);
        sig_eps_12(simStressCur[i-1], eps_22_p_Cur[i-1], p_12_Cur[i-1],
                array[i][0],epsrat_12,eps_22_e_Cur[i-1],array[i][0]-array[i-1][0],
        dam12Cur[i], dam12Cur[i-1], exp(theta_cur[j][12]),
        exp(theta_cur[j][22]), exp(theta_cur[j][24]), exp(theta_cur[j][25]),
```

```
        exp(theta_cur[j][26]), exp(theta_cur[j][27]), &simStressCur[i],
        &eps_22_e_Cur[i], &eps_22_p_Cur[i], &p_12_Cur[i]);
        Y12New[i] = Y_12(exp(theta_new[j][11]), exp(theta_new[j][12]),
                exp(theta_new[j][13]), exp(theta_new[j][19]),
        exp(theta_new[j][20]), dam12New[i-1], dam22New[i-1],
        simStressNew[i-1], 0, Y12New[i-1]);
        Y22New[i] = Y_22(exp(theta_new[j][11]), exp(theta_new[j][18]),
                exp(theta_new[j][20]), dam22New[i-1], 0, Y22New[i-1]);
        dam12New[i] = dam_12(Y12New[i], Y22New[i],
                exp(theta_new[j][15]), exp(theta_new[j][17]),
        exp(theta_new[j][18]), exp(theta_new[j][19]), exp(theta_new[j][20]),
        exp(theta_new[j][22]), epsrat_12);
        dam22New[i] = dam_22(Y12New[i], Y22New[i], exp(theta_new[j][14]),
                exp(theta_new[j][16]), exp(theta_new[j][18]), exp(theta_new[j][19]),
        exp(theta_new[j][20]), exp(theta_new[j][21]), epsrat_22);
        sig_eps_12(simStressNew[i-1], eps_22_p_New[i-1],p_12_New[i-1],
                array[i][0], epsrat_12,eps_22_e_New[i-1],array[i][0]-array[i-1][0],
        dam12New[i], dam12New[i-1], exp(theta_new[j][12]),
        exp(theta_new[j][22]), exp(theta_new[j][24]), exp(theta_new[j][25]),
        exp(theta_new[j][26]), exp(theta_new[j][27]), &simStressNew[i],
        &eps_22_e_New[i], &eps_22_p_New[i], &p_12_New[i]);
        Sum1[j] += log(normDist(array[i][1], simStressNew[i], sigma));
        Sum2[j] += log(normDist(array[i][1], simStressCur[i], sigma));
    }
    delete [] simStressCur;
    {...}
    delete [] p_12_New;
}
```

```
unsigned long int getDim(const char *filename){
    ifstream infile;
    unsigned long int count;
    string s;
    if (!infile){
        cerr << "Cannot␣open␣file␣" << endl;
        return (-1);
    }
    count = 0;
    infile.open(filename);
    while (!infile.eof()){
        getline(infile, s);
        count++;
    }
    infile.close();
    return count;
}
```

```
double normDist(double X, double mean, double stddev){
    const double Pi = 3.14159265358979;
    return(1/(exp(pow(X-mean, 2)/(2.*pow(stddev, 2)))*sqrt(2*Pi)*stddev););
}
```

NOTE: original file was obtained from
http://home.online.no/ pjacklam/notes/invnorm/index.html
further additions were made

```
double normalInv(double p, double mean, double stddev){
#define  A1   (-3.969683028665376e+01)
#define  A2    2.209460984245205e+02
#define  A3   (-2.759285104469687e+02)
#define  A4    1.383577518672690e+02
#define  A5   (-3.066479806614716e+01)
#define  A6    2.506628277459239e+00
#define  B1   (-5.447609879822406e+01)
#define  B2    1.615858368580409e+02
#define  B3   (-1.556989798598866e+02)
#define  B4    6.680131188771972e+01
#define  B5   (-1.328068155288572e+01)
#define  C1   (-7.784894002430293e-03)
#define  C2   (-3.223964580411365e-01)
#define  C3   (-2.400758277161838e+00)
#define  C4   (-2.549732539343734e+00)
#define  C5    4.374664141464968e+00
#define  C6    2.938163982698783e+00
#define  D1    7.784695709041462e-03
#define  D2    3.224671290700398e-01
#define  D3    2.445134137142996e+00
#define  D4    3.754408661907416e+00
#define P_LOW    0.02425
#define P_HIGH   0.97575
    double x, q, r, u, e;
    if ((0 < p ) && (p < P_LOW)){
        q = sqrt(-2*log(p));
        x = (((((C1*q+C2)*q+C3)*q+C4)*q+C5)*q+C6) / ((((D1*q+D2)*q+D3)*q+D4)*q+1);
    }
    else{
        if ((P_LOW <= p) && (p <= P_HIGH)){
            q = p - 0.5;
            r = q*q;
            x = (((((A1*r+A2)*r+A3)*r+A4)*r+A5)*r+A6)*q /(((((B1*r+B2)*r+B3)*r+B4)*
                r+B5)*r+1);
        }
        else{
            if ((P_HIGH < p)&&(p < 1)){
                q = sqrt(-2*log(1-p));
                x = -(((((C1*q+C2)*q+C3)*q+C4)*q+C5)*q+C6) / ((((D1*q+D2)*q+D3)*
                        q+D4)*q+1);
            }
        }
    }
    if(( 0 < p)&&(p < 1)){
        e = 0.5 * erfc(-x/sqrt(2)) - p;
        u = e * sqrt(2*M_PI) * exp(x*x/2);
        x = x - u/(1 + x*u/2);
    }
    return (mean + stddev * x);
}
```

In-plane damage model

```
double E_1(double E_1_0c, double E_1_0t, double gamma, double eps_is_fc_absolut,
        double eps_us_fc_absolut, double eps_is_ft, double eps_us_ft, double d_u_fc,
        double d_u_ft, double D_11, double D_11_R, double eps_11, double epsrat_11){
    double eps_i_fc, eps_u_fc, eps_i_ft, eps_u_ft, d_11_t, d_11_c, eps_is_fc,
        eps_us_fc, E_1_s;
    eps_is_fc = -1. * eps_is_fc_absolut;
    eps_us_fc = -1. * eps_us_fc_absolut;
        if (eps_11 < 0.){
        eps_i_fc = eps_is_fc * (1. + D_11_R * fabs(epsrat_11));
        eps_u_fc = eps_us_fc * (1. + D_11_R * fabs(epsrat_11));
        if (eps_11 <= eps_u_fc){
            d_11_c = 1. - (1. - d_u_fc) * eps_u_fc / eps_11;
        }
        if (eps_u_fc < eps_11 && eps_11 <= eps_i_fc){
            d_11_c = d_u_fc * (eps_i_fc - eps_11) / (eps_i_fc - eps_u_fc);
        }
        if (eps_i_fc < eps_11){
            d_11_c = 0.;
        }
        if (eps_11 <= eps_i_fc){
            E_1_s = E_1_0c * (1. + gamma * eps_11) * (1. - d_11_c);
        }
        if (eps_i_fc < eps_11 && eps_11 <= 0.){
            E_1_s = E_1_0c * (1. + gamma * eps_11);
        }
    }
        if (eps_11 >= 0.){
        eps_i_ft = eps_is_ft * (1. + D_11_R * fabs(epsrat_11));
        eps_u_ft = eps_us_ft * (1. + D_11_R * fabs(epsrat_11));
        if (eps_u_ft <= eps_11){
            d_11_t = 1. - (1. - d_u_ft) * eps_u_ft / eps_11;
        }
        if (eps_i_ft <= eps_11 && eps_11 < eps_u_ft){
            d_11_t = d_u_ft * (eps_i_ft - eps_11) / (eps_i_ft - eps_u_ft);
        }
        if (eps_i_ft > eps_11){
            d_11_t = 0.;
        }
        if (0. <= eps_11 && eps_11 < eps_i_ft){
            E_1_s = E_1_0t;
        }
        if (eps_i_ft <= eps_11){
            E_1_s = E_1_0t * (1. - d_11_t);
        }
    }
    return (E_1_s * (1. + D_11 * fabs(epsrat_11)));
}
```

```
double sig_11(double sig_11_prev, double epsrat_11, double eps_11, double deps_11,
        double E_1_0c, double E_1_0t, double gamma, double eps_is_fc,
        double eps_us_fc, double eps_is_ft, double eps_us_ft, double d_u_fc,
        double d_u_ft, double D_11, double D_11_R){
        double dE_1, dsig_11;
        dE_1 = E_1(E_1_0c, E_1_0t, gamma,eps_is_fc,eps_us_fc,eps_is_ft,eps_us_ft,
```

```
                d_u_fc, d_u_ft, D_11, D_11_R, eps_11 + deps_11, epsrat_11) -
                E_1(E_1_0c,E_1_0t, gamma, eps_is_fc, eps_us_fc, eps_is_ft,
                eps_us_ft, d_u_fc, d_u_ft,       D_11, D_11_R, eps_11, epsrat_11);
        dsig_11 = deps_11 * E_1(E_1_0c, E_1_0t, gamma, eps_is_fc, eps_us_fc,
                eps_is_ft, eps_us_ft, d_u_fc, d_u_ft, D_11, D_11_R, eps_11,
                epsrat_11) +dE_1 * eps_11;
    return (sig_11_prev + dsig_11);
}
```

```
double Y_12(double E_2_0, double G_12_0, double b, double Y_12_U, double d_max,
        double dam_12, double dam_22, double sig_12, double sig_22,
        double Y_12_prev){
    double Y_12;
    if (dam_12 < d_max && dam_22 < d_max){
        Y_12 = sqrt(pow(sig_12, 2) / (2 * G_12_0 * (1 - dam_12)) + b *
                (pow(max(sig_22, 0.), 2) / (2 * E_2_0 * (1 - dam_22))));
        if (Y_12 < Y_12_prev){
            Y_12 = Y_12_prev;
        }
    }
    else{
        Y_12 = Y_12_U;
    }
    return Y_12;
}
```

```
double Y_22(double E_2_0, double Y_22_U, double d_max, double dam_22,
        double sig_22, double Y_22_prev){
    double Y_22;
    if (dam_22 < d_max){
        Y_22 = sqrt(pow(max(sig_22, 0.), 2) / (2 * E_2_0 * (1 - dam_22)));
        if (Y_22 < Y_22_prev){
            Y_22 = Y_22_prev;
        }
    }
    else{
        Y_22 = Y_22_U;
    }
    return Y_22;
}
```

```
double dam_12(double Y_12, double Y_22, double Y_12_0, double Y_12_C, double Y_22_U,
        double Y_12_U, double d_max, double D_12, double epsrat_12){
    double Ydyn_12_0, Ydyn_12_C, dam_12;
    Ydyn_12_0 = Y_12_0 * (1 + D_12 * fabs(epsrat_12));
    Ydyn_12_C = Y_12_C * (1 + D_12 * fabs(epsrat_12));
    if (Y_12 < Y_12_U && Y_22 < Y_22_U){
        dam_12 = max(Y_12 - Ydyn_12_0, 0.) / Ydyn_12_C;
    }
    if (Y_12 >= Y_12_U || Y_22 >= Y_22_U || dam_12 > d_max){
        dam_12 = d_max;
    }
    return dam_12;
}
```

```
double dam_22(double Y_12, double Y_22, double Y_22_0, double Y_22_C, double Y_22_U,
        double Y_12_U, double d_max, double D_22, double epsrat_22){
    double Ydyn_22_0, Ydyn_22_C, dam_22;
    Ydyn_22_0 = Y_22_0 * (1 + D_22 * fabs(epsrat_22));
    Ydyn_22_C = Y_22_C * (1 + D_22 * fabs(epsrat_22));
    if (Y_12 < Y_12_U && Y_22 < Y_22_U){
        dam_22 = max(Y_22 - Ydyn_22_0, 0.) / Ydyn_22_C;
    }
    if (Y_12 >= Y_12_U || Y_22 >= Y_22_U || dam_22 > d_max){
        dam_22 = d_max;
    }
    return dam_22;
}
```

```
double E_2(double eps_22_e, double epsrat_22, double dam_22, double E_2_0,
        double D_22){
    double E_2_s, E_2;
    if (eps_22_e < 0)
    {E_2_s = E_2_0;}
    if (eps_22_e >= 0)
    {E_2_s = E_2_0 * (1 - dam_22);}
    E_2 = E_2_s * (1 + D_22 * fabs(epsrat_22));
    return E_2;
}
```

```
double G_12(double dam_12, double epsrat_12, double G_12_0, double D_12){
    double G_12_s, G_12;
    G_12_s = G_12_0 * (1 - dam_12);
    G_12 = G_12_s * (1 + D_12 * fabs(epsrat_12));
    return G_12;
}
```

```
double sig_eps_22(double sig_22_prev, double eps_22_p_prev, double p_22_prev,
        double eps_22, double epsrat_22, double eps_22_e_prev, double deps_22,
        double dam_22, double dam22_prev, double E_2_0, double D_22, double R_0,
        double D_R, double beta, double m, double a, double *sig_22,
        double *eps_22_e, double *eps_22_p, double *p_22){
    double dE_2, dsig_22, R0dyn, R;
    dE_2 = E_2(eps_22_e_prev, epsrat_22, dam_22, E_2_0, D_22) -
        E_2(eps_22_e_prev, epsrat_22, dam22_prev, E_2_0, D_22);
    dsig_22 = deps_22 * E_2(eps_22_e_prev, epsrat_22, dam_22, E_2_0, D_22) +
        dE_2 * eps_22_e_prev;
    *sig_22 = sig_22_prev + dsig_22;
    R0dyn = R_0 * (1 + D_R * fabs(epsrat_22));
    R = R0dyn + beta * pow(fabs(p_22_prev), m);
    if (dam_22 < 1)     {
        if (fabs(a) * fabs(max(*sig_22, 0.) / (1 - dam_22) + min(*sig_22, 0.)) -
                R <= 0){
            *eps_22_e = *sig_22 / E_2(eps_22_e_prev, epsrat_22, dam_22, E_2_0,
                D_22);
            *eps_22_p = eps_22_p_prev;
            *p_22 = p_22_prev;
        }
        else{
            *sig_22 = (1 - dam_22) * R / a; //pow(a, 2);
```

```
            *eps_22_e = *sig_22 / E_2(eps_22_e_prev, epsrat_22, dam_22, E_2_0,
                D_22);
            *eps_22_p = eps_22 - *eps_22_e;
            *p_22 = p_22_prev + a * (1 - dam_22) * deps_22;
        }
    }
    else{
        *sig_22 = 0;
        *eps_22_e = 0;
        *eps_22_p = eps_22 - *eps_22_e;
        *p_22 = p_22_prev + a * (1 - dam_22) * deps_22;
    }
    return 0;
}
```

```
double sig_eps_12(double sig_12_prev, double eps_12_p_prev, double p_12_prev,
        double eps_12, double epsrat_12, double eps_12_e_prev, double deps_12,
        double dam_12, double dam_12_prev, double G_12_0, double D_12,
        double R_0, double D_R, double beta, double m, double *sig_12,
        double *eps_12_e, double *eps_12_p, double *p_12){
    double dG_12, dsig_12, R0dyn, R;
    dG_12 = G_12(dam_12, epsrat_12, G_12_0, D_12) - G_12(dam_12_prev, epsrat_12,
        G_12_0, D_12);
    dsig_12 = deps_12 * G_12(dam_12, epsrat_12, G_12_0, D_12) + dG_12 *
        eps_12_e_prev;
    *sig_12 = sig_12_prev + dsig_12;
    R0dyn = R_0 * (1 + D_R * fabs(epsrat_12));
    R = R0dyn + beta * pow(fabs(p_12_prev), m);
    if (dam_12 < 1){
        if (fabs(*sig_12 / (1 - dam_12)) - R <= 0){
            *eps_12_e = *sig_12 / G_12(dam_12, epsrat_12 + deps_12, G_12_0, D_12);
            *eps_12_p = eps_12_p_prev;
            *p_12 = p_12_prev;
        }
        else{
            *sig_12 = (1 - dam_12) * R;
            *eps_12_e = *sig_12 / G_12(dam_12, epsrat_12 + deps_12, G_12_0, D_12);
            *eps_12_p = eps_12 - *eps_12_e;
            *p_12 = p_12_prev + 2 * (1 - dam_12) * deps_12;
        }
    }
    else{
        *sig_12 = 0;
        *eps_12_e = 0;
        *eps_12_p = eps_12 - *eps_12_e;
        *p_12 = p_12_prev + 2 * (1 - dam_12) * deps_12;
    }
    return 0;
}
```

Out-of-plane model

```
double GIcValue(double E_0, double t_max_n, double G_u_n, double eps_n,
```

```
        double hcont){
    double eps_i, eps_u, modelValue;
    eps_n = eps_n * hcont;
    eps_i = t_max_n / E_0 * hcont;
    eps_u = 2. * G_u_n / t_max_n;
    if (eps_n > 0) {
        if (fabs(eps_n) < eps_i) {
            modelValue = 0.5 * E_0 * pow(eps_n, 2.);
        }
        else {
            if (fabs(eps_n) < eps_u) {
                modelValue = 0.5 / E_0 * pow(t_max_n, 2.) * hcont +
                        (pow(eps_n, 2.) / 2. - pow(eps_i, 2.) / 2) * t_max_n /
                (eps_i - eps_u) - (eps_n - eps_i) * eps_u * t_max_n /
                (eps_i - eps_u);
            }
            else{
                modelValue = G_u_n;
            }
        }
    }
    if (0.5 / E_0 * pow(t_max_n, 2.) * hcont > G_u_n) {
        modelValue = 100.;
    }
    return modelValue;
}
```

```
double GIIcValue(double G_0, double t_max_s, double G_u_s, double eps_s,
        double hcont){
    double eps_i, eps_u, modelIIValue;
    eps_s = eps_s * hcont;
    eps_i = t_max_s / G_0 * hcont;
    eps_u = 2 * G_u_s / t_max_s;
    if (fabs(eps_s) < eps_i) {
        modelIIValue = 0.5 * G_0 *pow(eps_s, 2.);
    }
    else {
        if (fabs(eps_s) < eps_u) {
            modelIIValue = 0.5 / G_0 * pow(t_max_s, 2.) * hcont + (pow(eps_s, 2.) /
                2 - pow(eps_i, 2.) / 2) * t_max_s / (eps_i - eps_u) -
                (eps_s - eps_i)*eps_u * t_max_s / (eps_i - eps_u);
        }
        else {
            modelIIValue = G_u_s;
        }
    }
    if (0.5 / G_0 * pow(t_max_s, 2.) * hcont > G_u_s) {
        modelIIValue = 100.;
    }
    return modelIIValue;
}
```

```
void ModelCalc(double (*array)[outPlaneDataArrayWidth], unsigned long int dim,
        double **theta_cur, double **theta_new, double hcont, double sigma,
        double *Sum1, double *Sum2, unsigned long int j){
    unsigned long int i;
```

```
    double *delta = new double[dim];
    {...}
    double *GIcCur = new double[dim];
    for (i=0; i < dim; i++){ // dim - 1, due to explicit scheme
        delta[i] = array[i][1]/pow(array[i][0], 3.) * 3.*(array[i][0]*
                pow((array[i][0]-array[0][0]), 2.)/2. - pow((array[i][0]-
        array[0][0]), 3.)/6.);
        strain[i] = delta[i]/hcont;
        GIcCur[i] = GIcValue(exp(theta_cur[j][11]), exp(theta_cur[j][29]),
                exp(theta_cur[j][28]), strain[i], hcont);
        GIcNew[i] = GIcValue(exp(theta_new[j][11]), exp(theta_new[j][29]),
                exp(theta_new[j][28]), strain[i], hcont);
        Sum1[j] += log(normDist(array[i][2], GIcNew[i], sigma));
        Sum2[j] += log(normDist(array[i][2], GIcCur[i], sigma));
    }
    delete [] delta;
    {...}
}
```

```
void ModelIICalc(double (*array)[outPlaneDataArrayWidth], unsigned long int dim,
        double **theta_cur, double **theta_new, double hcont, double h, double L,
        double sigma, double *Sum1, double *Sum2, unsigned long int j){
    unsigned long int i;
    double *delta = new double[dim];
    {...}
    double *GIIcCur = new double[dim];
    for (i=0; i < (dim-1); i++){ // dim - 1, due to explicit scheme
        delta[i] = -2. * array[i][1]*pow(array[i+1][0], 3.)*h /
                (3.*pow(array[i+1][0], 3.)+ pow(L, 3.)) * (3.*pow(array[0][0], 2.)/
        pow(array[i+1][0], 3.) - 3/array[i+1][0]);
        strain[i] = delta[i]/hcont;
        GIIcCur[i] = GIIcValue(exp(theta_cur[j][12]), exp(theta_cur[j][31]),
                exp(theta_cur[j][30]), strain[i], hcont);
        GIIcNew[i] = GIIcValue(exp(theta_new[j][12]), exp(theta_new[j][31]),
                exp(theta_new[j][30]), strain[i], hcont);
        Sum1[j] += log(normDist(array[i][2], GIIcNew[i], sigma));
        Sum2[j] += log(normDist(array[i][2], GIIcCur[i], sigma));
    }
    delete [] delta;
    {...}
}
```

Miscellaneous programs

This program is used to create histogram data from multiple MCMC output file. In its current implementation the histogram data is generated for 27 parameters. Input for this command line tool are:

1. burn-in range

2. step size

3. list of MCMC output files

```
#include <iostream>
#include <fstream>
#include <string>
#include <stdio.h>
#include <stdlib.h>
#include <math.h>
#include <limits>
using namespace std;

const int nParameters = 27;
const int nBin =100;

unsigned long int getDim(const char *filename);
int minValueFromArray(long unsigned int *array, int dim);
int maxValueFromArray(long unsigned int *array, int dim);
void getMinMax(double ***array, unsigned long int nFiles,
        unsigned long int fileLength, int numParameters,
        double *minima, double *maxima);
int main(int argc, char **argv)
{
    const int inputShift = 3;
    if (argc > (inputShift+1)){
        const int nInputFiles = argc-inputShift-1;
        long unsigned int i, j, k, l;
        long unsigned int burnInRange, stepSize;
        long unsigned int minDim, maxDim;
        ifstream infile;
        ofstream outfile(argv[argc-1]);
        long unsigned int *dimArray = new long unsigned int[nInputFiles];
        burnInRange = strtoul(argv[1],NULL,0);
        stepSize = strtoul(argv[2],NULL,0);
        for (i = 0; i < (nInputFiles); i++) {
            dimArray[i] = getDim(argv[i+inputShift]);
        }
        minDim = minValueFromArray(dimArray, (nInputFiles));
        maxDim = maxValueFromArray(dimArray, (nInputFiles));
        if (maxDim != minDim){cout<<"␣*␣INFO␣*␣Input␣files␣have␣different
␣␣␣␣␣␣␣␣␣␣␣␣␣␣␣␣dimensions!␣max:␣"<< maxDim << "\t␣minDim:␣" << minDim << endl;}
        double ***pData;
        pData = (double ***) malloc((nInputFiles) * sizeof(double **));
        if (pData != NULL){
            for(i=0; i<(nInputFiles) ; i++)
            {pData[i] = (double **) malloc(minDim * sizeof(double *));
                if (pData[i] != NULL){
                    for( j=0; j<minDim; j++)
                    {pData[i][j] = (double *) malloc(nParameters * sizeof(double));
                        if (pData[i][j] == NULL){
                            printf("Memory␣allocation␣failed.␣Exiting....");
                            return 1;
                        }
                    }
                } else {
                    printf("Memory␣allocation␣failed.␣Exiting....");
                    return 1;
                }
```

```
            }
        } else {
            printf("Memory␣allocation␣failed.␣Exiting....");
            return 1;
        }
        for (i=0; i<(nInputFiles); i++) {
            infile.open(argv[i+inputShift]);
            for (j=0; j<minDim; j++) {
                infile >> pData[i][j][0] >> pData[i][j][1] >> pData[i][j][2] >>
                        pData[i][j][3] >> pData[i][j][4] >> pData[i][j][5] >>
                pData[i][j][6] >> pData[i][j][7] >> pData[i][j][8] >>
                pData[i][j][9] >> pData[i][j][10] >> pData[i][j][11] >>
                pData[i][j][12] >> pData[i][j][13] >> pData[i][j][14] >>
                pData[i][j][15] >> pData[i][j][16] >> pData[i][j][17] >>
                pData[i][j][18] >> pData[i][j][19] >> pData[i][j][20] >>
                pData[i][j][21] >> pData[i][j][22] >> pData[i][j][23] >>
                pData[i][j][24] >> pData[i][j][25] >> pData[i][j][26];
            }
            infile.close();
        }
        double *minima = new double[nParameters];
        double *maxima = new double[nParameters];
        double *binSize = new double[nParameters];
        unsigned long int (*bin)[nBin] = new unsigned long int[nParameters][nBin];
        double (*normBin)[nBin] = new double[nParameters][nBin];
        unsigned long int stepCount;
        getMinMax(pData, nInputFiles, minDim, nParameters, minima, maxima);
        for (i = 0; i < nParameters; i++) {
            binSize[i] = (maxima[i] - minima[i]) / (nBin - 1);
            for (j = 0 ; j < nBin; j++) {
                bin[i][j]=0;
            }
        }
        stepCount = stepSize;
        for (l =0; l < nInputFiles; l++) {
            for(i = 0; i < minDim; i++) {
                if (i >= burnInRange && stepCount == stepSize){
                    for (j=0; j < nParameters; j++) {
                        for (k = 0; k < nBin; k++){
                            if ((pData[l][i][j] >= minima[j] + k * binSize[j]) &&
                                (pData[l][i][j] < minima[j] + (k+1) * binSize[j])){
                                bin[j][k]++;
                                break;
                            }
                        }
                    }
                    stepCount = 0;
                }
                if (i >= burnInRange){stepCount++;}
            }
        }
        for (i = 0; i < nParameters; i++){
            for (j=0; j < nBin; j++) {
                normBin[i][j]= ((double) bin[i][j]/(minDim*nInputFiles))/binSize[i];
            }
        }
        for (i=0; i < nBin; i++) {
```

```
            for (j=0; j<nParameters; j++) {
                outfile << (minima[j] + i * binSize[j]) << "\t" <<
                        normBin[j][i] << "\t";
            }
            outfile << endl;
        }
        free(pData);
        pData = NULL;
        delete [] minima;
        delete [] maxima;
        delete [] binSize;
        delete [] bin;
        delete [] normBin;
    } else {
        cerr << "No␣file␣available␣for␣reading." << endl;
        cout << endl;
        cout << "This␣script␣was␣compiled␣for␣" << nParameters << "␣parameters!"
                << endl;
        cout << endl;
        cout << "Usage␣of␣the␣program:" << endl;
        cout << "command␣<burn-in␣range>␣<step␣size>␣<input␣file␣1>
␣␣␣␣␣␣␣␣␣␣␣␣␣␣␣␣<input␣file␣2>␣...␣<input␣file␣n>␣<output␣file>" << endl;
        cout << endl;
        return 1;
    }
        return 0;
}
```

```
unsigned long int getDim(const char *filename){
    ifstream infile;
    unsigned long int count;
    string s;
    if (!infile){
        cerr << "Cannot␣open␣file␣" << endl;
        return (-1);
    }
    count = 0;
    infile.open(filename);
    while (!infile.eof()){
        getline(infile, s);
        count++;
    }
    infile.close();
    return count;
}
```

```
int minValueFromArray(long unsigned int *array, int dim){
    double value = std::numeric_limits<double>::infinity();
    long unsigned int i;
    for (i=0; i<dim; i++) {
        value = min((double) value, (double) array[i]);
    }
    return value;
}
```

```
int maxValueFromArray(long unsigned int *array, int dim){
```

```
    double value = -std::numeric_limits<double>::infinity();
    long unsigned int i;
    for (i=0; i<dim; i++) {
        value = max((double) value, (double) array[i]);
    }
    return value;
}
```

```
void getMinMax(double ***array, unsigned long int nFiles,
        unsigned long int fileLength, int numParameters, double *minima,
        double *maxima){
    unsigned long int i, j, k;
    for (i = 0; i < numParameters; i++) {
        minima[i] = std::numeric_limits<double>::infinity();
        maxima[i] = -std::numeric_limits<double>::infinity();
    }
    for (i = 0; i < nFiles; i++) {
        for (j = 0; j < (fileLength - 1); j++) {
            for (k = 0; k < numParameters; k++) {
                minima[k] = min(minima[k], array[i][j][k]);
                maxima[k] = max(maxima[k], array[i][j][k]);
            }
        }
    }
}
```

This program can be used to compute the mean values and corresponding standard deviations from multiple input files. In its current form the command line tool expects data for 27 parameters are. The program requires the following inputs:

1. burn-in range
2. step size
3. list of input files

```
#include <iostream>
#include <fstream>
#include <string>
#include <stdio.h>
#include <stdlib.h>
#include <math.h>
#include <limits>
using namespace std;
const int nParameters = 27;
unsigned long int getDim(const char *filename);
int minValueFromArray(long unsigned int *array, int dim);
int maxValueFromArray(long unsigned int *array, int dim);
int main(int argc, char **argv)
{
    const int inputShift = 3;
    if (argc > (inputShift+1)){
        const int nInputFiles = argc-inputShift-1;
        long unsigned int i, j, k, meanStart, meanStepLength;
```

```
        long unsigned int minDim, maxDim;
        ifstream infile;
        ofstream outfile(argv[argc-1]);
        long unsigned int *dimArray = new long unsigned int[nInputFiles];
        meanStart = strtoul(argv[1],NULL,0);
        meanStepLength = strtoul(argv[2],NULL,0);
        for (i = 0; i < (nInputFiles); i++) {
            dimArray[i] = getDim(argv[i+inputShift]);
        }
        minDim = minValueFromArray(dimArray, (nInputFiles));
        maxDim = maxValueFromArray(dimArray, (nInputFiles));
        if (maxDim != minDim){cout<<"␣*␣INFO␣*␣Input␣files␣have␣different
␣␣␣␣␣␣␣␣␣␣␣␣␣␣␣␣dimensions!␣max:␣"<< maxDim << "\t␣minDim:␣" << minDim << endl;}
        double ***pData;
        pData = (double ***) malloc((nInputFiles) * sizeof(double **));
        if (pData != NULL){
            for(i=0; i<(nInputFiles) ; i++)
            {
                pData[i] = (double **) malloc(minDim * sizeof(double *));
                if (pData[i] != NULL){
                    for( j=0; j<minDim; j++)
                    {
                        pData[i][j] = (double*)malloc(nParameters*sizeof(double));
                        if (pData[i][j] == NULL){
                            printf("Memory␣allocation␣failed.␣Exiting....");
                            return 1;
                        }
                    }
                } else {
                    printf("Memory␣allocation␣failed.␣Exiting....");
                    return 1;
                }
            }
        } else {
            printf("Memory␣allocation␣failed.␣Exiting....");
            return 1;
        }
        for (i=0; i<(nInputFiles); i++) {
            infile.open(argv[i+inputShift]);
            for (j=0; j<minDim; j++) {
                infile >> pData[i][j][0] >> pData[i][j][1] >> pData[i][j][2] >>
                        pData[i][j][3] >> pData[i][j][4] >> pData[i][j][5] >>
                pData[i][j][6] >> pData[i][j][7] >> pData[i][j][8] >>
                pData[i][j][9] >> pData[i][j][10] >> pData[i][j][11] >>
                pData[i][j][12] >> pData[i][j][13] >> pData[i][j][14] >>
                pData[i][j][15] >> pData[i][j][16] >> pData[i][j][17] >>
                pData[i][j][18] >> pData[i][j][19] >> pData[i][j][20] >>
                pData[i][j][21] >> pData[i][j][22] >> pData[i][j][23] >>
                pData[i][j][24] >> pData[i][j][25] >> pData[i][j][26];
            }
            infile.close();
        }
        double *theta_mean = new double[nParameters];
        double *theta_M2 = new double[nParameters];
        double *theta_delta = new double[nParameters];
        double *theta_variance = new double[nParameters];
        double *theta_stddev = new double[nParameters];
```

```
        unsigned long int meanStepCount, meanCount;
        meanStepCount = meanStepLength;
        meanCount = 0
        for (i = 0; i < nParameters; i++){
            theta_mean[i] = 0.;
            theta_M2[i] = 0.;
        }
        for (i = 0; i < minDim; i++) {
            if (i >= meanStart && meanStepCount == meanStepLength){
                for (k = 0; k < nInputFiles; k++) {
                    meanCount++;
                    for (j = 0; j < nParameters; j++) {
                        theta_delta[j] = pData[k][i][j] - theta_mean[j];
                        theta_mean[j] += theta_delta[j] / meanCount;
                        theta_M2[j] += theta_delta[j] *
                                (pData[k][i][j] - theta_mean[j]);
                        if (meanCount-1 == 0) {
                            theta_variance[j] = 0.;
                        }
                        else{
                            theta_variance[j] = theta_M2[j]/(meanCount-1);
                        }
                        theta_stddev[j] = sqrt(theta_variance[j]);
                    }
                }
                meanStepCount = 0;
            }
            if (i >= meanStart){meanStepCount++;}
        }
        for (i=0; i<nParameters; i++) {
            outfile << theta_mean[i] << "\t" << theta_stddev[i] << endl;
        }
        free(pData);
        pData = NULL;
        delete [] theta_mean;
        delete [] theta_M2;
        delete [] theta_delta;
        delete [] theta_variance;
        delete [] theta_stddev;
    } else {
        cerr << "No␣file␣available␣for␣reading." << endl;
        cout << endl;
        cout << "This␣script␣was␣compiled␣for␣" << nParameters <<
                "␣parameters!" << endl;
        cout << endl;
        cout << "Usage␣of␣the␣program:" << endl;
        cout << "command␣<burn-in␣range>␣<step␣size>␣<input␣file␣1>
␣␣␣␣␣␣␣␣␣␣␣␣␣␣␣␣␣<input␣file␣2>␣...␣<input␣file␣n>␣␣<output␣file>" << endl;
        cout << endl;
        return 1;
    }
return 0;
}
```